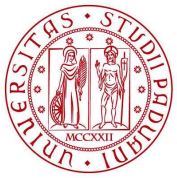

UNIVERSITÀ
DEGLI STUDI
DI PADOVA

Sede amministrativa: Universitá degli studi di Padova

SCUOLA DI DOTTORATO DI RICERCA IN ASTRONOMIA
INDIRIZZO: Astronomia
XXIII CICLO

Planet detection with SPHERE and EPICS

Direttore della scuola: Ch.mo Prof. Giampaolo Piotto
Coordinatore d'indirizzo: Ch.mo Prof. Giampaolo Piotto
Supervisore: Ch.mo Prof. Raffaele Gratton

Dottorando: Dino Mesa

Summary

In the last fifteen years a large amount (more than 500) of extrasolar planets has been found. However, until now the great majority of them has been discovered exploiting indirect techniques like e.g. the radial velocity method (that gives, actually, the most important contribution), the transit method, the microlensing method and others.
Direct imaging of extrasolar planets would be very important to sample the external parts of the extrasolar systems where the most important indirect methods (e.g. radial velocity) are not able to get until now, and to test the model on the formation of the planetary systems. However, direct imaging of extrasolar planets is very difficult because of the great luminosity contrast ($\sim 10^{-6 \div -7}$ for a giant planet and $\sim 10^{-9}$ for an Earth-like planet) and the small separation (few tenths of arcsec for a planet at ~ 10 AU at some tens of pc) between the companion object and the central star. Until now just a few extrasolar planets have been imaged around stellar or substellar (brown dwarfs) objects.
In the near future, some instruments like SPHERE (that will operate at ESO VLT) promise to be able to largely improve the number of planets that will be found through direct imaging. These instruments to work properly, however, we should be able to strongly reduce the impact of the speckle noise. To this aim, various differential imaging methods have been developed in these years like e.g. the Spectral Differential Imaging (that exploits the spectral characteristics of the searched planets), the Angular Differential Imaging (that exploits the rotation of the Field of View to subtract the static speckle pattern) and the Spectral Deconvolution (that exploits the spectral characteristics of the speckle pattern itself). All these methods have been tested during the simulations that we performed on the SPHERE IFS performances with some modifications to adapt them to the characteristics of the instrument (see Section 3.2). The results of these simulations confirm that, using the SPHERE IFS instrument in association with differential imaging techniques, we will be able to get luminosity contrasts between the companion object and the central star of the order of some 10^{-7} at separations of less than 1 arcsec. Moreover, from our simulations, it seems that spectral deconvolution can get slightly better contrasts with respect to the spectral differential imaging method.
An example of possible data analysis on real data is given in Chapter 2 where I present the results of the analysis performed on data from the NACO Large Program.
In Section 3.3 I then present the results of an analysis made to test the astrometric potential of SPHERE IFS exploiting, in particular, the characteristics of the speckle pattern. It results that these methods should allow an astrometric precision better than 1 mas. In Section 3.4 I then present a possible pipeline developed for the IFS data reduction with the aim to find and characterize eventual companion objects.
A further development in the field of direct imaging of extrasolar planets should be reached with EPICS, which is an instrument designed to work at the future ESO European Extremely Large Telescope (E-ELT). It is at present in the post Phase A. In Chapter 4 I present the results of a laboratory experiment aimed to test the possible advantages in using an apodizer in place of a traditional pupil mask. It resulted that, probably due to the presence of ghosts, we are not able to strongly reduce the cross-talk

using an apodizer but however its level is well below the requested values.
Finally in the same Chapter I present the preliminary opto-mechanical design of the IFS that will be part of EPICS. This design has been presented at the Phase A meeting of the instrument.

Sommario

Negli ultimi quindici anni un gran numero (piú di 500) di pianeti extrasolari sono stati scoperti. Comunque, fino ad oggi la gran parti di essi é stata scoperta sfruttando tecniche indirette come per esempio le velocità radiali (che forniscono in effetti il contributo piú importante), il metodo dei transiti, il metodo che sfrutta il microlensing e altri.
L'imaging diretto di pianeti extrasolari sarebbe estremamente importante perché permetterebbe di campionare le zone piú esterne dei sistemi planetari extrasolari dove i metodi indiretti principali (per esempio le velocità radiali) non sono in grado di arrivare fino ad ora e perché permetterebbe di testare i modelli di formazione dei sistemi planetari. Ad ogni modo, l'imaging diretto di pianeti extrasolari é estremamente difficile a causa del grande contrasto di luminosità ($\sim 10^{-6\div-7}$ per un pianeta gigante e $\sim 10^{-9}$ per un pianeta di tipo terrestre) e della piccola separazione (pochi decimi di arcsec per un pianeta a $\sim$ 10 UA e a qualche decina di pc dal Sole) fra il pianeta e la stella centrale. Fino ad oggi solo pochi pianeti extrasolari sono stati scoperti per mezzo di imaging diretto attorno a oggetti stellari e substellari (nane brune).
Nel prossimo futuro, alcuni strumenti come SPHERE (che opererà al VLT dell'ESO) dovrebbero essere in grado di aumentare di molto il numero di pianeti scoperti tramite imaging diretto. Perché questi strumenti funzionino nel modo migliore, sarà comunque necessario ridurre fortemente il rumore dovuto alle speckle. A questo scopo, un certo numero di metodi di imaging differenziale sono stati sviluppati in questi anni come per esempio lo *Spectral Differential Imaging* (che sfrutta le caratteristiche spettrali del pianeta che stiamo cercando), l'*Angular Differential Imaging* (che sfrutta la rotazione del campo di vista per la sottrazione del pattern di speckle statico) e la *Spectral Deconvolution* (che sfrutta le caratteristiche spettrali dello stesso speckle pattern). Tutti questi metodi sono stati testati nel corso delle simulazioni che abbiamo effettuato allo scopo di controllare le performance dell'IFS di SPHERE con alcune modifiche pensate per adattarli alle caratteristiche dello strumento (vedere il Paragrafo 3.2). I risultati di queste simulazioni confermano che, usando l'IFS di SPHERE assieme ad alcune di queste tecniche di imaging differenziale, saremo in grado di ottenere contrasti di luminosità tra un pianeta e la stella centrale dell'ordine di qualche 10^{-7} per separazioni inferiori ad 1 arcsec. Inoltre, dalle nostre simulazioni, sembra che la *spectral deconvolution* permetta di ottenere contrasti leggermente migliori di quelli ottenuti con lo *spectral differential imaging*.
Un esempio di analisi di dati provenienti da un caso reale é dato nel Capitolo 2 dove presento i rsultati dell'analisi effettuata sui dati ottenuti con il *NACO Large Program*.
Nel Paragrafo 3.3 presento i risultati dell'analisi svolta per verificare il potenziale per l'astrometria dell'IFS di SPHERE sfruttando, in particolare, le caratteristiche dello *speckle pattern*. Il risultato di questa analisi é che questi metodi dovrebbero consentire una precisione astrometrica migliore di 1 mas. Nel Paragrafo 3.4, presento invece una possibile *pipeline* sviluppata per l'analisi dei dati provenienti dall'IFS con lo scopo, in particolare, di trovare e caratterizzare pianeti.
Un ulteriore sviluppo nel campo dell'imaging diretto di pianeti extrasolari dovrebbe essere ottenuto con EPICS che é uno strumento progettato per operare presso il futuro *European Extremely Large Telescope* dell'ESO. Lo strumento si trova al momento in

post Fase A. Nel Capitolo 4 presento i risultati di un esperimento di laboratorio che aveva lo scopo di verificare i possibili vantaggi ottenuti sostituendo un apodizzatore ad una maschera tradizionale nella pupilla dello strumento. Da questo esperimento é risultato che, probabilmente a causa della presenza di *ghost*, non siamo in grado di ridurre il *cross-talk* usando un apodizzatore ma che, ad ogni modo, il suo livello é ben sotto i valori richiesti.
Infine, in questo Capitolo presento il progetto opto-meccanico preliminare dell'IFS che sarà parte di EPICS. Questo progetto é stato presentato al meeting per la Fase A dello strumento.

Contents

List of Figures

List of Tables

Chapter 1

Introduction

1.1 Search of extrasolar planets

Since the discovery of the first Jupiter mass companion object around the solar type star 51 Pegasi in 1995 (Mayor & Queloz , 1995), more than 500 planetary objects orbiting around stars other than the Sun have been discovered exploiting different techniques. In this Chapter I will present a brief review of the most important of these methods.
Great part of the extrasolar planets detected until now has been discovered exploiting indirect methods, that is exploiting some of the effects caused on the light from the host star by the presence of the planet. The indirect techniques can be divided into three wide categories:

1. methods that exploit the dynamical perturbation of the star given by the presence of a companion objects. This category comprises three different methods:
   - the radial velocity technique
   - the astrometric perturbation technique
   - the timing delay technique
2. the transit technique
3. the microlensing technique

1.1.1 Dynamical perturbation of the star

The motion of a planet around its host star will cause a motion of the star around the barycentre of the star-planet system with a period P equal to the orbital period of the planet and with a semimajor axis a_S equal to:

$$a_S = a_p \cdot \left(\frac{M_p}{M_S} \right) \tag{1.1}$$

where a_p and M_p are the semimajor axis and the mass of the planet respectively while M_S is the mass of the star. This fact can be exploited to implement the methods that are described below.

Radial velocity technique

A great majority of the extrasolar planets that have been discovered until now, has been detected using this technique. The orbit of the star around the barycentre of the star-planet system causes a periodic variation of the radial velocity (RV) of the star. The semi-amplitude of this variation is given by the following formula:

$$K = \left(\frac{2\pi \cdot G}{P}\right)^{\frac{1}{3}} \cdot \frac{M_p \cdot \sin i}{\left(M_p + M_S\right)^{\frac{2}{3}}} \cdot \frac{1}{(1-e^2)^{\frac{1}{2}}} \tag{1.2}$$

where i is the inclination angle between the normal to the orbital plane and the line of sight and e is the eccentricity of the planetary orbit.
Clearly, because the radial velocity variations increase with the planet mass and decrease with the separation, this method tends to find preferably giant planets in close orbits. In order to detect the planet signal, accuracies of better than $15m \cdot s^{-1}$ are needed. To this aim it is necessary the use of moderately large telescope and long integration times to obtain the required high S/N and high resolution spectra required.
To find Earth-like planets we would need accuracies of the order of $0.03m \cdot s^{-1}$ that are not possible with the actual instruments while the perspective is more favorable for the next decade. However, the real problem for this high precision is due to the intrinsic variations in stellar radial velocities (jitter). While some improvements are possible, they are very expensive in terms of telescope time.

The astrometric perturbation technique

The projection on the celestial sphere of the motion of a star orbiting around the star-planet barycentre appears as an ellipse with an angular semi-major axis α given by the following formula:

$$\alpha = \left(\frac{M_p}{M_S}\right) \cdot \left(\frac{a}{d}\right) \tag{1.3}$$

where α is expressed in arcsec, the semimajor axis of the planetary orbit a is expressed in AU and the distance between the star and the Sun is expressed in pc. The value of α for a Jupiter like planet at a distance of 10 pc is 500 mas, while for a Earth-like planet at the same distance it is 0.3 mas. From equation 1.3, it is apparent that this method is particularly sensible to planets with large semimajor orbital axis (and then long orbital period). This technique is then complementary to the radial velocity method. Note however that is very difficult to realize instruments having this extremely high astrometric accuracy over long time intervals.

The timing delay technique

The extreme accuracy of the signal from evolved objects like millisecond pulsars allows to exploit them to find companion objects eventually orbiting around them. The period of the radio signal will vary proportionally to planet mass (M_p) and to its orbital period

(P) according to the formula (Wolszczan , 1997):

$$\tau_p = 1.2 \cdot \left(\frac{M_p}{M_{Earth}}\right) \cdot \left(\frac{P}{1yr}\right)^{\frac{2}{3}} \tag{1.4}$$

In equation 1.4, the value of τ_p is calculated in millisecond. This technique allowed to detect a 2 earth masses planet around $PSR1257 + 12$ that were the first extrasolar planets actually detected (Wolszczan & Frail , 1992).

1.1.2 The transit technique

This method allows to detect an extrasolar planet measuring the diminishing of the stellar flux due to the transit of the companion object on the stellar disk. The luminosity fall is given by the following relation:

$$\frac{\Delta L}{L} \simeq \left(\frac{R_{planet}}{R_*}\right)^2 \tag{1.5}$$

From this formula we have that to find a Jupiter-like planet we need a photometric precision of the order of 1%, while to find an Earth-like planet we need a photometric precision of 0.007%. While for the Jupiter-like case observations from the Earth with small telescopes can be used, to detect Earth-like planets space observations are needed.
The probability to observe a transit is of the order of:

$$p \sim \frac{R_*}{a} \tag{1.6}$$

It is clear that the probability diminishes when the orbital radius a increases and, then, this method find more easily companion objects near to the central star. The length of a transit is then given by:

$$t_T \leq \frac{PR_*}{\pi a} \tag{1.7}$$

Solar spots, flares pulsations and any other photometric variations can mimic a planetary transit. For this reason the best targets to be used for the transit method are low activity stars (e.g. G-K spectral type stars). Moreover, photometric binaries might appear to have a light curve virtually indistinguishable from that of transiting planets under various circumstances. For this reason, radial velocity confirmation is needed to establish the real nature of the system. This is the main bottleneck of transit observations.
From the transit method we can directly infer the planetary radius and, if the planet has been detected with the radial velocity method too, we can obtain its mass M_p from the minimum mass ($M_p \cdot \sin i$). From these values we can then estimate important physical quantities as the average density and the surface gravity of the planet. Moreover, various spectral informations can be obtained from both principal (planet in front of the star) and secondary (star in front of the planet) transit. This allows a fine physical characterization of transiting planets.

1.1.3 The microlensing technique

This method was proposed by Paczynski (1986) with the aim to search dark stellar mass objects in the halo of our galaxy. It occurs when a stellar mass object (at tipically a few Kpc from the Sun) lenses the image of another star (the object) at a few times this distance. It is distinguished by the usual gravitational lensing by the fact that different images generated by the lens object are too close each other to be separated spatially. For this reason, the total effect is a temporarily enhancement of the luminosity of the lensed object. While for a single lensing object the light curve describing the phenomenon is symmetric with a single maximum, if the optical lens consists of two (or more) point like objects the resulting light curve becomes much more complex. It is possible to define curves in the space where the magnifying effect become very large (caustic). When the magnified object crosses these zones, the light curve shows various secondary maxima. The position of the caustic on the image plane and its shape depends from the planet-star mass ratio and from the planet-star separation. The main effect of the variation of the companion mass, is to narrow the secondary maxima, so that a good sampling of the light curve allows to detect planets with small masses.
The main disadvantage of this method is that the microlensing event is very improbable, so that we have to observe toward very crowded field of view to enhance the probability. Moreover, once observed, it is very improbable that a planet discovered with this technique will be observable again and, given that the stars eligible for this method are at a distance of some Kpc from the Sun, its targets cannot be detected with other techniques (like radial velocities) that work properly only for very nearby stars. In spite of these limitations, the microlensing technique may provide useful statistical informations on the frequency of planets over a wide range of masses and separations.

1.2 Imaging of extrasolar planets

Direct imaging of extrasolar planets would be very important to overcome some of the problems that plagues the indirect methods described in the previous Paragraphs. In particular the motivations for the imaging of extrasolar planets are:

- Detection of a companion object around active stars is possible just through direct imaging. In particular, this is true for very young stars that are the ambient where, according to the most common formation theories, the planets form.

- Photometry of the planets at different wavelengths would give a first direct test of the atmospheric models.

- The determination of the planets luminosity at different ages will give informations about the planetary evolution.

- Spectroscopy of the companion objects will give informations about the chemical composition and about the physical properties (e.g. temperature or presence of clouds). This would allow a further test of the atmospheric models.

- The detection of the planetary polarimetric signal dominated by reflected ligth (especially from clouds) would provide very important informations about the planetary atmosphere.

However, the imaging of extrasolar planets is at the moment very challenging because of the very high luminosity contrast between the companion objects and the star ($\sim 10^{-6}$ corresponding to 15 magnitudes for a Jupiter-like planets and $\sim 10^{-10}$ corresponding to 25 magnitudes for an Earth-like planet) and the small angular separation between them (few tenths of arcsec for a planet at $\sim$ 10 AU at some tens of parsec). At this moment, just a few planetary mass objects have been imaged around stellar and substellar objects like e.g. HR8799 (Marois et al. , 2008), Fomalhaut (Kalas et al. , 2008), 2M 1207 (Chauvin et al. , 2009) and βPictoris (Lagrange et al. , 2010).
The next generation of instruments aimed to the imaging of extrasolar planets will exploit extreme adaptive optics (XAO) systems to correct aberrations up to a high order, providing a high Strehl ratio (SR), and high efficiency coronagraphs to attenuate the on-axis PSF and reduce its diffraction pattern. The combination of these two devices should be able to reduce the stellar background down to a value of around 10^{-5} at separations of few tenths of arcsec. The residual background will be given mainly by the speckle noise generated by the atmosphere and the telescope pupil phase distortion. To further improve the contrast achievable with these instruments, it will be mandatory to apply differential imaging techniques, such as angular differential imaging (ADI) (Marois et al. , 2006), the simultaneous spectral differential imaging (S-SDI) (see e.g. Marois et al. 2005) and the spectral deconvolution (SD) (see Thatte et al. 2007).
In the next years in particular two instruments will be able to exploit these techniques to do imaging of extrasolar planets. These are the Gemini Planet Imager (GPI) at the Gemini South Telescope (Macintosh et al. , 2006) and SPHERE at the ESO Very Large Telescope (VLT) (Beuzit et al. , 2006). A further development will be EPICS (Kasper et al. , 2010) at the future 42 m ESO European Extremely Large Telescope.
SPHERE (see Chapter 3) and EPICS (see Chapter 4) have been argument of my work that is described in this thesis.

1.3 Speckle noise theory

In this Paragraph we present a short theory about the formation of the speckle pattern. The arguments exposed here are mainly taken from Racine et al. (1999).
A short exposure image of a point source can be seen as the interference pattern between different coherent light beams of typical diameter r_0 (defined as Fried length) distributed over the full aperture of the telescope. A single subpupil of size r_0 would form a PSF of width λ/r_0, while two such subpupils separated by D (where D represents the telescope diameter) constitute a two beam interferometer. They will form a pattern of fringes of width $\sim \lambda/D$ and, as a result of the randomly varying phase difference between the two aperture, this fringes move within the broad PSF envelope. The introduction of other subpupils produces different patterns of interference. Where these fringes interfere constructively a bright speckle of width $\sim \lambda/D$ appears. The

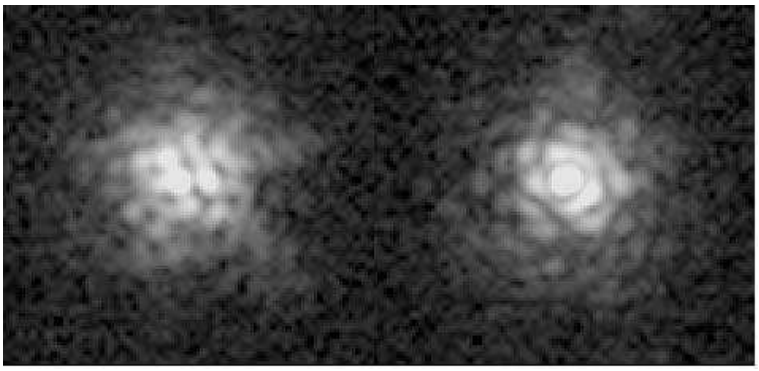

Figure 1.1: Short exposure (0.1 s) natural (left) and AO-compensated (right) images of a star obtained with the CFHT bonnette AO-system at $\lambda = 1.6\mu m$ and $D/r_0 \sim 4$. The grey scale is logarithmic in intensity (from Racine et al. 1999). Notice that the increasing Speckle brightness toward the PSF center and the appearance of the bright diffraction limited core with size $\sim 2\lambda/D$.

numerical density of the speckle pattern is given from:

$$n_{sp} = \frac{0.342}{\pi \cdot \left(\frac{\lambda}{D}\right)^2} \tag{1.8}$$

In Adaptive Optics compensated images a fraction of the stellar light F, given by the Strehl ratio SR, is deviated into a bright central speckle with dimensions $\sim 2\lambda/D$, leaving the rest of the flux given by $(1 - SR) \cdot F$ into the halo speckles that, averaged by time, give origin to the smooth long exposure halo (see Figure 1.1).

The variability of the wavefront gives origin to the speckle noise. The speckle pattern, indeed, changes randomly over a small fraction of a second and an area of the detector will measure a different speckle brightness for each τ_0 that defines the speckle lifetime given from:

$$\tau_0 \sim \frac{r_0}{\Delta v} \tag{1.9}$$

where Δv is the velocity dispersion in the turbulent seeing layers across the telescope line of sight.

The speckle noise, however, is not simply given from the number of speckles recorded in one area of the detector times the mean speckle brightness because speckles are not independent events but are produced through interference and their number per unit of area is necessarily constant as showed by equation 1.8.

The enormous complexity of the speckle noise forces to avoid any analytical treatment and to perform numerical simulations where atmospheric parameters, telescope, AO and coronagraph specifications are inputs and realistic screens of the residual phase distortions are generated. The simulated speckle noise can then be compared to that obtained during observation at the telescope. The results of these simulations demonstrate that speckle noise dominates by a factor of $10^2 - 10^4$ over other noise contributions in the AO-compensated region of a telescope PSF.

1.4 Correction of speckle noise

Various effects limit the contrast that can be achieved using an high contrast imager like SPHERE or EPICS IFS. We order them according to the following classes:

1. Calibration of the stellar coronagraphic halo
2. Instrumental effects (e.g. spurious effects associated with cross-talk between the various IFU sub-pupils - see Paragraph 3.2.8).
3. Photon noise
4. Detector issues (noise associated with detector read-out noise, thermal background and limited accuracy on detector flat field, detector persistence)
5. Noise possibly introduced in the operations of data reduction and analysis (e.g. interpolations).

In this work, we focus most attention on the estimation of the residuals associated with the calibration errors (we defined in this way all the errors given by sources other than the photon noise) of the stellar coronagraphic halo, that is one of the most difficult to be corrected.

1.4.1 Theoretical concepts

In the following I give a short theoretical analysis of performance limitations of high contrast differential imaging in terms of instrumental wavefront errors. A complete description should include estimations of the effects of:

- Beam shift due to atmospheric refraction
- Fresnel propagation (”instrumental scintillation”)
- Pupil shift between telescope and instrument
- Zenith variations (pupil de-rotator, ADC prisms)
- Effect of pre and post coronagraph absolute differential aberrations

The purpose of this section is to build a model of the instrument linking wavefront specifications for each optical surface to final instrument performances based on this theory.

Basic definition

Let us consider the phase errors $\Phi_F = 2\pi WFE/\lambda$, and let us assume that they are small enough to ignore second order terms and higher. Consider odd and even components

of phase map, hence separate real and imaginary parts of its Fourier Transform considering phase errors small enough to ignore the second and higher order of the Fourier series:

$$E_F = Pe^{i\Phi} \sim P(1 + i\Phi_F) \tag{1.10}$$

In our notation:

- WFE, wavefront map in nm
- Φ, phase map in radians
- P is the Fourier coefficient
- $\Phi = \Phi^e + i\Phi^o$
- $\phi = FT(\Phi) = \phi^e + i\phi^o$

Non-coronagraphic imaging

In this notation, the image-plane amplitude without coronagraph (notation: $q = p \otimes \phi$) is:

$$e_F = FT(E_F) = p \otimes (\delta + i\phi_F^e - \phi_F^o) = p - q_F^o + i \cdot q_F^e \tag{1.11}$$

The image without coronagraph is then:

$$I_F = |e_F|^2 = (p - q_F^o)^2 + (q_F^e)^2 = p^2 - 2pq_F^o + {q_F^e}^2 + {q_F^e}^2 = I_{Airy} + I_{pinned} + I_o \tag{1.12}$$

where I_{pinned} are the "pinned speckles" and

$$I_o = {q_F^e}^2 + {q_F^o}^2 = |p \otimes \phi_F|^2 = (2\pi/\lambda)^2 |FT(PW_F)|^2 = (2\pi/\lambda)^2 PSD_{2D} \tag{1.13}$$

An ideal coronagraph removes the "coherent" part of the pupil field:

$$E_C = E_F - P \sim iP\Phi_F \tag{1.14}$$

Hence the image-plane amplitude is:

$$e_C = FTE_C = p \otimes (\phi_F^e - \phi_F^o) = -q_F^o + iq_F^e \tag{1.15}$$

And image intensity is:

$$I_C = |e_C|^2 = {q_F^e}^2 + {q_F^o}^2 = I_o = (2\pi/\lambda)^2 PSD_{2D} \tag{1.16}$$

Azimuthal statistic

The PSD_{2D}, like the image, is speckled, i.e. noisy. For an isotropic phase map, the statistical parameters of the second order speckle pattern (PSD_{2D}) are expected to have a cylindrical symmetry. I define the following notation for azimuthal statistics:

- Azimuthal average: <>
- Azimuthal standard deviation: <<>>

For better clarity, I define the PSD in terms of its azimuthal average:

$$PSD =< PSD_{2D} > \tag{1.17}$$

Different phase screens with the same statistical parameters will then have identical PSD although the exact shape of their PSD_{2D} will be different.
Averaging the PSD_{2D} for a large number of phase screens will yield a 2D function whose radial profile will be identical to the individual (azimuthally averaged) PSD. This PSD averaging applies to the atmosphere. We now elaborate the formulae for:

$$\Phi = \Phi_{ATM} + \Phi_{INSTR} \tag{1.18}$$

We find instantaneous intensity composed of PSD_{2DATM}, $PSD_{2DINSTR}$ and a cross term. For a long exposure, $PSD_{2DATM} = |FT(\Phi_{ATM})|^2$ reduces to the PSD_{ATM}, which has zero azimuthal standard deviation, plus a cross term, containing $FT(\Phi_{ATM})$ whose time average is zero.
We are left with the instrumental $PSD_{2DINSTR}$ showing speckles added to the PSD_{ATM} halo. So, azimuthal average of long exposure image is:

$$< I_{coro} >= (2\pi/\lambda)^2(PSD_{ATM} + PSD_{INSTR}) \tag{1.19}$$

and the azimuthal standard deviation of the long exposure image is:

$$\sigma(I_{coro}) = (2\pi/\lambda)^2 << PSD_{2DINSTR} >> \tag{1.20}$$

From this we obtain:

$$\sigma(I_{coro}) = (2\pi/\lambda)^2 \cdot PSD_{INSTR} \tag{1.21}$$

Summarizing we expect that the overall shape of PSF I_{coro} at entrance of IFS will be essentially that given by the atmosphere, and then related to PSD_{ATM}, while its variance will be dominated by the instrumental PSD_{INSTR}.
An important consequence is that different sources of noise might have different dependence on I_{coro}, $\sigma(I_{coro})$, or even be independent from them. This has an important impact in the evaluation of the performances of SPHERE and other IFS based high contrast imagers, and on their optimization. Table 1.1 summarizes the main dependences. I will find that for SPHERE, which has moderately large value for WFE_{Inst} (only about a third of WFE_{Atm}), photon noise dominates only for faint sources ($J > 4$), while calibration errors dominate for brighter sources effectively limiting its detection performances. High contrast imagers characterized by much smaller values of WFE_{Inst} are expected to behave better for bright sources. However, when $WFE_{Inst} << WFE_{Atm}$, constraints on flat field errors might be very stringent, and these systems might be effectively flat field limited for bright sources.

1.5 Simultaneous Spectral Differential Imaging (S-SDI)

In this section, we will combine the previous considerations with the differential imaging approach of Marois et al. (2000). These authors only consider a single value for the

Dependence	WFE Dependence	Noise type
I_{coro}	WFE^2_{atm}	Photon Noise Flat Field Noise
$\sigma(I_{coro})$	WFE^2_{Inst} (sometimes WFE^2_{NCP})	Calibration errors Cross-Talk Interpolation errors
Additive noise	None	Read Out Noise Sky Background

Table 1.1: Dependences of main sources of noise

WFE, thus neglecting the details of the distribution of the PSD with spatial frequency on the pupil plane. Furthermore, the analysis of Marois et al. (2000) was made for a non-coronagraphic system that is not the case for SPHERE and EPICS. However, we assume that the Marois et al. (2000) approach applies to these systems by considering the instrumental wavefront error WFE_{Inst}. Albeit rough, this approach allows to take into consideration most of the relevant effects, and predict simulated performances of differential imagers within reasonably good approximation. However, we should remind that following the treatment of the previous subsection, we should expect that the general shape of the PSF should be determined by WFE_{Atm} rather than by WFE_{Inst}. This will play a significant role when we will consider sources of errors other than residuals of speckle correction.

Contrast from monochromatic images

Following Marois et al. (2000), the order of magnitude of the residuals after correction of "non common path errors" and "speckle phase chromatism" can be obtained starting from the relation connecting wavefront errors and Strehl Ratio. We will assume that this last represents the typical strength of speckles. This relation is given by the Marechal approximation:

$$SR = 1 - (2\pi \cdot WFE/\lambda)^2, \tag{1.22}$$

where SR is the Strehl Ratio, WFE represents the r.m.s. of the phase delay of the wavefront and λ is the wavelength. For monochromatic images, the dependence of contrast C from WFE and λ at a given radial distance is then given by:

$$C_{Mono} \sim 1 - SR = (2\pi WFE/\lambda)^2, \tag{1.23}$$

where the WFE to be considered here is WFE_{Inst}, at least for long enough exposures.

Contrast from Single Differences

Within this approach, speckle chromatic errors are null only if SR is independent from λ, which is obviously not a typical case. In general, we may assume that the exact functional dependence of SR on wavelength is not known, and consequently also the

way speckles change with wavelength is also unknown, although we may expect that for well corrected systems (large SR values), the dominant term is proportional to the inverse of wavelength squared, so that differential imaging may achieve a gain of at least an order of magnitude in contrast.
From Marois et al. (2000), we have then:

$$C_{SD} = 2 \cdot d\lambda/\lambda \cdot C_{Mono} \tag{1.24}$$

where $d\lambda$ is the separation between the wavelengths at which the two images are taken. In absence of other sources of noise, the gain in contrast expected from single differences with respect to monochromatic images is then proportional to $\lambda/(2d\lambda)$, which is about an order of magnitude when parameters typical of differential imagers are considered. We note that this approach gives a linear dependences of contrast on wavelength separation $d\lambda$, the limiting value is set by the slope of the wings of the spectral features used for differential imaging, and values as large as $\sim$ 20-30 can be obtained in favorable cases.

Non common path errors

The Marois et al. (2000) approach can be easily extended to take into account non common path errors. Using the same development considered for speckle chromatism errors, we get a more general formula for single differences:

$$\begin{aligned} C_{SD} &\sim (4\pi^2/\lambda^2)[2 \cdot WFE^2_{Inst} \cdot d\lambda/\lambda + WFE^2_{NCP}] \\ &= [2 \cdot d\lambda/\lambda + (WFE_{NCP}/WFE_{Inst})^2] \cdot C_{mono} \end{aligned} \tag{1.25}$$

where the first term of the sum represents the speckle chromatism errors, and the second one the non-common path errors, here WFE_{NCP} is the WFE error related to non-common path. We will thereinafter assume that non-common path errors are static, and can not be then eliminated by longer exposures. This formula may be used for both single and double difference method (for IRDIS, in the first case WFE_{NCP}=10 nm, in the second WFE_{NCP}=4 nm).

Contrast from double difference

A further improvement can be obtained using double differences. Marois et al. (2000) proposed a different approach using three different wavelengths and combining them in a way described by this formula:

$$\Delta^2 I = (I_1 - I_2) - k(I_1 - I_3) \tag{1.26}$$

where k is a factor constant over all the pixel of the considered images. This method, the double difference method, should give a contrast gain given by:

$$\frac{\Delta^2 I}{I} \cong (3 - 2\sigma^2_\Phi)\sigma^2_\Phi \frac{\Delta\lambda_{12}\Delta\lambda_{13}}{\lambda^2} \tag{1.27}$$

Simplifying their notation[1], we write the contrast that can be achieved using this technique as:

$$C_{DD} \sim (12\pi^2/\lambda^2) WFE^2_{Inst} \cdot (d\lambda/\lambda)^2 = 3 \cdot (d\lambda/\lambda)^2 \cdot C_{Mono} \quad (1.28)$$

In absence of other sources of noise, the gain in contrast expected from double differences should then be proportional to $(\lambda/d\lambda)^2/3$. While very large gains seems apparently possible using double differences, it should be noticed that while for single differences there is quite a large flexibility in the value of $d\lambda$, in the case of double differences $d\lambda$ is fixed at $\sim 0.08\mu m$ by the intrinsic width of the spectral features of a methane dominated giant planets (that is the spectra that we assume for this method) used in differential imaging. For this reason, the gain possible with double differences is limited to about 70 (for methane dominated spectra), irrespective of the spectral resolution provided by IFS.

Contrast from multiple single/double difference

Further gains are possible if differential imaging techniques are applied to various sets of wavelengths (pairs for single differences, triples for double differences), which is possible using IFS. In this case, we expect a gain which is approximately proportional to the square root of the indipendent sets of wavelength used. It must be noticed that to be considered independent from each other, the different bands should sample different projected slit widths. In the limit of super-sampling (projected slit width $\sim$ 2 pixels), the number of independent spectral bands is then about half that of the pixels along the spectra. Furthermore, pairs are made of two different bands (the band with the planet signal and the reference band without it), and a few bands can not be used because they have some planet signal only. In the case of the SPHERE IFS, some $\sim$ 10 pairs (and a similar number of triples) can be used, resulting in a further gain by a factor of about 3.
Two main aspects should be considerd:

- The combination of differential images should be made in such a way to enhance the planet signal above background. This requires that reference images (those without the planet signal) should be rescaled for the wavelength difference with respect to the image where the planet signal is present, and that these in turn should not be scaled. The scheme adopted in the SPHERE simulations is described in more detail in Section 3.2.4.

- The combination of different differential images can be optimized according to the expected noise level, by adopting an optimized weighting scheme. This is different, depending on which source of noise dominates. An adequate noise model is then required to optimize planet detection.

[1]The formula considered by Marois et al. (2000) is more general, considering also the possibility that the wavelength separation between the individual bands were not constant. Here, we rather assumed that $\lambda_2 - \lambda_1 = \lambda_3 - \lambda_2 = \Delta\lambda$.

	Calibration noise	Multiplicative Noise
Monochromatic Coronagraphic Image	Φ^2_{Inst}	a
Single Difference	$2 \cdot \Phi^2_{Inst} \cdot (\Delta\lambda/\lambda)$	$sqrt2 \cdot a$
double Difference	$3 \cdot \Phi^2_{Inst} \cdot (\Delta\lambda/\lambda)^2$	$sqrt3 \cdot a$
Non-common path	Φ^2_{NCP}	$sqrt2 \cdot a$
Multiple Single Differences	$2 \cdot \Phi^2_{Inst} \cdot (\Delta\lambda)/sqrtn_{pairs}$	$sqrt2 \cdot a/sqrtn_{pairs}$
Multiple Double Differences	$3 \cdot \Phi^2_{Inst} \cdot (\Delta\lambda/\lambda)^2/\sqrt{n_{triples}}$	$sqrt3 \cdot a/sqrtn_{triples}$
Rotation (uncorrelated)	Above/$\sqrt{[\alpha r/(2 \cdot \lambda/D)]}$	
Rotation (correlated, azimuthal filter	Above/$[\alpha r/(2 \cdot \lambda/D)]$	

Table 1.2: Summary of calibration noise dependences

Table 1.2 summarizes the expected dependences of calibration noise (contrast) expected for differential imaging techniques. Both Single and Double Multiple Differences might be considered. However, in practice, Double Multiple Differences do not yield results better than Multiple Single Differences (see e.g. Figure 3.7), because the wavelength separation to be considered is generally large.

1.6 Temporal speckle variation: Angular Differential Imaging (ADI)

The approach we followed insofar is general, and it can be applied to both static and time variable speckles. For what concern time variable speckles, we expect that their impact scale down with the square root of time, so that it may become small in long exposures. Static speckles do not change and their impact should not scale down with time. However, static speckles may be calibrated and removed from images using Angular Differential Imaging (ADI, see Marois et al. 2006). ADI is a PSF calibration technique that consists of the acquisition of a sequence of images with the telescope rotator turned off (at the Cassegrain focus) or adjusted (Nasmyth) to keep the instrument and telescope optics aligned. This setup improves the stability of the quasi-static PSF structure throughout the sequence, while it causes a slow rotation of the field of view (FOV) with respect to the instrument. Note that only the FOV, not the PSF, rotates with time. Since the FOV rotates during an exposure, companion PSFs are smeared azimuthally. Let us now assume aberrations which are static with respect to the pupil, while field rotates. In this case it is not only possible to reduce the noise due to static speckles because different independent background speckles are sampled while the planet image moves with respect to the fixed speckle pattern (which would give a square root reduction factor), but rather directly subtract them by simply assuming that the speckle pattern measured in two epochs, one when the planet was in a location, and the other one when the planet is not anymore there, are identical. This principle (which is essentially the same concept of the double calibration adopted with IRDIS) can very easily be applied to IFS data simulations by simply filtering out low frequency azimuth variations of the signal obtained after de-rotating images so that the

planet image keep fixed. This is different from the traditional ADI technique because of the peculiar nature of the IFS simulations (see Paragraph 3.2 for more detail). It can then be combined with other differential imaging techniques in order to improve achievable contrasts.
Of course this procedure works for static speckles (that is speckles that do not change with the time) fixed with respect to the pupil (which is what we are assuming), and also for quasi-static speckles that have a lifetime significantly longer than the time required by the field to rotate more than an Airy disk at the planet location, practically a few minutes in most interesting cases if only field rotation due to Earth rotation is considered. The procedure can be optimized by adopting an azimuth filtering, whose cut-off frequency is a function of radial distance. This is essentially what we are doing in the procedure described in Section 3.2.5. We found that the effect of this filtering is more efficient at relatively large separations. However we find that this is very effective already in the region 0.2-0.5 arcsec for a field rotation of 30 degrees.
It should be noticed that the square root factor would still apply in the case of speckles with lifetimes shorter than the time required by the field to rotate by an Airy disk at the planet location, which practically means of the order of a few minutes, depending on the location in the field. In fact, in this case, speckles can not be removed by this calibration procedure. However, since the noise due to (uncorrelated) speckles with lifetimes shorter than the total exposure time should increase with the square root of the exposure time, the limiting contrast should increase with the square root of time, like in a photon noise limited case. The conclusion is that at least with IFS there should be always a significant gain in having long exposures (note that the same approach should also be applicable to IRDIS).
Let us now consider this issue in a quantitative way. We begin by considering the case of quasi-static speckles, which is the minimum gain we can get when exploiting field rotation. The improvement in contrast S in this case is given by:

$$S_{QS} = S_0 / \sqrt{[1 + \alpha r/(2\lambda/D)]} \tag{1.29}$$

where S_0 is the contrast for the no rotation case, r is the separation, α is the rotation angle (in radians), λ is the wavelength and D is the telescope diameter. If r=0.5 arcsec, α =30 degrees, we have a gain of 0.91 mag if $\lambda = 1.25\mu m$, and of 0.78 mag if $\lambda = 1.6\mu m$. Gain should be $\sqrt{3}$ times larger for a rotation of 90 degrees.
The gain is larger for static speckles. While in principle they may even cancel out after azimuthal filtering, in practice this is not possible, because there is always a loss of information in the filtering procedure. With the method we adopted, a fraction of the speckles remains uncorrected. This is due to the fact that in order not to cancel out the planet signal (which has a spatial frequency similar to the speckles), we have to average signal within a number of pixel n_p along the arc, which is larger than the typical size of a planet image (this is the same to say that we should have a cut-off frequency lower than the typical spatial frequency of planetary signal). This implies that speckles falling in the bins at an angular distance equal to half of the field rotation from the planet position can not be canceled out. The net gain with respect to un-rotated images with optimal filtering will then be equal to :

$$S_{static} = S_0 / [1 + \alpha r / 2\lambda / D] \tag{1.30}$$

With respect to the case of the quasi-static speckles, the gain is:

$$S_{Static} = S_{QS} / \sqrt{[1 + \alpha r/(2\lambda/D)]} \quad (1.31)$$

Practically speaking, for r=0.5 arcsec and α=30 degrees, we then expect a further gain of 0.91 mag if $\lambda = 1.25\mu m$, and of 0.78 mag if $\lambda = 1.6\mu m$. This further gain is significant, but still some residual pattern remains uncorrected.
Equations 1.30 and 1.31 have two important consequences:

1. Since the rotation of the field with respect to the pupil increases with time, there is a considerable reduction of the static aberration calibration limit with time. The gain depends on the declination of the target, but it may be much larger than the values quoted above.

2. For a given separation, the subtraction of static and quasi-static speckles is more efficient for larger telescope, by a factor proportional to D (in the first case) and to $\sqrt{D}$ in the second one.

Table 3.6 compares calibration 5σ limiting contrast (in mag) for SPHERE using the analytic approach with results of detailed simulations. Results are for a location at 0.5 arcsec from field centre with calibration of static speckles by means of field rotation. On the whole, the comparison is fairly good, altough the gain obtained from simulations is somewhat smaller than expected from the analytic model. This is likely due to division of images in quadrants due to the coronagraph. Azimuthal filtering do a quite good job in improving results.

1.7 Spectral Deconvolution

1.7.1 Principle

Thatte et al. (2007) proposed a different way to look at the data cube, that is called spectral deconvolution. This method may be considered as an extension of the double difference imaging of Marois et al. (2000), but it has the merit to better emphasize regularities of the speckle pattern (see also Sparks & Ford 2002). The principle is that speckles are expected to change regularly with wavelength (see left panel of Figure 1.2). After appropriate radial scaling of the monochromatic images (proportionally to the wavelength λ), spectra for each spaxel should be well reproduced by a smooth function, likely represented by a low order polynomial with $1/\lambda$ as independent variable (see Figure 1.3). If such polynomials are then subtracted, and the images are rescaled back, the resulting data cube should result clean of speckles (however, as Figure 1.3 illustrates, some residuals are still present in realistic simulations; for the SPHERE CAOS simulations, residuals with respect to a low order polynomial in a $1/\lambda$ are of the order of 5-10%; since some $\sim$ 30 spectral points are used, the expected improvement using this method is of about 50-100 over the monochromatic coronagraphic images). The method to work properly, it should be possible to clean the image from the planet image. In the scaled images, the radial location of the planet images changes proportionally to wavelength (see central panel of Figure 1.2). Outside a given separation

(bifurcation point), speckle pattern at a given wavelength can be reconstructed (and eliminated) using regions unaffected bt the planet image (see right panel of Figure 1.2). Inside the bifurcation point a (less reliable) iterative procedure is required, which makes some assumptions about the shape of the speckle pattern to be subtracted.
The radial coordinate of the bifurcation point is given by:

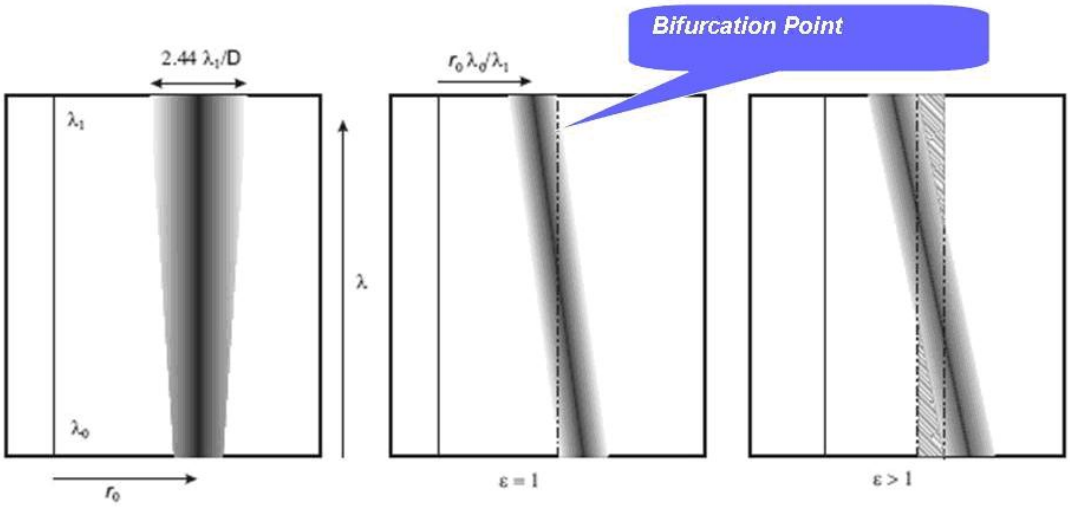

Figure 1.2: Illustration of the principle of the spectrum deconvolution method by Thatte et al. (2007). The different diagrams represents slices of the IFS data cube with radial and wavelength coordinates. The shadowed area represents the area covered by the planet image. The right panel represents the original data cube, while the other panels represent the data cube after transformation of the radial coordinate proportionally to wavelength. After this transformation, the speckle pattern should be represented by a low order polynomial in $1/\lambda$. Note that the planet spectrum occupies now an inclined band on this transformed plane. The right panel shows how the large inclination of the planet spectrum that is obtained outside the bifurcation point allows to define areas free from the planet image at any radial coordinate.

$$r = 2\epsilon 1.22(\lambda_0/D)[\lambda_1/(\lambda_2 - \lambda_1)] \tag{1.32}$$

where λ_1 and λ_2 are the minimum and the maximum wavelength of the IFS spectra (0.95 and 1.35 μm for the z-J-mode and 0.95 and 1.70 μm for the z-H-mode in the case of SPHERE), λ_0 an intermediate value, D the telescope diameter and ϵ a suitable parameter relates to the "inclination" of the spectra of the planet within the datacube in the scaled images. If $\epsilon = 1$ we have the situation where, at a given scaled radial distance, there is no spectral region clean from the planet image. If $\epsilon > 1$ there is some part of the scaled image free from the planet signature, that can be used to reconstruct the speckle profile. The bifurcation point for the SPHERE IFS is at about 0.20 arcsec

Technique	Spectral differential Imaging	Spectral deconvolution
Assumption about planetary spectrum	Yes (e.g. methane dominated)	None
Assumption about speckle dependence on wavelength	None, if spectra are hyper sampled	Can be modeled (e.g. by a low order polynomial)
Calibration errors after subtraction	$2\Phi^2_{Inst}(\Delta\lambda/\lambda)/\sqrt{n_{pairs}}$ (for multiple single difference), $3\Phi^2_{Inst}(\Delta\lambda/\lambda)^2/\sqrt{n_{triples}}$ (for multiple double differences)	0 (if modeling is correct), practically $\sim 0.05 - 0.1\Phi^2_{Inst}/\sqrt{n_\lambda}$ (even neglecting Fresnel propagation)
Useful regions of spectrum	Those where methane bands are absent, to be compared to those where they are strong (both $\sim 1/3$ of spectrum)	Region of spectrum not contaminated by planet flux ($= 1/f(\alpha)$)
Region of applicability	Inside Nyquist radius	Outside bifurcation point

Table 1.3: Comparison between Spectral Differential Imaging and Spectral Deconvolution.

for the z-J-mode, and at about 0.12 arcsec for the z-H-mode. This corresponds to about 7-8 λ/D in the first case, and 4-5 λ/D in the second one. This is only slightly larger than the Innner Working Angle of the Coronagraph. This procedure can then be safely applied over most of the field of view of the SPHERE IFS.

1.7.2 Planet detection with spectrum deconvolution

Table 1.3 compares advantages and limitations of spectral differential imaging and spectral deconvolution techniques when looking for extrasolar planets on IFS data cube. This table indicates that both methods have their merits: at variance with the spectral differential imaging, spectral deconvolution does not require any assumption about the planetary spectrum, but requires that speckle dependence with wavelength can be modeled with a limited number of parameters, which might be difficult if e.g. Fresnel propagation errors are important. While in spectral differential imaging the fraction of the spectrum that can be used is determined by the spectral properties of the planet (e.g. extension of the regions free from and obscured by methane bands, which are both about half of the total spectrum length), in the case of the spectrum deconvolution it is limited by the spectral extension of speckles $f(\alpha)$, which depends on distance from field center.

The fraction of the spectrum that can be used with respect to the total for SPHERE IFS is given in Figure 1.4. This fraction is null within the bifurcation point, and it raises rapidly at larger separations (it is about 70-80% at the Adaptative Optic Outer working Angle, depending on the mode).

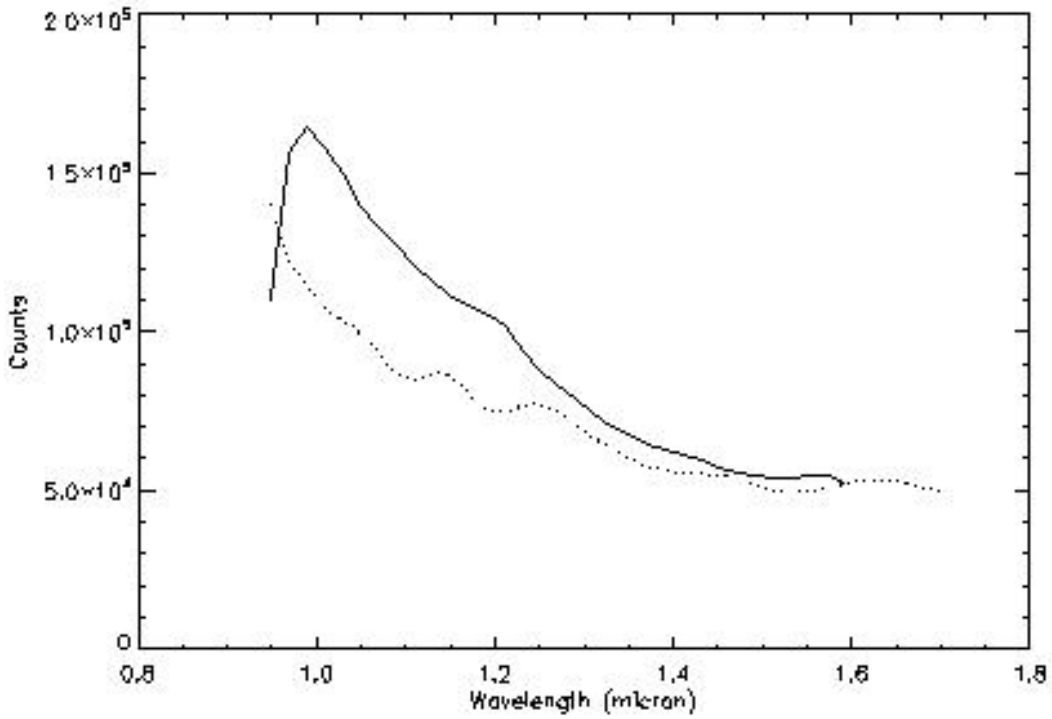

Figure 1.3: Example of the simulated spectrum on a spaxel rescaled according to wavelength for SPHERE IFS (the z-H-mode is considered here). The dotted line is the spectrum entering the IFS (that is our ”ideal” IFS). The solid line is the spectrum as measured on the detector of IFS (after appropriate data reduction). Note that the run of the spectrum is not perfectly smooth.

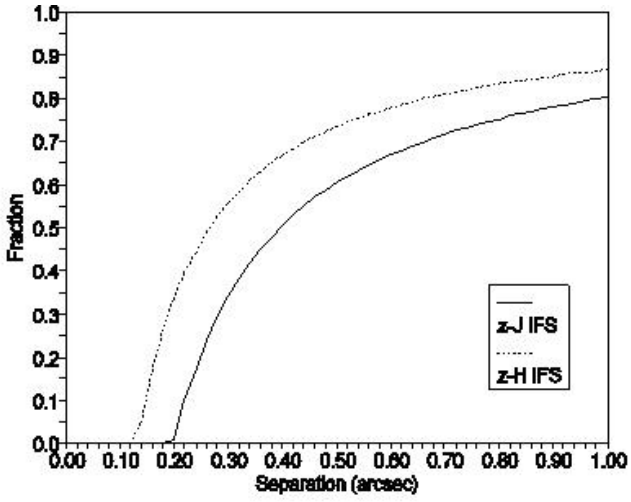

Figure 1.4: Fraction of spectrum usable to determine speckles using the Spectral Deconvolution technique, in the case of the SPHERE IFS.

1.8 Fresnel propagation

Optics in out of pupil location have an important impact on performances due to Fresnel diffraction. The main phenomenon at work here is the Talbot effect as described by Marois et al. (2006). An optic which is not conjugated to a pupil plane will modify the light distribution in a chromatic way because at this location the beam intensity distribution depends on wavelength through diffraction effects. The closer the optics are to a focal plane, the larger will be this chromaticity. Even more severe is the fact that this chromaticity is no longer smooth, but cyclic along the spectrum, when the optic is conjugated to a height that is several times the Talbot length. The Talbot length L_T is defined as:

$$L_T = 2\Lambda^2/\lambda \tag{1.33}$$

where λ is the light wavelength and Λ is the period of the aberration considered in the plane conjugated to the optic. For an aberration with a given period, the pupil complex amplitude representing the electromagnetic field changes from a pure wavefront error to a pure amplitude error over half of the Talbot length. Since the Talbot length is different for different periods (hence speckles in the field), a decorrelation occurs which depends on angular separation. The more an optic is far from pupil plane, and more the distance is larger than multiples of Talbot length, the more the decorrelation along spectral domain will be and speckle correlation is broken. In the case of SPHERE, Talbot effect is expected to be significant for those optical components located before the lenslet arrays (which samples the focal plane) and close to focal planes on very slow beams (entrance window, ADC, derotator and coronagraphic mask). It may likely introduce serious limitations on the performances. We notice that its impact also depends

on the way the IFS data cube is analyzed. As we have seen in Section 1.7, the spectral deconvolution method assumes a smooth and well modelled variation of speckle intensity with wavelength, and this assumption is likely false if the Talbot effect is important. Note that this is crucial for a very efficient suppression of speckles ($\sim 10^{-3}$) exploiting chromatic dependence. On the other hand, such a smooth dependence of speckles on wavelength is not strictly required when using a classical differential imaging approach, insofar the spectra are properly sampled in wavelength (hyper-sampling condition), and a much smaller speckle suppression factor ($\sim 10-20$ for each pair of images) is considered, like it is in the case for SPHERE.
Of course, this does not mean that Talbot effect has no impact on the contrast we may get with SPHERE. Appropriate simulations will be presented and discussed in Chapter 3.

Chapter 2

NACO

In this chapter I describe the analysis of the high contrast images of a large number of young stars observed within the NACO Large Program. This analysis was performed using a new data analysis code, prepared by the author. This code stems from the one originally prepared for the analysis of the SPHERE simulations, described in Chapter 3. However, a number of modifications and improvements were needed when using real data. They are described in the text.
Results for every individual star are given in Appendix A.

2.1 NACO Large Program

NACO is an ESO instrument installed at the Nasmyth B focus of the UT4 ot VLT. It provides adaptive optics assisted imaging, imaging polarimetry, coronagraphy and spectroscopy for wavelengths in the range between 1 and 5 μm. See Lenzen et al. (2003) and Rousset et al. (2003) for more details on this instrument.
Exploiting this instrument, the members of the SPHERE consortium designed a survey called NACO Large Program with the aim to provide an homogeneous and statistically significant study of the occurence of Extrasolar Giant Planets (EGP) and of Brown Dwarfs (BD) in wide orbits (5-500 AU) around young nearby stars. From a careful analysis of public data, a target sample of 110 young, nearby star has been selected. This study should be able to characterize the close star environment down to the planetary masses. The results will offer a unique systematic study to determine the mass and period distributions of EGP and BD at wide separations. These data, combined with all other available deep imaging data, will be used to constrain the theoretical models, including: the formation and evolution mechanisms, the physical and chemical properties of ultra-cool atmospheres, and the calibration of evolutionary models in the substellar regime.
The sample has been selected from stars recently identified in young co-moving groups and from spectrosopic surveys taking into account their declination ($< 25°$), their age (<200 Myr), their distance (<100 pc) and their R-band brightness (R<9.5). The age selection criteria was based on different diagnostics (kinematics, isochrones, Lithium,

$H\alpha$ emission, X-ray activity, stellar rotation and chromospheric activity). Known close visual (0.1-6.0 arcsec) and spectroscopic binaries have been rejected.
Stars were observed in the H-band with the S13 mode (1 pixel corresponding to 0.013 arcsec). During observations conducted in November 2009 a shift of the star relative to the coronagraphic mask position was observed. Its amplitude seems to be correlated to the field rotation motion, i.e. the parallactic angle and therefore the star declination. For this reason stars were observed without the coronagraph during the following observation runs (February, June and July 2010).
I concentrated my analysis on the targets observed during the February 2010 run.

2.2 Description of the analysis procedure

The input of the analysis procedure is a certain number of datacubes composed of the same number of images. The number of datacubes and the number of images for every datacube can change for different targets. Every image is composed by 1024×1026 pixels. The different targets saturate the detector by factor of 10-20 depending on their brightness.
The procedure is divided roughly in two different parts. The first one is applied separately to every single datacube while the second one consists in making an appropriate median of the rotated images obtained from the first part of the procedure.
The first part of the procedure is made of a series of different steps that can be repeated more than one time if necessary:

1. Definition of the centre of rotation of the FOV and of the angle of rotation.
2. Definition of the centre of the star for every single image of the datacube.
3. Subtraction of the median stellar profile from the image.
4. Bad pixel filtering of the images to eliminate hot pixels and cosmic rays.
5. Adding again the correct stellar profile to every single image.
6. Rotation of every single image.
7. New definition of the centre of the images obtained after the rotation.
8. New subtraction of the stellar profile from the rotated images.
9. All the images are shifted in such a way that the centre of the star has the same position.
10. High pass filtering of all the images.

The whole procedure is automatic except for the definition of the centre of rotation (it can however be taken as a default value). The time requested by a complete reduction depends clearly from the number of datacubes and from their dimensions, but it is however a matter of some hours.

2.2.1 First part: filtering and rotating images

In the following subsections, I describe in more details the single steps listed above.

Definition of the centre of rotation

The FOV rotates during the exposure around a point that does not correspond to the position of the central star. To define this centre of rotation we exploit the changes of the position of the background objects (if any) for different images taken at different times. The number of background objects is different from target to target. Indeed, we have more than 20 background objects visible in the raw data for the star TYC_ 8979_ 1683_ 1, but normally the number is at most 2 or 3 objects. We defined the position of a single source in the first image of the datacube and in the last one (in our analysis we exclude the last image of every datacube because it resulted to be systematically of worst quality with respect to the other ones). We then define a straight line passing for these two positions and the straight line perpendicular to it and passing for the intermediate point of the segment between these two points. The centre of rotation will be along this line and could be defined by the intersection of two different lines for a pair of objects. Clearly every couple of lines will give a different position of the centre and to obtain a final value we use the median over all the calculated positions. The centre of rotation position has been assumed to be the same for all the stacks of images. The positions of the centre of rotation that we found with this method is slightly different for different objects. However, after some test, we decided to use for all the star the same centre of rotation attributing the variation measured from star-to-star random errors. The position we adopted was the centre found for TYC_ 8979_ 1683_ 1: X=575.521: Y=420.500. This choice was given by the greatest number of background objects for this target that give more statistical reliability to the final result. The angle of rotation of every single image is calculated from the parallactic angle that we obtain from the header of the FITS image using an appropriate IDL routine.

Definition of the position of the centre of the star

This step has the aim to define the centre of the central star in the image. As said previously this position does not correspond to the centre of rotation and, however, does not correspond with the centre of the image. To define that, we have exploited two possible solutions:

- we used a 2D Gaussian fit through the IDL routine gauss2dfit.
- we have an initial guess of the centre position through an inspection by eye of the image. The procedure then calculates the sum of the standard deviation in annuli centered on the current position of the centre of the star. It then performs an iterative process changing the position of the centre of the star to try to minimize the value of this sum. We adopted a maximum number of iterations of 20.

The differences between the two procedures is normally not larger than 1-2 pixels. At the moment we have adopted the first solution that seems to give more reliable results.

However, this step is one of the more tricky of the entire procedure and has to be further improved.

Subtraction of the stellar profile

This operation is needed to allow us to perform the following bad pixel filtering. To subtract the stellar profile we simply subtract the value of the standard deviation calculated in different annuli defined around the position of the centre as obtained from the previous step.

Bad pixel filtering

This step of the procedure has been thought to eliminate hot pixel and cosmic rays from the images. For every pixel of the image the eight adjacent pixels are considered. If the counts for the considered pixel is higher than the median of the eight adjacent plus four times their standard deviation, we give to the considered pixel the value of the median of the adjacent pixels. This procedure works pretty well if we are considering an isolated hot pixel, while it does not work if we have more adjacent hot pixels.

Adding the stellar profile and rotation of the image

After the rotation of the images, the centre of the star changes its position and we have to reapply the centering procedure. However, to be able to apply this procedure (both the Gaussian and the one with minimization of the standard deviation in different annuli, see above in this Paragraph), we need to consider the stellar profile. We then sum the previously subtracted noise to the filtered images just before their rotation.
Once this has been done, we can rotate every single image with the aim to make sure that all the background objects in all the images have the same position (after an appropriate recentering). This step is made simply exploiting the ROT standard IDL routine. We run this routine setting the INTERP keyword that allows to use for the bilinear interpolation (the routine foresees the possibility of a cubic convolution interpolation but we verified that in this way the procedure is slower and does not give a better result).

Shift of the images

The next two steps are the repetitions of steps 2 and 3 on the rotated image to define the new centre position for all the image and to subtract the profile from them. We can then skip these two steps and pass to the description of the procedure to shift all the images in such a way that after this procedure they all have the same position for the centre of the central star (and of all the background objects). To obtain this we make a double spline interpolation along the x and y coordinate in the first case and along the y and the x coordinate in the second case. We then made a mean of the two images obtained in this way.

High-pass filtering

The last step is to make a high-pass filter on the obtained image simply subtracting from every pixel the median of the $n \times n$ pixels sub-image centered on the considered pixel. The value of n is determined as a function of the distance from the position of the star (that is 2 very near to it and up to 8 for the largest distances).

2.2.2 Second part: median and ADI

From the first part of the procedure we obtain a reduced datacube from every raw data datacube. All the images of this datacube have the same position angle. The first step of the second part of the procedure is to make a median on this datacubes using the IDL routine MEDARR.
We then obtain from every datacube a single median image. All these images are then rotated of the appropriate parallactic angle corresponding to the first image of the original datacube and again we take a median of all these images to obtain the final one.
Another possibility is to apply to the images resulting from the first median, a very simple routine for the Angular Differential Imaging. Our aim in preparing this procedure was not to perform an high performance ADI like e.g. LOCI (Lafreniere et al. , 2007) and ANDROMEDA (Mugnier et al. , 2008) but just to make a simple comparison with our method. This routine rotates the different images of the appropriate angle. To every pixel of the rotated images we give a different weight according to the rotation angle. We give a weight equal to zero for very small rotations to avoid to subtract the planet itself and, for the other images, we give a lower weight for the most rotated images. From every image we subtract all the images with a greater index in the final data-cube.
We tested other possible routine to make ADI, with different ways to assign the weights, but they did not seem to work better than this one. In general, it does not seem that our routine for angular differential imaging works better than the procedure that does not use it. This is probably due to the fact that the Angular Differential Imaging method does not work properly if the centre of rotation of the image does not coincide with the centre of the target star.
From a comparison with higher level ADI procedures like LOCI and ANDROMEDA, we find results comparable with those obtained with our no ADI procedure.

2.3 Results

2.3.1 Final images

The target star TYC_ 8979_ 1683_ 1 (age=68.7 Myr; mag(H)=7.474; distance=54.12 pc; Sp.Type=G7V) has been considered as a test case because of the great number of field objects that can be seen even in the raw data (more than 20 objects).
In Figure 2.1 we displayed the image resulting from our data reduction procedure when we do not apply the Angular Differential Imaging method for this target. This result is obtained by simply filtering the single images, rotating them by the appropriate angle and making median on the final datacubes. More than fifty objects can be seen by a

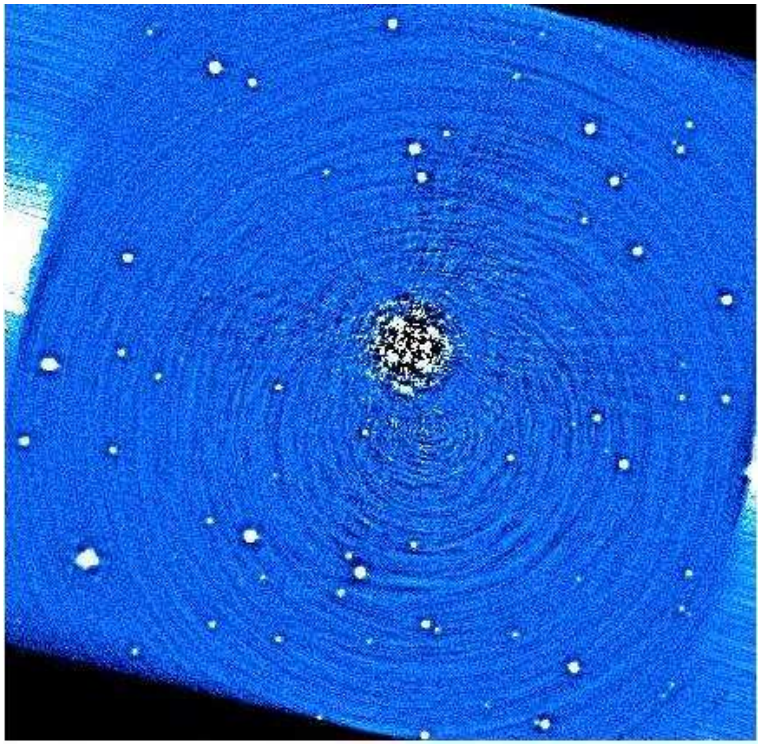

Figure 2.1: Final Image resulting from our data reduction procedure without the application of the Angular Differential Imaging procedure for the test case target TYC_8979_1683_1.

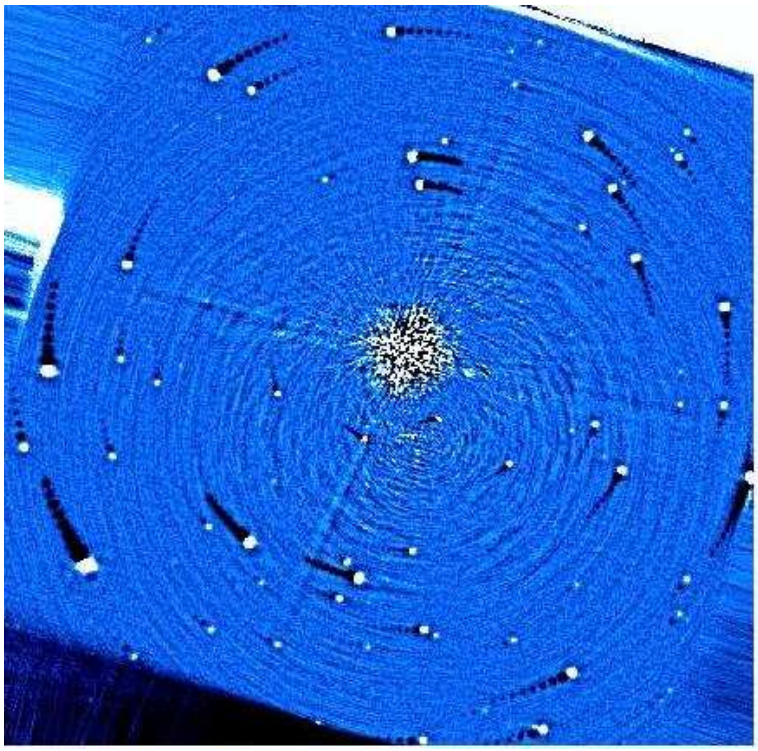

Figure 2.2: Final Image resulting from our data reduction procedure with the application of the Angular Differential Imaging procedure for the test case target TYC_8979_1683_1.

Threshold factor	N. sources	N. spurious sources
4.0	82	8
4.5	76	3
5.0	72	3

Table 2.1: Number of real (second column) and spurious (third column) sources found by our code according to different values of the threshold factor (first column) in units of the local standard deviation.

simple visual inspection of the image. In Figure 2.2, instead, we displayed the same target after the application of the Angular Differential Imaging procedure. As anticipated in the previous Paragraph, we are not able to find more sources in the final image after the application of the Angular Differential Imaging method. This is not an unexpected result given that the gain of the ADI procedure is only at small separations from the star where the speckle noise dominates.
On the first image we can then apply a procedure for the automatic search for point sources. This procedure find an object if the median flux in a circle (1 pixel radius) centered on a certain pixel, is greater than the median flux in an external annulus (radii of 3 and 5 pixel) around the same pixel plus the value of the standard deviation in this annulus multiplied for a given threshold factor. According to the value of the threshold, we are able to find more (or less) of the objects visible in the image. In Table 2.1, I show the number of real and spurious objects found according to different values of the multiplicative factor. For the case of 4.5 and 5.0 we find the same number of spurious objects (3 but we have to notice that one of them is outside the useful part of the image while the other two are very near to the centre of rotation of the images so that they are effects of the rotation itself). However, in the case with a value of 4.5 we are able to find 4 objects more than using a value of 5.0. In the case with 4.0, we are able to find 6 more real objects, but the number of spurious ones begin to be quite important. This results are graphically displayed in Figure 2.3 and in Figure 2.4 for the case with a multiplicative factor of 4.0 and 4.5 respectively. From these results we can then conclude that the better results for the multiplicative factor is between 4.0 and 4.5.
However, at this moment, this procedure is not able to identify all the sources that we are able to identify by a visual inspection and this latter seems to be again the most effective method to identify sources on the image.

Precision of the method

With the aim to test the errors in the determination of the correct position of the objects of our method we performed our data reduction method on the first and the second half of the datacube separately. We then applied on the resulting image the automatic procedure for the search of objects (the value of the detection threshold in this case was 5.0). We found 60 objects in common between the two different images and to evaluate the error we computed the difference in pixel with respect to the position of the same object in the image resulting from all the datacubes. In Figure 2.5 I display the dependence of the error on the position from the S/N of the found object. As expected

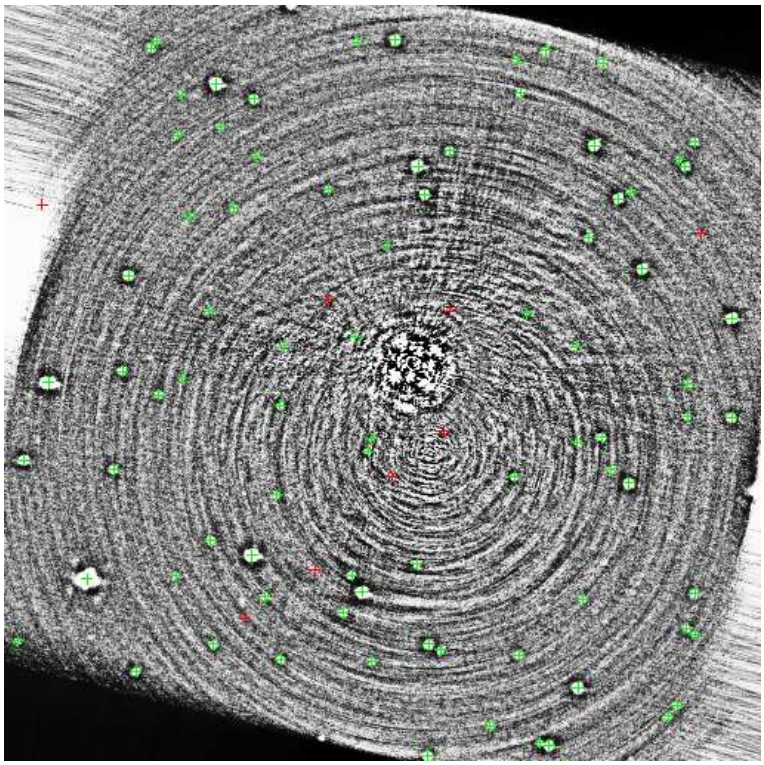

Figure 2.3: Position of the real (green crosses) and spurious (red crosses) objects found using our automatic method for the case with a multiplicative factor of 4.0.

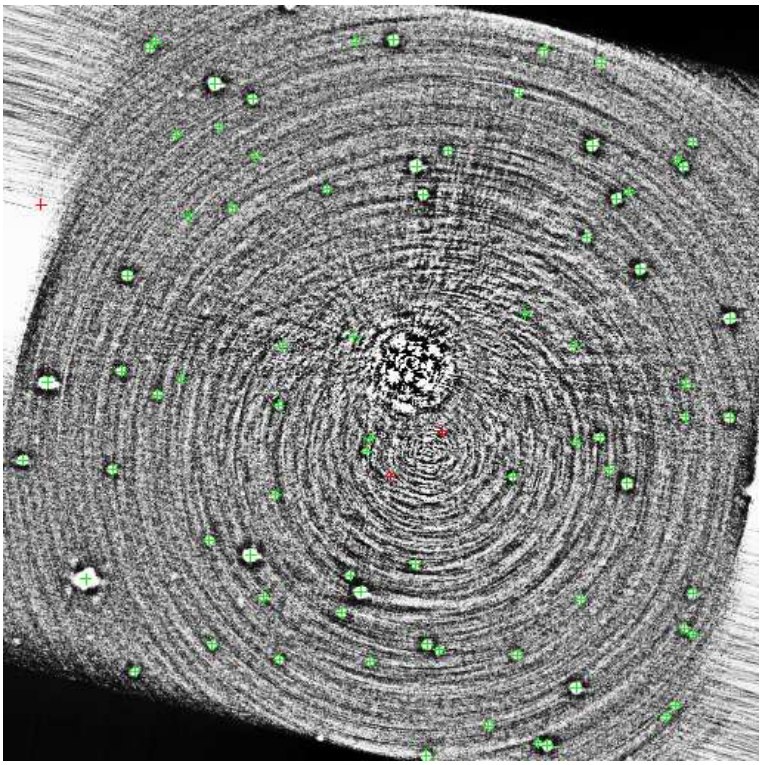

Figure 2.4: Position of the real (green crosses) and spurious (red crosses) objects found using our automatic method for the case with a multiplicative factor of 4.5.

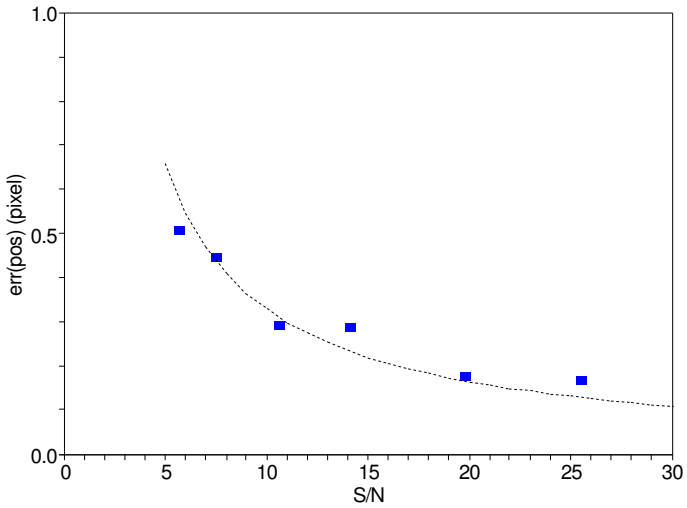

Figure 2.5: Error on the objects position as a function of the S/N. The dotted line represents the expected results for a Gaussian distribution of the error.

the results agree with those expected for a Gaussian distribution of noise, so that it is possible to evaluate the error on the position just knowing the value of the S/N.
From the analysis of the same images it is possible to estimate even the photometric error on the flux determinations made using the automatic procedure. In Figure 2.6 we made a comparison between the determination of the flux of the found objects in the first and the second half of the datacubes. In general, the agreement is quite good and the points of the plot are on a straight line. Finally, in Figure 2.7 I display the photometric error as a function of the S/N. In this case the agreement with a Gaussian distribution (dotted line in the Figure) is not so good as in the case of the error on the position, but the difference is still small.

2.3.2 Noise plots

A way to visualize the effective capability of our method to reduce the noise on the final image and to detect faint companions is to plot the standard deviation along circles at the same separation from the target star (multiplied for a factor of 5). In this way we can do a comparison between the final image obtained with the method without and with the ADI. In Figure 2.8, we displayed this result for the test case target TYC_ 8979_ 1683_ 1. To avoid the great number of peaks in the final plots, due to the great number of stars in the Field of View, we divided every circle at the same separation in different segment, we calculated the standard deviation on every single segment and made a median in such a way to reduce the impact of the field stars. We are able to

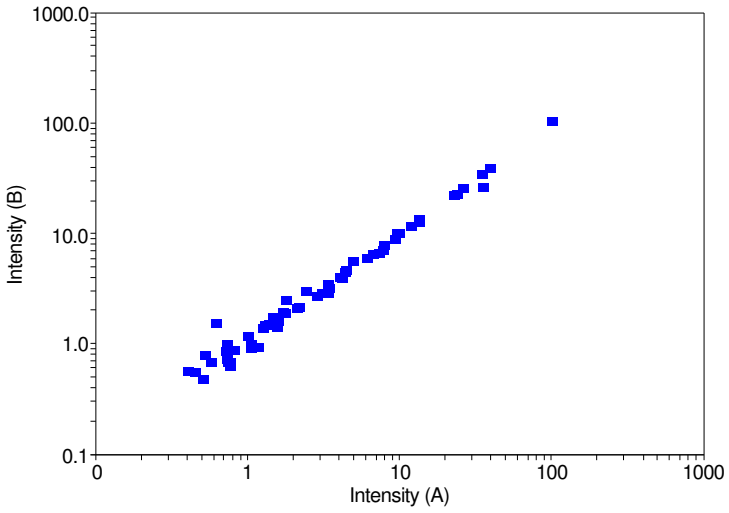

Figure 2.6: Comparison between the intensity of the two images of the two half of the datacubes.

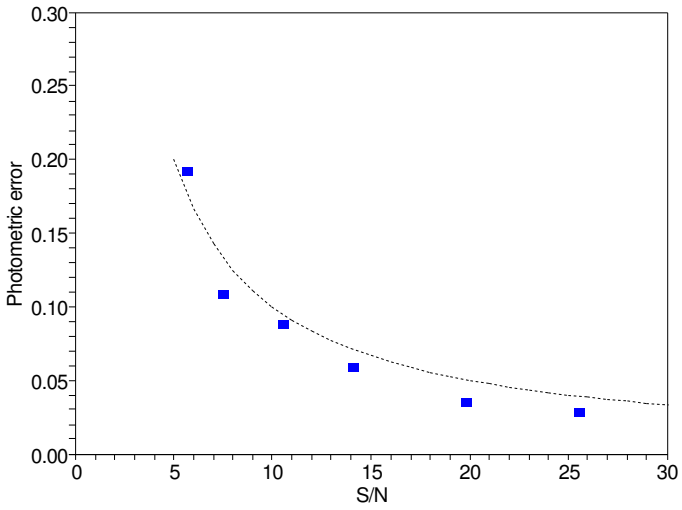

Figure 2.7: Photometric error as a function of the S/N. The dotted line represents the gaussian distribution of the error.

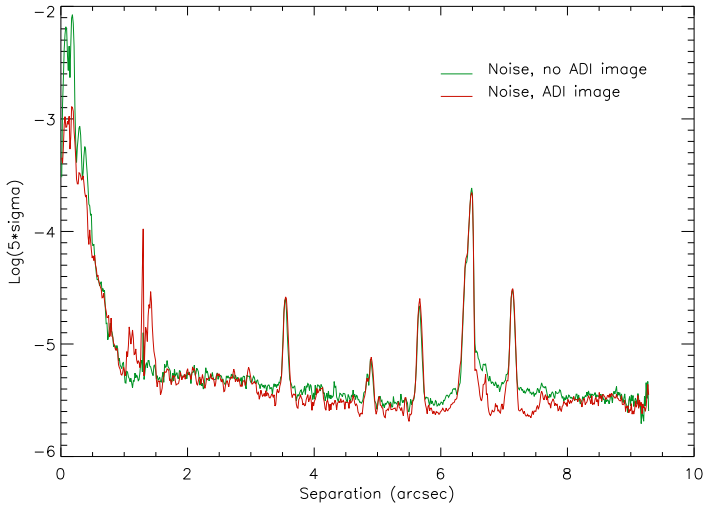

Figure 2.8: Plot of the standard deviation (multiplied for a factor of 5) versus the separation from the target star for the test case TYC_ 8979_ 1683_ 1 for the image without (green line) and with (red line) ADI.

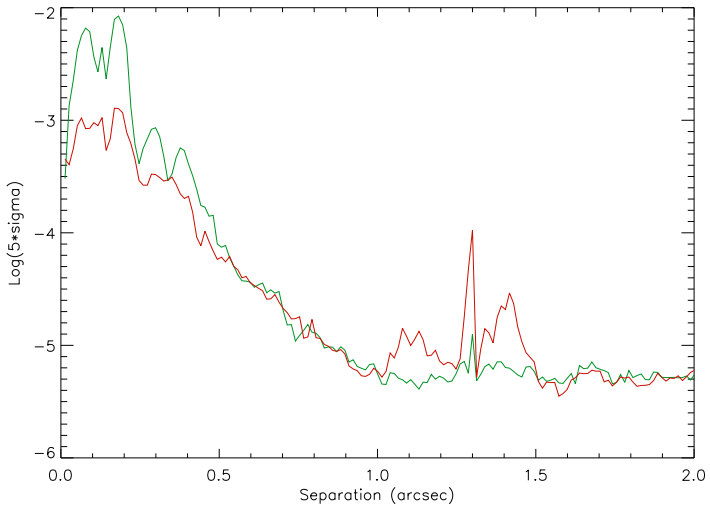

Figure 2.9: Same plot of Figure 2.8 but just the inner part (separation less than 2 arcsec from the central star) is displayed.

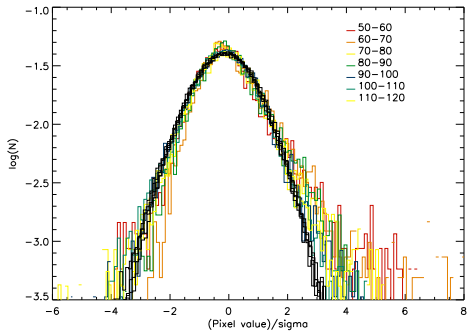

Figure 2.10: Histograms with the distribution of the pixels values in different annuli at different separation from the central star. The black plots are for separations from the central star greater than 120 pixels. In this case the step is of 40 pixels. The distribution is perfectly gaussian. The coulored plots are for inner annuli. In this case the step is of 10 pixels. It is apparent that the inner are the annulus the less gaussian is the distribution.

reduce the number of the peaks but, however, some of them remain on the final plot. We made the plot both for the image without the application of the ADI (green line in the image) and with the ADI (red line). From the comparison of these two plots, it is apparent that the noise in the two images is very similar at all the separations from the target star. We have an appreciable gain using the ADI method just very near to the centre of the star (for the inner ~ 0.5 arcsec) where, however, the noise is very high. In Figure 2.9 we display the same plot showed in Figure 2.8 but just for separations less than 2 arcsec from the central star. In this way it is enlighted the part of the plot where we have a gain using the ADI procedure.

2.3.3 Flux distribution

In Figure 2.10 the distributions of the pixel values at different separation from the central star is displayed. The black plots represents the distribution in circular annuli at separation from the central star ranging from 120 to 400 pixels. In this cases the distributions are nearly identical and have a Gaussian distribution. This is due to the fact that at such separations the background photon noise dominates over all other sources of noises (e.g. the speckle noise).
The coulored plots, instead, represent distributions into circular annuli with separations ranging from 50 to 120 pixels from the central star. In these cases the step of the annuli is of 10 pixels. It is apparent that, going nearer to the central star, the deviations from a Gaussian distribution become bigger and bigger. This is due to the increasing importance of the speckle noise with respect to the photon noise. Indeed, we expected a Gaussian distribution only if the photon noise is the most important source of noise.

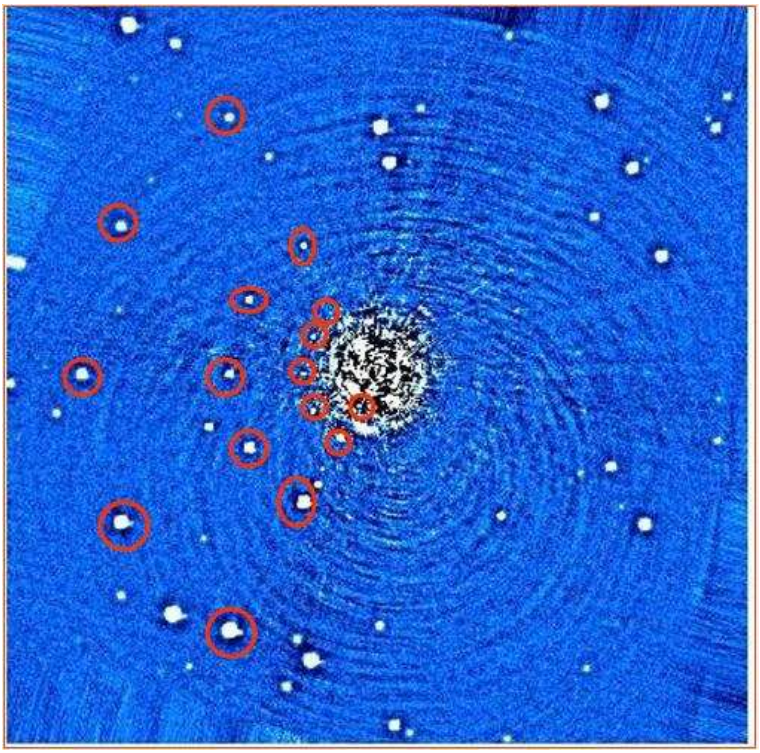

Figure 2.11: Fake objects found using our reduction method into the TYC_ 8979_ 1683_ 1 field of view. The sixteen objects found are marked with a red circle.

2.3.4 Test with fake planets

To test the effectiveness of our method in finding companion objects we apply it to a set of datacubes where 35 fake objects were injected at different separations and different luminosity contrast with respect to the central star. In these datacubes all the images were cut to a dimension of 800×800 pixels and the star was centered at the position (400,400). The separations of the fake planets from the central star were: 5, 10, 20, 40, 80, 160, 320 pixels corresponding to 0.065, 0.13, 0.26, 0.52, 1.04, 2.08 and 4.16 arcsec respectively assuming a pixel scale of 0.013 arcsec/pix. At every separation 5 different fake objects were injected at different parallactic angles of 30, 60, 90, 120, 160 degrees. The objects with PA=30 have a flux of 2.5 ADU (coorresponding to a contrast of $C \sim 2.14 \times 10^{-5}$), at PA=60 of 5 ADU ($C \sim 4.28 \times 10^{-5}$), at PA=90 of 10 ADU ($C \sim 8.56 \times 10^{-5}$), at PA=120 of 20 ADU ($C \sim 1.71 \times 10^{-4}$) and at PA=150 of 40 ADU ($C \sim 3.42 \times 10^{-4}$).
From Figure 2.11 it is apparent that we are able to find all the objects at distance of 1.04 arcsec and more. Moreover we are able to identify the most luminous object at a the separation of 0.52 arcsec.

Chapter 3

SPHERE

3.1 Introduction to SPHERE

The primary objective of SPHERE (Spectro-Polarimetric High-contrast Exoplanet Research - see e.g. Beuzit et al. (2010)) instrument for the VLT is the discovery and the study of new extra-solar giant planets orbiting nearby stars by direct imaging of their circumstellar environment. The whole design of SPHERE is optimized to reach the highest contrast in a limited field of view and at short distances from the central star. Both evolved and young planetary systems will be detected through their reflected light (differential polarimetry in the visible) and through their intrinsic emission (using IR differential imaging and integral field spectroscopy).
SPHERE is built by a consortium of eleven institutes of five European countries, together with ESO. The consortium includes the following institutes:

- Laboratoire d'Astrophysique de l'Observatoire de Grenoble (LAOG) - Grenoble, France
- Max Planck Institute for Astronomy (MPIA) - Heidelberg, Germany
- INAF - Osservatorio Astronomico di Padova - Padova, Italy
- Laboratory of Astrophysics (LAM) - Marseille, France
- Laboratoire d'etudes spatiales et d'instrumentation en astrophysique (LESIA) - Paris, France
- Fizeau - Nice, France
- Observatoire de Geneve - Geneva, Switzerland
- Eidgenssische Technische Hochschule Zurich (ETHZ) - Zurich, Switzerland
- University of Amsterdam - Amsterdam, The Netherlands
- Netherlands Institute for Radio Astronomy (NOVA/ASTRON) - Dwingeloo, The Netherlands

- ONERA - Chatillon, France

The Final Design Review took place at the end of 2008 and SPHERE is now in the integration phase. The delivery is foreseen for the beginning of 2012 and the start of science observations for the end of the same year.
High contrast imaging like that provided by SPHERE is expected to be the most efficient technique to discover planets in the outer region of the planetary systems. SPHERE will give a gain of two order of magnitude in contrast with respect to the existing instruments (like e.g. NACO - see previous Chapter) and, with a list of potential targets including several hundreds of stars, it will provide a clear view of the frequency of giant planets in wide orbits (more than 5 AU). The expected detections number of several tens will allow a first statistical discussion of the properties of the planetary systems. It should then be possible to derive the distributions of planets parameters such as mass, semi-major axis and eccentricities.
The target for SPHERE can be divided in different categories:

- Nearby young association (10-100 Myr, 30-100 pc): these targets will have brigther sub-stellar companions
- Young active F-K dwarfs in the solar neighborhood (age<1 Gyr, $d < 50$pc)
- Nearest stars (within 20 pc from the Sun, no constraint on the age): these targets will allow to probe the smallest orbits and eventually to detect planets by directly reflected light
- Stars with known planets (F-G-K stars within 50-100 pc)
- Young early type stars

To reach these scientific objectives SPHERE should be able to:

- make high contrast imaging to be able to detect giant planets 15 magnitude fainter than their host star at 0.5 arcsec (for stars with $J < 6$).
- access to very small angular separation (down to 0.1 arcsec).
- mantain optimal performances for targets up to a visible magnitude ~9 to be able to build a large enough target list (a few hundreds stars).
- access to a large enough wavelength range to be able to characterize the detected objects.

3.1.1 SPHERE general design

SPHERE complete opto-mechanical design is showed in Figure 3.1. The instrument is divided in four subsystems:

1. the Common Path and Infrastructure (CPI). It includes pupil stabilizing fore optics (tip-tilt and rotation), calibration units, the SAXO extreme adaptive optics system and the near-infrared and visible coronagraphic devices.

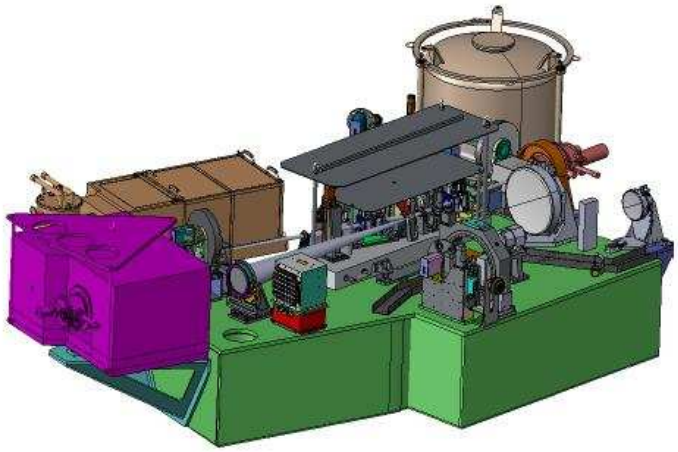

Figure 3.1: SPHERE complete opto-mechanical design.

2. the InfraRed Dual Imaging Spectrograph (IRDIS), a differential imaging camera
3. the Integral Field Spectrograph (IFS)
4. the Zurich Imaging Polarimeter (ZIMPOL), a visible imaging polarimeter

SPHERE will be entirely enclosed in a thermal/dust protecting cover. The Common path contains various innovative components specifically developed for the project: toroidal mirrors, achromatic 4-quadrant and Lyot coronagraphs.
The SAXO extreme adaptative optics system (Petit et al. , 2008) include a 41×41 high-order deformable mirror from CILAS and a 40×40 lenslet visible Shack-Hartmann wavefront sensor based on a 240×240 pixels electron multiplying CCD220 from EEV. For what concern coronagraphy (Boccaletti et al. , 2008), it will reduce the intensity of the stellar peak by a factor of al least 100 and it will eliminate the diffraction features due to the pupil edges. It will include an achromatic 4-quadrant phase mask coronagraph, a classical Lyot coronagraph and an apodized Lyot coronagraph.
The IRDIS science module (Dohlen et al. , 2008) covers a wavelength range between 0.95 and 2.32 μm with an image scale of 12.25 mas consistent with Nyquist sampling at 0.95 μm. The FOV is 11×12.5 arcsec both for direct and dual imaging. Dual band imaging is the main mode and it provides images in two neighboring spectral channels. Two parallel images are projected onto the same 2k×2k, 18 μm pixels detector of which they occupy half of the available area. A series of filter pairs is defined in correspondence to different spectral features in modeled extrasolar planets spectra. On the other hand, the classical imaging mode allows high resolution coronagraphic imaging of the circumstellar environment through all the NIR bands. In addition it is possible to perform long-slit spectroscopy at resolving powers of 50 and 500.
ZIMPOL (Thalmann et al. , 2008) will operate in the wavelength range between 0.6

and 0.9 μm, with an instantaneous FOV of 3×3 arcsec and with an access to a total FOV of 8 arcsec in diameter by an internal field selector. The ZIMPOL optical train is split in two optical arms with the use of a polarizing beamsplitter each of them feeding a different detector. The two arms have the ability to measure simultaneously the two complementary polarization states in the same or in distinct filters.
In the next Section 3.1.2 I will present the general design of the IFS of SPHERE.

3.1.2 SPHERE IFS

The heart of IFS is a new kind of lens based Integral Field Unit (IFU) called BIGRE that is placed at the interface of the instrument with the SPHERE Common Path and it is optically conjugated with the telescope Focal Plane. The beam coming from the telescope has a $F/\# = 316$. This allows to sample the diffractive PSF - arising from the AO compensation and the coronagraphic spatial filtering - at the Nyquist limit. The purpose of this instrument is thus to realize diffraction limited integral feld spectroscopy with the high contrast capabilities of the BIGRE device. To this scope the whole IFS system should only reimage and disperse the slits coming from the IFU with the highest optical stability and a good optical quality. The optimized IFS is a fully dioptric optical design, composed by several optics located along a straight optical axis. IFS is projected to work, in two different wavelength ranges: 0.95 - 1.35 μm with a resolution of ~50 (z-J-mode) and 0.95 - 1.65 μm with a lower resolution of ~30 (z-H-mode). The two resolution are achieved using two different Amici prism (Oliva , 2000) dispersers. The two working wavelength ranges are defined by a combination of band pass, high pass and low pass filters mounted in two locations: inside the dewar (low pass filter) and just in front of the prisms (band pass filter fo the z-J-mode and high pass filter for the z-H-mode).
From a general point of view the IFS is composed of several main sub-systems (see Figure 3.2):

- the IFU
- the collimator
- a filter wheel with several neutral density filters limiting the flux received by the IR detector during the FF calibration
- a prism slide to select between the two different prisms
- a camera mounted on a focusing slide and a piezoelectric slide for dithering
- a 2k×2k Hawaii 2RG detector with pixels of 18 μm working in the wavelength range between 0.95 - 2.32 μm and mantained at low temperature in a cryostat.

BIGRE

BIGRE is a new scheme for the integral field unit based on a dual-lenslet device (see Figure 3.3), that solves problems related to the classical single lenslet (TIGER) design when used for such applications. BIGRE provides much lower cross-talk signals than

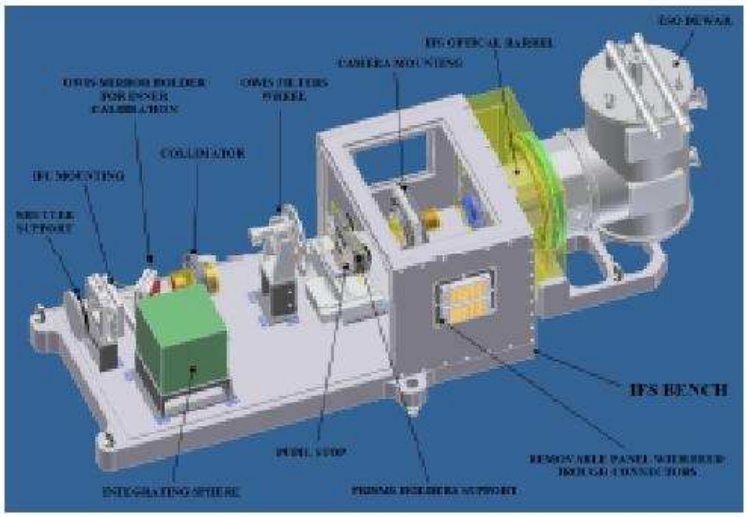

Figure 3.2: The SPHERE IFS opto-mechanical design.

TIGER, allowing a more efficient use of the detector pixels and a considerable saving of the overall cost of a lenslet-based integral field spectrograph.

Figure 3.3 shows a BIGRE spaxel working at the diffraction limit with an un-resolved entrance pupil. The first lens lies on the telescope focal plane and reimages a micropupil at its focal distance. The electric field imaged onto this optical plane is a sinc function (one dimension) or a Jinc function (two dimensions). This signal is filtered by a top-hat transmission function and finally reimaged onto an image plane by the second lens. The distance between this intermediate pupil plane and the second lens is its focal length. A complete description of the BIGRE theory can be found in Antichi et al. (2009).

3.2 Simulations

One of the main goal of this thesis is to present and discuss the detailed simulations performed to predict the performances of the SPHERE IFS. In this Section I describe the tools that we used for these simulations and the results that we obtained from these simulations.

3.2.1 Simulation tools

The SPHERE simulations are based on three codes:

- CAOS described in Carbillet et al. (2004)

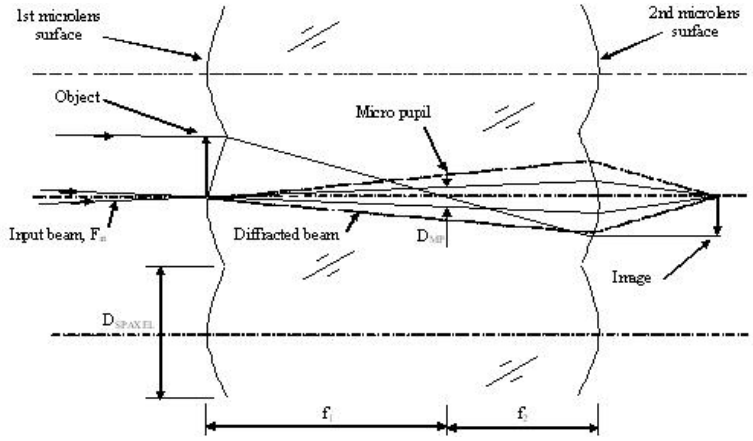

Figure 3.3: Scheme of a BIGRE lenslet array.

- CSP (CHEOPS Simulation Program, where CHEOPS is a former version of SPHERE)
- bigre-sf, a shorter IDL program that simulates light passing through seven adjacent lenslets.

CAOS and CSP are both based on Fraunhofer propagation. In these codes, all image manipulations (addition of wavefront errors, effect of stops, etc.) are made on either focal or pupil planes, and the transformation from one plane to the other one is made by Fourier transforms. The main difference between the two codes is that CSP (that is used only starting from the microlenses plane) assumes that the input data are real, that is, it uses only the PSF on the lenslet plane produced by the previous optics. On the other hand, the CAOS IFS module properly considers both real and imaginary part of the image forming on the lenslet plane, and can then be used to study the impact of light propagation through the BIGRE (e.g. the impact of interference among different apertures, that we called coherent cross talk) and of scintillation. This code is very time consuming and a complete run of simulations using it resulted to be not reliable. However, CSP allows to include coherent cross-talk among lenslets (not really interference nor scintillation) through a parametric approach. The value of the parameter can be calibrated using our third code (bigre-sf) that simulates the wave propagation considering both the real and the imaginary part of the image through a small number of lenslets (one central lenslet and the six lenslets that are around it). For all these reasons, we decided to use the code called CSP to perform all the simulations while the SPHERE CAOS Package was used to provide real intensities over the IFU entrance focal plane as input for CSP. To this aim we performed simulations using the CAOS IRDIS module with 100 atmospheric phase screens at 64 different wavelengths ranging between 0.95 and 1.35 μm for the Y-J-mode or between 0.95 and 1.70 μm for the Y-H-mode. The choice to make simulations with only 64 wavelengths was given by the fact that for a greater number of wavelengths the program saturates our computer.

Part	Output	Code used
Image formation	PSF on microlenses (=spaxels)	CAOS
IFS Instrument simulation	Spectra on detector	CSP/CAOS
Data reduction	Data Cube	CSP
Data Analysis	Reconstructed images and spectra	CSP

Table 3.1: Scheme followed in the simulations.

Note however that 64 wavelengths are enough to properly sample the expected spectral extension of speckles over the whole field of view with approximately two sampling per pixel (hypersampling condition - see Antichi et al. 2009) and this should guarantee that interpolation errors are under control. On the other hand, the CSP code requires as an input 269 PSFs at different wavelengths and to obtain them we performed interpolation starting from the ones resulting from the CAOS simulations.
Being based on the Fraunhofer approximation, both CAOS, CSP and bigre-sf codes are inadequate to study the impact of wavefront errors arising from optics not on the pupil plane, for which Fresnel propagation should be considered (Yaitskova et al. , 2010). For this reason, a few simulations which take into account Fresnel propagation have been performed using the PROPER code (see Section 3.2.6).

CAOS and CSP

Sections from 1.4 to 1.7 provide a frame to guide and interpret the complex numerical simulations to be performed for IFS. This frame is consistent with the IRDIS simulation approach and theoretical expectations.

For what concerns the formation of coronagraphic images, this part is common to IRDIS. The numerical tool used is also identical (CAOS, see Carbillet et al. 2004 and in particular the SPHERE Package developed for CAOS, see Carbillet et al. 2008) with consistent input parameters (see Table 3.2). The only difference is the larger number of wavelengths considered. Coronagraphic images are simulated at this stage as a function of wavelength, of coronagraph, including AO correction and all assumptions on common path optics.

For what concerns the IFS instrument simulations:

- Conceptual limitations of IFS were examined considering the input data cube formed by the coronagraphic images provided by CAOS at different wavelengths. We call this data cube "Ideal IFS", because it corresponds to a perfect IFS that is able to faithfully reproduce the input data.

- Practical limitations of the IFS were examined using a dedicated module (CSP). It, in particular, includes the important BIGRE optical design and hexagonal configuration.

[1] Fresnel propagation here is meant to represent the error due to the fact that AO corrections are estimated at a wavelength different from those used for science observations, and it is simply treated as an additional WFE. This approach cannot be used to estimate the impact of Fresnel propagation on speckle chromaticity within the wavelength range of IFS, considered in Section 3.2.6

Parameter	IRDIS	IFS
AOC settings		
Seeing	0.85”	0.85”
Wavefront outer scale	25 m	25 m
m_v	2-8	0-8
Zenith angle	30°	30°
Wavelength	1.6 μm	1.6 μm
Instrumental jitter	3 mas	3 mas
Ratio of common ref. obj.	0.97	No
COP Settings		
INstrument WFE	34.5 nm	34.5 nm
AO Calibration WFE	7.4 nm	7.4 nm
Fresnel propagation WFE[1]	4.7 nm	4.7 nm
Beam shift WFE	8 nm	8 nm
Defocus WFE	4 nm	No
Pupil shear	0.002 D	0.002 D
Pupil rotation	0°	0°
Differential rotation WFE	0 nm	0 nm
Differential beam shift WFE	0 nm	0 nm
Double difference	Reference star at the same parallactic angle	No
Instrument settings		
Coronagraph	Achromatic 4-quadrant	Achromatic 4-quadrant
Filter	J3J4	z-J, z-H
Number wave-length/filter	5	269
Polarizations effect	No	No
Chromatic up/down corono	0/10 nm	0/10 nm
Chromatic defocus up/down corono	0/0 nm	0 nm
Offset pointing	0.5 mas	0.5 mas

Table 3.2: Parameters used in the CAOS simulations.

- Another routine (IFS module of CAOS) has been developed independently, in particular to properly take into account the complex nature of wave propagation (that is, including phases). An early version was checked to provide consistent results with CSP. An updated version has been developed to also include BIGRE and hexagonal configuration. After consistency checks, it allowed to perform full simulations on this same platform. However, since this procedure is very slow and has other practical limitations (see Section 3.2.4), we used it only to show consistency with the CSP results.
- Photon noise, Flat Field noise and/or read-out noises are introduced at the end of this part of the simulation.
- We consider the z-H-mode in addition to the z-J-mode.
- We carefully considered the interpolation routines used in the CSP code.

For what concerns data reduction, this part produces three-dimensional data cubes starting from bi-dimensional detector images. It includes various steps (finding spectrum on detector and identifying them with IFU lenslets=spaxels; subtract background; flat fielding; wavelength calibration; rebinning in wavelength). This is done within CSP and to improve these results we try to improve the effectiveness of interpolation routines (see below).
For what concerns data analysis, this part includes analysis of the data cube in order to extract the planetary signal from monochromatic images. This has an important impact on the final results. A description of the algorithms implemented for multiple Differential Imaging and Spectrum Deconvolution is given in Section 3.2.4.

Interpolation routines

Various analysis steps require interpolations (either in the spectra, or when scaling images). These interpolations introduce numerical noise, and should be kept at minimum. We tested various interpolation routines: FREBIN, CONGRID and a special routine written by us which perform cubic spline interpolation in two dimensions, based on the one-dimensional SPLINE IDL routine applied to the two dimensions consecutively. This last procedure produced the best results. We tried also a routine based on Fourier transform for bi-dimensional interpolations (required in image re-scaling), but it did not produce better results, and it was then not used in our calculations.
The evaluation of the different routines was performed by a comparison of the final contrast that can be reached with the different interpolation methods.

Image formation: results with CAOS

Input simulations were made using the version 2.3 of the code. The adopted simulations used 100 atmospheric phase screens, and the standard parameters listed in Table 3.2. In Figure 3.4 we display a monochromatic image provided by CAOS, used as input to the CSP simulations. The bright ring corresponding to the Outer Working Angle of the AO is obvious in the image. We made simulations both for the z-J-mode (0.95-1.35 μm) and the z-H-mode (0.95-1.70 μm).

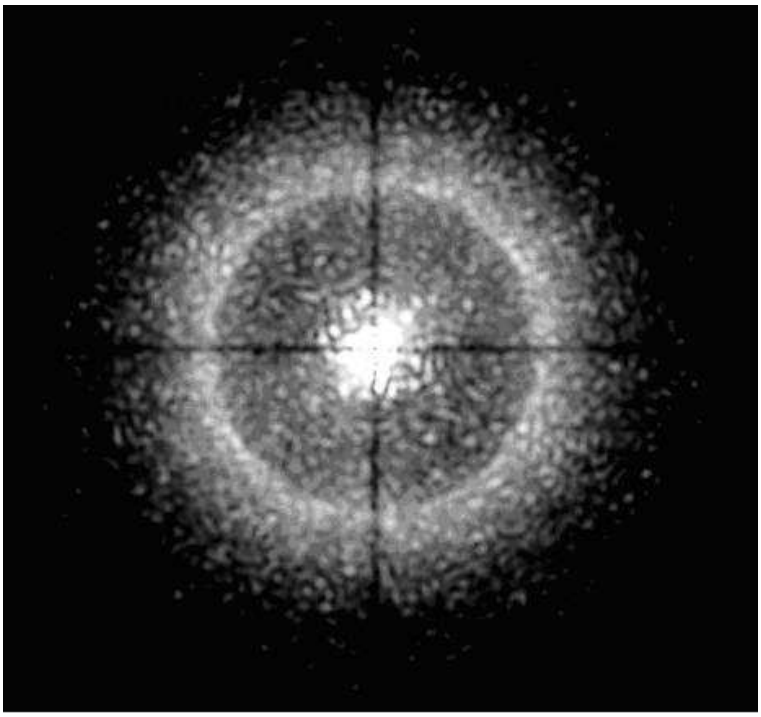

Figure 3.4: Monochromatic image from CAOS simulation, used as input to the CSP simulations.

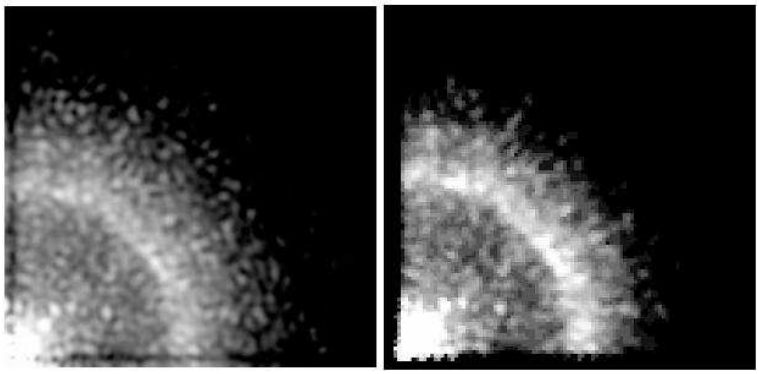

Figure 3.5: Left: Monochromatic image from CAOS simulation, used as input to the CSP simulation. Right: monochromatic image at a very similar wavelength as output of the CSP IFS simulation. Only the first quadrant is shown.

Interpolation errors	$err_{Int} \cdot \sigma(I_{coro})$
Cross Talk	$CT \cdot \sigma(I_{coro})$
Flat Field	$err_{FF} I_{coro} \sim err_{FF} \sigma(I_{coro})(WFE_{Atm}/WFE_{Inst})^2$

Table 3.3: Summary of multiplicative errors dependences.

3.2.2 Multiplicative errors

From what said in Section 1.4, it is clear that gains between one to almost two order of magnitude are possible using differential imaging. However, when estimating the actual gain that can be achieved in practice, there are other parameters which must be considered, even in the case of extremely bright sources, where photon and read out noise can be neglected. In fact, even in this case we should consider that the fidelity of monochromatic images actually obtained in a differential imager is limited by a number of further effects. We may divide them into two groups:

1. Errors that depend on I_{coro}:
   - Flat field
2. Errors that depend on $\sigma(I_{coro})$:
   - Cross Talk
   - In data reduction, interpolation errors done when extracting a data cube from the Integral Field Spectra, or when rescaling the images before subtracting them
   - In the simulations, additional interpolation errors may be done when generating the monochromatic images that are used to estimate the Integral Field Spectra (these last errors only exist in the simulations).

We may represent all these errors as additional terms in analytic estimates of the contrast achieved. Table 3.3 summarizes the expected dependences for multiplicative errors.

Cross Talk

Signal in one pixel depends on signal on close pixels due to cross talk. A more extensive discussion of cross talk in Section 3.2.8. Cross Talk is caused by various mechanisms:

- Cross Talk between adjacent pixels at the detector level, at the level of a few 10^{-2}. This is more important for IRDIS.
- The instrumental PSF causes a broadening of the images. The effect is small, due to the exceedingly good optical quality of both IRDIS and IFS (where it is called incoherent cross talk).

Cross Talk source	Value	IRDIS	IFS
Detector Cross Talk	a few 10^{-2}	Impact on final SR	Impact on LSF
Instrumental PSF	A few 10^{-4}	Impact on final SR	Impact on LSF (inchoerent CT)
Coherent Cross Talk	A few 10^{-3}		Impact on final SR

Table 3.4: **Summary of Cross-Talk**

- In IFS, interference between adjacent lenses causes a coherent signal (coherent cross talk) of the order of a few 10^{-3}.

In IFS the two first effects may be considerd together, as a degradation of the PSF. We will generally neglect them in data reduction. Table 3.4 gives a summary of the various cross talk effects.

3.2.3 Static speckles: comparison with simulations results

Table 3.5 compares predictions for limiting contrast for SPHERE obtained using the analytic approach described in Section 1.5, with results of detailed simulations. Results are for a location at 0.5 arcsec from field centre, and do not include the improvements possible using calibration procedures (double differences for IRDIS, multiple differences and azimuthal filtering for IFS).
The agreement between predictions by the simple analytic approach and more detailed simulations is generally good. This good agreement shows that:

- The analytic approach described in Paragraph 1.5 allows to predict quite well the results of the detailed simulations.
- The agreement is obtained for all different scientific instruments: this confirms that the simulations are consistent each other.

3.2.4 IFS instrument simulations

CSP simulations: comparison with ideal IFS

In Figure 3.5 we compare the first quadrant of the same image shown in Figure 3.4 with the output of the CSP IFS simulation at the same wavelength. Save for different grey scale and the loss of resolution due to the pixel size, the output image is very similar to the input one, showing the fidelity of SPHERE IFS according to our simulations. The effects of IFS as simulated by CSP may be represented by the introduction of a small multiplicative error (see Section 3.2.2) that has marginal effects on the instrument performances.

Data analysis for CSP simulations

Data analysis has a large impact on the contrast achievable with SPHERE IFS. Here I present the algorithm that I applied to implement the Differential Imaging and the

		IRDIS		IFS
		1.19μm	1.60μm	**z-J**
Model	**No coro PSF (mag)**	9.9	9.3	9.9
	5 sigma Single Image	10.7	11.1	11.12
	Single Difference	12.95 ($\Delta\lambda$ = 0.08μm)	13.65 ($\Delta\lambda$ = 0.08μm)	14.14 ($\Delta\lambda$ = 0.036μm)
	Multiple Single Difference			15.49
	Non common path WFE (nm)	10	10	
	Single difference	13.5	13.9	
	Overall limit	12.8	13.4	15.49
Simulations	**5 sigma Single Difference**	10.68	11.1	11.12
	Single difference	12.97 ($\Delta\lambda$ = 0.08μm)	13.94 ($\Delta\lambda$ = 0.08μm)	14.35 ($\Delta\lambda$ = 0.036μm)
	Multiple Single difference			15.45

Table 3.5: 5σ limiting contrast (in mag) for SPHERE using the analytic approach described in Paragraph 1.5 compared with the results of detailed simulation. Results are for a location at 0.5 arcsec from filed centre with no double difference or field rotation.

		IRDIS		IFS
		1.19μm	1.60μm	**z-J**
Model	**No rotation**	12.8	13.4	15.49
	30 degrees field rotation	13.7	14.2	16.40
	30 degree azimuthal filtering	14.6	15.0	17.31
	Double difference	15.5	15.9	
Simulations	**No rotation**	12.97	13.94	15.45
	30 degree field rotation			15.86
	30 degree azimuthal filtering			16.63
	double difference	15.15	15.5	

Table 3.6: Calibration 5σ limiting contrast (in mag) for SPHERE using the analytical approach (see Paragraph 1.5) compared with results of detailed simulations. Results are for a location at 0.5 arcsec from field centre with calibration of static speckles by means of field rotation.

Spectral Deconvolution methods described in Section 1.5 and in Section 1.7 respectively.

General Features

Some features are common to both Differential Imaging and Spectral Deconvolution:

- The data extraction package in CSP generates the data cube consisting in 33 (for the z-J-mode) or 38 (for the z-H-mode) calibrated monochromatic images from the bi-dimensional detector data. This procedure includes signal extraction, wavelength calibration and rebinning of spectra at a constant and common wavelength step. An interpolation along the spectrum is required. Note that this interpolation to be executed properly without aliasing, super- and hyper-sampling conditions on the spectra provided by the IFS should be verified (this was considered when designing the SPHERE IFS). As mentioned in Section 3.2.1, we verified that results obtained using CSP are close enough to those provided by the "ideal IFS" (the input data provided by the CAOS simulations of the atmosphere and Common Path) so that we may safely conclude that approximations in instrument simulation and data reduction within CSP have no significant impact on the results we show.

- In general, we assume that observations are done with the pupil fixed with respect to the IFU. In this case, field rotates with time on an alt-az telescope, a typical value being 30 degrees over 1 hr exposure time. In this framework, Azimuthal Filtering (that is along arcs at constant radius) of the monochromatic images may be used to reduce the noise (Angular Differential Imaging, see Section 1.6). Such a filtering might be implemented in the Data Analysis without need of any interpolation. Our procedures was the following:

  - For each given spaxel, we searched for all spaxels which have a similar separation (distance from centre); practically, the annulus width was set to 1 spaxel.
  - We plotted the value of the intensity at the selected wavelength for each of these spaxels against azimuth angle
  - We draw a fitting line through these points (practically, a cubic spline curve through the average of these points within arcs of length $4\lambda/D$, to avoid canceling the planet signal)
  - We subtracted the intensity value read on the fitting line from intensity at the selected wavelength in the spaxel
  - The procedure is then repeated for all the wavelengths
  - The procedure is iterated aver all spaxels

- We assume that a planet is detected whenever signal is above a detection limit in the final images. Noise in the final images is determined using the same routine used to examine the IRDIS image produced by CAOS. This routine determines

statistical properties of the image center. Detection limit was set at 5σ (i.e. standard deviations); this is appropriate when there is significant rotation of the pupil with respect to the field (see Marois et al. 2008).

Multiple Differential Imaging
The data cube produced by CSP extraction package can be used to implement a differential imaging procedure that allows detection of planets. The procedure we devised is as follows:

1. Images are divided into two groups: planetary images (that is images at wavelengths where the planet is present), and reference images (that is images at wavelengths where the planet signal is very weak or absent).

2. We may then distinguish two cases:

   - Single differences:
     - A reference image is assigned to each planetary image.
     - For each pair, the reference image is spatially scaled to the planetary image according to the wavelength ratio between the wavelengths of planetary and reference image
     - The scaled reference image is subtracted from the planetary image
   - Double differences:
     - two reference images are assigned to each planetary image, one with wavelength respectively shorter and longer than that of the planetary image
     - for each tern, the reference images are spatially scaled to the planetary image according to the wavelength ratio between the wavelengths of planetary and reference images.
     - The three images are combined according to the double difference formula by Marois et al. (2000).

3. The procedure at step 2 should eliminate most of the speckle pattern. If the pairs are selected so that the planet image is present only in one of the two images, the planet image will not be canceled out.

4. A weighted average of the "cleaned" differential image will provide the best final image to be used for planet search. Note that since the planetary images are not scaled, the planet position will not shift with wavelength.

There are two critical issues in this procedure:

1. Each interpolation introduces noise. In our approach, the number of interpolation to be made in the data analysis module is effectively reduced to only one per pair (two per tern when using the double difference approach).

2. Pairing of monochromatic images, and the optimal weights should be given according to the noise model.

- If errors are dominated by photon noise, the best procedure should be to give the same weights to all pairs. In this case pairs should be selected in order to have similar (or even constant) wavelength separation.
- If errors are dominated by calibration errors (speckle residuals) the best procedure in single differential imaging is to create pairs having the smallest possible wavelength separation, compatible with the gradients present in the planetary spectra. In this case weights should be assigned according to the inverse of the square of wavelength separation.
- For what concern double differences, this last approach is limited by the intrinsic width of the emission peaks in the planetary spectrum. Practically, we expect very small advantage by creating terns with the smallest possible wavelength differences. It should then be more advantageous to have various terns with the same wavelength difference, and give the same weight to all of them.

Spectral Deconvolution
Spectral Deconvolution should offer some advantage with respect to the differential imaging approach even for planet detection, at least outside the bifurcation point, because it makes use of all the spectrum. The procedure we followed is composed of four steps:

- We scaled single images provided by the CSP data extraction algorithm to a reference wavelength (in this case we choose the central wavelength between the ones of the 33 (or 38) monochromatic images). Because of this rescaling the planet will be in different positions in every image.
- We plotted the spectrum for every spaxel of the rescaled data cube (see Figure 1.3) and calculated a polynomial fitting function using $(1/\lambda)$ as independent variable. The poynomial degree depends on the distance from the center of the image in units of the bifurcation radius. The value of this fitting function is then subtracted to every spectrum. This should eliminate or at least reduce the speckles or diffraction residuals.
- The subtracted images are then rescaled back to the original scale according to their wavelength, in order to mantain fixed the planet position in all of them. At this point, we have a data cube that should be cleaned of speckles and diffraction residuals
- In order to search for planet signal, the three-dimensional data cube is collapsed to a bi-dimensional image given by the cross-correlation of the spectra in each spaxel with a template planet spectrum. This procedure enhance the S/N of the final image. In general, in our simulations we use methane dominated spectrum. However, we notice that the same procedure can be followed with a flat spectrum, or an L spectral type template.

Examples of application of this procedure are shown in Figure 3.6, where we show detection of planets with contrasts of 10^{-6} (left) and 10^{-7} (right) at 0.6 arcsec from the

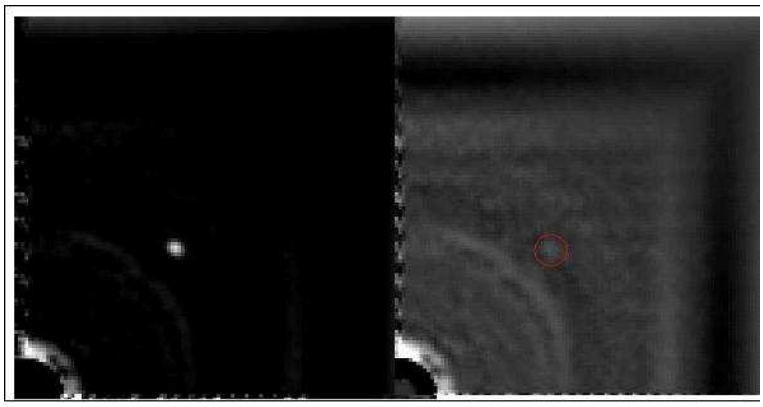

Figure 3.6: Detection of planets with contrast of 10^{-6} (left) and 10^{-7} (right) from z-H-mode data using the spectral subtraction method. The star is a G2V at 10 pc, 1 hr exposure time and 30 degrees field rotation. 5σ limiting contrast is about 10^{-7} for such a simulated observation.

central star. These simulated data corresponds to the observation of a G2V star at 10 pc using the z-H-mode. We assumed a total of 1 hr exposure time, during which the field of view rotated by 30 degrees with respect to the pupil. We determined a 5σ limiting contrast of about 10^{-7} for such a simulated observation, so that the case for the fainter planet is just at the threshold limit.

3.2.5 Numerical estimation of calibration errors

This section describes results of the simulations made using the methods described in Sections 1.5, 1.6, 1.7 and 1.8 focusing on the calibration errors, that is the limiting contrast for the case of very bright objects.

Differential imaging

Results obtained with the multiple difference method are shown in Figure 3.7. This Figure also shows that no further gain is instead obtained using multiple double differences. This is due both to the impact of multiplicative errors (considered in Section 3.2.2) and to the fact that realistic double differences should be made using rather large wavelength separation, due to the intrinsic width of the methane bands.
It should finally be noticed that optimal weighting scheme to be used depends on the relative values of different sources of noise.

Azimuthal filtering (Angular Differential Imaging)

As described in Section 1.6, substantial improvement in contrast can be achieved by exploting rotation of the field of view with respect to the pupil. The improvement is better

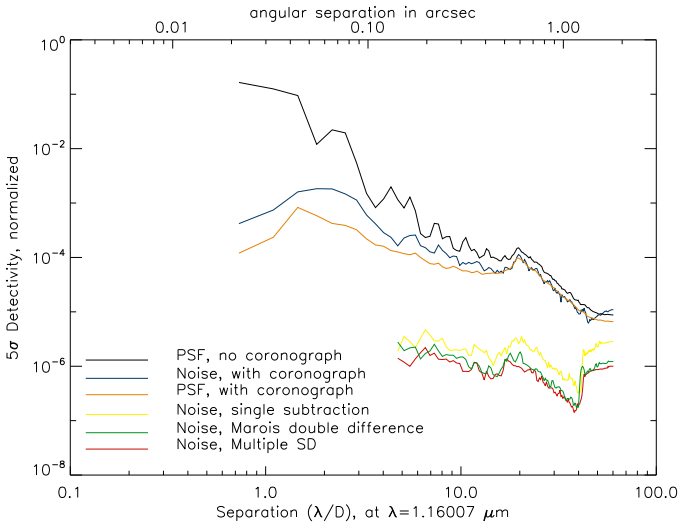

Figure 3.7: Comparison between 5σ contrast obtained with single difference (yellow line), with the multiple Single difference method (red line) and with multiple Double Differences (green line) from IFS simulations. The results are for a simulation with only calibration errors.

at large separation (see figure 3.8). If quasi-static speckles dominate, the gain runs with the square root of the angle (and of separation), since the planet image sample different noise realizations while rotating around the stellar image. In the case where static speckles (or quasi-static speckles with long lifetime) dominate, an azimuthal filtering procedure can be applied, with further substantial gain in contrast. The procedure outlined in Sections 1.6 and 3.2.4 (that can be applied in the case of both static and long life quasi-static aberrations) allows a gain linearly proportional to the field rotation angle and separation (see Figure 3.9).

Spectral Deconvolution

As discussed in Section 1.7, spectral deconvolution should provide better results than multiple Differential Imaging at separations larger than the bifurcation radius. As mentioned there, however, even in the case of Spectral Deconvolution, the contrast that can be achieved even for bright sources is limited.

Figure 3.10 displays the run of the 5σ calibration limit for a very bright star. The case shown is for 30 degrees field rotation with azimuthal filtering. Results with spectral deconvolution are indeed slightly better than those obtained using multiple Differential Imaging, but the difference is small, about 0.2 dex ($\sim$ 0.5 mag). As expected, better results are obtained when the z-H-mode is considered (see Figure 3.11). In this case the difference is about 0.3 dex ($\sim$ 0.7 – 0.8 mag), and the gain is appreciable even at

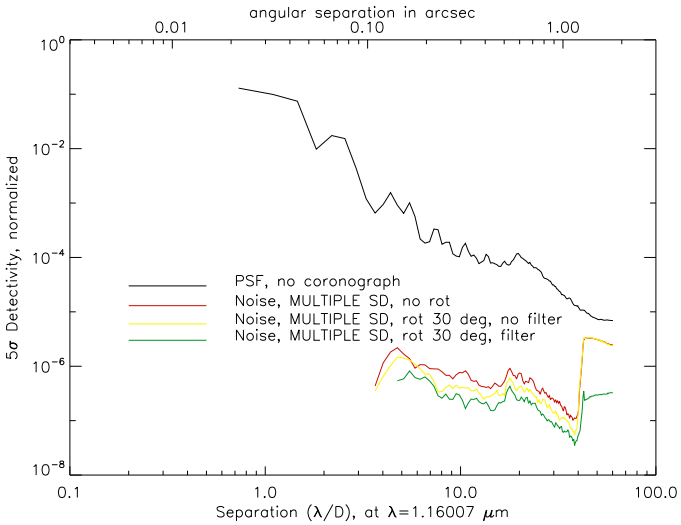

Figure 3.8: Run of the 5σ calibration limit with separation for three cases: (i) no field rotation (red line); (ii) rotation by 30 degrees with no azimuth filter applied (yellow line); (iii) rotation by 30 degrees with azimuth filter applied (green line).

quite small sperarations (0.15 arcsec).

Summary

Table 3.7 summarizes the 5σ calibration limit at various separations as obtained from our simulations. Whenever applicable (outside the bifurcation radius), the spectral deconvolution provides better contrast than multiple Differential Imaging. Also, the z-H-mode allows to get better contrast with respect to the z-J-mode, save that for widest separations. However, we notice that success of the Spectrum Deconvolution method is related to the assumption of a smooth variation of speckles with wavelength, which may be jeopardized by the effects of Fresnel propagation that was neglected in this simulations.

3.2.6 Simulations with Fresnel propagation

To confirm the results of the simulations listed in the previous Sections we performed new simulations using a new version of the CAOS software that incorporates the PROPER code to take account of the Fresnel propagation effects. The result of these simulations is composed by a datacube of 64 PSFs that are used as an input for the CSP code as described in Section 3.2.1. To save computing time, we performed these simulations not considering the effects of the atmosphere (using only one atmospheric screen). Of course, this is not realistic, yielding optimistically too good contrasts. However, the

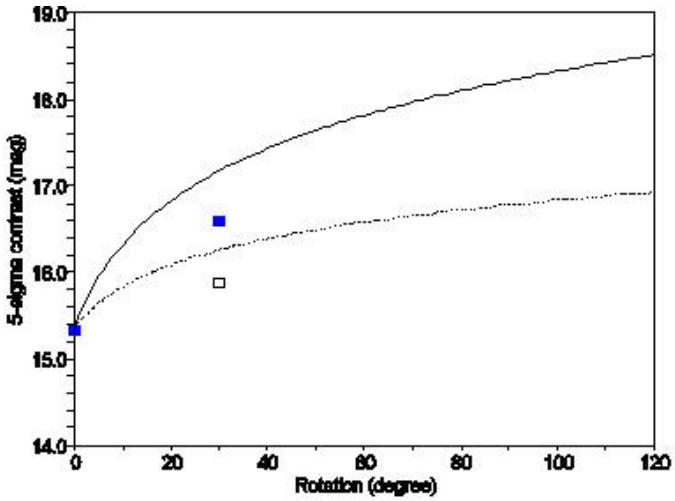

Figure 3.9: Run of the 5σ calibration limit at 0.5 arcsec with rotation of the field with respect to the pupil. The open symbols and the dashed line are results of simulations and expectations from the model described in Paragraph 1.6 for the case of uncorrelated noise (quasi-static speckle); the filled symbols are the same but for the case of static speckles, filtered out using the method described in Section 3.2.5

Mode	Data Analysis	Separation		
		0.15 arcsec	0.5 arcsec	1.0 arcsec
z-J-mode	Multiple Differential Imaging	2.06×10^{-6} (14.21 mag)	3.09×10^{-7} (16.27 mag)	9.89×10^{-8} (17.51 mag)
	Spectral Deconvolution	Inside Bifurcation Radius	1.64×10^{-7} (16.96 mag)	7.68×10^{-8} (17.79 mag)
z-H-mode	Multiple Differential Imaging	1.61×10^{-6} (14.48 mag)	1.87×10^{-7} (16.82 mag)	1.87×10^{-7} (16.82 mag)
	Spectral Deconvolution	5.85×10^{-7} (15.58 mag)	1.13×10^{-8} (17.37 mag)	1.55×10^{-7} (17 .03 mag)

Table 3.7: 5σ calibration limit (30 degrees field rotation, azimuthal filtering).

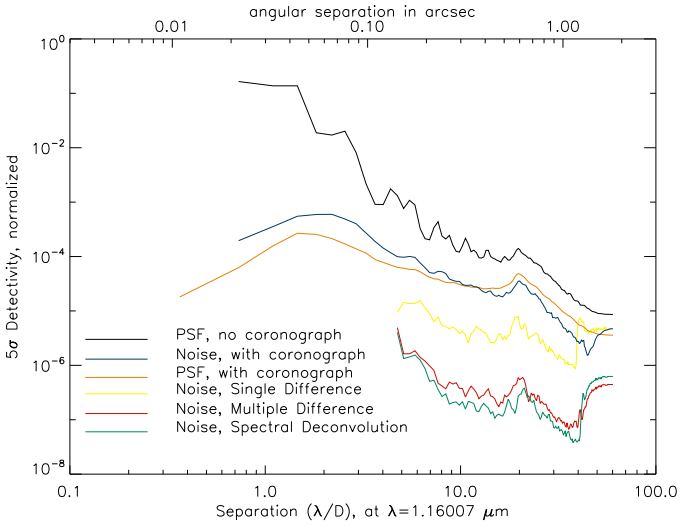

Figure 3.10: Run of the 5σ calibration limit with separation for a very bright star; the case shown is for 30 degrees field rotation with azimuthal filtering. Red line is the result obtained with multiple differential imaging; the green line is with the Spectral Deconvolution method.

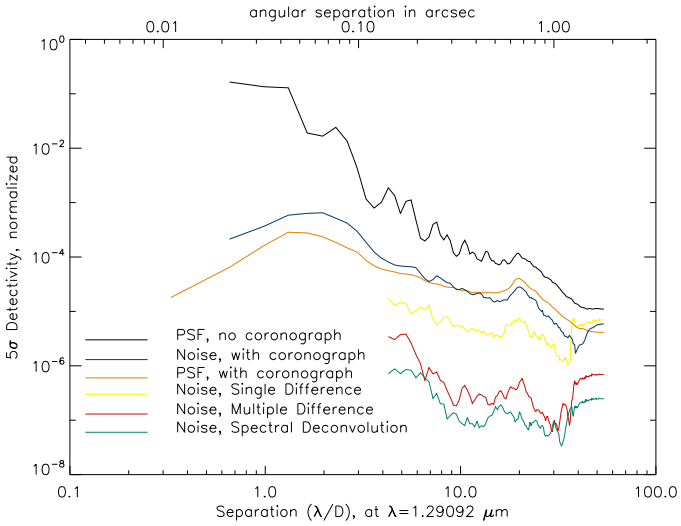

Figure 3.11: Same of Figure 3.10, but for z-H-mode.

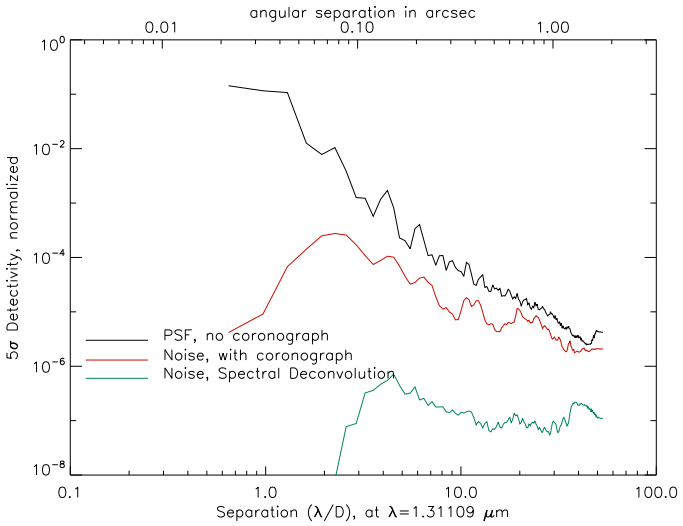

Figure 3.12: Plot resulting from a simulation without the Fresnel propagation and without any rotation of the field of view (z-H-mode).

comparison is still meaningful to evaluate the impact of the Fresnel propagation.
The following parameters are adopted during the Fresnel propagation calculations made using the CAOS SPHERE Package:

- Pre-coronagraphic optics: for the DTTS the conjugated distance is of 414 km and the WFE r.m.s. is of 5 nm. The PSD has f^2 profile.
- For the post mask optics we have the collimator with a conjugated distance of 396 km and the WFE r.m.s. of 15 nm.
- For the post-coronograph optics we have the folding mirror 2 with a conjugated distance of 1492 km and with a WFE r.m.s. of 10 nm, the folding mirror 3 with a conjugated distance of 4440 km and the WFE r.m.s. of 10 nm and the field lens with a conjugated distance of 10722 km and a WFE r.m.s. of 15 nm.

In Figure 3.12 and in Figure 3.13 we report an example of the results of such simulations for a case without any rotation of the field of view and considering the z-H-mode without and with the Fresnel propagation respectively. It is apparent from a visual inspection of these two images that the results are very similar for the two considered cases. Similar results have been obtained for simulations performed under different conditions. A numerical confirmation of this result can be obtained by Table 3.8 where values of the contrast at different separations from the central star are listed both for the case without Fresnel propagation and for the case with Fresnel propagation. The listed values are very similar in the two considered cases. It is then clear that we can conclude that the Fresnel propagatio has not a very important impact on the results of

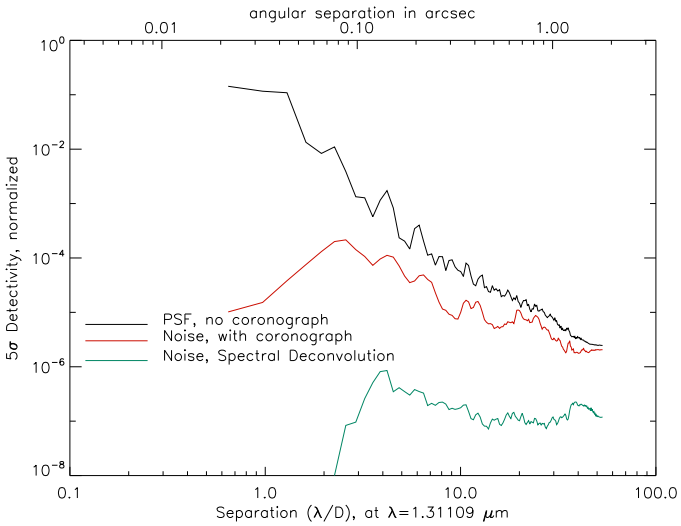

Figure 3.13: Same of Figure 3.12 but with the Fresnel propagation.

Sep. (arcsec)	No Fresnel	Fresnel
0.2	2.40×10^{-7}	3.50×10^{-7}
0.4	8.35×10^{-8}	1.31×10^{-7}
0.6	1.17×10^{-7}	1.23×10^{-7}
0.8	9.80×10^{-8}	1.12×10^{-7}
1.0	9.76×10^{-8}	1.19×10^{-7}

Table 3.8: Values of the contrast at different separations for simulations with and without taking account of Fresnel propagation.

our simulations so that te results reported in the previous Sections can be considered valid.

3.2.7 Photon Noise

Analytical predictions

Multiple Differential Imaging

In the photon noise limit, the contrast is given by the ratio between the signal given by

$$C_{ph} = \frac{S_{pl}}{\sigma(S_{pl} + S_{sky} + S_{star})} \tag{3.1}$$

where S_{pl} represents the number of photons within the diffraction peak of an image of the planet, S_{sky} and S_{star} are the number of photons from the sky and from the star in the same area of the planet. Since for those cases close to the detection limit the stellar background dominates over the planet, we will neglect this last (but we should take into account the contribution by the sky, which is important for faint objects). Of course, detection requires low false alarm probability. This is reasonably achieved for a S/N=5 (see Marois et al. (2008) for a discussion of those cases where this limit is enough).

Figure 3.14 displays the approximate limiting contrast for photon noise limited cases

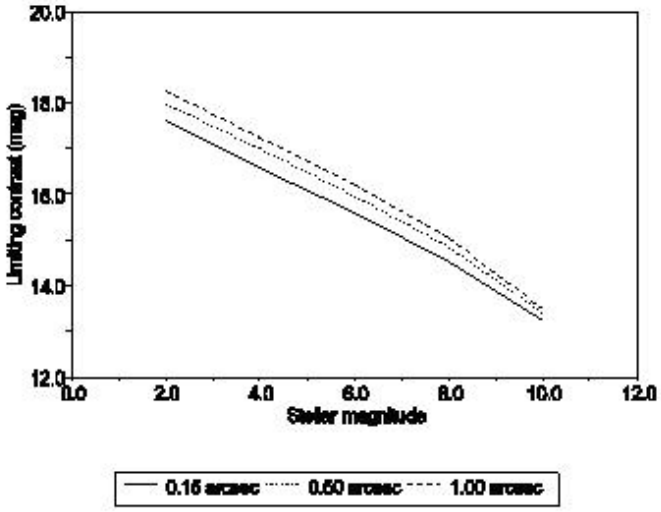

Figure 3.14: Expected 5σ limiting contrast as a function of stellar magnitude, if only photon noise is considered for the SPHERE IFS. Results are for 1 hour observations in the z-J-mode. Different lines correspond to different separations.

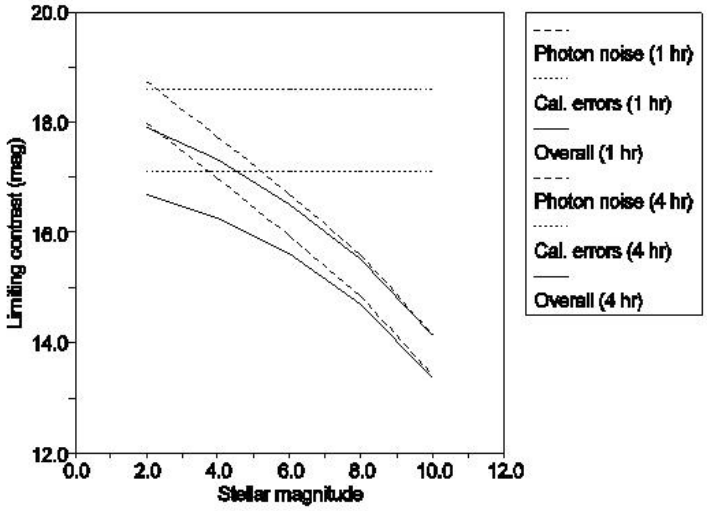

Figure 3.15: Expected 5σ limiting contrast as a function of stellar magnitude for the ideal SPHERE IFS. Results are for 1 (30 degrees field rotation) and 4 hours (120 degrees field rotation) observations in the z-J-band and separation of 0.5 arcsec. Dashed lines are for calibration errors alone; dotted line is for photon noise alone; solid line is combining both calibration errors and photon noise.

as a function of stellar magnitude for 1 hour observations in the case of SPHERE. The parameters of the simulations used to obtain this Figure are listed in Table 3.2.
Figure 3.15 displays the approximate limiting magnitude expected for an ideal SPHERE IFS as a function of stellar magnitude, showing the relative contribution of calibration errors and photon noise. We are considering 1 and 4 hours observations (corresponding to 30 and 120 degrees field rotation) in the z-J-band; results are for a separation of 0.5 arcsec. This Figure shows that with a properly designed IFS, photon noise should be the main factor limiting achievable contrast but for the very bright objects with $J < 2.5$. Figure 3.15 shows that the limiting contrast at 0.5 arcsec for a 1 hour observation of a J=8 star for an ideal IFS is 14.7 mag, that is essentially set by photon noise. This shows that the Top Level Requirements (contrast of 10^{-6}, that is 15 mag, for a separation of 0.5 arcsec from a J=8 star in 1 hour integration time) cannot be reached by an even perfect IFS, when using multiple Differential Imaging in the z-H-mode.
Spectral Deconvolution should provide a significant gain over Multiple Differential Imaging in the photon noise limited case, because a larger fraction of the spectrum can be used for speckle subtraction and planet detection. Figure 3.16 gives the gain in contrast (with respect to the multiple Differential Imaging) in the photon noise limited observations expected from this simple consideration. We expected a significant gain, about a factor of ~ 2 at the AO Outer Working Angle.

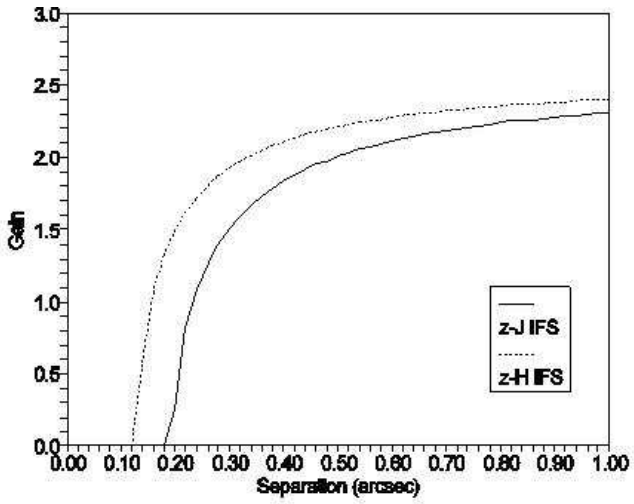

Figure 3.16: Expected gain when using spectral deconvolution technique over the differential imaging technique in the photon noise limited case.

Numerical results

We may compare the results of the analytic approach described in Paragraph 1.5 with the results of our detailed simulations (see Figure 3.17 and Figure 3.18). Results of

simulations for both multiple differential imaging (filled symbols) and spectral deconvolution (empty symbols) are shown. Overimposed are predictions based on only photon noise (thin solid and dashed lines, respectively), and taking into account also the calibration errors (thick solid and dashed lines, respectively). The calibration errors were 16.27 (z-J-mode) and 16.96 (z-H-mode) mag for the multiple differential imaging method, and 16.82 (z-J-mode) and 17.37 (z-H-mode) mag for the Spectrum Deconvolution method (see Table 3.7). The larger values for the z-H-mode is due to the wider spectral range used, which allows to use more independent wavelength pairs.

These simulations suggest a gain close to a factor of 4 expected in the photon noise

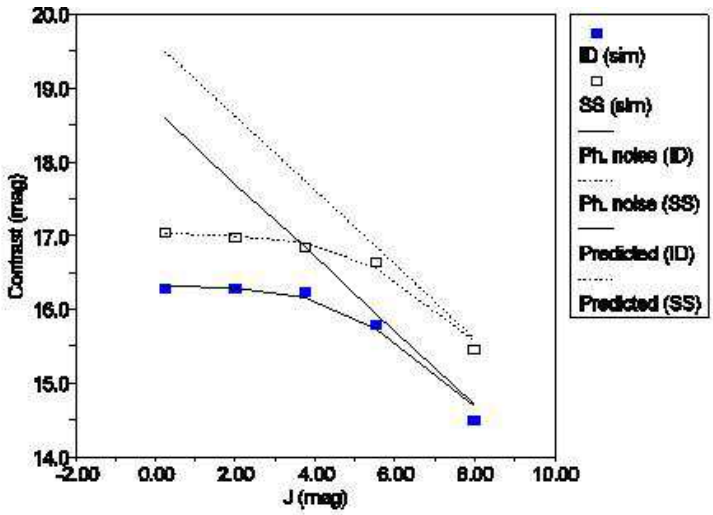

Figure 3.17: 5σ contrast at 0.5 arcsec for observations in the z-J-mode, as a function of stellar magnitude. 1 hour exposure, field rotation by 30 degrees and azimuthal filtering were assumed. Results of simulations for both multiple differential imaging (filled symbols) and spectral deconvolution (empty symbols) are shown. Overimposed are predictions based on only photon noise (thin solid and dashed lines, respectively), and taking into account also the calibration errors (thick solid and dashed lines, respectively).

limited case when using spectral Deconvolution for the z-H-mode, while the gain is slightly smaller (about a factor of 2) for the z-J-mode. This substantial gain should allow to reach the TLR on contrast (10^{-6}, that is 15 magnitude, at a separation of 0.5 arcsec for a star with J=8; from SPHERE Technical Specifications). Note also that while we expect to be photon noise limited for $J > 4$ when using multiple Differential Imaging, we expect the observation to be calibration limited for $J < 4$ to $J < 6$ (depending on the wavelength range) when using spectral deconvolution.

The values plotted in Figure 3.17 and Figure 3.18 have been estimated neglecting Fresnel propagation. However, as noticed in Section 3.2.6, this should not be too important in the case of SPHERE.

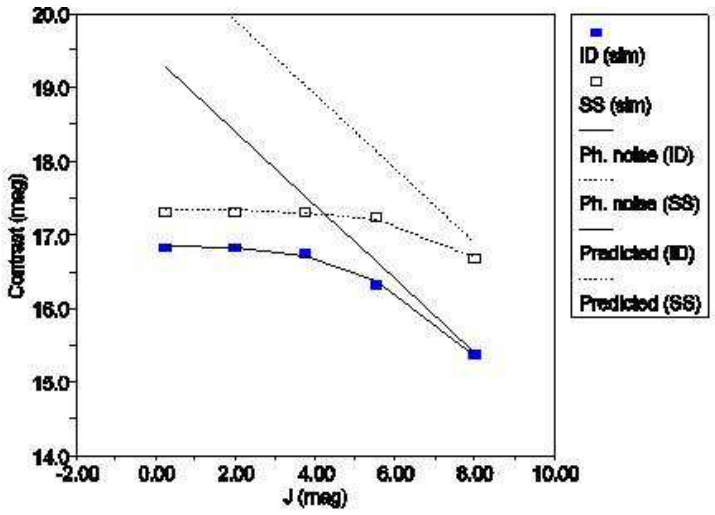

Figure 3.18: Same as Figure 3.17 but for the z-H-mode.

Summary

The TLR contrast specification is:
TLRC.2 This observation mode shall make possible to achieve a contrast of 10^{-6} *(goal* 10^{-8}*) at 0.5" from a bright (*$J < 8$*) star in J band (assuming a line contrast of 5) in 1 hour integration time with SNR=5.*
From our simulations it results that for a star with J=8, we are limited by photon noise and not by calibration errors. Using multiple Differential Imaging data analysis for the z-J-mode alone (that is, the mode currently foreseen for the Near Infrared Survey), we concluded that we are able to arrive close to this TLR, but not to satisfy it.
However this TLR can be achieved in both the z-J-mode and z-H-modes using the spectral deconvolution method for data analysis, and only in z-H-mode when using the multiple Differential Imaging method. The reason of the superiority of the Spectral Deconvolution with respect to the multiple Differential Imaging is that a wider spectral region is used when subtracting the stellar background and searching for planets. As expected, the z-H-mode allows better results, again because a wider spectral range is exploited.

3.2.8 Other factors that may limit the contrast

Apart from calibration errors and photon noise, various effects might limit the contrast achievable with the SPHERE IFS. The most relevant are cross talk, read out noise and flat field accuracy. The impact of cross-talk is discussed in this Section.

Cross Talk

Cross Talk is a major issue for IFS. It is in principle possible to reduce it to very low values by an appropriate instrument design. However, this optimization may require a more complex system and some reduction in other instrument performances. Analysis of its relevance for planet detection is then required to optimize the IFS design.
In order to estimate the impact of Cross Talk on planet detection using SPHERE IFS, we proceeded as follows:

1. We define Cross Talk as the sum of two components:
   - Incoherent Cross Talk, that is simply due to extension of the wings of the lenset PSF's (to distinguish it from coronagraphic PSF, we will use the abbreviation LSF for the lenslet PSF). This is properly taken into account in the CSP simulations, where the wings of the LSF are considered over an area including adjacent pixels.
   - Coherent Cross Talk, due to constructive interference between rays from different lenslets. This is the sum of a term for every adjacent lenslet, each given by the the product of the electric fields due to adjacent lenslets times a phase term depending on the optical path difference between the two beams, averaged over a detector pixel. Coherent Cross Talk cannot be computed exactly using CSP (which does not include phase term for the beam within the IFS). However, the last version of the CSP include a multiplicative factor that may be used to test the impact of Cross Talk on planet detection, once that it has been estimated elsewhere. Moreover, the last version of CAOS simulation for IFS takes explicitly this term into account (see Section 3.2.1).
2. We then evaluated (Section 3.2.1) the impact of different levels of coherent Cross Talk on planet detection. This allows to justify the specifications on coherent Cross Talk, updating the value given in the SPHERE Technical Specifications (10^{-3}, goal 10^{-4}). An order of magnitude justification of this result may be obtained using the simple model for the multiplicative errors and their contribution to the contrast given in Section 3.2.2.
3. We evaluated the Cross Talk parameter using the bigre-sf code, designed for this purpose and checked against experimental results (see Antichi et al. (2009)). The value of the cross-talk obatined from this code is compared with that obtained from analysis of the system, so that appropriate optimization of the IFS design can be achieved. Similar results were obtained using the CAOS IFS simulations described in Section 3.2.

Impact of coherent Cross Talk using a parametric approach

The impact of coherent Cross Talk was estimated by repeating the evaluation of planet detectability with CSP (that is able to consider it just in parametric way) with different values for the coherent Cross Talk parameter (0, 10^{-2}). The results of these simulations are given in Table 3.9, where we give the average contrast in the 0.15-1 arcsec area as

Analysis method	Coherent Cross Talk	Separation		
		0.15 arcsec	0.5 arcsec	1.0 arcsec
Multiple Differential Imaging	0	1.94×10^{-6} (14.28 mag)	1.87×10^{-7} (16.82 mag)	1.37×10^{-7} (17.17 mag)
	10^{-2}	1.94×10^{-6} (14.28 mag)	1.87×10^{-7} (16.82 mag)	1.65×10^{-7} (16.96 mag)
Spectrum Deconvolution	0	1.10×10^{-6} (15.03 mag)	1.13×10^{-7} (17.37 mag)	1.36×10^{-7} (17.17 mag)
	10^{-2}	1.10×10^{-6} (15.03 mag)	1.13×10^{-7} (17.37 mag)	1.54×10^{-7} (17 .03 mag)

Table 3.9: The same as Table 3.7, but for different values of Cross Talk (only values for the z-H-mode are given.

a function of the Cross Talk parameter, respectively. We found that the impact of coherent Cross Talk is very small if the Cross Talk is less than 0.01, while it becomes significant for a cross-talk of 0.1 (note that this is due more to a loss of signal than to a raise of noise). For a Cross Talk of 10^{-2} there is a small loss in the inner regions, and actually a (very) small gain in the outer ones. This last result might seem surprising but it is due to the fact that IFS slightly oversamples speckles. The effect of coherent Cross Talk on monochromatic images is to replace the value of the intensity on a lenslet (at a given wavelength) with a linear combination of this same value (which still has by far the dominant value), and of an average of the values (at the same wavelength) in the adjacent lenslets. Insofar images are oversampled, the average of adjacent lenslets is a good proxy for the value in the lenslet itself, while adopting an average over several spaxels slightly decrease noise. Once coherent Cross Talk is taken into account, intensity in the pixel is modified only very marginally, at levels smaller than 10^{-3} even for large values of the Cross Talk.

As a conclusion we can affirm that the specification for the Cross Talk originally given was overstated. Even a value of Cross Talk as large as 10^{-2} can be accepted without noticeable effect on planet detection.

3.3 Astrometry with SPHERE IFS

3.3.1 Science based on astrometry with SPHERE

Many scientific programs to be carried out with SPHERE require measures of the relative position of the faint companions with respect to the star. These include (in order of complexity):

1. **Physical connection between the components** (parallax, proper motion): this requires accuracies better than $\sim$ 5 mas, allowing estimates of parallaxes with errors of 10% at 20 pc and transverse motions with an accuracy of 2 km/s at 100

pc over 1 year baseline.

2. **orbital solution** (period, semi-major axis, eccentricity, plane inclination, etc.): requires an accuracy depending on the fraction of orbit covered by observations. 1 mas should be well enough for periods less than 5 years.

3. **Identification of unseen companions** and/or determination of relative masses from secular orbit perturbations: requires an accuracy better than 1 mas, on a timescale depending on the characteristic period (likely years).

4. **Determination of companions mass** by motion of the star with respect to background objects. For planetary masses, expected amplitudes are below 1 mas, while for brown dwarf masses a larger signal is expected (consider e.g. the case of a 0.2 M_o star, with a 10 M_{Jup} companion at 1 AU at 10 pc: the amplitude of the orbital motion is in this case $\sim$ 5 mas). Rough estimates of the masses can then be obtained if appropriate background objects are found and an astrometric accuracy of 0.1 mas can be achieved.

5. **Identification of close companions to the planet**: requires an accuracy depending on the characteristics of the close companions; even under very favourable circumstances (mass ratio of 100, and a separation of 10 mas, that is 0.1 AU at 10 pc), the amplitude of motion of the visible faint companion is 0.1 mas. This is at the limit of feasibility.

The top level requirements for astrometry with SPHERE was set at a quite conservative value of 5 mas, with a goal of 1 mas. However we will show that SPHERE should be able to reach a much better astrometric accuracy for bright enough sources, possibly as good as $<$ 1 mas, so that scientific programs 2 and 3, and even 4 and 5, might be reached under favourable circumstances.

3.3.2 SPHERE potential for astrometry

We will hereinafter generally consider relative positions of the faint companion with respect to the bright central star image. Occasionally, it might be possible to determine absolute positions using background objects.
We construct a total error budget in the relative positions of the companion with respect to the bright central star image including the following terms:

1. **Photometric accuracy of centering of the faint companion image**. The centering accuracy along each axis is approximately given by:

$$err = 1.06\sqrt{(w \cdot dx)}/(S/N)mas \tag{3.2}$$

where w is the FWHM of the image, dx is the pixel size (in mas) and S/N is the signal-to-noise ratio of detection (see Cayrel 1988).
Assuming 1 pixel =12.25 mas, and the FWHM of the image equal to 2 pixels, we have that err=18/(S/N) mas. For limiting detection (S/N=5) we then have err=3.6 mas.

For detections with $S/N < 50$ (that is contrast $< 10^{-5}$), the photometric error limits the astrometric capabilities of SPHERE. For brighter companions, when the speckle noise is less important how we have seen from the results of the simulations, star centering might be the most important source of error.

2. **Accuracy of centering of the central star**. In the next Sections we describe this part of the error budget. We consider two cases:
   - SPHERE used without coronagraph
   - SPHERE used with coronagraph

3.3.3 SPHERE used without coronagraph

An excellent discussion of expected astrometric performance of AO assisted imaging is given in Cameron et al. (2008). According to this discussion, the main limiting factors are:

- **Differential Tilt Jitter**, expected value (at 1 arcsec separation)=0.05 mas, scaling down with $\sqrt{(\tau_0/t)}$, and up with the square of the separation. Since τ_0/t is expected to be < 0.01 in all practical cases, the differential tilt jitter should contribute no more than a few micro arcsec to the astrometric error budget.
- **Distortion**: for constant gravity system, it should depend on temperature and pressure, which should cause scale variations. Distortion map can be prepared. Distortion calibrations have been prepared assuming an error budget of 5 mas (SPHERE Technical Specifications), but it should practically yield 1 mas accuracy : however the discussion in Section 3.3.7 shows that an accuracy of 0.1 mas could be obtained if moderate dithering on the instrument distortion grid is available.
- **Atmospheric refraction**: it can be taken into account with appropriate modelling (see Helminiak 2009), provided that local measures of temperature, pressure and relative humidity are included, even if some uncertainties would still be present. For broad band observations, spectral distribution of flux should be taken into account. This is not needed in narrow band imaging. Considering reasonable errors for the measures of temperature, pressure and relative humidity, narrow band imaging should allow to keep errors related to atmospheric refraction within a few tens of microarcsec.
- **Measurement errors**: $\sim$ 0.01 pixels(=0.1 mas for SPHERE). It should scale down with 1/t. If 1000 individual exposures are used (tipically $\sim$ 20 minutes exposures), measurament errors contribute no more than a few microarcsec to the astrometric error budget.

We conclude that SPHERE without coronagraph should allow errors of < 0.1 mas, mainly limited by residual errors in the evaluation of the distortion map, altough uncertainties in correcting atmospheric refraction are not negligible. Locally, accuracy may be better (down to a few tens microarcsec).

3.3.4 SPHERE used with coronagraph

As we have seen, SPHERE should allow very good astrometric performances when used without the coronagraph. The coronagraph should degrade performances, making it more difficult to recover the original location of the centroid of light distribution of the guiding star. In fact, any asymmetry present in the coronagraph illumination would result in an asymmetric distribution of flux. On the other hand, field center accuracy based on AO/DTTS correction is limited at 2 mas, with 0.5 mas reproducibility (goal: 0.2 mas - as defined by the SPHERE Technical Specifications).
We wish to explore alternative ways of determining image center in the presence of the coronagraph. We will consider various alternatives, exploiting different image features:

- Diffraction peak
- Speckle shift with wavelength
- Outer working angle corona
- Speckle symmetry

Image centering from diffraction peak

While strongly attenuated, some residuals of the diffraction peak should still be present. This might be used for centering the image. We expect however that the coronagraph itself strongly modifies the shape of this peak, because it affects differently odd and even terms of the Taylor series representing the PSF (see Perrin et al. 2003). Determination of the ”undisturbed” location will be then affected. Corrections are model dependent, it will be then very hard to reduce errors below a few mas, that is not better than given by AO/DTTS.

Image centering from radial shifts of speckles

In this subsection we will consider how the expected radial shifts of the speckles with wavelengths can be exploited for image centering, even in presence of a coronagraph. In this Section we assume that the nominal field centre is at a position given by X=117.0, Y=117.0. Actually the real position of the field centre cannot be determined with precision in these simulated images due to the instrumental jitter that has been introduced in the CAOS simulations that has a value of 3 mas as can be seen in Table 3.2. For this reason, in the summary of the Paragraph we will assume as the position of the field centre the one obtained using the method with the smallest error.

Results of detailed simulations

Detailed simulations are clearly required to properly estimate the contribution of individual sources of errors. The procedure we followed included these steps:

- We considered the data cube obtained from a standard IFS simulation

- We first considered a pair of images at different wavelengths λ_1 and λ_2 ($\lambda_2 > \lambda_1$). We considered well separated wavelengths, for which we expect a similar deviation due to the ADC.
- We filtered low frequency signal using the IDL SMOOTH function; The cutoff frequency was 5.0 (pixel) for the image at the shortest wavelength, and $5.0\lambda_2/\lambda_1$ at the longest wavelength.
- We compiled lists of peaks in the two images using the routine FIND by IDL, with a FWHM =2.0 for the shortest wavelength and FWHM=$2.0\lambda_2/\lambda_1$ at the longest wavelength.
- We then paired peaks in the two lists by looking at those peaks in the list at longer wavelength whose location was within 5 pixels from any pixel in the list at the short wavelength, scaled by λ_2/λ_1 (with respect to an approximate identical center).
- Finally, we repeated the whole procedure for all independent pairs of wavelengths, and compared results.

The simulation we considered is the case of a coronagraphic observation of a G2V star at 10 pc. Main results are given in Table 3.10. The first two columns of this Table gives the wavelength pairs used in the combination. As mentioned above, these pairs give identical deviation from the ADC, a condition necessary for the method. The third column gives the number of speckles used. Field center can be determined typically from 60-100 speckles from each pair of images; errors are too large for fainter speckles. We found that position of each speckle can be measured with an accuracy of about 6 mas on a single monochromatic image. This implies that the stellar position can be measured from a wavelength pair with an accuracy of about 6.5 $\lambda/(\lambda_2 - \lambda_1)$ mas (see Columns 6 and 9 of Table 3.10). The expected proportionality of the centering errors with $\lambda/(\lambda_1 - \lambda_2)$ is clearly illustrated by Figure 3.19. Considering the number of speckles that can be used in each determination, the error of the center position, obtained averaging results from individual speckles, is then 0.7 $\lambda/(\lambda_2 - \lambda_1)$ mas (see Columns 5 and 8 of Table 3.10). Different pairs of images give independent estimates of the field center. A weighted average of the results from various pairs provides the center of the star at coordinates X=116.47, Y=116.50 (x=6.5 mas, y=6.1 mas from nominal field center, X=117.0, Y=117.0), with an error of about 0.12 pixels ($\sim$ 1.5 mas). Speckles centering errors are then much more important than speckle anisoplanatism that would limit the accuracy to $\sim$ 0.2 mas. Note that for this application, IFS is clearly advantegeous with respect to IRDIS because many wavelengths can be used simultaneously. This offers a number of advantages:

- many independent pairs can be obtained and wavelength separation between monochromatic images may be much larger. By itself, this implies a full order of magnitude advantage for IFS.
- the variation of position with wavelength due to refraction can be modeled much better. Note that if the offset between the centers of IFS and IRDIS images would

be known (this is possible, with some limitation due to differential refraction), IFS might be used to improve IRDIS astrometry.

We notice that noise in these stellar position determinations agree with expectations. In fact, the centering error for each speckle is $\sqrt{2}\pi^{1/4}FWHM/(S/N)$ (Cayrel , 1988). Using the distribution of speckle intensity according to Marois et al. (2008), we expect that the strong speckle tail of the distribution scales down exponentially with speckle strength, with a decrease of an order of magnitude in number of speckles for a variations of ~ 3 in units of average signal. We are here considering about 10% of the speckles with larger values. This implies a typical S/N~3 for each speckle used in the determination of center position. If we now consider that FWHM=2 pixels=24.5 mas, and S/N~3, typical centring error should be ~ 0.5 pixel~6 mas, in agreement with simulations. This excellent agreement is confirmed by the comparison of observed scatter of speckle positioning (here the difference between location expected from the scaling law with wavelength and observation) as a function of speckle strength (see Figure 3.20, with the prediction that this error should be inversely proportional to S/N (that is signal, assuming a constant noise).
We note that the exact threshold value used to select speckles is not too critical: in fact adopting a higher threshold, the better accuracy in center position is almost exactly compensated by the smallest number of speckles available for this estimate.

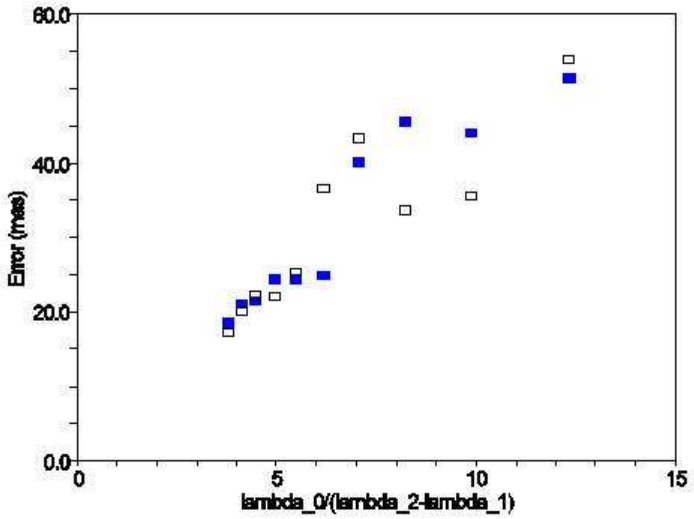

Figure 3.19: r.m.s. scatter of determinations of stellar positions from individual speckles measuresd in pairs of monochromatic coronagraphic images, as a functionof the wavelength difference. Filled and open symbols represent the scatter along the x and y axis respectively.

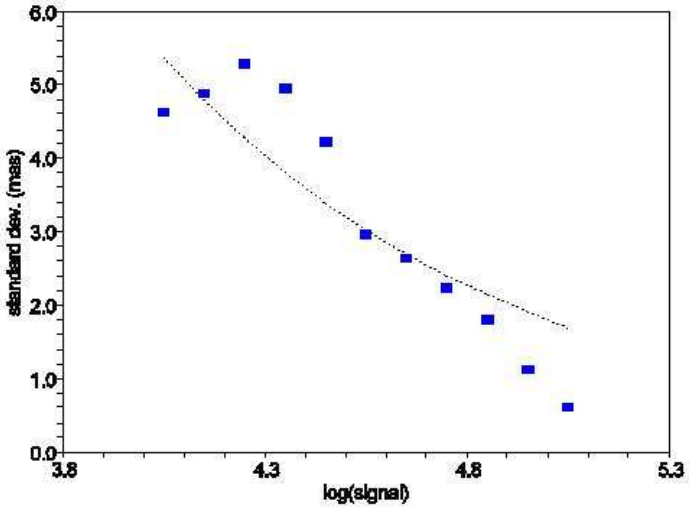

Figure 3.20: Run of the scatter (standard deviation) of measured speckle position with respect to expectations (from scaling with wavelength) as a function of speckle strength (squares). The dashed line represents the expected error, inversely proportional to S/N (that is signal).

λ_1 (μm)	λ_2 (μm)	N speck-les	$< X >$ (mas)	Err(X) (mas)	r.m.s.(X) (mas)	$< Y >$ (mas)	Err(Y) (mas)	r.m.s.(Y) (mas)
1.028	1.340	58	-7.4	2.4	18.5	-3.8	2.3	17.2
1.040	1.328	74	-3.7	2.5	21.1	-7.3	2.3	20.0
1.052	1.316	70	-6.3	2.6	21.5	-8.4	2.6	22.1
1.064	1.304	75	-8.5	2.8	24.4	-9.4	2.5	22.0
1.076	1.292	82	-8.7	2.7	24.4	-7.5	2.8	25.3
1.088	1.280	85	-6.4	2.7	24.9	-6.4	4.0	36.5
1.100	1.268	100	-3.5	4.0	40.1	-2.9	4.3	43.3
1.112	1.256	98	-4.8	4.6	45.6	-0.6	3.4	33.7
1.124	1.244	98	-8.9	4.5	44.2	-6.5	3.6	35.5
1.136	1.232	104	-6.2	5.0	51.4	-2.3	5.3	54.0
Mean			-6.4	1.0		-5.5	1.1	

Table 3.10: Centering using speckle positions from pairs of monochromatic images. Only one quadrant was used here, errors should be halved using the full image.

Image centering from Outer Working Angle Corona

Another technique to center stellar images exploits the corona expected at the edge of the AO Outer Working Angle (see Figure 3.21). This procedure has important advantages:

1. It uses monochromatic images, and then can be applied well to both IFS and IRDIS images.

2. The procedure is reasonably accurate, allowing image centering at ~ 1 mas (see below).

The idea behind this method is to measure the location of the peaks at the Outer Working Angle corona of a radial cut of the image on opposite sides of the center for different position angle. In practice, our procedure is:

- to plot the radial cut of the image (see Figure 3.21); we actually plot the values of individual pixels whose coordinates are close to each radius (see Figure 3.22).

- to fit parabolas (in log flux) through these points in regions close to the expected local maxima due to the Outer Working Angle corona on both sides of the image with respect to the center (see Figure 3.22). The maxima of these parabolas give the best estimate of the position of the Outer Working Angle corona for each position.

- We may then plot the mean point between these maxima as a function of position angles (see Figure 3.23, where crosses are the results obtained at different wavelengths).

- The maximum of the best fit sinusoid (red curve in Figure 3.23) gives the offset and position angle of the star with respect to field centre.

Inspection of Figure 3.23 reveals that images at different wavelengths generally give consistent offset of the mean position at a given position angle, while this mean position fluctuates quite significantly (~ 1 pixel, that is ~ 12 mas) around the best sinusoid while position angle changes. This error in the mean position can be attributed to individual offsets of strong speckles, affecting the measure of the corona position. Since ~ 130 independent position angle can be exploited, we expect that the final accuracy of star centering should be ~ 1 mas.

To estimate the error in star centering, we extracted randomly ~ 65 position angles from the stack of measures, and fitted a new sinusoid through these points. The procedure was repeated 20 times. The r.m.s. of individual measures represents an estimate of the error done in this procedure, when half of the points position angles are used. The error on the best estimate (using all 130 position angles) is then obtained by dividing this value for $\sqrt{2}$. Using this procedure, the error is estimated to be 0.088 pixels, that is 1.1 mas.

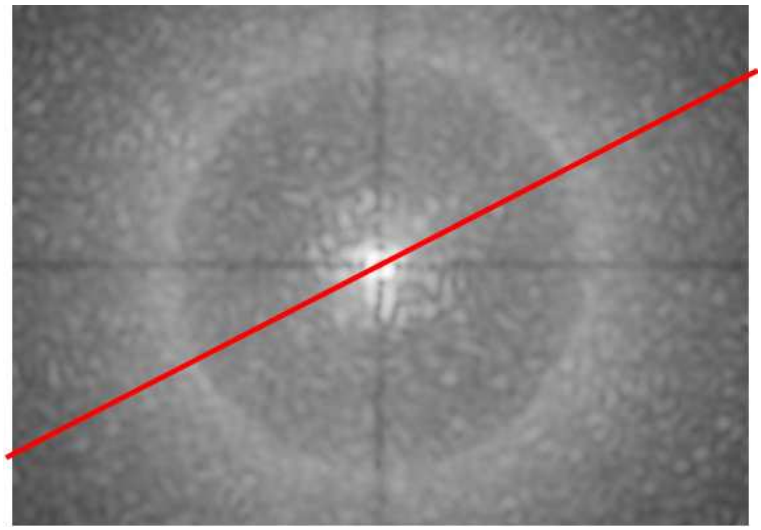

Figure 3.21: Simulated monochromatic image provided by SPHERE, when using 4-quadrant coronagraph. The image is at 1.26 μm. The red line marks an arbitrary selection for a radial cut through the image, the one used in Figure3.22. Some 140 similar cuts are possible, sampling different pixels at the approximate location of the Outer Working Angle, which is the bright corona clearly visible in this image.

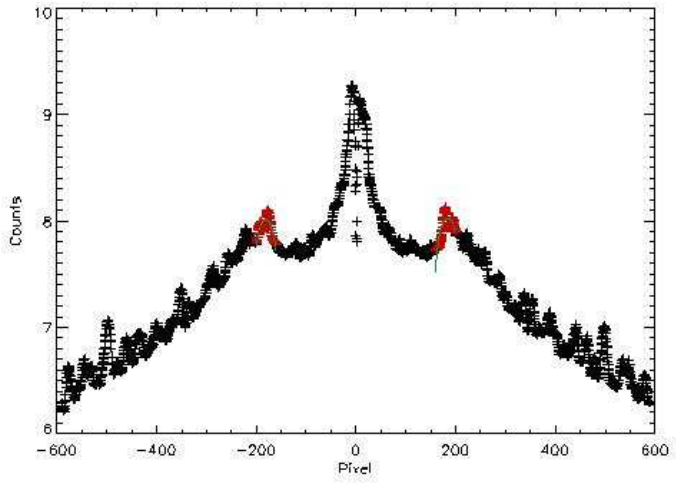

Figure 3.22: Radial cut through the coronagraphic image of Figure 3.21. Note the core asymmetry due to slight offset of the star on the coronagraph (about 6 mas along this direction). Points marked in red are those used to find the Outer Working Angle corona. Overimposed are parabolas fitting through these points (in green).

Speckle symmetry

Speckle arising from even terms of the Taylor series development of the PSF will be symmetric (Perrin et al. , 2003), while those due to odd terms (like pinned speckles) will be antisymmetric. ”Even terms” speckles can then be used to define the center position. In real cases, we cannot easily separate symmetric and antisymmetric speckles. However, we can select those speckles that look symmetric, because they may be found on opposite sides of the image center. We expect that these speckles will be predominantly due to even terms, only perturbed by other fainter speckles possibly due to odd terms. We may further assume that the perturbation due to odd term speckles be either isotropic or have a radial symmetry. In both cases median position between the speckles on both sides of the star center will give a good estimate of the image centre. It is possible to show that this procedure should provide the best possible estimate for the stellar center. In fact, since the centering accuracy of each speckle is ~ 6 mas, the centre coordinate given by the averaging of symmetric speckles should have an accuracy of about 4.2 mas. Since we may form ~ 100 pairs of symmetric speckles, we expect that a single monochromatic image may provide the image centre with an accuracy of about 0.4 mas. The accuracy is still improved by adopting various monochromatic images. However, we are practically limited by speckle anisoplanatism and contamination (which reproduces almost unaltered in different monochromatic images) to about 0.25 mas.

We compared this expectation with results from detailed simulations. We adopted the

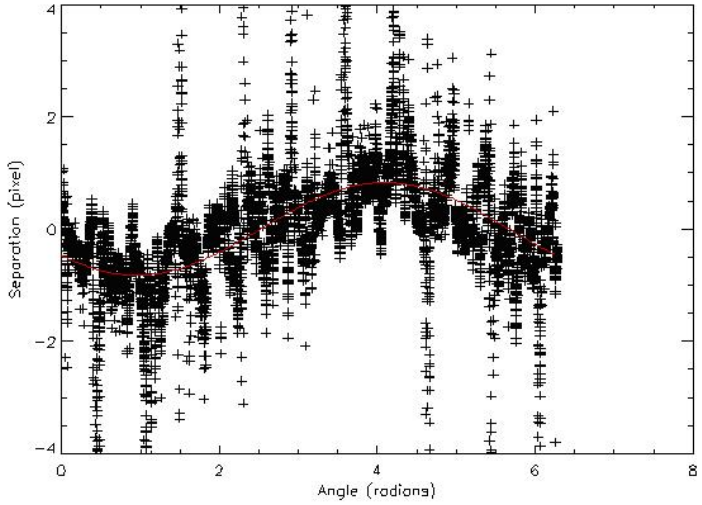

Figure 3.23: Offset from field centre of the mid point of Outer Working Angle corona positions as a function of position angle. Overimposed is the best fit sinusoidal curve. The maximum of this sinusoid gives best offset and position angle of the stellar image. In this plot, 1 pixel=12.25 mas.

following procedure:

- We considered the data cube obtained from a standard IFS simulation.
- For each monochromatic image, we filtered low frequency signal using the IDL function SMOOTH. The cutoff frequency was 5.0 pixels.
- We identified speckles using the IDL FIND procedure in the upper and lower halves of the images separately.
- We then looked in the list of speckles found in the lower half of the images for those speckles that are within a given searching radius[2] from the expected symmetric position deduced from those speckles found in the upper half of the image.
- We then derived the mean of the position of the speckles paired using this procedure. Each one of this pair provided an estimate of the stellar position.
- The procedure was repeated at all wavelengths. Results are shown in Figure 3.24, which show the stellar position mesuread in this way from 7660 pairs of

[2]In this example, we adopted a rather large value of 4 pixels for the search radius. This allows to clearly show the clustering of points due to real pairs with respect to a background of random pairs. However, a smaller search radius should be adopted in usual data analysis.

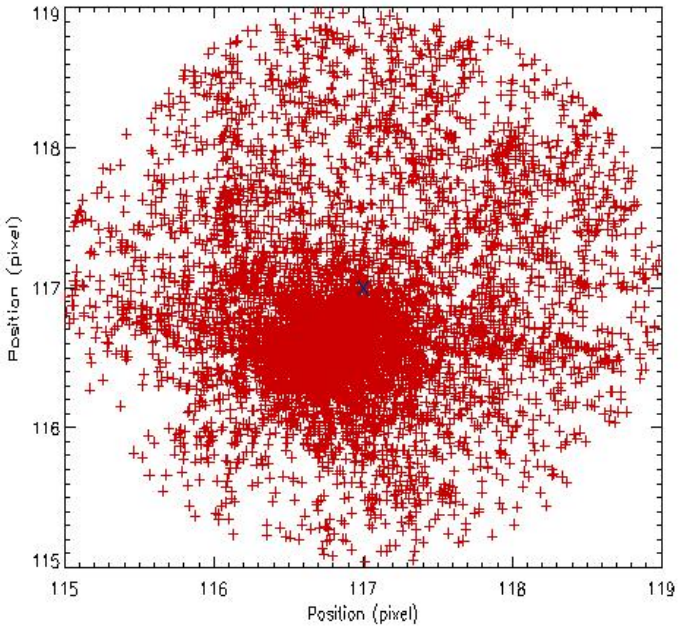

Figure 3.24: Stellar image position derived from individual pairs of symmetric speckles; each point represents a position derived from an individual speckle. The search algorithm looks for speckles within a circle of 4 pixels radius. For this reason all star position estimates lie within a circle with a radius of 2 pixels from the image centre position, which is marked with a black x. A fraction of speckle pairing is due to random fluctuations, and it is responsible for the uniform background filling the whole search circle. However, about half of the pairs are real pair of symmetric speckles. They are responsible for the clustering of points around coordinates (116.75,116.58). Only these points are used for image centering.

Method	X (mas)	Y (mas)
Speckle wavelength shift	-3.4 ± 1.0	-1.0 ± 1.1
Outer Working Angle corona	-4.1 ± 0.8	-3.2 ± 0.8
Speckle symmetry	0.0 ± 0.3	0.0 ± 0.4

Table 3.11: Stellar position determinations in a coronagraphic image using various methods.

speckles, measured on 33 monochromatic images. Since the search algorithm looks for speckles within a circle of radius 4 pixels, all star position estimates lie within a circle with a radius of 2 pixels from the image centre position.

- A fraction of speckle pairs is simply due to random fluctuations, and it is responsible for the uniform background filling the whole search circle. However, about half of the pairs (3800 in 33 images, that is ~ 115 pairs in each image) are real pairs of symmetric speckles. They are responsible for the strong clustering of points around coordinates X=116.75, Y=116.85 (that is x=-3.1, y=-5.1 pixels from nominal field centre). Only these points are used for image centering, using a Gaussian fitting. The standard deviation of the Gaussian is 0.34 pixels along x and 0.22 pixels along y. Essentially, the same result is obtained considering each monochromatic image separately.

- The quadratic sum of these values (0.40 pixels, that is 5.0 mas) give the centering error from individual pairs measured on monochromatic images. This value coincides with that expected combining quadratically the speckle centering error (6 mas) divided by $\sqrt{2}$ (because the average value determined from two speckles on opposite sides of the centre is considered), with the speckle anisoplanatism error (~ 1.75 mas), and the error due to parity of faint contaminants (~ 2 mas).

We expect that speckle centering errors should scale down with the number of independent measures ($n_{speckle} \times n_{wavelength}$). On the other hand, errors due to anisoplanatism and contaminants should scale down simply with $n_{speckle}$. Since $n_{speckle} \sim 115$ and $n_{wavelength}$=33, the final error in stellar position provided by this technique is then 0.26 mas for IFS and 0.37 mas for IRDIS (where only two monochromatic images can be used).

3.3.5 Summary

Table 3.11 compares determinations of the stellar position on a simulated image using various methods. The various determinations are not much different from each other. As said at the beginning of this Paragraph we assume as a position of the field centre the one obtained using the method with the lower error on its determination (that in this case is the third method presented). For this reason in Table 3.11 we report the value of the filed centre positions as a difference from the value obtained with the third method.

Table 3.12 summarizes astrometric errors expected with IFS and IRDIS. Provided adequate calibrations are available, star position can be accurate to ~ 0.1 mas in a non

Method	IFS	IRDIS
Planet centering		
Measurement errors	18/(S/N)	
Stellar centering		
Non coronagraphic images		
Differential tip-tilt jitter	< 0.01	
Distortion	< 0.10	
Atmospheric refraction	< 0.05	
Measurement errors	< 0.01	
Coronagraphic images		
DTTS	~ 1	~ 1
Diffraction peak	5-10	5-10
Speckle wavelength shift	1.5	~ 5
Outer Working Angle corona	1.1	~ 1.5
Speckle Symmetry	0.26	0.37

Table 3.12: Summary of SPHERE astrometric errors (in mas).

coronagraphic observations, and to 0.25 (0.35) mas for IFS (IRDIS) in coronagraphic observations. Planet positions will typically have lower accuracy, depending on S/N of observations. If bright background objects are present in the field, very accurate astrometry is potentially possible.

3.3.6 Background objects and absolute astrometry

Absolute astrometry allows to study motion of the star (and of any faint companion) around the common barycentre (as well as proper motion of the star and absolute parallax). This is possible whenever background objects are detected in the field. Notice that this test is feasible even if no faint companion is actually detected. In general, absolute astrometry with SPHERE should not be competitive with PRIMA observations. However, this mode comes out free of cost and it requires much less telescope time: it can then be considered in a preliminary discussion of data. In order to evaluate the relevance of this mode, we should consider the expected density of background objects (excluding local overdensities).
To estimate this quantity, we first remind that in imaging mode, in the outer part of the IRDIS field where RON and sky dominate, the limiting magnitudes for S/N=5 detection in 1 hour of exposure time is H=25 for point sources and approximately 3 mag worse for galaxies (assuming an image size of ~ 0.3 arcsec).
Expected densities of background objects are as follows:

- Stars: ~0.1-1 star with $16 < R < 26$ for IRDIS field (depending on galactic coordinates - Bahcall & Soneira 1981), all detectable.
- Galaxies: ~4 galaxies with $B < 27.5$ ($K < 24$) for IRDIS field (Metcalfe et al. 1995, Madau & Pozzetti 2000 and Smail et al. 1995); 0.6 (detectable) for

IRDIS field with $I < 23$ (limiting magnitude for a detection with $S/N > 5$). However galaxies are well resolved by SPHERE (typical size ∼0.3 arcsec ∼20 pixels even at a redshift of $z > 1$): images are then spread over a few 10^2 pixels. Usefulness for astrometry is then reduced. Typical astrometric precision from a galaxy is ∼20 times worse than from a stellar image (for a galaxy having the same integrated luminosity than a star).

- Clusters in external galaxies: a cluster with $M_v \sim -7$ (a typical globular cluster) only detectable with the SPHERE out to $(m - M) \sim 31 - 32$, that is Virgo cluster distance. They are then of very limited use.

- High redshift supernovae (SNe): SNe ($M_H \sim -18$) should be detectable by SPHERE even if in high redshift galaxies with $(m - M) \sim 43 - 44$. In local galaxies, on average we have ∼ 1SNe/100 years. At high redshift the rate is likely > 10 times larger (see Madau plots). We then expect $> 1 SNe/galaxy$ every 10 years. The SNe should be luminous for ∼2 months, and there are ∼4 galaxies for IRDIS field. We then expect ∼0.1 SNe for IRDIS field. A number of SNe could be then observable during the survey. They should be easily distinguished from faint companions from proper motions, and from background galactic stars from variability.

We note that limitations due to the proper motion of the star (expected values for most targets are a few hundreds mas/year) are not too strong.
Absolute (with respect to time) astrometric accuracy is then of the order of < 1 mas in the favorable (but not very rare) cases in which a star (or over a limited time range a high redshift SNe) is in the field, and of the order of 5 mas in those cases where detectable galaxies are in the field.

3.3.7 Astrometric grid calibration

Distortion effects and lateral color are not negligible for SPHERE, if astrometry at < 1 mas accuracy is desired. For instance, lateral color due to Common Path optics is expected to be about 1 mas at the corner of the IFS field. Suitable calibrations are then required in order to recover correct astrometry. Instrumental distortions and scale variations can be monitored using the internal astrometric grid. The accuracy of positions of individual spots in the grid is 500 nm, corresponding to 0.9 mas. This is enough for measures accurate to ±1 mas, but not enough for calibrating astrometry to ±0.1 mas accuracy.
Is it possible to use the astrometric grid also for very accurate (±0.1 mas) astrometry? The main advantages of the astrometric grid are:

- calibrations can be performed frequently and during daytime.

- the spots are holes on a hard surface. Measures are then very repeatable, save for zero-point offsets (due to slight positioning errors) and scale variation (due to thermal effects). In principle this discloses the possibility to measure the offsets of individual points of the grid, and to correct results for this effect. This requires

measurements of spots position with an accuracy of 50 nm, which seems very difficult.

We may however exploit these advantages establishing the following calibration procedures:

- Distortion: the basic idea is to measure the variation of scale along the FoV measuring a number of spots whose relative position is known with an error of ±0.9 mas[3]. Accuracy can be improved by "dithering" the grid, that is using a different set of spots for any (approximate) location of the field. This requires oversampling of the grid, and at least one motorized axis (this last is already available), because the grid is mounted on a slide. Assuming a 10 step dithering (which represents a moderate oversizing of 30% of the IRDIS/ZIMPOL FoV in the direction of the slide motion) allows to reduce errors in individual points to ±0.3 mas. Furthermore, only low order surfaces would be used to fit data, so that errors in individual points can be further reduced. Distortion is not expected to change fast with time because SPHERE is in a constant gravity configuration. The same distortion pattern correction should then be applicable over quite long intervals.

- Scale variation: in this case, we want to measure the overall instrument scale, which is expected to change with temperature and pressure. This may be obtained by monitoring the separation of individual spots. In this case, it is better to use always the same spots and simply evaluate the scale factor required to match their relative locations, with respect to a reference spot pattern. Once a large number of such measures are available, correlations with temperature and pressure can be constructed, so that appropriate look up table can be derived, reducing the number of calibrations required.

Note that these calibrations should be repeated whenever coronagraph and Common Path neutral density filters are exchanged. In principle, this procedure should allow instrumental distortion measures with errors of ∼0.1 mas, allowing to keep the astrometric potential of SPHERE.

3.4 Spectral classification with SPHERE IFS

The SPHERE IFS simulations described previously in Chapter 3 demonstrated the ability of this instrument to image extrasolar planets down to a luminosity contrast of $\sim 10^{-7}$ respect to the central star. However, to fully characterize the new discovered planets (e.g. temperature, chemical composition of the atmosphere, etc.), it should be important to be able to reconstruct their spectra at a good fidelity level.
To this aim we developed a pipeline to perform a data analysis on the calibrated data cube resulting from our simulations (the data cube in our case is composed by 33 images at different wavelengths for the z-J-mode and by 38 images for the z-H- mode).

[3]Zero point error of the grid is significantly larger, but this is irrelevant for this calibration, because the zero point offset can be accurately determined using cross correlation

This analysis procedure could be applied in the future to the data from the real instrument, too. The procedure is composed by different steps:

1. Speckle noise subtraction from the original data cube using the spectral deconvolution algorithm.
2. Summing all the resulting images to create a single multi-wavelength image.
3. Search for objects on the summed image.
4. Extraction of a spectrum for every object found.
5. Spectral classification of every object.

In particular, for what concern the spectral extraction and classification, we tried to answer to the following questions:

1. Are the output spectra independent from the position of the planet on the image?
2. How the output spectrum varies with the separation from the central star?
3. How the output spectrum varies with the luminosity contrast with the central star?
4. Is the method used sensible to the spectral type of the planet?
5. Are we able to disentangle planetary companions from field stars using a single epoch spectrum alone (i.e. without requiring second epoch observation for common proper motion evaluation)?

In the following Paragraphs we describe the procedure used to address these questions and the results that we obtained.

3.4.1 Procedure description

The input for the CSP simulation code was the same PSFs used for previous simulations (see Section 3.2.1) with the FoV rotating by 30° during the observations. The central star is a G0V and it is at a distance of 10 pc (this corresponds to a magnitude of J=3.75). To answer to the first question concerning the spectral extraction and classification listed above, we made simulations with 5 identical planets (same input spectra) at the same separation from the central star and the same luminosity contrast respect to the host star.
To answer to the second question we performed different simulations with companion objects at the following separations from the central star:

- 0.3 arcsec
- 0.5 arcsec
- 1.0 arcsec

For what concern simulations with companion objects at a separation of 0.3 arcsec, it resulted that in the simulations with 5 objects they were very near each other. This could create some disturb in the objects detection and in the correct spectra extraction. For this reason we performed three different simulations with the same separation but with only 2 objects in different positions. We have then 6 different objects for every different case at 0.3 arcsec.
To answer to the third question we performed different simulations with the following luminosity contrast between the planets and the central star:

- 10^{-5}
- 3×10^{-6}
- 10^{-6}
- 3×10^{-7}

To answer to the fourth question we performed different simulations using four different input spectra:

- The spectrum of a late type T dwarf (T7 spectrum).
- The spectrum of an early type T dwarf (T2 spectrum).
- The spectrum of a late type L dwarf (L8 spectrum).
- The spectrum of an early type L dwarf (L0.5 spectrum)

To answer to the fifth question, finally, we performed our simulations using, as input spectrum, an M2 spectral type too (that is a flat spectrum at the spectral resolution of the SPHERE IFS).

3.4.2 Short description of the analysis procedure

In the following we briefly describe the procedure that we adopted to reduce the data cube that we obtained from our simulations. All the IDL routines that are used in this procedure has been implemented by the author. This procedure can be seen as a starting point for a future reduction procedure to be applied to the real data from the IFS. The general structure of the procedure that we used for our reduction pipeline can be visualized in the flow chart showed in Figure 3.25.
The output of the CSP code simulations is a data cube composed by 33 (or 38 - see above) monochromatic images of the FoV (only a quadrant of the image is actually used for these simulations) spanning over all the wavelength range of the IFS instrument ($0.95 \div 1.35 \mu m$ for the z-J-mode and $0.95 \div 1.70 \mu m$ for the z-H-mode). The first step of our procedure is to perform on these images the speckle subtraction exploiting the spectral deconvolution method (this choice has been made because the spectral deconvolution has resulted to be the most effective method to do the speckle subtraction from the results of our previous simulations - see Section 3.2.5).

To extract the planet signal, the single bi-dimensional and monochromatic images

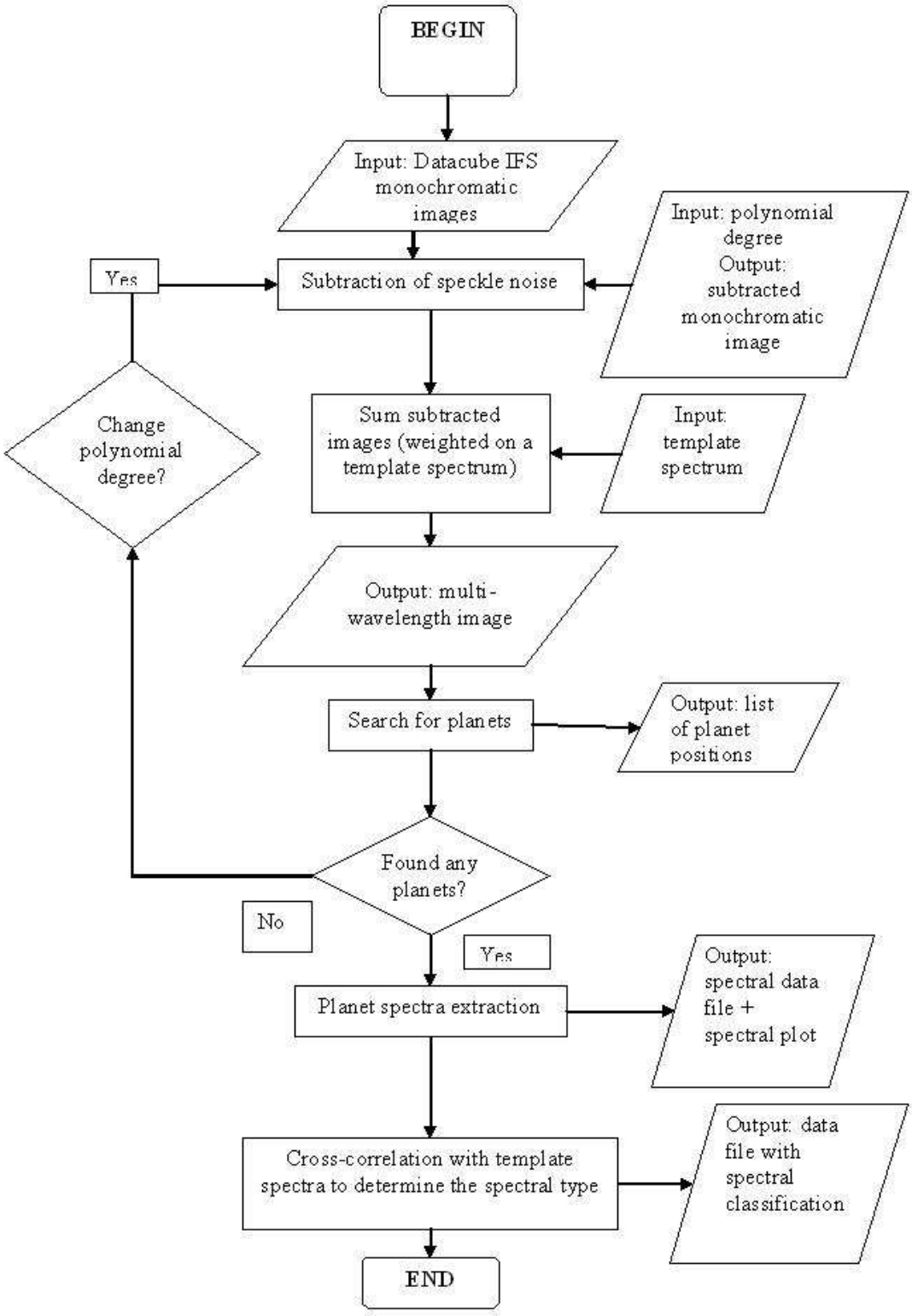

Figure 3.25: Flow chart explaining the reduction procedure for the SPHERE IFS dataset.

that composed the data cube resulting from the above described procedure are then summed together with a different weight given by the cross-correlation with a template spectrum. In our procedure we used the input spectrum of the CSP code, but in the real cases, when the planet spectrum is not known, this part of the procedure should be repeated for a series of template spectra. The final result is then a single multi-wavelength image where the planet signal should be strongly enhanced.
On this multi-wavelength image we then perform an automatic search for companion objects of the central star. This part of the procedure is composed by three different steps:

- For every pixel of the image we compare the flux included in a circle centered on the analyzed pixel and the flux into an external annulus. The radii values of the circle and of the annulus can be chosen by the user but, for our analysis, we always adopted the values of 1.5, 2 and 4 (pixels) respectively. The user can choose the type of statistic to be done on these regions: a mean or a median. For our analysis we adopted the second case that seems to give better results. The program find an object if the value found for the inner circle is greater than the value for the outer corona plus the standard deviation (on the outer corona) multiplied for a factor that can be chosen by the user and that has to be considered carefully case by case.

- The procedure then, if finding more than one object into a radius of 3 pixels, retains only the most luminous one.

- Finally a 2-dimensional Gaussian fit is performed on a small region around the newly discovered object to find its precise position (in 1/1000 of pixel). We try to minimize the difference between the extracted PSF and the fitting function performing an iterative procedure that search for the minimum of the difference by changing the parameters of the Gaussian fitting function.

We then extracted the spectrum of the newly found object simply summing the flux of the pixels at a distance less than 1 pixel on every subtracted monochromatic image and subtracting from this value the median from an external annulus. We make the same extraction for two positions at a distance of $\pm\lambda/D$ from the object position (but at the same separation) to evaluate the spectral noise. Subtracting the mean of these two spectra from the object spectrum can then improve the final spectral classification that is the last step of our procedure.
To classify the newly discovered objects, we compared the output spectra of our simulations with template spectra (from T0 to T8 for the T dwarfs and from L0 to L8 for the L dwarfs with the spectral type L7 substituted with L7.5 because we were not able to find such a spectrum in the literature, as well as of F1V, G0V, K5V, M2V and M8V type stars spectra). In Figure 3.26, Figure 3.27 and Figure 3.28 we show the template spectra used for this work. Spectral classification was obtained by a cross-correlation (using the IDL routine C_CORRELATE) between the output spectrum of each simulation and the template spectra. The spectral type with the highest cross-correlation coefficients is the spectral type assigned to the simulated planet. The data for the T type dwarf template spectra has been taken from the A.J. Burgasser per-

sonal site and are results of various paper of this author (Looper, Kirkpatrick and Burgasser (2007) for T0, Burgasser et al. (2004) for spectra from T1 to T5 and for T8 and Burgasser et al. (2006) for T6 and T7). The data for the L-type dwarfs spectra have been taken from Testi et al. (2001). The stellar spectra have been taken from the IRTF Spectral Library (`http://irtfweb.ifa.hawaii.edu/~spex/IRTF_Spectral_ Library/index.html`).

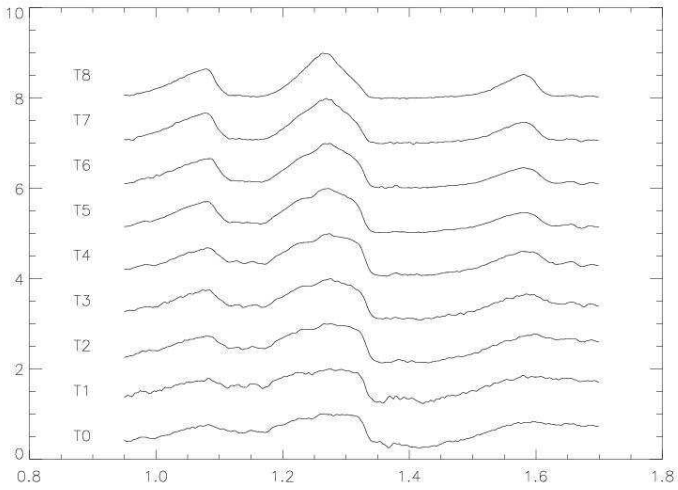

Figure 3.26: Template spectra for the T type dwarfs.

3.4.3 Results

z-J-mode

In Figure 3.29 and in Figure 3.30 we show the final multi-wavelength images that we obtained from the simulations performed with a T7 and a L0 input spectrum. From the left panel to the right one we show the simulation at a separation of 0.3, 0.5 and 1.0 arcsec respectively, while from the the top to the bottom we show the simulations at decreasing contrast. It is evident that the planets are clearly visible apart the case with a separation of 0.3 arcsec and a contrast of 3×10^{-7} for the T7 spectrum. It is moreover apparent the presence, in the final images, of structures along the central star-companion object direction that are due to the speckle subtraction method. These structures are much more evident in the early spectral type objects than in the case of late spectral type objects (this is especially true for the higher contrast objects). This results in a greater disturb when trying to find an object and in a worst capability to reconstruct its spectrum.

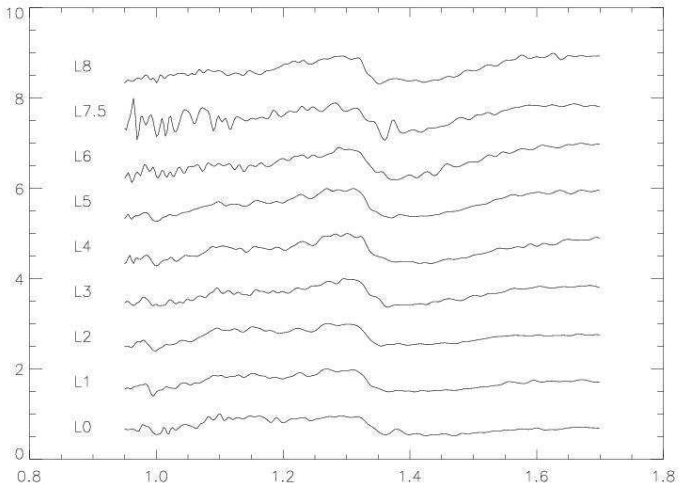

Figure 3.27: Template spectra for the L type dwarfs.

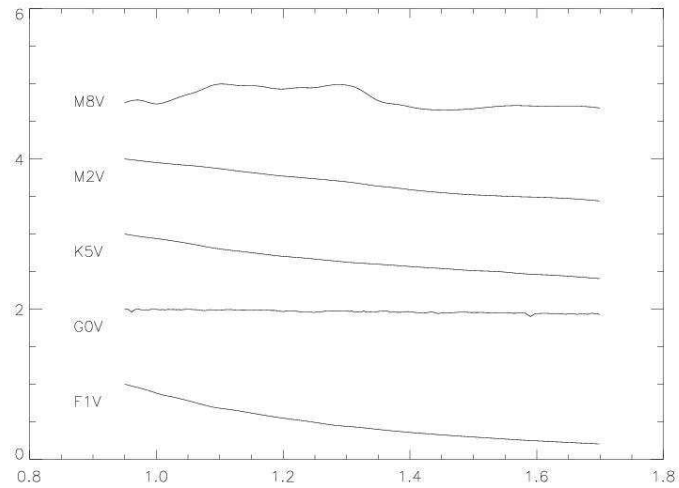

Figure 3.28: Template spectra for stars of various spectral types.

	0.3 arcsec	0.5 arcsec	1.0 arcsec
10^{-5}	6(0)	5(0)	5(0)
3×10^{-6}	6(0)	5(0)	5(0)
10^{-6}	6(5)	5(0)	5(0)
3×10^{-7}	0(0)	4(0)	3(2)

Table 3.13: Number of companions found for every z-J-mode simulation for the case of the T7 spectral type input spectra. In parentheses are indicated the number of spurious objects found.

	0.3 arcsec	0.5 arcsec	1.0 arcsec
10^{-5}	6(0)	5(5)	5(6)
3×10^{-6}	6(0)	5(4)	5(0)
10^{-6}	6(0)	5(3)	5(0)
3×10^{-7}	3(6)	5(0)	5(0)

Table 3.14: Same of Table 3.13 but for T2 spectral type.

	0.3 arcsec	0.5 arcsec	1.0 arcsec
10^{-5}	6(0)	5(6)	5(6)
3×10^{-6}	6(0)	5(5)	5(2)
10^{-6}	6(4)	5(0)	5(0)
3×10^{-7}	3(6)	5(0)	5(0)

Table 3.15: Same of Table 3.13 but for L8 spectral type.

	0.3 arcsec	0.5 arcsec	1.0 arcsec
10^{-5}	6(0)	5(6)	5(5)
3×10^{-6}	6(2)	5(4)	5(0)
10^{-6}	5(0)	5(2)	5(0)
3×10^{-7}	3(8)	5(4)	5(0)

Table 3.16: Same of Table 3.13 but for L0 spectral type.

	0.3 arcsec	0.5 arcsec	1.0 arcsec
10^{-5}	6(0)	5(5)	5(4)
3×10^{-6}	6(5)	5(3)	5(0)
10^{-6}	5(0)	5(2)	5(0)
3×10^{-7}	2(4)	5(1)	5(0)

Table 3.17: Same of Table 3.13 but for M2 spectral type.

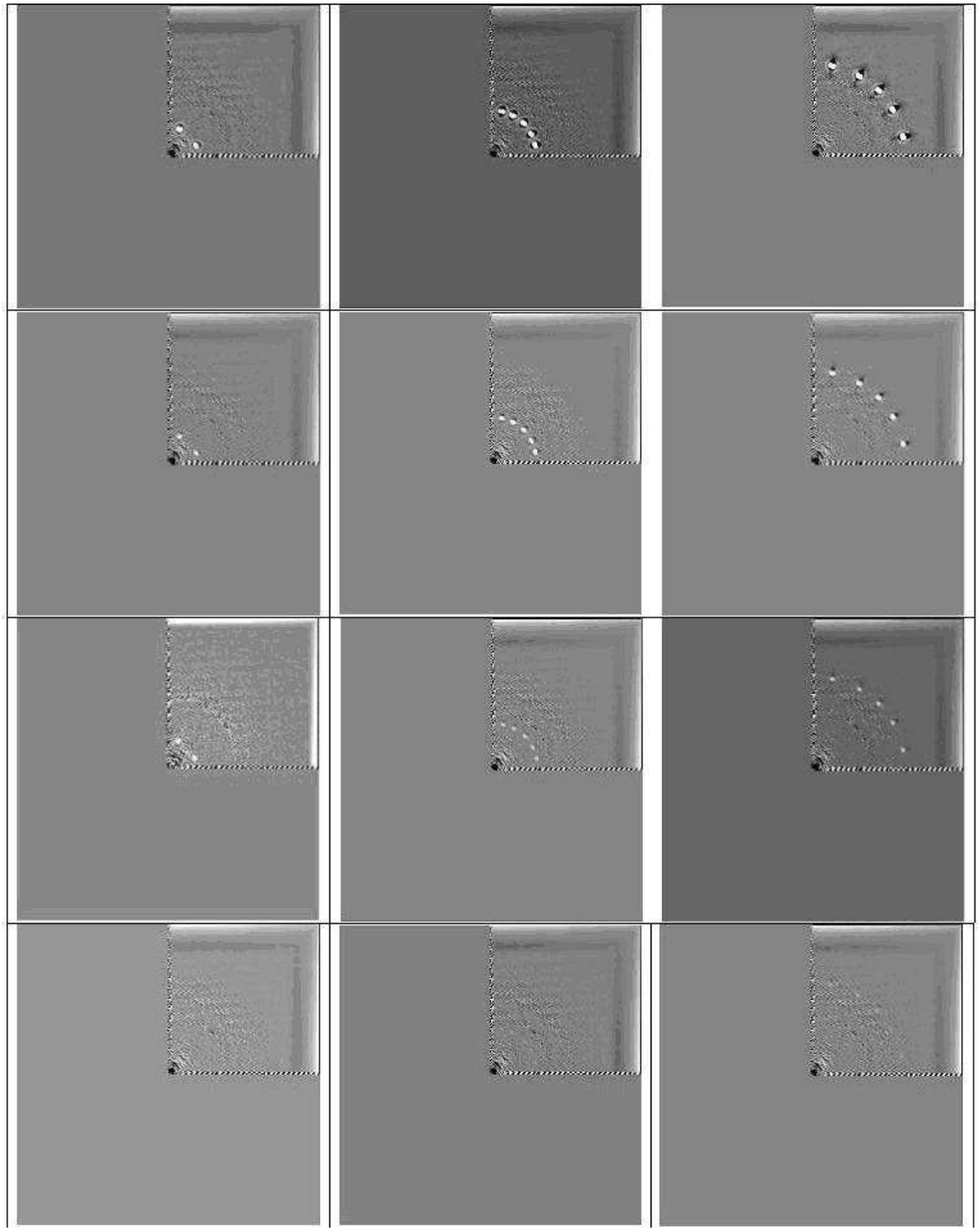

Figure 3.29: Final multi-wavelength images obtained for simulations of the z-J-mode at different contrast (0.3, 0.5 and 1.0 from left to right) and with different contrasts respect to the central star (10^{-5}, 3×10^{-6}, 10^{-6} and 3×10^{-7} from top to bottom) with a T7 spectral type input spectrum.

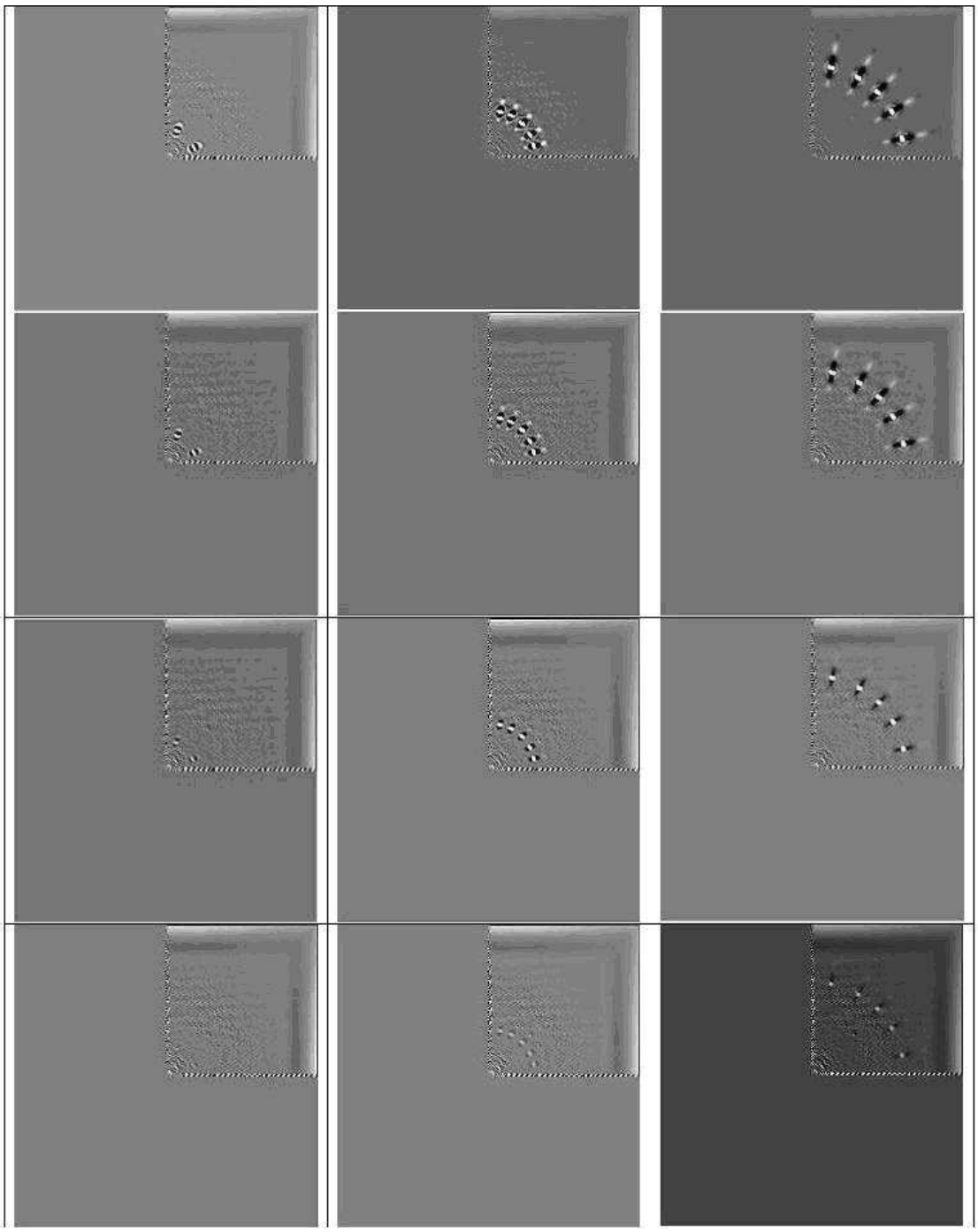

Figure 3.30: Same of Figure 3.29 but for L0 spectra type input spectrum.

In Table 3.13, Table 3.14, Table 3.15, Table 3.16 and Table 3.17 we report the number of companion objects found for every simulation that we made. It is evident that we are able to find almost all the simulated objects down to a contrast of 10^{-6}, while we can lose a lot of them for a contrast of 3×10^{-7} (this is in particular true for a low separation from the central star - i.e. 0.3 arcsec in our simulations).

In Figure 3.31 we show the histogram with the number of objects found for every

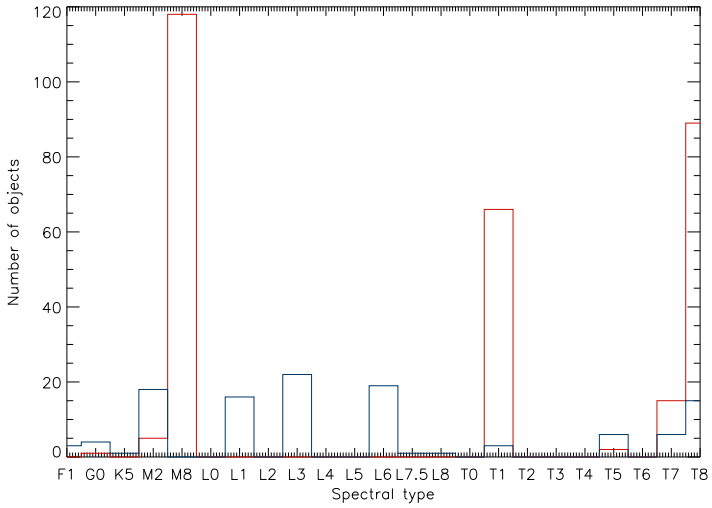

Figure 3.31: Histogram with the number of objects (red) and of spurious objects (blue) found for every spectral type in the z-J-mode case.

spectral type with our procedure plotted in red while in blue is plotted the number of spurious objects found for every spectral type. For what concerns the simulated objects we can see three high peaks corresponding to the M8, T1 and T8 spectral types. The M8 peak is given by the contribution of objects with both an M2 (used to simulate possible flat spectrum contaminants) and L0 input spectrum. The T1 peak is given by the objects with L8 and T2 input spectra. In this case however the peak is quite low and the objects classification is more dispersed. Finally, the T8 peak is given by T7 input spectra objects. These results are confirmed by Table 3.19 where we report the mean Spectral Type determined by our procedure compared to the input spectrum Spectral Type for different contrasts with respect to the central star. In this Table all the separation are considered together. In general, apart for the case of L0 input spectra, it seems that our procedure tends to classify the objects with later Spectral Types than the effective ones.

For what concerns the spurious objects we do not have any particular peak in the final distribution.

In Figure 3.32 we show the same distribution of the red histogram in Figure 3.31 but dividing it according to the input spectral type. This image confirms what we said pre-

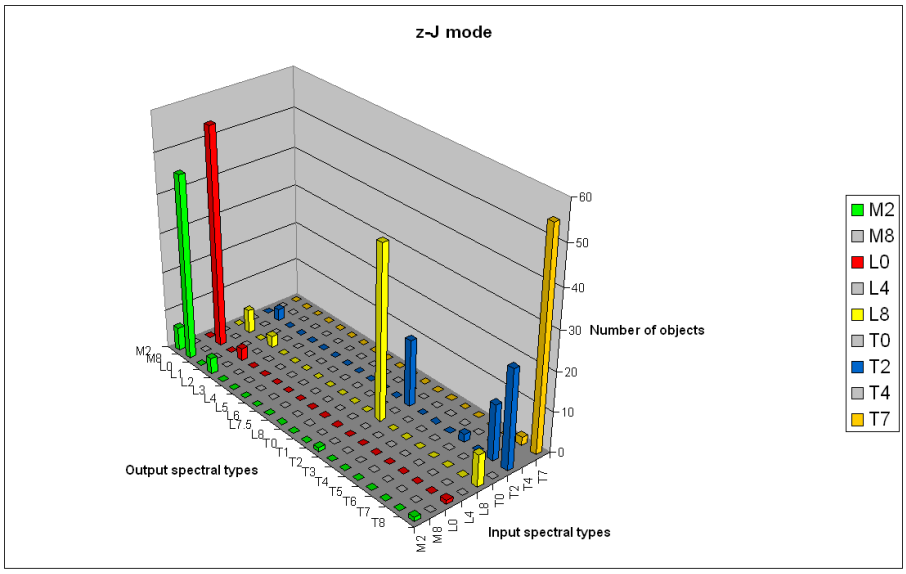

Figure 3.32: Distribution of the spectral types of the found objects for the different input spectral types for the z-J-mode. The spectral types indicated with the grey color have not been used as input for our simulations and habe been inserted into the image only to space out the used spectral types and make clearer the image.

Sp. Type.	Found Objects	% Found Objects	Spurious Objects	% Spurious Objects
T7	55 out of 64	85.9	7 out of 62	11.3
T2	61 out of 64	95.3	24 out of 85	28.2
L8	61 out of 64	95.3	29 out of 90	32.2
L0	60 out of 64	93.8	31 out of 91	34.1
M2	59 out of 64	92.1	24 out of 83	28.9

Table 3.18: Number and percentage of found objects and of spurious objects subdivided by simulation input spectrum for the z-J-mode case.

viously showing that both M2 and L0 spectral types are preferentially recognized ad M8 spectral type while L8 input spectral type is preferentially classified as T1 spectral type (even if in this case the distribution is much more dispersed. Finally, T2 input spectral type is generally classified as T1 or T7-8 spectral type with a small preference for the latter while T7 input spectral type is generally classified as T8.
In Table 3.18 we report the general numbers of found objects in our simulations exploiting this procedure. It is apparent that we are able to find more than the 90% of the simulated objects. Most of the lost objects come from the worst case simulations (that is contrast of 3×10^{-7} and a separation of 0.3 arcsec). In the last two columns of this Table we reported the number and the percentage of the spurious objects found. The number is quite high especially for the earlier Spectral Type simulations.

z-H-mode

Like for the z-J-mode case we show in Figure 3.33 and in Figure 3.34 the final multi-wavelength images that we obtained from the simulations of the z-H-mode. The two cases are quite similar but, from a more careful observation of the images, it results clear that the z-H-mode allows to obtain more evident objects. Moreover, for the case with a contrast of 3×10^{-7} and a separation of 0.3 arcsec, where for the z-J-mode case the planets were not visible, they are quite clearly visible for the z-H-mode.

Like for the z-J-mode case, in Table 3.20, Table 3.21, Table 3.22, Table 3.23 and in Table 3.24 we listed the number of simulated planets that we found with our automatic procedure for the z-H-mode (like for the previous Tables the number of spurious objects are listed in parentheses).
From these Tables it is evident that this method is more effective in finding companions objects using the z-H-mode than using the z-J-mode. This is especially true when we are at large separations from the central star. Indeed, at a separation of 1.0 arcsec all the simulated planets are easily found independently from the input spectral type and the number of spurious objects is very low. For the 0.5 arcsec case we are able to find almost all the objects put in the simulations even if in this case we find a greater number of spurious objects. This is even more true for the 0.3 arcsec separation case where, while we are able to find almost all the simulated objects (apart some objects at the lower contrasts) differently from the z-J-mode case, we also tend to find an higher number of spurious objects. The spurious objects are in particular found for earlier

Input Sp. Type	Contrast	Mean output Sp. Type	St. Dev. on Sp. type
T7	10^{-5}	T8.0 (16 obj.)	0.0
T7	3×10^{-6}	T8.0 (16 obj.)	0.0
T7	10^{-6}	T8.0 (16 obj.)	0.0
T7	3×10^{-7}	T8.0 (7 obj.)	0.0
T2	10^{-5}	T5.6 (16 obj.)	3.2
T2	3×10^{-6}	T5.6 (16 obj.)	3.2
T2	10^{-6}	T5.6 (16 obj.)	3.2
T2	3×10^{-7}	T5.8 (13 obj.)	5.7
L8	10^{-5}	T0.2 (16 obj.)	5.8
L8	3×10^{-6}	T1.6 (16 obj.)	4.2
L8	10^{-6}	T1.2 (16 obj.)	3.8
L8	3×10^{-7}	T0.2 (13 obj.)	3.1
L0	10^{-5}	M8.0 (16 obj.)	0.0
L0	3×10^{-6}	M8.0 (16 obj.)	0.0
L0	10^{-6}	M8.0 (15 obj.)	0.0
L0	3×10^{-7}	M8.0 (13 obj.)	0.0
M2	10^{-5}	M7.6 (16 obj.)	1.2
M2	3×10^{-6}	M8.0 (16 obj.)	0.0
M2	10^{-6}	M8.0 (15 obj.)	0.0
M2	3×10^{-7}	M6.0 (12 obj.)	5.5

Table 3.19: Mean spectral type for the extracted spectra compared to the input spectra at different contrasts (both 0.3, 0.5 and 1.0 arcsec separation simulations) for the z-J-mode case.

	0.3 arcsec	0.5 arcsec	1.0 arcsec
10^{-5}	6(0)	5(0)	5(0)
3×10^{-6}	6(0)	5(0)	5(0)
10^{-6}	6(0)	5(0)	5(0)
3×10^{-7}	5(1)	5(0)	5(0)

Table 3.20: Same of Table 3.13 bur for the z-H-mode.

	0.3 arcsec	0.5 arcsec	1.0 arcsec
10^{-5}	6(0)	5(0)	5(0)
3×10^{-6}	6(0)	5(0)	5(0)
10^{-6}	6(0)	5(0)	5(0)
3×10^{-7}	6(0)	5(0)	5(0)

Table 3.21: Same of Table 3.14 but for the z-H-mode.

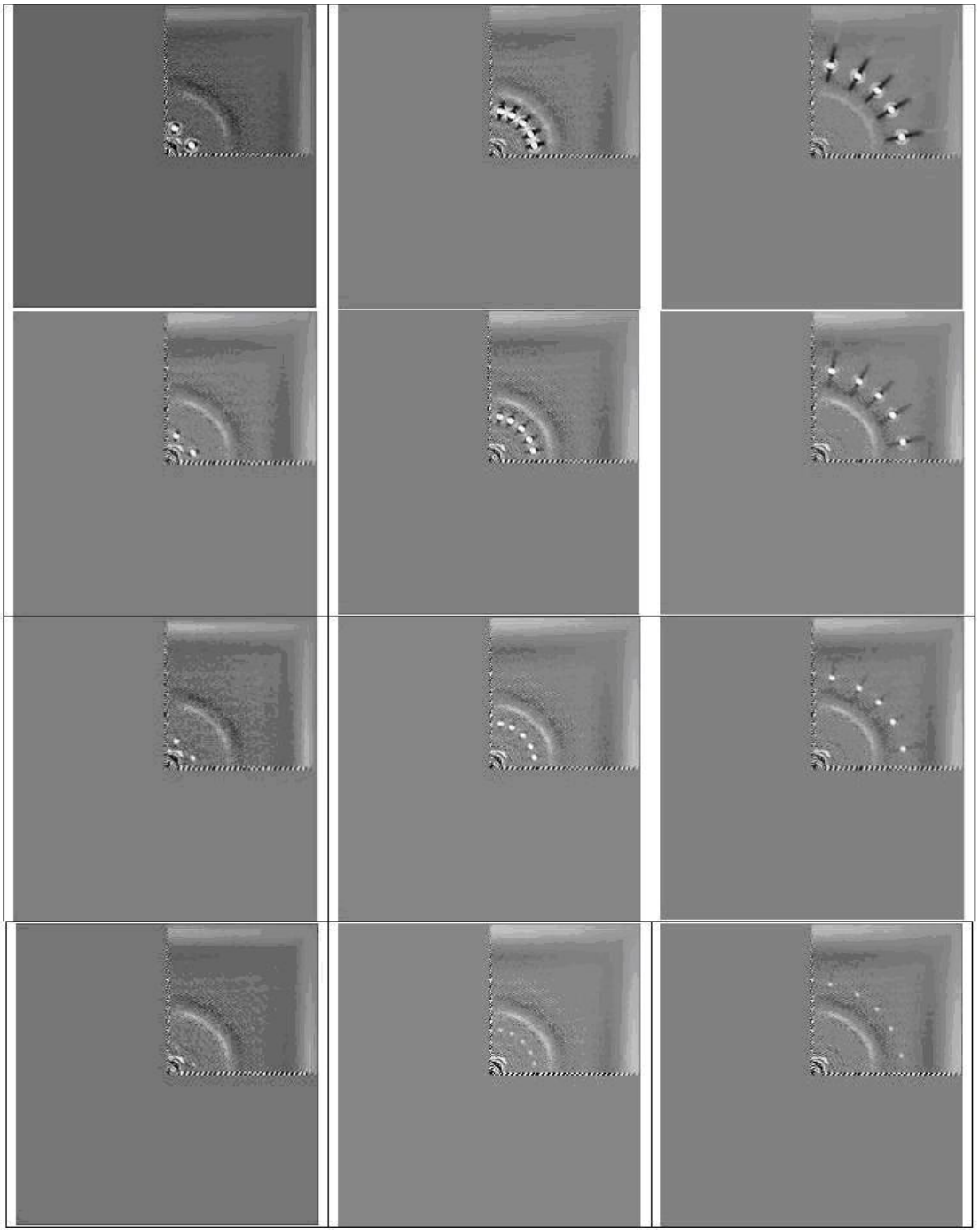

Figure 3.33: Same of Figure 3.29 but for the z-H-mode.

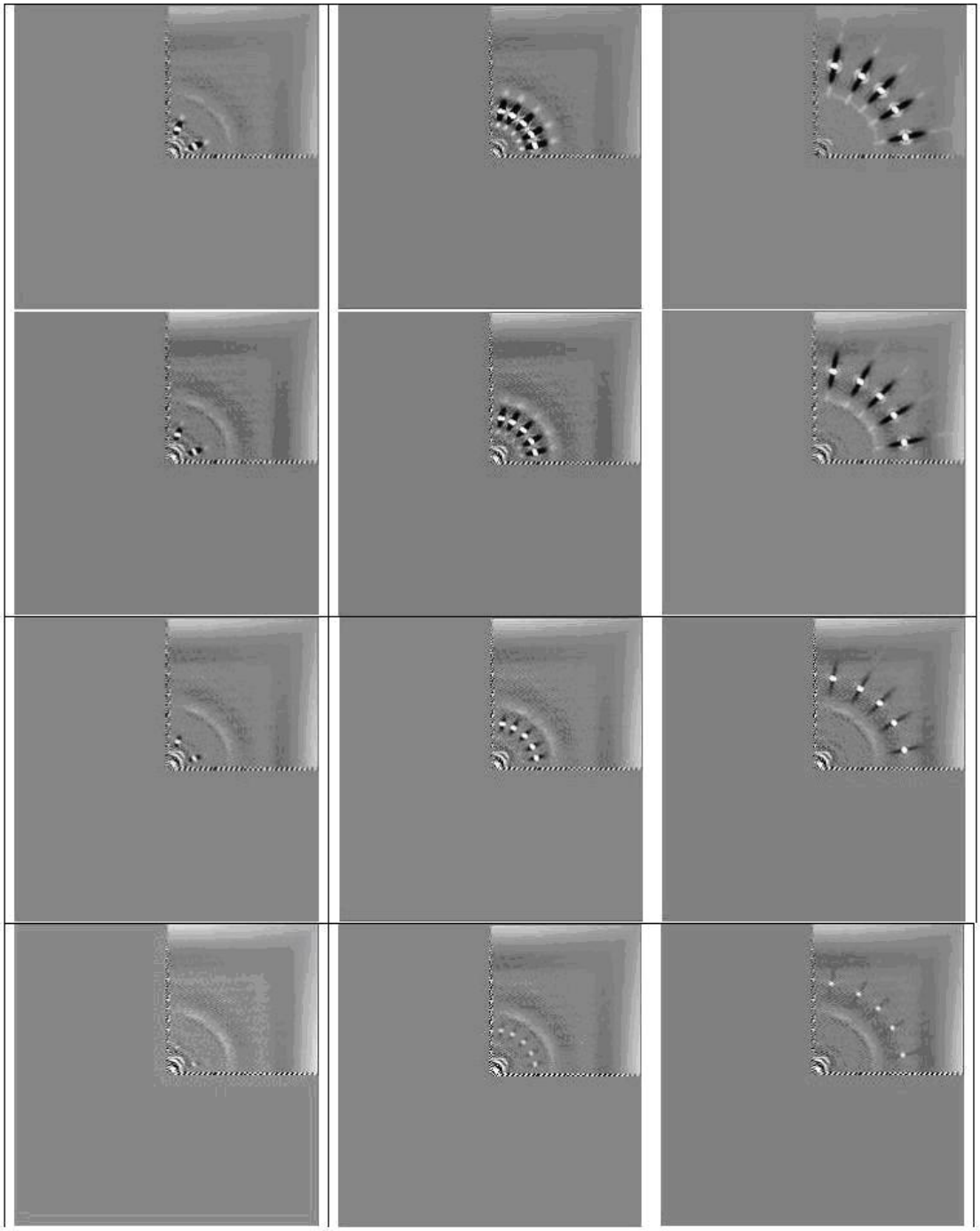

Figure 3.34: Same of Figure 3.30 but for the z-H-mode.

	0.3 arcsec	0.5 arcsec	1.0 arcsec
10^{-5}	6(2)	5(3)	5(0)
3×10^{-6}	6(4)	5(0)	5(0)
10^{-6}	4(1)	5(0)	5(0)
3×10^{-7}	5(2)	5(0)	5(0)

Table 3.22: Same of Table 3.15 but for the z-H-mode.

	0.3 arcsec	0.5 arcsec	1.0 arcsec
10^{-5}	6(5)	5(4)	5(0)
3×10^{-6}	6(6)	5(2)	5(0)
10^{-6}	6(4)	5(0)	5(0)
3×10^{-7}	5(1)	5(0)	5(0)

Table 3.23: Same of Table 3.16 but for the z-H-mode.

	0.3 arcsec	0.5 arcsec	1.0 arcsec
10^{-5}	6(7)	5(4)	5(0)
3×10^{-6}	5(1)	5(1)	5(0)
10^{-6}	6(1)	5(0)	5(0)
3×10^{-7}	4(0)	5(0)	5(0)

Table 3.24: Same of Table 3.17 but for the z-H-mode.

Sp. Type.	Found Objects	% Found Objects	Spurious Objects	% Spurious Objects
T7	63 out of 64	98.4	1 out of 64	1.6
T2	64 out of 64	100.0	0 out of 64	0.0
L8	61 out of 64	95.3	12 out of 73	16.4
L0	63 out of 64	98.4	22 out of 85	25.9
M2	61 out of 64	95.3	14 out of 75	18.7

Table 3.25: Same of Table 3.18 but for the z-H-mode.

spectral types (L and M) while for the T-type objects we find only one spurious object (considering all the simulations) as it is clear from Table 3.25. This is probably given by the fact that the radial structures caused by the spectral deconvolution method are much more intense for L and M-type simulations than for the T-type ones (this can be easily seen by a comparison between Figure 3.33 and Figure 3.34)

In Table 3.25 we report the number and the percentage of found objects and the number and the percentage of spurious objects for the z-H-mode simulations. By a comparison with Table 3.18 that reports the same values for the z-J-mode simulations, it is apparent that our procedure is much more effective in finding the simulated planets objects if we use the z-H-mode. Moreover the percentage of spurious objects that we find with our method is lower in this second case.

In Figure 3.35 we show the histogram with the number of objects found for every spectral type with our procedure (plotted in red), while in blue is plotted the number of spurious objects found for every spectral type (same of Figure 3.31 for the z-J-mode). Like for the previous case, we have three main peaks. The first one is at M8 Spectral Type and it is due to the contribution from the simulations with M2 and L0 input spectra objects. Like for the z-J-mode case these two spectral types seem to give origin to a degeneracy. The second peak is around the T4 Spectral Type and it is mainly given by the T2 input spectra simulations but from the L8 simulations too. The L8 simulations does not give in general correct identification. Indeed, these objects are recognized alternatively as L2 Spectra Type or as an early T Spectral Type. The last peak is around the T7 Spectral Type and it is given exclusively by the T7 simulations objects (the T8 recognitions are given by the simulation at 0.3 arcsec separation). In general, however, the spectral classification is better with z-H-mode. This is demonstrated from the higher values of the cross-correlation coefficients that we obtain in this second case.

In Figure 3.36 we present the distribution of the found objects for the z-H-mode case. Like for the z-J-mode case, the M2 and L0 input spectral types are generally classified as M8 spectral type. Even for the z-H-mode the L8 input spectral type has a dispersed classification with a preference for the T4 spectral type. For what concerns the later spectral types, the T2 input spectral type is generally classified as T4 or T3 while the T7 input spectral type is generally correctly classified as T7 with a lower number of T8 classifications.

Finally, in Table 3.26 we report the mean Spectral Type calculated for simulations with the same input spectra and the same contrast (case with different separation are then considered together). In the last column of this Table we report the standard deviation

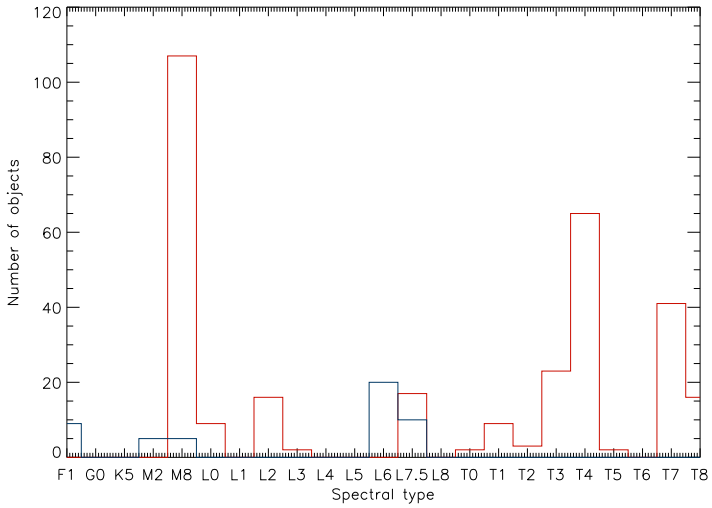

Figure 3.35: Same of Figure 3.31 but for the z-H-mode.

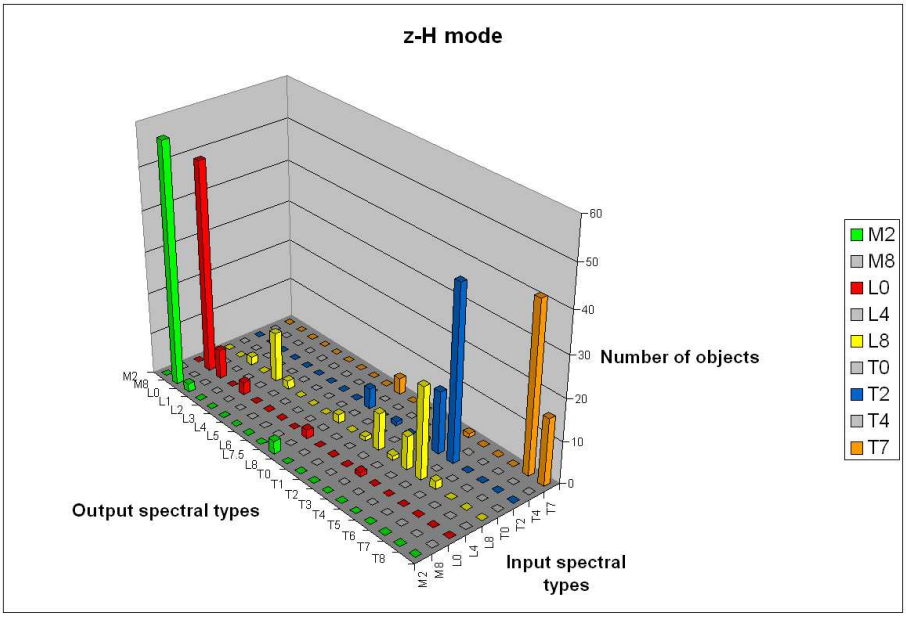

Figure 3.36: Same of Figure 3.32 but for the z-H-mode.

Input Sp. Type	Contrast	Mean output Sp. Type	St. Dev. on Sp. type
T7	10^{-5}	T7.3 (16 obj.)	0.2
T7	3×10^{-6}	T7.4 (16 obj.)	0.3
T7	10^{-6}	T7.4 (16 obj.)	0.3
T7	3×10^{-7}	T4.0 (15 obj.)	4.1
T2	10^{-5}	T4.0 (16 obj.)	0.0
T2	3×10^{-6}	T4.0 (16 obj.)	0.0
T2	10^{-6}	T3.6 (16 obj.)	0.3
T2	3×10^{-7}	T1.2 (16 obj.)	2.3
L8	10^{-5}	L4.8 (16 obj.)	4.6
L8	3×10^{-6}	T1.1 (16 obj.)	4.0
L8	10^{-6}	T3.0 (14 obj.)	1.4
L8	3×10^{-7}	T0.8 (15 obj.)	2.0
L0	10^{-5}	M8.2 (16 obj.)	0.8
L0	3×10^{-6}	M8.2 (16 obj.)	0.8
L0	10^{-6}	M8.3 (16 obj.)	0.8
L0	3×10^{-7}	L1.8 (15 obj.)	3.5
M2	10^{-5}	M8.0 (16 obj.)	0.0
M2	3×10^{-6}	M8.0 (16 obj.)	0.0
M2	10^{-6}	M8.0 (16 obj.)	0.0
M2	3×10^{-7}	L0.4 (14 obj.)	3.0

Table 3.26: Same of Table 3.19 but for the z-H-mode case.

on the Spectral Type. These results have to be compared with the ones reported in Table 3.19 for the z-J-mode case. In general we can see that in this second case the standard deviations are smaller than in the previous one confirming that the z-H-mode is more effective in determining the objects spectral classification.

Effects of the gravity

To test further the capability of our procedure to distinguish different objects, we performed different simulations using as an input synthetic spectra of one object with $T_{eff} = 800°K$ and $\log(g) = 4.0$ and of another one with the same temperature and $\log(g) = 5.5$. All the simulations were performed for five different objects at a separation from the central star of 0.5 arcsec and a contrast of 3×10^{-6}. Furthermore, we performed simulations both for the z-J-mode and the z-H-mode.
For the simulations with the z-J-mode all the objects with $\log(g) = 4.0$ were recognized as T8 Spectral Type (with values of the cross-correlation coefficients around 0.75) while the objects with $\log(g) = 5.5$ were recognized as T7 (4) and T8 (1). In this second case the values of the cross-correlation coefficients are of the order of 0.77.
On the other hand, for the simulations with the z-H-mode, all the objects with $\log(g) = 4.0$ were recognized as T8 Spectral Type but with higher values of the cross-correlation coefficients than in the previous case (more than 0.93) while all the objects with $\log(g) =$

	log(g) = 4.0	log(g) = 5.5
log(g) = 4.0	0.88	0.40
log(g) = 5.5	0.80	0.51

Table 3.27: Cross-correlation coefficients considering the effects of the gravity with z-J-mode.

	log(g) = 4.0	log(g) = 5.5
log(g) = 4.0	0.89	0.77
log(g) = 5.5	0.72	0.90

Table 3.28: Cross-correlation coefficients considering the effects of the gravity with z-H-mode.

5.5 were recognized as T6 spectral type (cross-correlation coefficients of the order of 0.92).
In Table 3.27 and in Table 3.28 we report the values of the mean coefficients from the cross-correlation between the output and the input spectra for the z-J-mode and for the z-H-mode respectively. From these results it is apparent that, while for the z-J-mode all the simulated objects are classified as log(g) = 4.0, in the case of the z–H-mode we are able to correctly classify the objects for what concerns the gravity effects.
In conclusion, we can say that, from our analysi,s it seems that to be able to correctly distinguish between objects with different gravity, the z-H-mode is the best solution.

3.4.4 Conclusions

From the final multi-wavelength images that are displayed in the previous pages we can say that the spectral deconvolution method allows to make imaging of extrasolar planets (both T-type and L-type) down to a luminosity contrast of $\sim 3 \times 10^{-7}$.
We can conclude that our procedure is able to find almost all the simulated objects at larger separation (0.5 and 1.0 arcsec) from the central star. It becomes less effective when we go down to a separation of 0.3 arcsec. However, we are able to find more than 90% of the simulated objects using the z-J-mode and more than the 95% of the objects with the z-H-mode.
For what concerns the spectral reproducibility, we can take the following conclusions:

- The positions on the image (if the separation from the central star is kept constant) does not seem to influence the ability of our procedure to determine the Spectral Type of the new discovered planets.
- The greater is the separation from the central star the greater is the possibility to reconstruct with precision the spectrum of the planets (considering planets with the same luminosity contrast).
- Planets with greater luminosity contrast have more easily a precise spectrum reconstruction.

- This method allows to reconstruct and to classify very well the T-type spectra while spectral reconstruction and classification seem to be less precise for earlier spectral types. However, even in these cases, the spectral classification has generally a precision of few spectral types (4 or 5 in the worst cases).
- For what concern the capability of the method to disentangle companion objects from field objects, we have showed that M2 and L0 spectral types tend to be both recognized as M8 spectral type. So, just for the L0 case, a certain degeneracy could be possible.
- The z-H-mode allows a better spectral classification respect to the z-J-mode.
- For what concerns the effects of the gravity, they are much better disentangled using the z-H-mode than the z-J-mode.

Chapter 4

EPICS

4.1 Introduction to EPICS

The Exoplanet Imaging Camera and Spectrograph (EPICS - see e.g. Kasper et al. 2010) is an instrument designed for the direct imaging and characterization of extra-solar planets with the European Extremely Large Telescope (E-ELT), the 42 m ESO future instrument currently going through its phase-B study. EPICS will be optimized for observations in the visible and in the near-IR and will have photometric, spectroscopic and polarimetric capabilities.
The most important science objectives for EPICS will be:

- Detection of low mass and wide orbit planets to explore the unknown regions of the mass-orbit function.
- Characterization of exoplanets down to rocky planets by direct imaging, spectroscopy and polarimetry.
- Detection of very young planets (age $\sim 10^7$ years or less) close to the ice-line to test planet formation and evolution models and to understand the processes driving the planetary formation.

Moreover EPICS will exploit the light collecting power and the angular resolution of E-ELT that will provide diffraction limited images even at optical wavelengths with angular resolution down to 5 mas. In this way, it will have a large impact on a large number of astrophysical fields from the solar system and disks to stellar astronomy.
In order to deliver these science goals, EPICS should fulfill the following main requirements:

- The luminosity contrast of the instrument has to better than 10^{-8} at 30 mas and than 10^{-9} beyond 100 mas.
- It has to be able to perform spectroscopic and polarimetric imaging, as well as medium resolution spectroscopy for the spectral characterization of exoplanet chemistry

- The spectral range will be from optical to near-IR wavelengths (0.6 - 1.65 μm).

To achieve these objectives a superb correction of the dynamic and quasi-static wavefront aberration introduced by the atmosphere and by the telescope is required. In order to correct for dynamic aberrations and to suppress the atmospheric turbulence residual halo to about 10^{-5} at small angular separations and to better than 10^{-6} close to the AO correction radius, EPICS implements a SCAO wavefront sensor (WFS) driving the E-ELT M4 through its telescope control software (TCS) followed by an XAO system using a roof-Pyramid WFS. Non-common path optical aberrations will be calibrated by focal plane wavefront sensing techniques and off-loaded to the XAO system. The diffraction pattern will be suppressed by apodizers and coronagraphs. As a result EPICS will achieve a high quasistatic PSF contrast of better than 10^{-6}.
These results will be further improved through data analysis techniques such as spectral deconvolution for the NIR IFS and differential polarimetry with the optical polarimeter EPOL. These techniques will provide the required luminosity contrast of the order of 10^{-8} at 30 mas and better than 10^{-9} at larger angular separation. This last step of PSF residuals calibration will be made possible through an optimization of the instrument optics for maximum efficiency of the speckle calibration techniques:

- A small and well-known speckle chromaticity is provide by minimizing amplitude aberrations introduced by the Fresnel propagation of optical errors
- A small instrumental polarization is provided by avoiding large angle reflections and a careful choice of coatings

Figure 4.1 shows the general EPICS opto-mechanical design. The NIR arm hosts an apodizer and zoom optics to provide an f/140 focus on the input of the IFS. The whole optical train up to the IFS input focus consists of optical components that are located in or close to the pupil plane to avoid mixing of phase into amplitude errors. Following this philosophy, diffraction suppression is achieved by amplitude apodization only. This solution is preferred over a coronagraph which would require a mask or some sort of re-imaging optics near the image plane. In order to attenuate the stellar light and to reduce problems with ghosting, stray light or detector saturation, a mask will be placed in the entrance image plane of the IFS.
Entering the optical arm, the light hits either a fully reflecting mirror for use with the IFS, or another gray beamsplitter that reflects 15% of the light towards the XAO WFS and transmits the rest to the differential optical polarimeter EPOL. The EPOL measurement concept is intrinsically achromatic, so an apodized Lyot coronagraph efficiently suppresses diffraction. The EPICS optical design minimizes the number of reflective optics at large inclination angles introducing instrumental polarization and foresees calibration devices for those that cannot be avoided such as the telescopes M4 and M5 mirrors.
The two science module that will be part of EPICS are:

- IFS, that is the subject of this Chapter and it will be treated diffusely in the next Sections
- EPOL that is the visible light (0.6 - 0.9 μm) coronagraphic imaging polarimeter. Much of the EPOL design derives from the SPHERE/ZIMPOL. EPOL provides

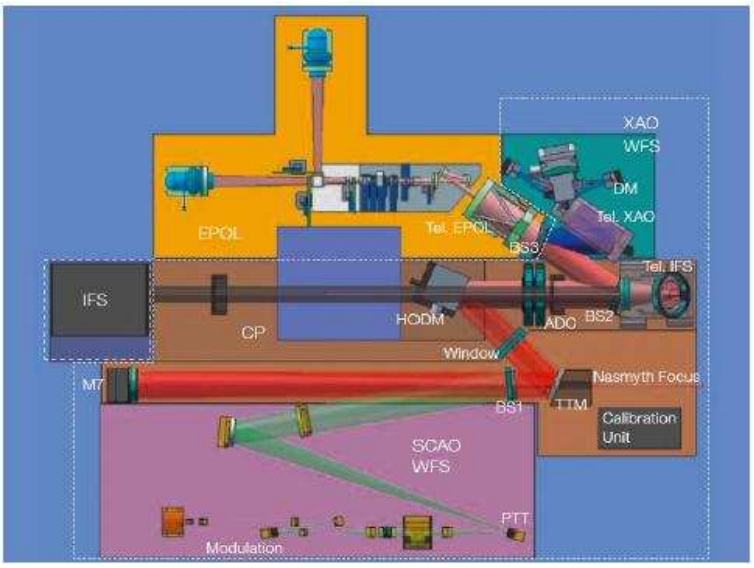

Figure 4.1: Top view of the EPICS opto-mechanical design.

a FOV of 2×2 arcsec sampled by 1.5 mas spaxels at the diffraction limit and various astronomical filters.

4.2 Apodized mask experiment

4.2.1 Principles

We consider the possibility of the apodization of the pupil mask of the EPICS IFS instrument (that is, the transmission profile of the mask is a smoothed one and no more a square function as in the case of a traditional pupil mask - see Figure 4.2) with the aim to reduce the chromaticity of the coherent cross-talk.

We, as a first step, have to choose the better profile for the apodized mask. To this aim we prepared an IDL programme that, given the fundamental characteristics of the BIGRE microlens array and other characteristics of the optical system, calculates the coherent cross talk (CCT), the incoherent cross talk (ICT) and the efficiency of the system for a certain number of wavelengths (in our calculations we performed it for 16 wavelengths). The input parameter for the BIGRE are:

- The pitch of the microlens array (200 μm)
- The mask obscuration for every microlens (0.95)
- The k factor (5.40)
- The pixel size of the detector (9 μm)

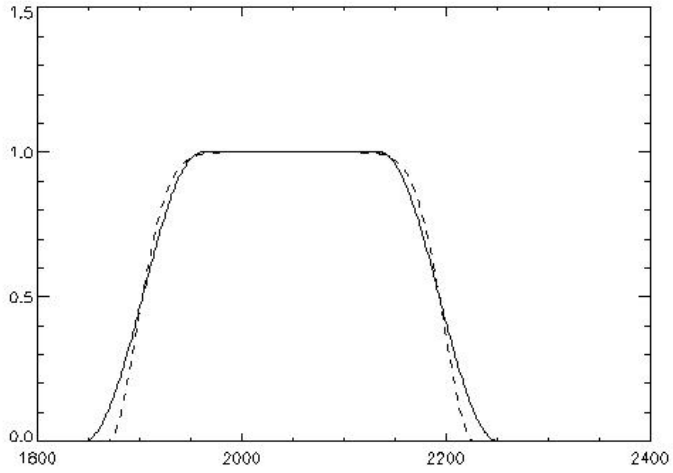

Figure 4.2: Transmission profiles for a Hanning apodizer with S=0.4 (solid line) and for a Gaussian apodizer with S=0.2 (dashed line). The same value of D=10.7 mm has been adopted in both cases. The horizontal scale is in pixel.

- The magnification of the IFS (2)
- The initial and the final wavelength at which the laboratory experiment has been performed (0.55 and 0.8 μm).

We consider three different apodization functions. In each case the degree of apodization can be changed modifing one parameter in the program. The apodization functions are:

- Hanning apodization
- Edge cosine apodization
- Gaussian apodization

The two main parameters used to define the characteristics of the apodized mask are:

- The diameter D of the mask, that is the diameter where transmission is 50% of maximum.
- The slope S of the transition part of the mask

From the results obtained running the above mentioned program we conclude that the Gaussian apodization gives clearly the better results regarding both the Coherent and Incoherent Cross Talk. In particular we can see that the Cross Talk is more or less one order of magnitude better than with the Hanning apodization while the Edge Cosine

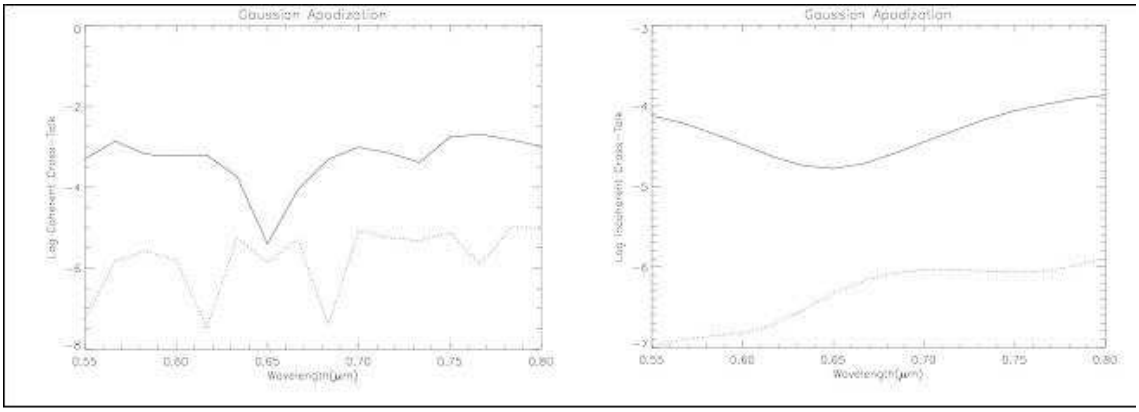

Figure 4.3: Coherent (left panel) and incoherent (right panel) cross talk as a function of wavelength. Solid line represents results without apodization; dotted line are results adopting a Gaussian apodization.

apodization gives even worse results. On the contrary the efficiency of the system using a Gaussian apodization seems to be slightly worse than the other two cases but however giving a good performance ranging from 80% for shorter wavelengths to 70% for the longer ones. Figure 4.3and Figure 4.4 displays the cross-talk and the efficiency, respectively, that we obtained for the gaussian apodization function. As a final result, we selected an apodized mask characterized by the values $D = 10.7 \pm 0.3$ mm and $S = 0.20 \pm 0.05$.

4.2.2 Goals of the laboratory experiment

The goals of the laboratory tests were:

- To verify that apodizers suitable to be located on the intermediate pupil of the IFS for EPICS can be constructed within specifications.
- To verify that the use of the apodizers reduces cross-talks as expected from models.
- To verify that transmission of apodizers agrees with model expectations.

In this Section I describe the main results of this optical experiment. They are:

1. The transmission obtained using the mask and the apodizer agrees well with the expectations.
2. Most of the light lost actually falls far from the center of the spots.
3. The cross-talk level that can be obtained with BIGRE IFS is very low, and fully compatible with its use for high contrast imagers, even when a compact configuration is adopted.

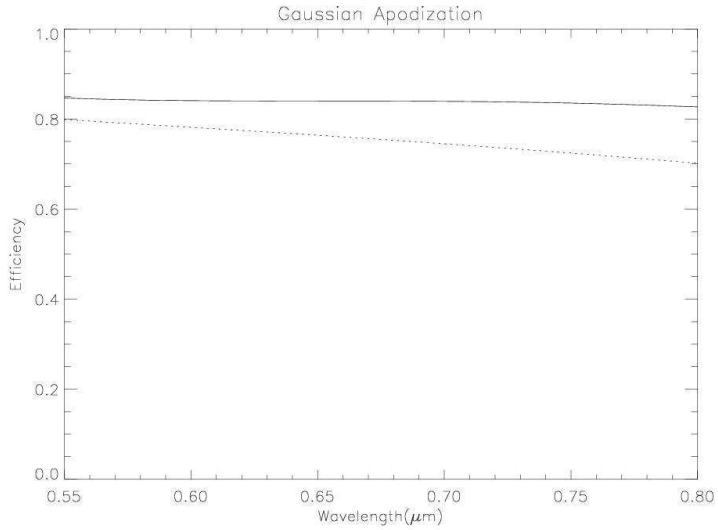

Figure 4.4: Transmission as a function of wavelength of the pupil mask. Solid line is without apodization, dotted line is with a Gaussian apodization.

4. Faint structures due to ghosts compromize the gain obtainable with an apodizer. Practically, results obtained with an apodizer or a simple mask are very similar.

4.2.3 Optical setup of the experiment

The experimental setup used to evaluate performances of the apodizer when inserted into the IFS is depicted in Figure 4.5. At the scope to save time, it has been used, with little modifications, the experiment yet mounted to prototype the IFS of SPHERE. It is composed by three different parts: the light source, the telescope simulator and the IFS simulator. The light source (LS) is a He-Ne laser (λ=633 nm). A variable neutral filter (VF - not showed in the Figure) attenuates the light source. After this element, there is a 100 mm focal length, 25.4 mm diameter lens used to focus the light onto a 25 μm pinhole (PH).

The telescope simulator is composed by a collimator lens (L1 in Figure 4.5) which is a 12.7 mm diameter, 38.1 mm focal length lens. At a distance equal to its focal length there is an iris diaphragm (D) simulating the telescope pupil. The diameter of its central hole is 1 mm. We have then a second lens (L2) which focalizes the light beam on the microlens array (BIGRE, MA - the array we used has been fabricated by AMUS, see Figure 4.6) entrance. L2 has a diameter of 50.8 mm and a focal length of 750 mm and it is located at a distance equal to its focal length from the diaphragm. In Table 4.1 one can find the basic characteristics of the BIGRE array and the tolerances on the parameters.

The IFS simulator starts just with the MA, behind which there is a folding mirror

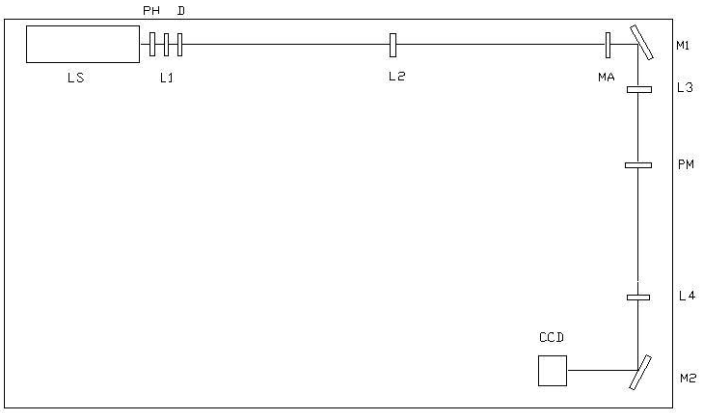

Figure 4.5: Layout for measure of the effect of the apodizer within the IFS.

Wavelength range	0.55 - 0.80 μm
Glass	SUPRASIL
Lenslet number	70×70
Pitch	$200.0 \pm 0.3 \mu m$
Curvature radius of the 1^{st} array surface	2.00 ± 0.10 mm
Curvature radius of the 2^{nd} array surface	0.367 ± 0.014 mm
Center thickness	7.53 ± 0.28 mm

Table 4.1: Main specifications of the BIGRE array.

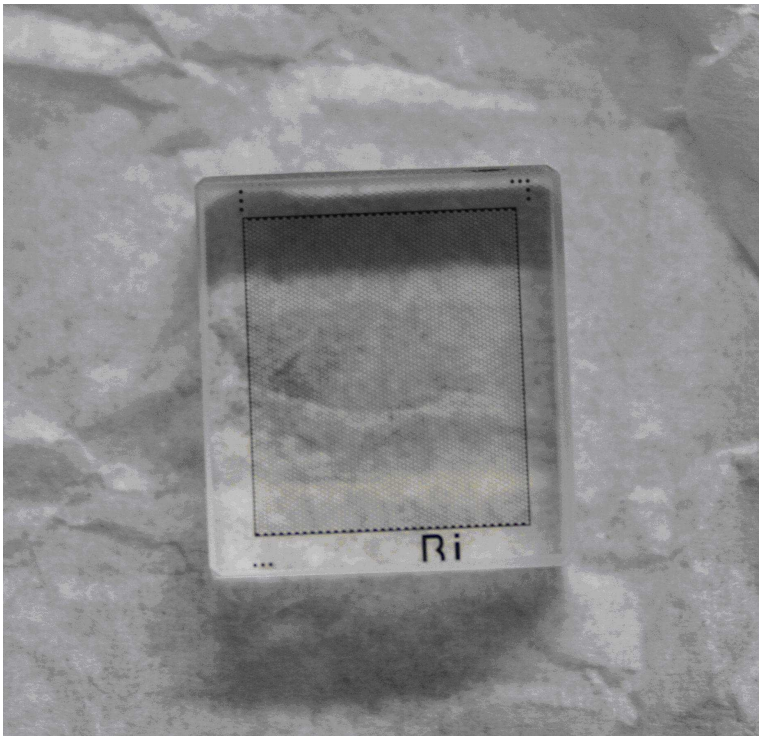

Figure 4.6: Image of the BIGRE lenslet array used in the experiment.

(M1) because the total length of the experiment is exceeding the optical table size (2.4 meters). At the distance of 250 mm from the microlens array we put a 50.8 mm diameter, 250 mm focal length lens (L3 in the Figure) that acts as a collimator. A 50.8 mm diameter, 500 mm focal length lens (L4) is at a distance of 750 mm from it. Between the lenses L3 and L4, in the pupil position (250 mm from the first lens) we put a pupil mask (PM). It can be of two different types:

- A 10.7 mm diameter non-apodized mask.
- A gaussian apodizer with a diameter of 10.7 mm (see previous Section). One can see a photo of the apodizer in Figure 4.8.

The CCD is a Finger Lake camera, with a KAF-0402ME Kodak sensor with a pixel size of 9 μm and a dimension of 768×512 pixels. The CCD is Peltier cooled, read out noise is 15 e^- RMS. Dark current is less than 10 pA/cm^2 at a temperature of 25°C. The full well capacity is 100000 e^-. With this configuration, each microlens projects onto the detector a circle aperture with a diameter of 8.1 pixels.

4.2.4 The apodizer

The apodizer was fabricated by AKTIWAVE, using the dot technique (Martinez et al. , 2010). Four apodizers have been fabricated:

- The parts have been fabricated with 10 μm pixels using Cr on BK7 substrates
- The spatially resolved transmission has been measured with a 12-bit Spiricon system and a coherent collimated source around 1053 nm.
- The measured transmission was processed to remove effects of background and nonuniformity of illumination.
- Data provided by the manufacturer include:
  - spatially resolved intensity transmission
  - radial intensity transmission for 8 different angles
  - average radial field transmission compared to specifications, minimal specification and maximal specification (calculated using the parameters sent with the specifications).
  - Average radial intensity transmission compared to specifications, minimal specification and maximal specification (calculated using the parameters sent with the specifications).

As an example, we reproduce tha data sheet provided by AKTIWAVE for one of the four apodizers in Figure 4.7. A photo of one of them is given in Figure 4.8. According to these data sheets, all the four fabricated parts meet the specification.
To reach the requested level of contrast on the image obtained it is necessary to prevent diffuse light to arrive on the detector. To this aim we covered the CCD with a cardboard box with a small hole on one side. We then build a simple cardboard structure to prevent light other than the experiment beam from entering the hole. One can see this in Figure 4.9.

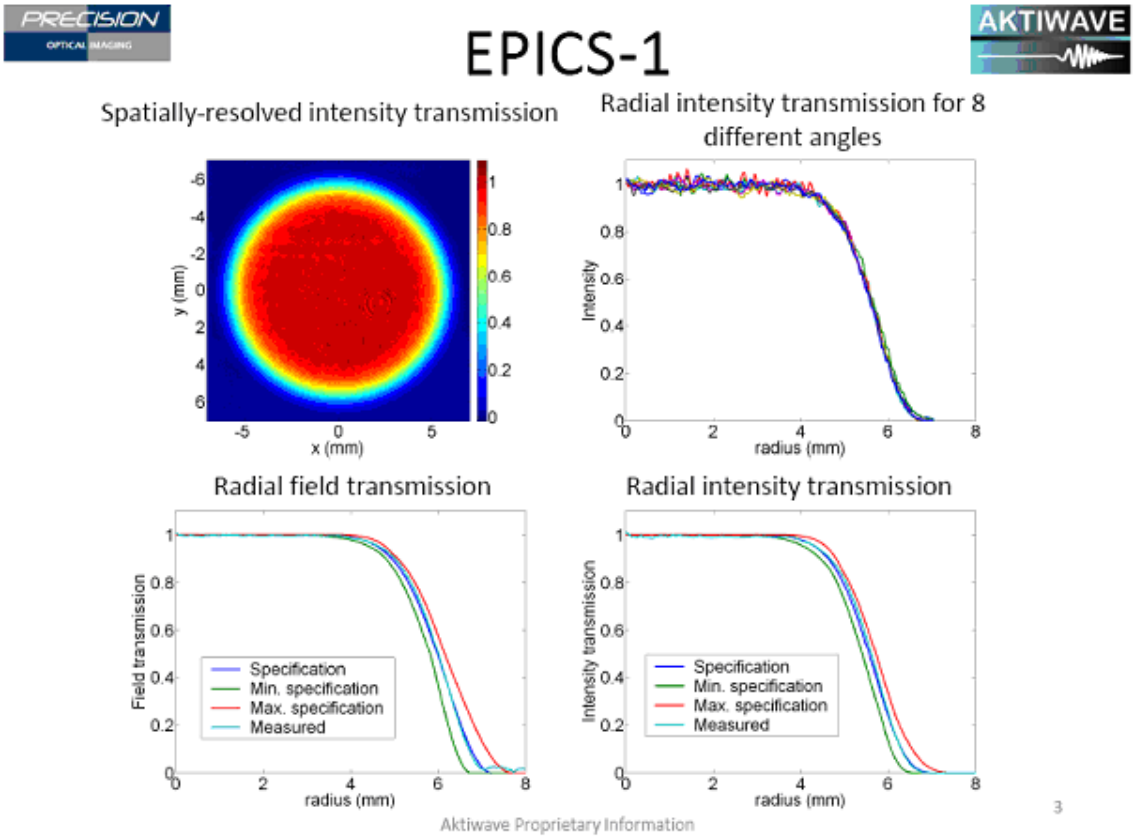

Figure 4.7: Example of a data sheet for one of the four apodizers provided by AKTIWAVE (results are very similar for all the masks).

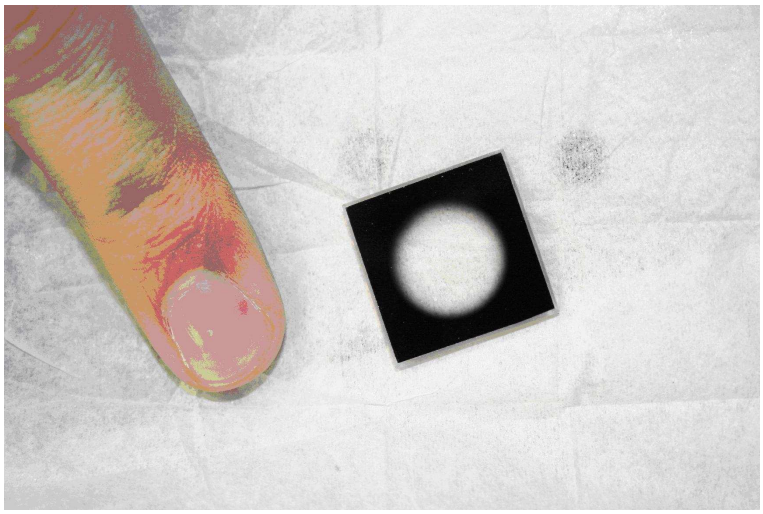

Figure 4.8: Photo of one of the apodized mask.

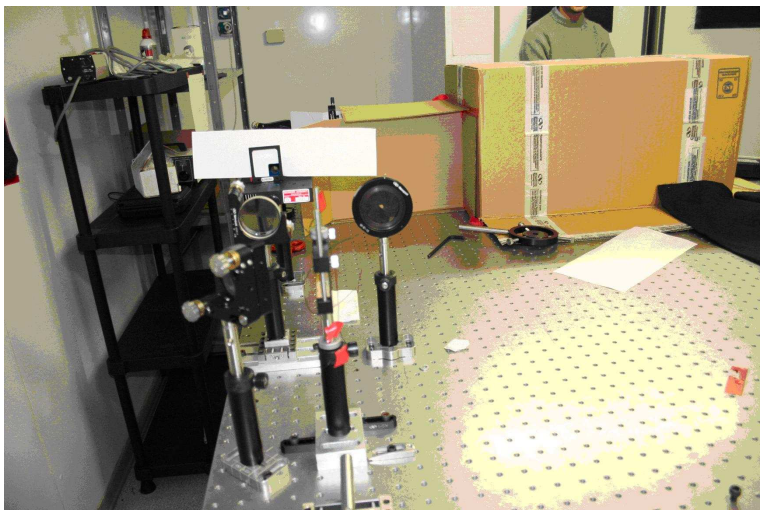

Figure 4.9: Particular of the experiment setup.

4.2.5 Data and results

Transmission

This section contains the results of the tests on the transmission of BIGRE with mask and apodizer. The tests were done using the same setup used to estimate the cross-talk. Four experiments were done, with different numbers of exposures for each run (100, 50, 50 and 50 respectively). In order to keep trace of any trend with time of the illumination by the laser or of any optical element, we alternated observation without any mask to observations done with the mask or the apodizer in each experiment. Care was devoted to reduce the concern due to the correct estimate of the background. The bias of the CCD used in this experiment (the backup one) oscillated between two values, which differed by ~200 counts (we called this difference detector offset). This detector offset was measured on all images and its effects removed. The background was estimated using the detector area farther than 20 pixels from the center of each spot. However, the background with no-mask is slightly higher (by about 2 counts/pixel/exposure) likely due to diffuse light, which is itself light passing through the intermediate pupil. We then used the background obtained with the mask also to estimate the background for the no mask case. The rest of the analysis and reduction is obvious.
We measured average counts within circular apertures of different radius (in pixels) around each spot, as well as over the total detector. These values were corrected for background and vignetting (see below). From these counts, we estimated the relative efficiency (with respect to no mask) within each circular apertures of different radius (in pixels) around each spot, as well as over the total detector. Results are shown graphically in Figure 4.10. These results indicate that mask and apodizer transmit close to expectations. Furthermore, a significant fraction of the light lost is far from center of the spots. Within the spot FWHM, transmission is about 90%, with respect to the no mask case, for both the mask and the apodizer.
In the intermediate pupil, we expect to see an Airy pattern (that is, the Fourier transform of the illumination of each single lenslet, that we assume to be uniform). The first, second and third rings of the Airy disk occurs at 1.22, 2.23 and 3.24 λ/D, etc. For our experiment these correspond to distances from the optical axis of 5.4, 9.88 and 14.33 mm respectively. The fractions of the total power contained within the first, second and third dark rings are 83.8%, 91.0% and 93.8% respectively. Since the diffraction pupil is in principle unlimited, some vignetting clearly occurs at the optical elements beyond the pupil (as well as at those before it), so that the normalization done (using the configuration without any mask on the pupil) is underestimated, resulting in efficiencies that are too large with respect to real ones for the cases where a mask is used.
Appropriate estimate of this vignetting is difficult. Vignetting occurred mainly at the 45° flat mirror after the intermediate pupil. The mirror is circular, with a diameter of 50 mm. The footprint is then an ellipse with semiaxes of 25 mm and 17.68 mm, corresponding to 4.7 and 3.3 λ/D respectively. If the beam were properly centered, the overall vignetting should be of about 5%. However, the beam was about 15 mm above the centre of the mirror in the first two experiments, resulting in further vignetting of some 3.5%. Some further vignetting occurs at the detector itself. The run of energy out of diameter shows that the detector should contribute $\sim 2-3\%$ to vignetting. We may

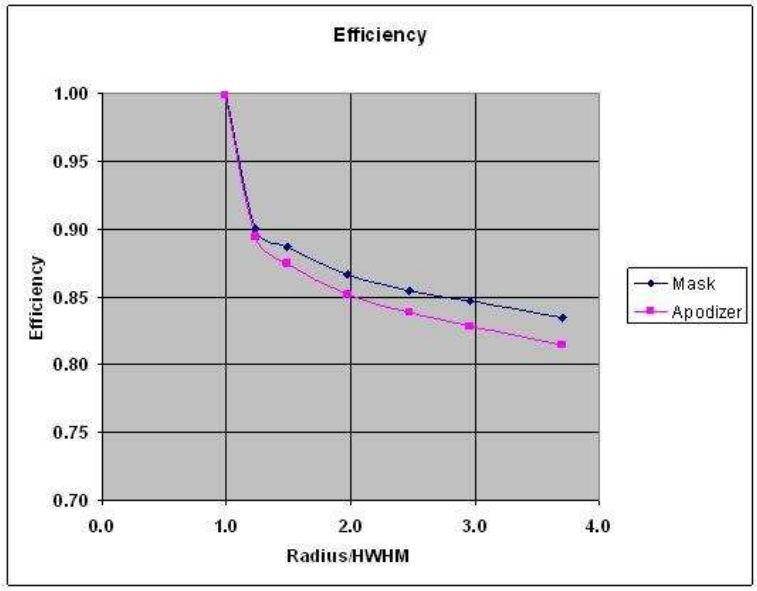

Figure 4.10: Relative efficiency for the cases Mask/No Mask and Apodizer/No Mask, within different circular apertures on the detector; the diameters of the aperture are given in units of half of the projected slit width (=HWHM). Save for very small apertures the mask is more efficient than the apodizer by about 2.5%.

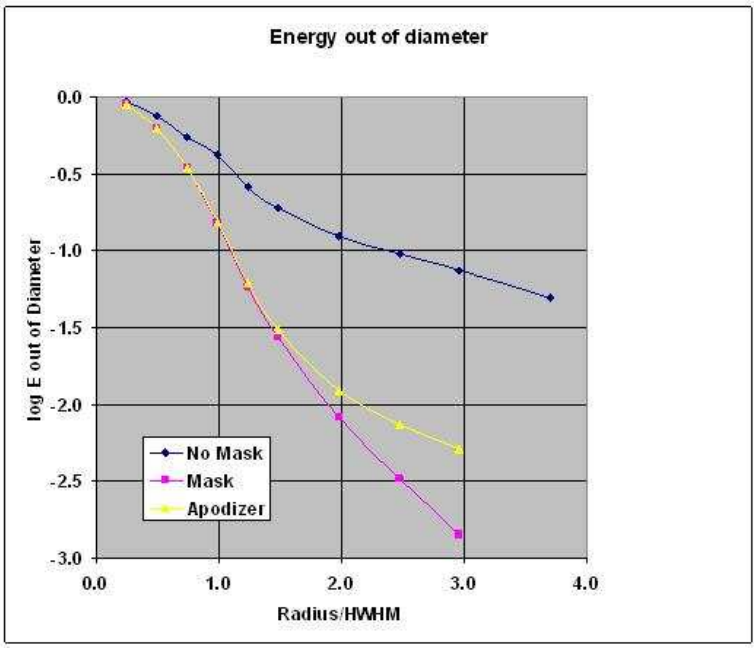

Figure 4.11: Energy out of diameter gives the energy which is out of the circles with a given diameter around each spot.

then estimate total vignetting at $\sim 7\%$. We adopted this value.
Figure 4.11 gives the energy out of the circular apertures of different radius (in pixels) around each spot, as well as over the total detector. These values are corrected for vignetting. The smaller this value, the more energy is concentrated within the spots. This would imply lower background and cross-talk levels. While the mask on the intermediate pupil already does a good job in reducing background and cross-talk, the apodizer is still more efficient on this respect.
In conclusion, this experiment shows that:

1. the transmission obtained using the mask and the apodizer agrees well with the expectations as showed in Table 4.2.

2. Most of the light lost actually falls far from the centre of the spots (see Figure 4.11). The measured efficiency within the FWHM of the spots (with respect to the No Mask case over the same area) is given in Table 4.3.

Cross-talk

This Section contains the results of the test on the cross-talk of the BIGRE with mask and apodizer. We illuminated the lenslet array with the He-Ne laser input beam. Since

	Measured	Expected
Mask	0.828 ± 0.017	0.840
Apodizer	0.786 ± 0.009	0.769

Table 4.2: Measured and expected values for the transmission with the mask and the apodizer.

Mask	0.919
Apodizer	0.962

Table 4.3: Measured efficiency within the FWHM of the sposts using the mask and the apodizer.

the IFS magnification is 2, the pitch projected on the detector is 400 μm, that is 44.4 pixels. Either a circular mask (diameter=10.7 mm, that is $2.5\lambda/D$) or a Gaussian apodizer were put on the IFS intermediate pupil. After several trials, best results were obtained considering 46 spots (=lenslet images) near the centre of the field. For these spots we measured encircled energy in a number of circular apertures. These were used to derive the Point Spread Function (PSF). Figure 4.12 gives the average PSF, as a function of distance from the spot centres. Care was devoted in data reduction to properly eliminate straylight. The steeper the PSF, the more energy is concentrated within the spots and the lower is the cross-talk. Briefly:

- The incoherent cross-talk (ICT) is the PSF measured at the location of the closest spot, that is at twice the Projected Slit Width (that is about 150 μm) in a compact design. In our design, this is 0.327 times the pitch for an hexagonal-C configuration, that is 14.5 pixels.
- The incoherent cross-talk measured by this experiment for this array is $\log ICT \ll -3$ if a mask or an apodizer are used. This shows that such a compact design is compatible with specifications of the BIGRE IFS for SPHERE and EPICS.
- The apodizer provides an ICT value very similar to that of a simple mask.
- The coherent cross-talk (CCT) is the $\sqrt{PSF}$ measured at one pitch, that is about 400 μm in our experiment. The CCT cannot however be directly measured and can only be deduced from comparisons with appropriate models. Such a comparison is made in Figure 4.13 which shows that at large distances from centre the PSF is much brighter than expected. The reason for this can be understood from inspection of Figure 4.14, which shows portions of average of 1000 images obtained with the mask or the apodizer, with a grey scale which put in evidence structures at very low levels of illumination (typically $< 10^{-4}$ of spot centres). At these very low levels, there are different kind of structures:
  - Charge transfer problems, due to the CCD. This causes the vertical elongation of the spots.

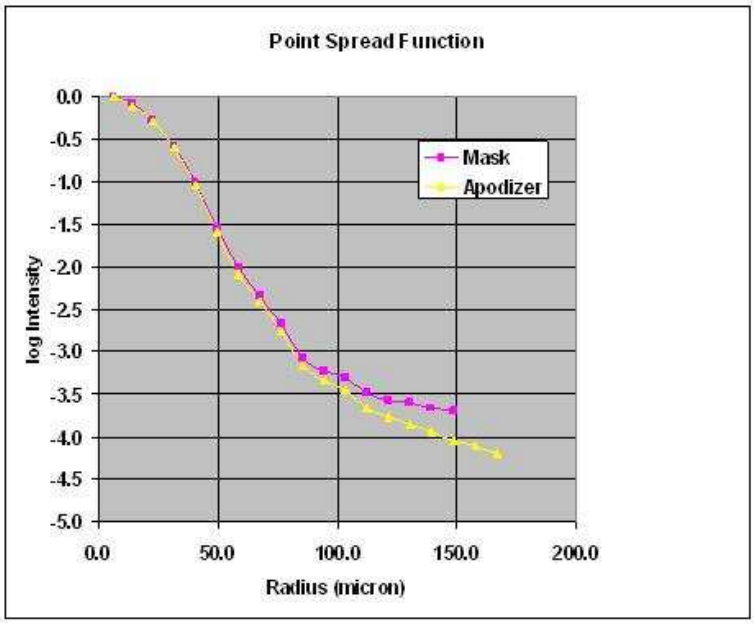

Figure 4.12: Log of the point spread function as a function of the distance from the spot centers.

- Airy rings, expected because of the finite size of the pupil stop. These are slightly more obvious in the case of the mask, but are present also for an apodized pupil.
- Spots that can be attributed to various ghosts, that are due to reflections between various surfaces that are close to the focal plane or to the pupil. These ghosts are actually very faint ($< 10^{-4}$), due to the use of efficient AR coatings, but yet visible on these images.

All these problems appear at a very low level, small enough that they are not likely to cause serious concern in the actual use of the IFS even for high contrast imaging. However, they are strong enough to almost cancel any difference between images obtained with mask and apodizer. We can then conclude that:

1. The cross-talk level that can be obtained with BIGRE IFS is very low and fully compatible with its use for high contrast imagers, even when a compact configuration is adopted.

2. Faint structures due to ghosts compromise the gain obtainable with an apodizer. Practically, results obtained with an apodizer or a simple mask are very similar.

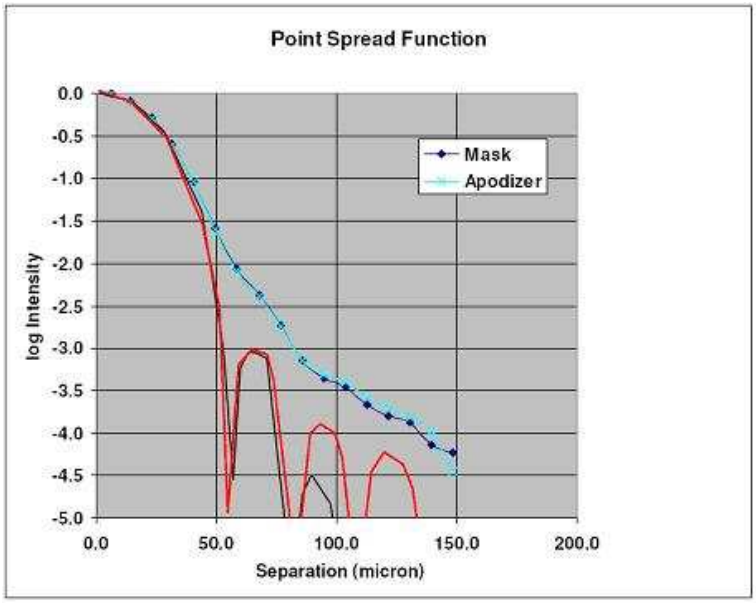

Figure 4.13: Comparison between the observed PSF, and theoretical expectations (red line: mask; black line: apodizer.

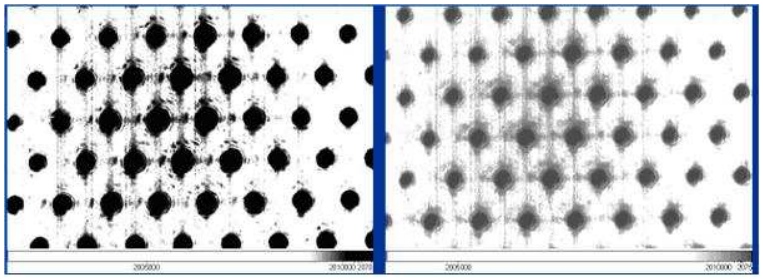

Figure 4.14: Portions of the mean of 1000 images obtained with mask (left) and with apodizer (right). A log intensity scale with cuts suitable to put in evidence very low illumination levels (typically below 10^{-4} of maximum illumination).

4.3 Optical design of EPICS IFS

4.3.1 Introduction to EPICS IFS optical design

The EPICS IFS optical design has been prepared taking account of the following parameters:

- Square FOV: 0.80 arcsec side (1.13 arcsec diagonal)
- Minimum wavelength: 0.95 μm
- Maximum wavelength: 1.65 μm
- 2 pixel spectral resolution: 130.5
- Detector pixel dimension: 15 μm
- Magnification of the IFS: 5.98
- Detector number of pixel: 8192×8192

One of the important choices that we made in the design was to minimize the number of components at cryogenic temperature. This greatly simplify opto-mechanics of our system. While this is made possible by the short maximum wavelength, it still requires care in the opto-mechanical design to avoid too large thermal background as seen by the detector, which we assumed to be sensitive up to 2.7 μm, as typical for Hawaii II detector.
The basic parameters of a BIGRE IFS are completely constrained if the following conditions are set:

- Nyquist sampling of the diffraction peak (at the shortest wavelength)
- Fresnel propagation inside the BIGRE optics
- Spherical aberration of BIGRE smaller than 1 pixel on the detector
- Super sampling (2 pixel sampling of projected entrance slit width on the detector)
- Hyper sampling (2 pixel sampling of a chromatic speckle at the edge of the field of view)
- Cross-talk condition (at least 1 pixel free between adjacent spectra, this translates into at least 4 pixels between the centre of adjacent spectra according to the BIGRE LSF profile)
- Minimal IFS input focal ratio (to minimize Fresnel propagation effects in the Common Path)
- Detector and pixel size (8192×8192 and 15 μm respectively)

The EPICS IFS is made of different basic element:

- The lenslet integral field unit (IFU)

- The collimator, accepting the diffractive beam exiting from the IFU over the whole field of view (FOV)
- A mask located in the intermediate pupil, which allows to reduce cross-talk and straylight (see previous Section).
- The disperser, actually a set of Amici prisms, grisms or Volume Phase Holographic gratings (VPH) depending on the requested resolution.
- The camera, focusing light on the detector
- The detector, a 8k×8k IR detector based on Hg-Cd-Te technique like for the Hawaii detectors. These detectors are assumed to be standards for the E-ELT.
- A calibration arm, providing suitable calibration images.
- A set of neutral density filters

The optical design of the EPICS IFS was prepared using our code for first order parameters determination, and ZEMAX ray-tracing for further optimization and analysis.

4.3.2 Integral Field Unit (IFU)

The lenslet based integral field unit that has been designed for the EPICS IFS is a BIGRE type. This IFU concept is described in Antichi et al. (2009), while its optical implementation can be found in the FDR documentation of the IFS of SPHERE.
The lenslet array configuration will be an Hexagonal F one. See Appendix B for a definition of the different configurations for an IFS based on an hexagonal lenslet array. It will be made of INFRASIL. The main characteristcs of this optical element are listed in Table 4.4. There will be actually two identical IFUs:

- The Full Field IFU
- The Long Slit IFU, where all lenslets but a strip of 6 (passing through the centre) are masked.

Lenslets in the central area of each IFUs will be masked by depositing a coating with high optical density, in order to avoid saturation of the detector by the bright diffraction core of the star (not attenuated by the coronagraph), while still allowing to determine the centre of the stellar image. The size of this partially masked area is 28×28 mas (12×12 lenslets). The logarithmic attenuation will be of the order of 3.5-4 for the full field mode, and of the order of 2 for the long slit mode. This will ensure $\sim 5\times10^4$ photons/DIT/detector pixel for a J=0 magnitude star. Observations of brighter objects require use of neutral density filters.
Each lenslet will be masked to a circular aperture by depositing an optically thick layer on it. This technique has been already used with success for the SPHERE BIGRE.

4.3.3 IFS optical recipe

Table 4.5 lists the most important characteristics of all the EPICS IFS optical surfaces.

IFU pitch (P)	**64.30** μm
IFU mask factor (mask)	**0.98**
Refraction index of the IFU	**1.447 (at 1.325** μm**)**
IFU de-magnification factor (K)	**7.03**
IFU first lens focal ratio (FR1)	**19.68**
IFU second lens focal ratio (FR2)	**2.80**
Number of lenses	**343×343**
Area of a single lens	**3580** μm^2
Diagonal length of the IFU	**28.98 mm**
IFU first lens focal length in the air	**1.240 mm**
IFU second lens focal length in the air	**0.176 mm**
IFU first lens focal length in the medium	**1.795 mm**
IFU second lens focal length in the medium	**0.255 mm**
IFU first lens curvature radius	**554** μm
IFU second lens curvature radius	**79** μm
IFU back focal distance	**0.202 mm**
IFU thickness	**2.050 mm**
IFS entrance slit size	**5.02** μm
IFU diffractive micropupil	**66.43** μm
IFU geometric micropupil	**9.85** μm

Table 4.4: EPICS IFU main characteristics.

Surface	Curv. (mm)	Dist. (mm)	Material	D (mm)	Rot. (deg)
BIGRE CIRC. MASK	**Plane**	**0.000**	**Air**	**0.064**	
BIGRE S1	**0.554**	**2.050**	**INFRASIL**	**0.064**	
BIGRE S2	**-0.079**	**10.202**	**Air**	**0.064**	
COLL. LENS 1 S1	**Plane**	**25.735**	**BAF2**	**32.373**	
COLL. LENS 1 S2	**69.927**	**29.787**	**Air**	**39.641**	
COLL. LENS 2 S1	**Plane**	**30.424**	**BAF2**	**58.905**	
COLL. LENS2 S2	**-41.602**	**35.900**	**S-NPH2**	**65.678**	
COLL. LENS 2 S3	**-69.395**	**72.660**	**Air**	**93.954**	
COLL. LENS 3 S1	**279.278**	**39.156**	**BAF2**	**103.968**	
COLL. LENS 3 S2	**-117.632**	**57.192**	**S-NPH2**	**102.842**	
COLL. LENS 3 S3	**-195.831**	**57.192**	**Air**	**109.462**	
COLL. LENS 4 S1	**72.751**	**15.596**	**S-BSM16**	**93.728**	
COLL. LENS 4 S2	**64.568**	**80.536**	**Air**	**83.875**	
MIRROR	**Plane**	**75.000**	**Air**	**112.157**	**45.000 (X)**
PUPIL STOP	**Plane**	**20.000**	**Air**	**60.152**	
DISPERSER S1	**Plane**	**11.000**	**BAF2**	**35.000**	**3.787 (Y)**
DISPERSER S2	**Plane**	**14.000**	**S-TIH6**	**35.000**	**-5.857 (Y)**
DISPERSER S3	**Plane**	**11.000**	**BAF2**	**35.000**	**5.857 (Y)**
DISPERSER S4	**Plane**	**19.000**	**Air**	**35.000**	**-3.787 (Y)**
CAM. LENS 1 S1	**136.635**	**9.689**	**S-NPH2**	**71.505**	
CAM. LENS 1 S2	**131.507**	**57.958**	**Air**	**70.002**	
CAM. LENS 2 S1	**-134.892**	**19.037**	**BAF2**	**79.028**	
CAM. LENS 2 S2	**-146.575**	**14.104**	**S-NPH2**	**85.047**	
CAM. LENS 2 S3	**-155.564**	**67.846**	**Air**	**90.281**	
CAM. LENS 3 S1	**1113.885**	**40.358**	**S-NPH2**	**104.985**	
CAM. LENS 3 S2	**614.295**	**9.271**	**BAF2**	**107.480**	
CAM. LENS 3 S3	**-405.792**	**17.607**	**Air**	**107.891**	
DEW. WIND. S1	**Plane**	**10.000**	**INFRASIL**	**108.528**	
DEW. WIND. S2	**Plane**	**813.010**	**Air**	**108.921**	
FILTER S1	**Plane**	**10.000**	**RG850**	**155.698**	
FILTER S2	**808.378**	**110.144**	**Air**	**156.202**	
IMAGE PLANE	**Plane**		**IMAGE**	**173.798**	

Table 4.5: EPICS IFS data.

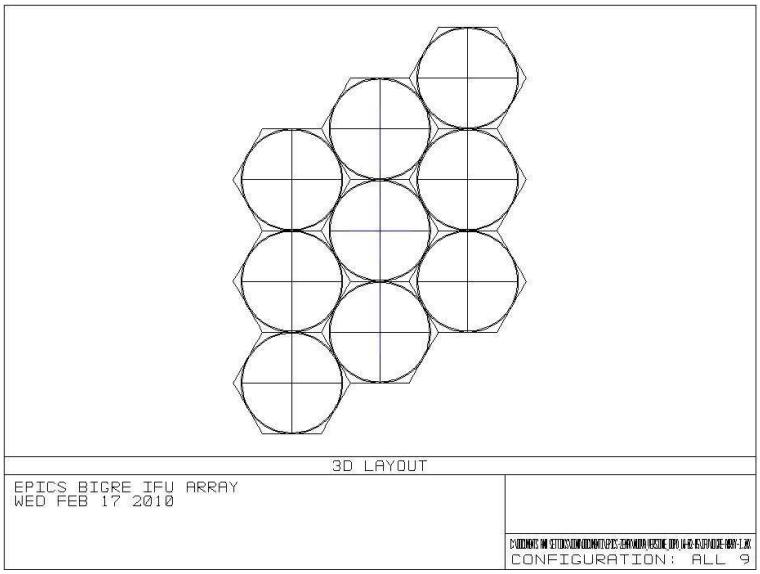

Figure 4.15: Front view of a portion of the EPICS BIGRE IFU. The mask deposited on the first surface makes every lens circular. In this way the diffractive propagation inside the IFS is axial symmetric.

4.3.4 BIGRE lenslet optimization

The BIGRE Optical System has been optimized considering that it should lie on a FR=126 focal plane at 5182 mm from the input pupil (see above in this Section). The first BIGRE surface should have an input focal ratio of FR_{IN}=126, a geometrical output focal ratio of FR_{IN}/K=17.92 where K is the de-magnification power of the BIGRE lenslets (given by the ratio between the focal lengths of the first and the second surface of the array) and generate a diffractive beam with a focal ratio equal to FR_{OUT}=2.66, according to the BIGRE theory. In Figure 4.15 a front view of 9 adjacent lenslets is shown while in Figure 4.16 a lateral view of a BIGRE single lenslet is shown.

4.3.5 Reversed collimator optimization

The IFS is a finite conjugate system with a magnification factor of m=5.98 composed of a collimator and a camera. The collimator creates an intermediate pupil image. We choose a collimator design with an effective focal length (EFFL)=160 mm providing a diffractive pupil with a diameter of 60.152 mm, which is roughly the double of the diagonal of the IFU (29.98 mm). With this choice, the collimator corrected FOV is 10.27 degrees. Given this great angle the collimator design is quite complex and we have to use a rather large number of lenses to reach a good enough optical quality (see Figure 4.17). The collimator we designed includes 6 lenses distributed over 4 groups:

Figure 4.16: Lateral view of a single EPICS BIGRE lenslet: the system re-images the E-ELT focal plane, where the lenslet first surface lies (left) onto the entrance slits plane outside the lenslet itself (right).

- a singlet made by S-BSM16 glass
- a doublet made by S-NPH2 and BAF2 glass
- a doublet made by S-NPH2 and BAF2 glass
- a singlet made by BAF2 glass

We have let room enough before the first lens because we have to insert a fold mirror at 45° inclination to change the direction of the optical axis downward. The diameter of the beam at this point of the optical design is less than 85 mm while the distance between the first lens and the last surface is ~155 mm, so that the design is adequate to this aim. In the Figure 4.18 and in the Figure 4.19 we plot spot diagrams for different fields of the optical design and the wavefront error vs. the wavelength at different fields of view.
The worst spot has an r.m.s. radius of 2.19 μm.
Note that given the large magnification of the IFS, the constraints on the optical quality of the collimator are severe.

4.3.6 Camera optimization

The IFS magnification should be m_{IFS} =5.98 so the camera focal length has to be 956.8 mm. Furthermore, the camera should be physically long in order to reduce the solid angle of the dewar window as seen by the detector. Coupled with low pass band cold filter, this allows reducing consistently the thermal background (see Section 4.7) even

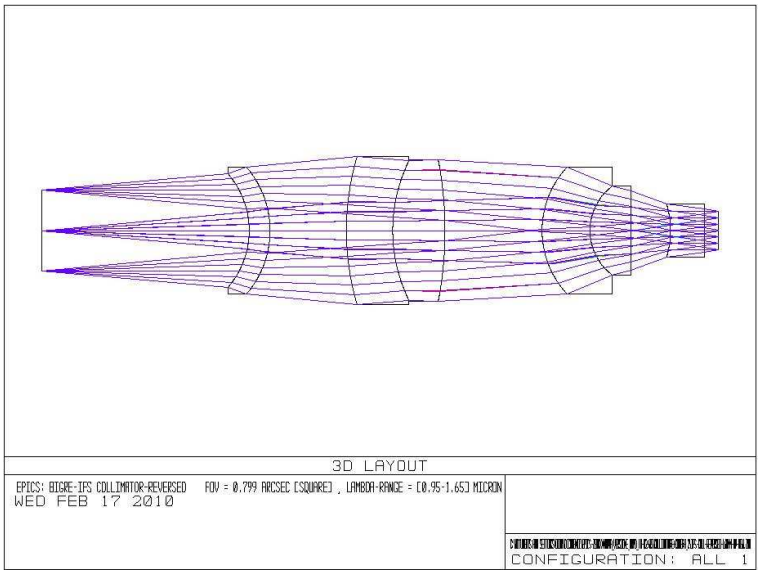

Figure 4.17: EPICS IFS Reversed collimator optical design. In this Figure the IFU is on right side while the IFS intermediate pupil is on the left.

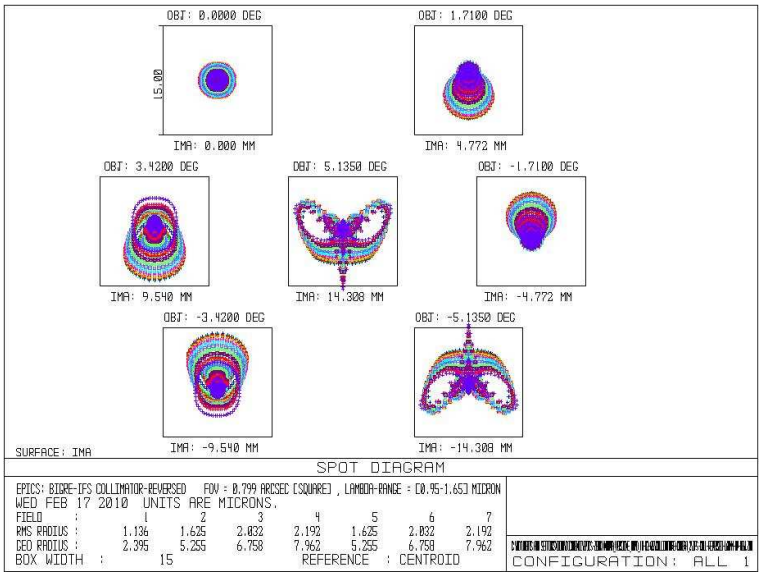

Figure 4.18: EPICS IFS reversed collimator spot radii for different fields.

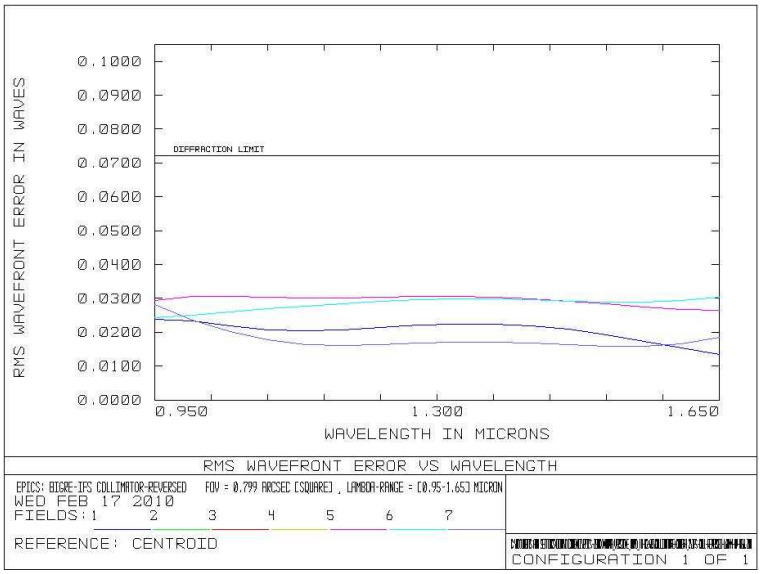

Figure 4.19: EPICS IFS reversed collimator wavefront error vs wavelength.

within a design which has no cold pupil. We have, however, to let room enough to insert the disperser prism between the pupil and the first camera lens. At this scope, we need at least a separation of 75 mm between the pupil and the first camera element.
In this case we can consider:

- a singlet made by S-NPH2 glass
- a first doublet made by BAF2 glass and S-NPH2 glass
- a second doublet made by S-NPH2 glass and BAF2 glass
- a flat dewar window made by INFRASIL
- a field lens (that should also acts as a low pass band filter cutting the thermal radiation) in front of the detector made by RG850. The first optical surface is flat, making easier its use as a cold filter.

Figure 4.20 shows the camera design. From this design we obtain a worst spot radius of 2.78 μm as it is showed in Figure 4.21.
Figure 4.22 shows the plot of the wavefront error versus the wavelength at different fields of view.

4.3.7 Collimator optics and Camera optics assembling

To join the design of the collimator optics (opportunely reversed) to the camera optics and to make a new quick focus is the way we adopted to obtain a diffraction limited

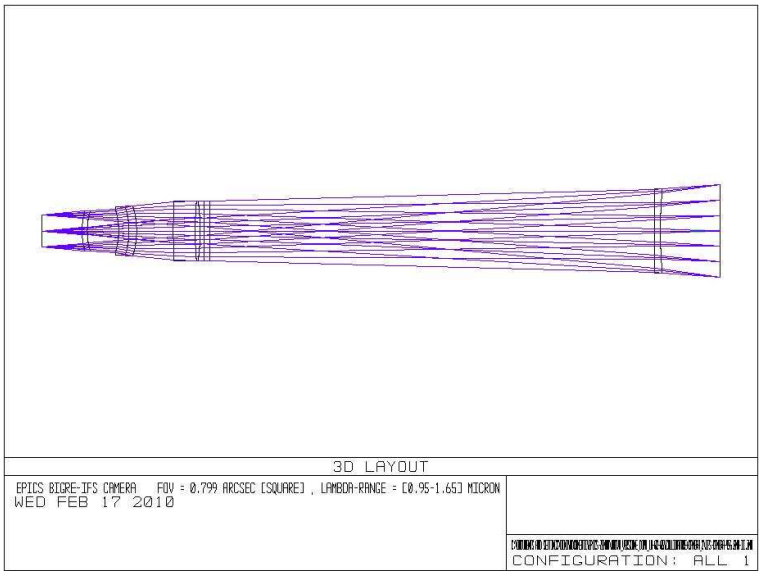

Figure 4.20: EPICS IFS Camera Optical design. In this Figure the IFS intermediate pupil is on the left while the detector is the last surface on the right.

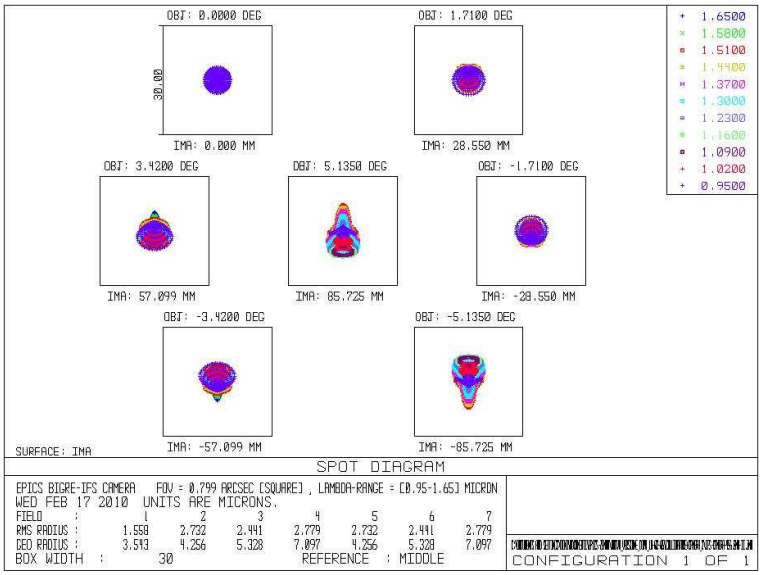

Figure 4.21: EPICS IFS Camera spot radii for different fields.

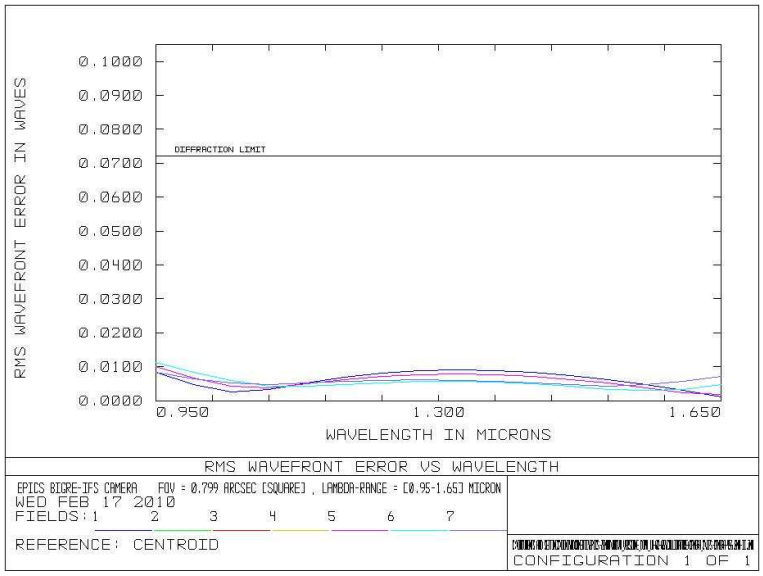

Figure 4.22: EPICS IFS Camera wavefront error vs. wavelength.

design.
The optical design from this procedure can be seen in Figure 4.23.

Figure 4.24 shows the spot diagrams for the obtained design. In this case the worst spot radius is of 12.35 μm, less than the dimension of a single detector pixel (15 μm). Figure 4.25 shows the plots for different fields of view of the wavefront error versus the wavelength.

4.3.8 IFS and folding mirror

The next step in our optical design is the introduction of the folding mirror after the last lens of the collimator and before the pupil stop. Figure 4.26 shows the optical design of the instrument with the 45° fold mirror.

Figure 4.27 shows the spot radii obtained after the introduction in the optical design of the fold mirror. As expected they are not changed from the results obtained for the EPICS IFS collimator+camera only (see Figure 4.24 for a comparison).
Figure 4.28 shows plots for different fields of view of the wavefront error versus the wavelength for this last case. There is no change respect to the EPICS IFS collimator + camera only (see Figure 4.25 for a comparison).

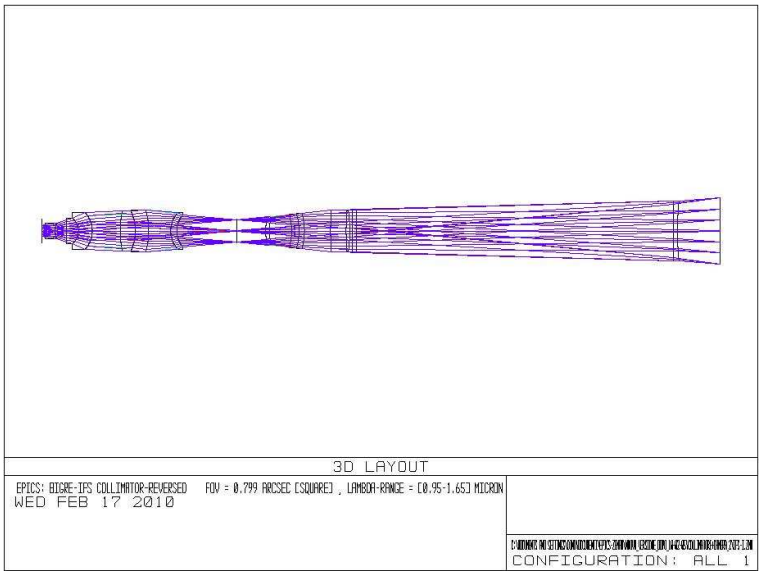

Figure 4.23: EPICS IFS Collimator+Camera Optical Design.

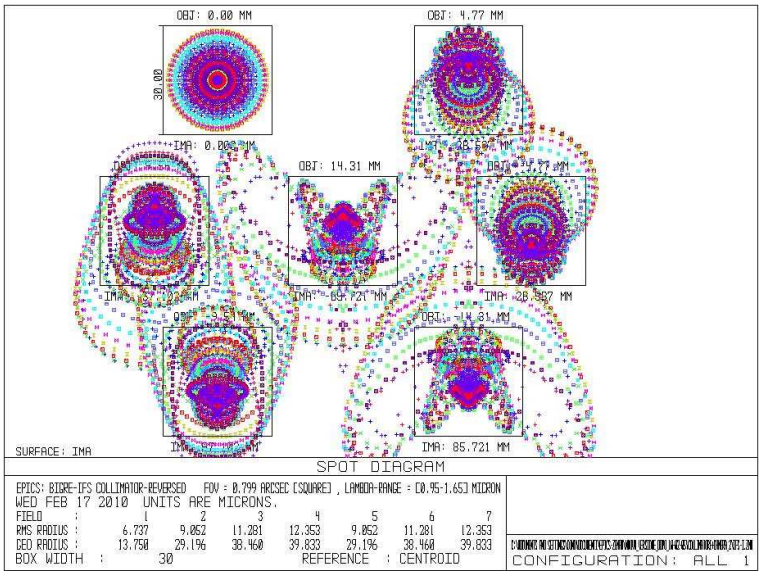

Figure 4.24: EPICS IFS Collimator+Camera spot diagrams at different fields.

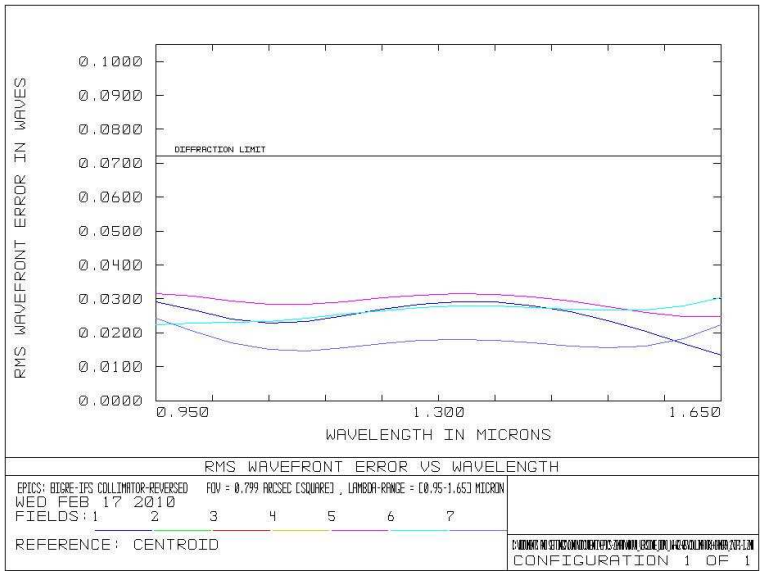

Figure 4.25: EPICS IFS Collimator+Camera wavefront error vs. wavelength plots.

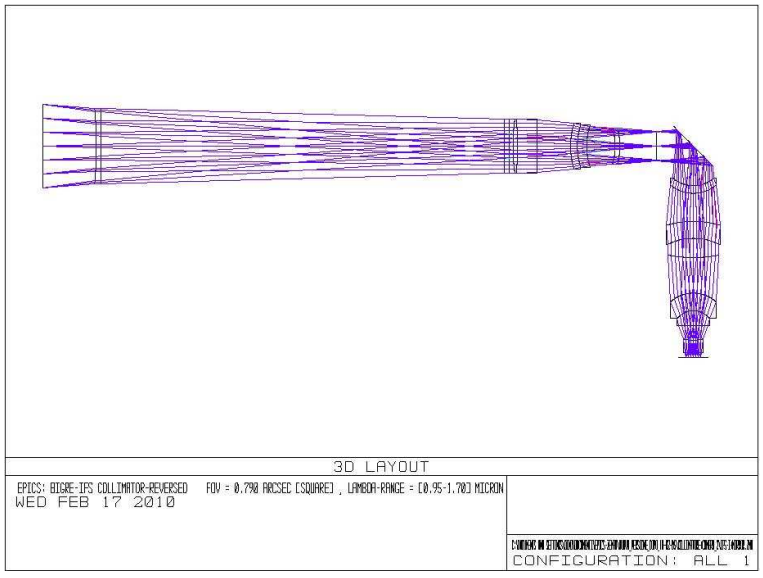

Figure 4.26: IFS+fold mirror+camera optical design.

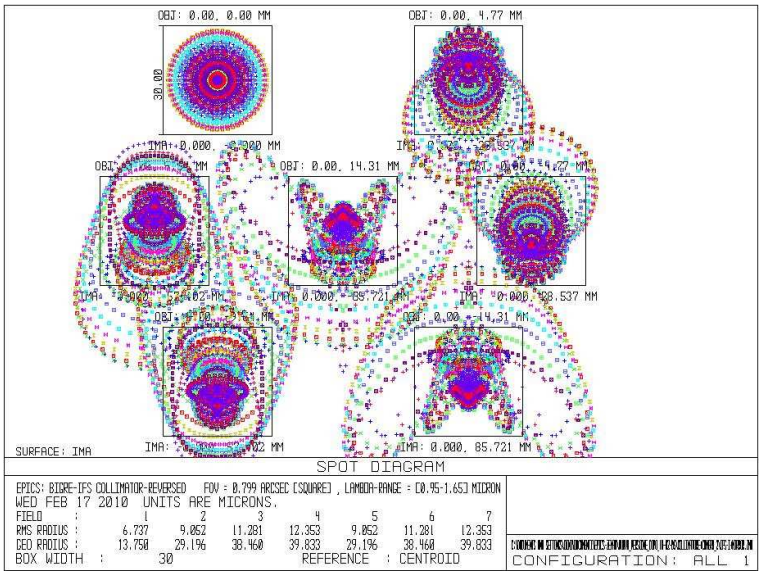

Figure 4.27: IFS+fold mirror+camera spot diagrams at different fields.

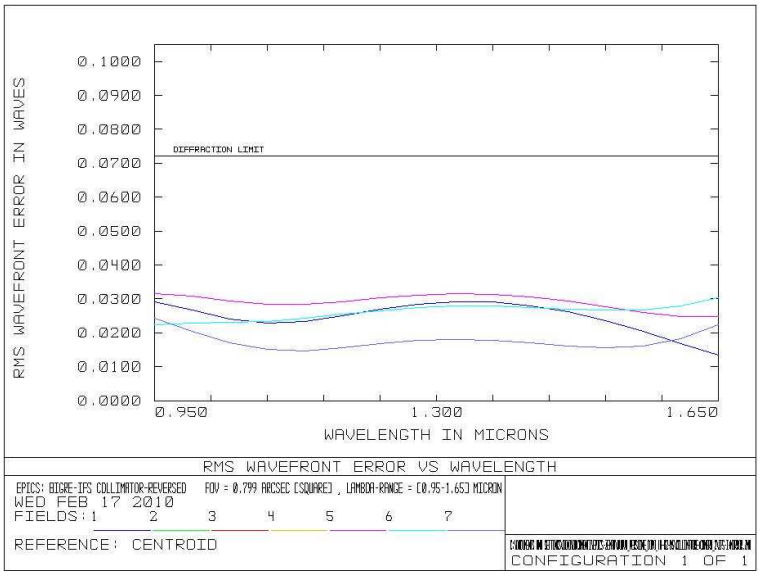

Figure 4.28: IFS+fold mirror+camera wavefront error vs. wavelength plots.

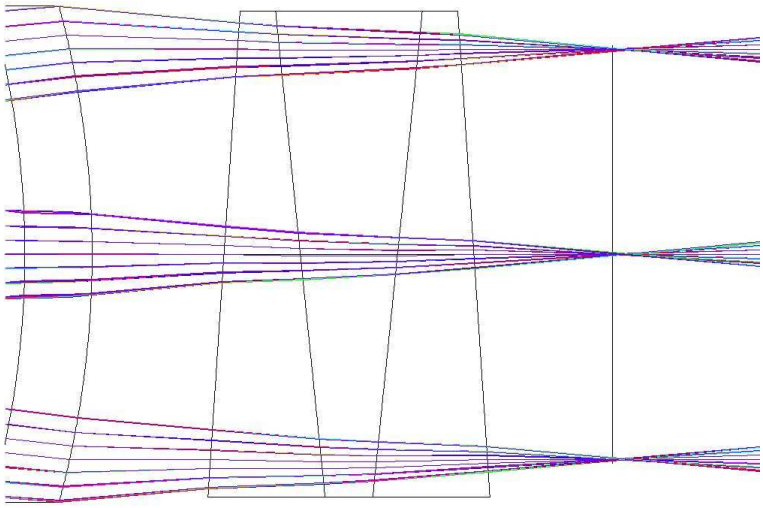

Figure 4.29: Disperser prism for EPICS IFS.

4.3.9 Disperser

The introduction of a disperser in the collimated beam after the pupil stop of the previous design is the last step to obtain the final design of the IFS. The basic disperser is an Amici prism (see Oliva 2000) as the one exploited in the SPHERE IFS design. The requested 2 pixel resolution is of 130.5 and the spectral length is of ~140.5 pixels.
Figure 4.29 shows the design for the EPICS IFS Amici prism. It is composed by three different prisms cemented together. The first one is composed by BAF2 glass and it is 11.0 mm thick, the second one is made by S-TIH6 and it is 14.0 mm thick and the last one is identical to the first one (see Table 4.5 for more informations about prism data).
Figure 4.30 shows the spot diagrams for different fields of the complete design (different colours stay for different wavelength). In the image the boxes have a side of 2100 μm (or 140.5 pixels) highlighting that the final length of the spectra is the requested one.
Figure 4.31 shows the wavefront error of the optical system versus the wavelength. The final result is a well diffraction limited system.
Figure 4.32 shows the run of 2-pixel spectral resolution with wavelength. The choice of the glasses and of the angles of the Amici prism results in a well compensated system, with a spectral resolution only mildly dependent on the wavelength.

4.3.10 Higher spectral resolution mode

To fully characterize the atmosphere of the extra-solar planets detectable with EPICS, we consider higher spectral resolution modes by replacing the Amici prism with other types of disperser. In particular, we are interested in an intermediate resolution mode (R=1500 or R=4000) and in a high resolution mode (R=20000). These modes require

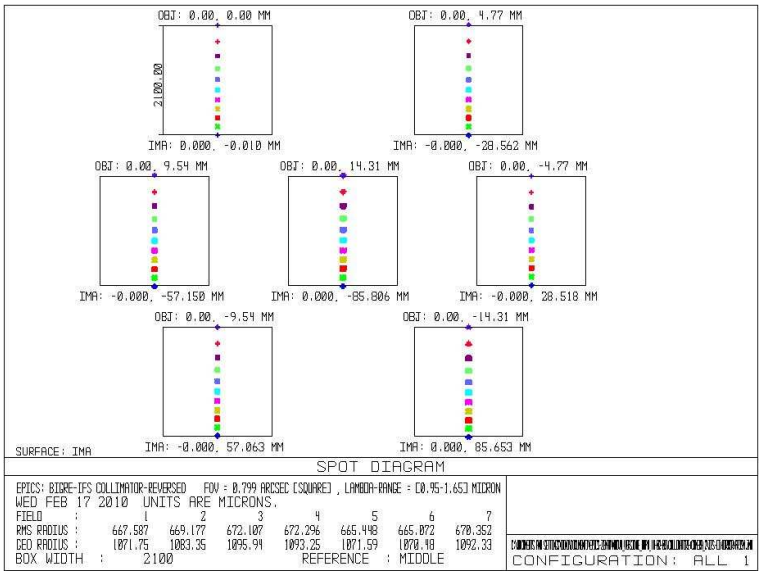

Figure 4.30: EPICS IFS spot diagrams for different fields.

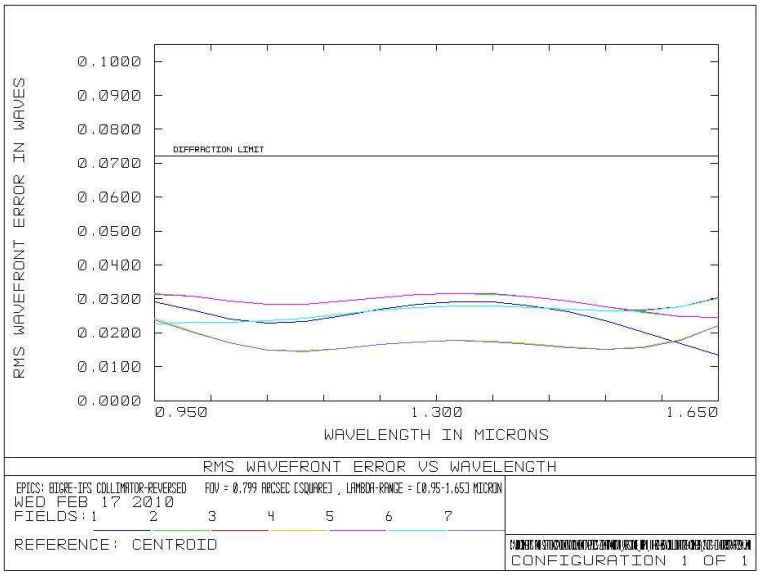

Figure 4.31: EPICS IFS wavefront error versus wavelength for different fields.

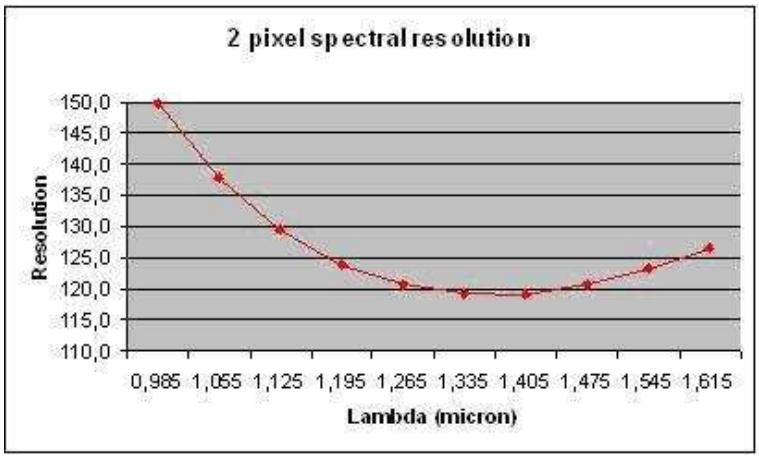

Figure 4.32: 2-pixel spectral resolution of the optical system at different wavelengths.

$\lambda(\mu m)$	**R**
0.985	**149.8**
1.055	**137.7**
1.125	**129.5**
1.195	**123.8**
1.265	**120.8**
1.335	**119.3**
1.405	**119.1**
1.475	**120.8**
1.545	**123.3**
1.615	**126.5**

Table 4.6: 2-pixel spectral resolution at different wavelengths.

long spectra (~ 2000 pixels for the intermediate resolution mode, the full detector size, that is ~8000 pixels, for the high resolution mode). Hence, only a portion of the FOV can be imaged on the detector, in practice a pseudo-slit, that is only 6 lenslets wide (0.014 arcsec). This pseudo-slit is obtained by replacing the usual IFU with a second one, where all but 6 rows of lenslets are masked. This is compatible with the adopted Hexagonal-F configuration. The pseudo-slit have an equivalent width of 0.014 arcsec at the largest wavelength. This is well enough to properly sample the central peak of the diffraction image of each planet. Moreover, it should pass through the centre of the FOV to allow to estimate and subtract the contribution of background speckles using the spectral deconvolution method. Note that this long-slit mode should obviously be used in a field stabilized mode.

Intermediate resolution mode

The intermediate resolution mode is obtained by replacing the Amici prism with a grism. To define its characteristics we used the formulas described below.
The relation between the resolution R and the number of grooves of the grating illuminated (N) is the following:

$$R = k \cdot N \tag{4.1}$$

In this case k is the order of the spectra and, since we are interested in the first order, we have that R=N=1500. As the diameter of the beam in the instrument at the level of the disperser is ~ 70 mm, we can find that the number of grooves per millimetre is of 21.43 mm^{-1}. The inverse of this value is the grating constant (i.e. the distance between two adjacent grooves) that is d=46.67 μm. We can now define the apex angle of the prism (A) using the formula:

$$\sin A = \frac{k \cdot \lambda}{d \cdot (n-1)} \tag{4.2}$$

Here λ is the central wavelength of the wavelength range (that is λ=1.3 μm) and n is the refractive index of the material with which is done the prism. As a first attempt, we used fused silica (n=1.447) and obtained A=3.57°.
We have now to find a catalogue grating (Richardson Grating Catalogue) with the correct number of grooves per millimetre and with a blaze angle equal (or however quite similar) to the apex angle of the prism. Unfortunately, we were able to find only a grating with 21.36 grooves per millimetre (that gives us the correct resolution - R=1495) but a blaze angle of 6.5°. This angle gives us an unacceptably large shift of the central wavelength with respect to the centre of the spectra.
For this reason, we had to decide to use a grating with 17.5 gr./mm and a blaze angle of 2.1°. This gives us a lower resolution (R=1225) but, changing appropriately the refraction index of the glass, a quite small shift of the central wavelength. To reduce this last parameter to zero we considered glasses with different refractive index. We found more than one possibility:

- S-BSM18: n=1.62163 (Ohara). Shift=3 pixels
- S-BAM12: n=1.61967 (Ohara). Shift=4 pixels

Grooves per millimetre (grating)	**17.5**
Blaze angle (grating)	2.1°
Apex angle (prism)	2.1°
Prism material refractive index	**~1.621**
Prisma material (glass type)	**S-BSM18 or S-BAM12 or S-TIM22**

Table 4.7: Most important parameters of the designed grism with R=1500.

Grooves per millimetre (grating)	**58**
Blaze angle (grating)	6.0°
Apex angle (prism)	6.0°
Prism material refractive index	**~1.721**
Prisma material (glass type)	**S-LAM60 or S-LAM2 or S-LAL59**

Table 4.8: Most important parameters of the designed grism with R=4000.

- S-TIM22: n=1.62316 (Ohara). Shift=9 pixels

In Table 4.7 one can find listed the more important characteristics of the grism that has been described in this Paragraph. Note that the spectrum length is about 2000 pixels, so that only a portion of the detector is illuminated. A possible alternative for the intermediate resolution mode is a disperser grism with a spectral resolution of ~4000. We calculated the parameters of the grism that could give us this dispersion using the procedure described above in this Paragraph and the parameters obtained are showed in Table 4.8.

Like for the previous grism, we look for a glass to reduce the shift of the central wavelength with respect to the centre of the spectra and like in the previous case we find more than one possible glass. The more promising ones are listed below:

- S-LAM60: n=1.72121 (Ohara). Shift=1 pixel
- S-LAM2: n=1.72155 (Ohara). Shift=2 pixels
- S-LAL59: n=1.72193 (Ohara). Shift=5 pixels

The resolution given by this disperser is slightly larger than the goal of R=4000, that is R=4060.

High resolution mode

A high resolution mode with a spectral resolution of R=20000 is foreseen too. In this case, we have to split the wavelength range into three shorter ranges to allow the resulting spectra be short enough to be contained on the detector (8k×8k pixels). In particular the wavelength ranges are:

- 0.950 - 1.150 μm. In this case the spectra should be 7619 pixels long.

- 1.150 - 1.400 μm. In this case the spectra should be 7843 pixels long.
- 1.400 - 1.650 μm. In this case the spectra should be 6557 pixels long.

A grism can not provide such high resolutions. We plan then to use for each of these three cases a volume phase holographic (VPH) grating (coupled with prism pairs to provide a not deviated beam) to substitute the grism.
To define the characteristics of the VPH in each of the three different cases we considered the classical grating equation:

$$m\nu\lambda = \sin\alpha + \sin\beta \tag{4.3}$$

where m is the order of the spectra (we assume m=1), ν is the frequency of the grating fringes, λ is the wavelength, α is the incidence angle while β is the angle of diffraction. The derivative of this formula gives us the following one:

$$m\nu = \frac{d\beta}{d\lambda} \cdot \cos\beta \tag{4.4}$$

where $\frac{d\beta}{d\lambda}$ is the spectral angular dispersion.
This value can be calculated dividing the length of the spectrum for the wavelength range (that give us the spectral linear dispersion) and dividing that for the camera focal length of the IFS (956.8 mm).
To evaluate the frequency of the grating fringes we can then write the above formula as:

$$\nu = D \cdot \cos\beta \tag{4.5}$$

where, for convenience, we have called D the angular dispersion. To obtain a result we have to know the value of the diffraction angle and at this scope we can exploit the fact that in order to optimize the efficiency we will work under the Bragg condition (where the incident angle is equal to the diffraction angle). So we have:

$$m\nu\lambda = 2 \cdot \sin\beta \tag{4.6}$$

Putting together equation 4.5 and equation 4.6, we can easily found that the tangent of β is given by:

$$\tan\beta = \frac{D \cdot \lambda}{2} \tag{4.7}$$

where λ is the central wavelength of each spectral range.
Table 4.9 presents the most important parameters of the designed VPHs for each spectral range as derived from the calculation described above in this Paragraph.

To avoid that the beam is deviated by the VPH, two prisms will be positioned just before and just after it, each with a side in direct contact with VPH surface. The two prisms will be done using the same material that is used to protect the VPH (in this document we make the hypothesis to use fused silica). Since the incidence angle and the angle of diffraction are the same, the two prisms will be equal but should have an opposite orientation. The two prisms have a particular apex angle for which the total deviation of the beam is equal to zero. This angle has been calculated for the central

Spectral range	**0.95 - 1.15** μm	**1.15 - 1.40** μm	**1.40 - 1.65** μm
Angular Dispersion	**0.60 rad/**μm	**0.49 rad/**μm	**0.41 rad/**μm
Diffraction Angle (β**)**	17.48°	17.34°	17.36°
Frequency of fringes (ν**)**	**572.29 lines/mm**	**467.73 lines/mm**	**391.32 lines/mm**

Table 4.9: Most important parameters of the designed VPHs.

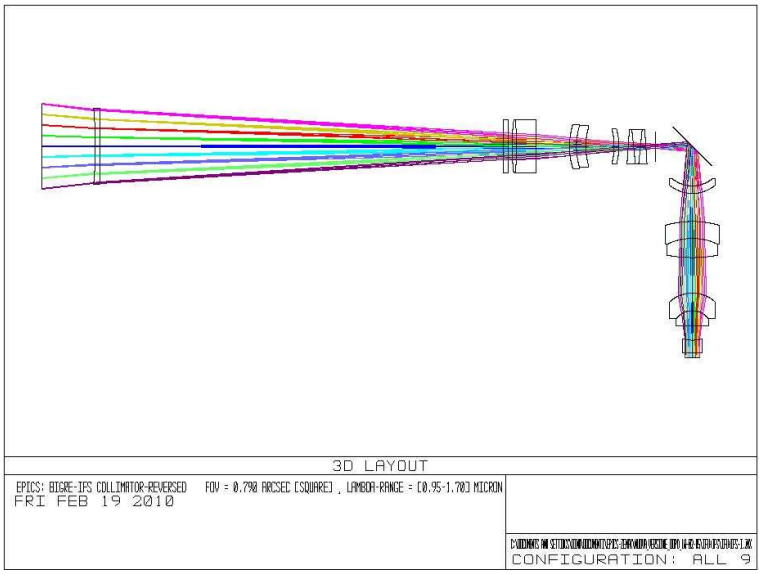

Figure 4.33: Ray tracing of the assembled BIGRE, collimator, disperser and camera.

wavelengths of each spectral range (that is 1.05, 1.275 and 1.525 μm). Since the fused silica refraction index is slightly different at these three wavelengths (1.4498, 1.4472 and 1.4443 respectively) we found three prism apex angles slightly different in the three cases. The results are listed below:

- 0.95 - 1.15 μm: 18.23°
- 1.15 - 1.40 μm: 18.14°
- 1.40 - 1.65 μm: 18.21°

4.3.11 Final optical design

The final step of our optical design is to introduce the BIGRE lenslet array before the IFS collimator. The final optical design is displayed in Figure 4.33.

4.3.12 Detector mosaic

The baseline IR detector for the EPICS IFS is a 2×2 mosaic of four 4k×4k standard E-ELT detectors (see ESO Technical Note INS-2009/02), with pixel size of 15 micron. According to specification, these detectors will have a 6 mm gap on one side and 3 mm on the other three. This will allow obtaining a 2×2 mosaic with gaps of 6 mm that is 400 pixels. This roughly corresponds to strips 0.05 arcsec wide projected on the sky: this is larger than simply the fraction of detector corresponding to the gap because spectra partially out of the detector will be more difficult to be used in data reduction. In particular if the FOV is centered on the camera, then the information about the centre of the FOV is lost. There are different possible solutions to solve this concern:

1. The mosaic can be decentered with respect to the FOV, so that the star image is visible on one of the four detectors. Required decentering is of some 0.05 arcsec. Part of the FOV close to the centre is lost. We may rotate the dewar (a motorized function already foreseen in the IFS design) to ensure that all the FOV is accessible. This can be obtained by rotating the dewar by a suitable multiple of 90°. Hereinafter, we consider this as the baseline solution because it does not require any special hardware. However, with this solution effective exposure time will depend on angle, resulting in some performance losses for fainter sources.

2. A special mosaic could be considered with a small (e.g. 256×256 pixels, that is 4 mm side) dedicated detector located at field centre. This small detector could be fed by 45° mirror, located a few mm in front of the focal plane. While this solution would allow keeping the mosaic centered on the FOV, it is not easy to implement mechanically.

3. Finally, a single 8k×8k pixels detector could be adopted. While this is not the standard NIR E-ELT detector, a similar detector has been considered by Teledyne (see Beletic et al. 2008). This detector has pixels of 10 μm, so that the optical design of the IFS camera should be revised. However, this is not critical (such a design was indeed prepared during our Phase A, and it had actually better performances than the baseline design). While this solution is clearly the best for the EPICS IFS, we do not consider it as the baseline because it is not the E-ELT standard.

4.3.13 IFS within EPICS

Figure 4.34 shows top and side views of the optical design of EPICS. The IFS is at the extreme left in these designs.

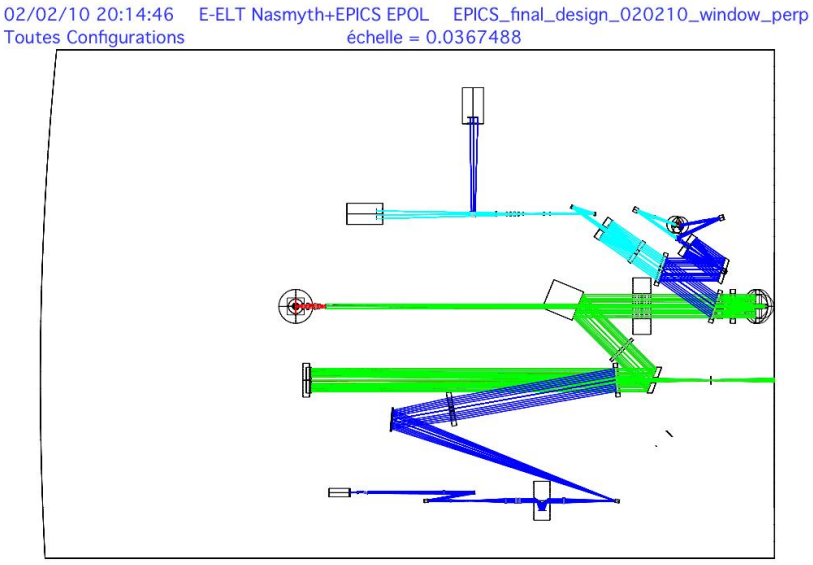

(a)

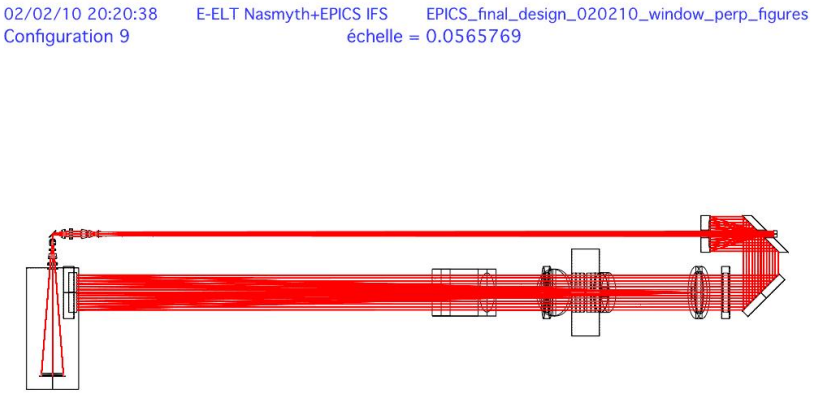

(b)

Figure 4.34: Top and side views of EPICS optical design. IFS is at the extreme left in these drawings.

4.4 Opto-mechanical design

4.4.1 Principles and Interfaces

The mechanical structure of the IFS will be self contained and rigid, so that it can be integrated and tested separately from the main bench of EPICS, during subsystem MAIT, before ARR. It will be then moved to the EPICS integrating center and attached to the EPICS optical bench during system MAIT.
The height of the optical axis on the optical table of EPICS is of 327 mm. All other mechanical interfaces will be defined in detail during Post Phase A, when a more complete and detailed mechanical design will be prepared. They will however allow to dismount and mount again IFS at the main bench within optical tolerances. A solution with spherolinders, similar to the one adopted for SPHERE IFS, might be considered.
A dummy reproducing the IFS weight and momentum will allow to test the mechanics of the EPICS Main Bench before it will actually be delivered to the EPICS Integration Center. A Common Path simulator will allow aligning and test of the IFS when still at Subsystem facility.

4.4.2 Main mechanical choices

We prepared a preliminary mechanical design of the EPICS instrument. This design considers a vertical distribution of the instrument. This has two advantages:

- It better fits into the space available for IFS.
- It is gravity independent

A drawback of this choice is that a number of optical surfaces are placed horizontally and are then more sensitive to dust deposition. Strict rules about the environment cleanliness at IFS subsystem integration facility, EPICS system integration facility and in the integration facility at the telescope are then required.
To reduce the potential impact of dust, we plan to close the whole IFS into a separate enclosure, within the already clean EPICS environment. A shutter will allow to completely seal the IFS when light from the Common Path is not needed. This also allows to perform internal calibration of IFS even when EPICS is used for other purposes.

4.4.3 Preliminary mechanical concept

The mechanical structure of the IFS is made of a vertical bench, to which three horizontal platforms (Upper, Intermediate and Lower), carrying the individual opto-mechanical components, are rigidly fastened. The whole structure is closed within a light and dust tight box.
Figure 4.35 shows the three platforms with the opto-mechanical components mounted on (the vertical bench is not shown). Figure 4.36 is an alternative view from a different view point, showing the hole in the lower platform that allows hosting the dewar (the two other platforms are not displayed in this image). Another hole in the Intermediate platform allows light from the Integrating Sphere to feed the IFS (in this case the Folding Mirror is removed from the optical path). A hole in the vertical bench allows light

from the Common Path to enter the IFS through the shutter.
The three platforms carry the various opto-mechanical components (indicated with different colours in these Figures):

- Top platform: the integrating sphere (orange)
- Intermediate platform:
  - IFU and their motorized stage (magenta)
  - Collimator (yellow)
  - Folding mirror (violet, mounted on a slide)
  - Filter wheel (blue)
  - Other elements of the calibrating arm (orange)
- Lower platform:
  - Disperser wheel (cyan)
  - Camera (red)
  - Dewar (green)

A dimensional scheme of the instrument is displayed in Figure 4.37. The dimension in the direction perpendicular to the drawing plane is 700 mm (so total size is 2000×1180×700 mm).

4.4.4 Motorized functions

IFS will be completely remotely operated. Table 4.10 lists the required motorized functions. The second column of the Table contains the element of the optical design to be moved, the third one the type of movement required, the fourth one the scope of the movement, the fifth one the range of the shift or of the rotation (if any), the sixth one the number of positions (if any), the seventh one contains a preliminary identified technical solution and the last one an estimate of the total weight to be moved. There are a total of 15 motorized functions plus the shutter. Most of these functions can be realized using on-the-shelf components. Only three special functions are required: two wheels (filter wheel and disperser wheel), and the rotating table carrying the dewar.

We integrated our mechanical design introducing the motorized stages for the mechanical parts that need them and the cryostat for the dewar. This part of the work has been done using the 'Solid Works' software. An image of this mechanical design is showed in Figure 4.38 (where again the vertical bench is not shown).

4.4.5 Weight Budget

From the mechanical design we can make an estimate of the total weight of the instrument. This should be of the order of 600 Kg. In Table 4.11 we listed the most important contributors to the total instrument weight.

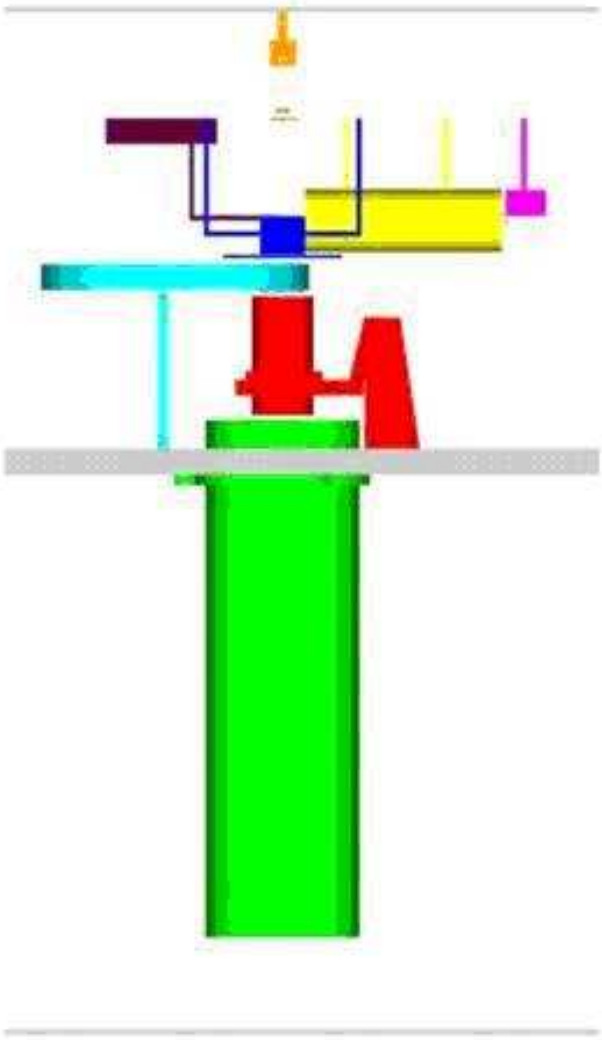

Figure 4.35: Lateral view of the EPICS IFS instrument for the proposed mechanical design.

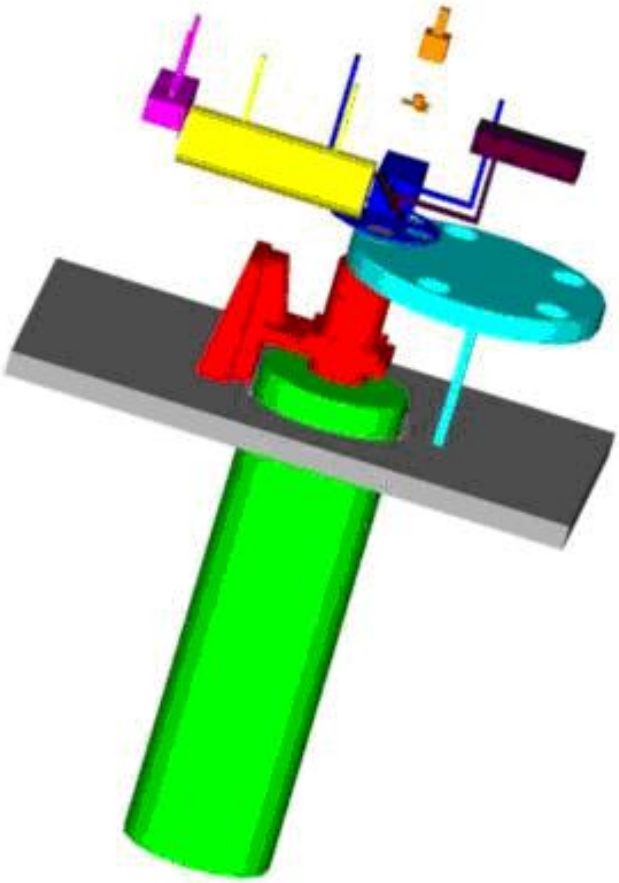

Figure 4.36: Proposed mechanical design for the EPICS IFS instrument (only the lower optical table is showed in this image - no part of the box.

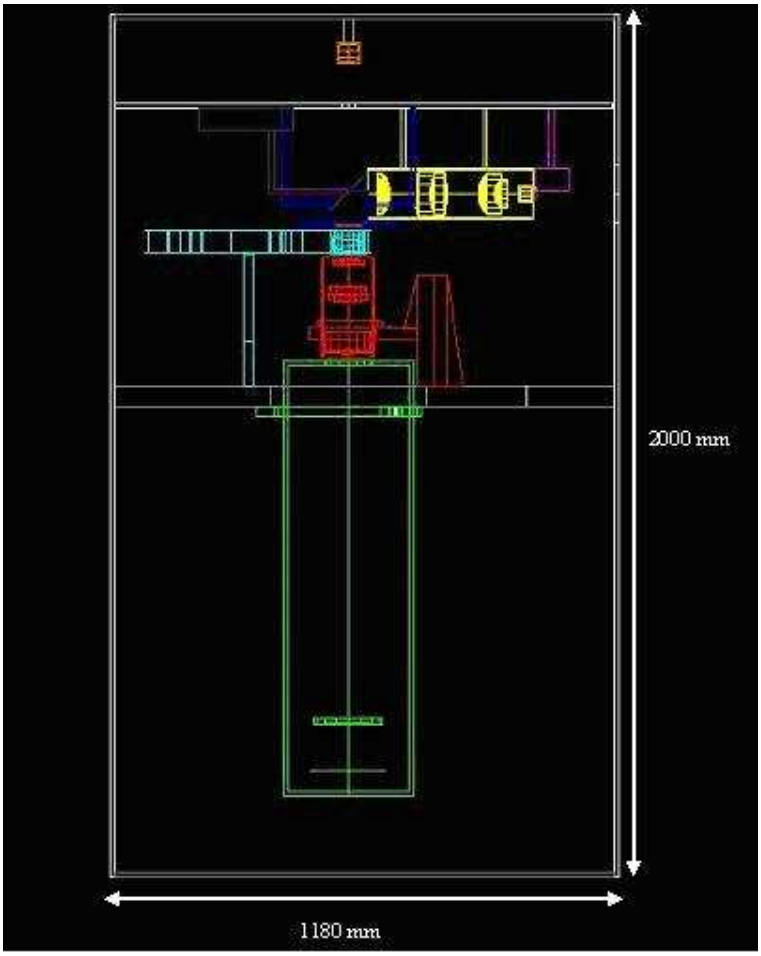

Figure 4.37: Schematic design of the EPICS IFS instrument with an indication of its dimensions.

N	Element	Type	Scope	Range	Accuracy	Number of positions	Proposed solutions	Total weight to be moved
1	**Shutter**		**Close IFS**				**MELES GRIOT**	TBD
2	**IFU**	**Slide**	**Select IFU**	**~50mm**	**36 μm half lenslet**	**2**	**OWIS (LIMES 84-70-HDS)**	**TBD**
3	**IFU**	**Rotating table**	**Rotate Pseudo long slit mode**	0° – 360°	**0.01 deg**		**OWIS (DMT 100-D53-HDS)**	**~1.5 kg**
4	**IFU**	**Rotating table**	**Rotate low resolution mode IFU**	0° – 360°	**0.01 deg**		**OWIS (DMT 100-D53-HDS)**	**~1.5 kg**
5	**Fold mirror**	**Slide**	**Select internal calibration arm**	**~50mm**	**1 mm**	**2**	**OWIS (LIMES 84-70-HSM)**	**~1.5 kg**
6	**Filter wheel**	**Rotating wheel**	**Select neutral density filter**	±270°	**0.01 deg**	**5**	**SPECIAL**	**~2kg**
7	**Disperser**	**Rotating wheel**	**Select disperser**	±270°	**0.01 deg**	**5**	**SPECIAL**	**TBD**
8	**Disperser**	**Rotating table 1**	**Rotate Amici prism**	0° – 360°	**0.01 deg**		**OWIS (DMT 200-D70-HDS)**	**~2.5 kg**
9	**Disperser**	**Rotating table 2**	**Rotate grism**	0° – 360°	**0.01 deg**		**OWIS (DMT 200-D70-HDS)**	**~2.5 kg**
10	**Disperser**	**Rotating table 3**	**Rotate VPH Y mode**	0° – 360°	**0.01 deg**		**OWIS (DMT 200-D70-HDS)**	**~2.5 kg**
11	**Disperser**	**Rotating table 4**	**Rotate VPH J mode**	0° – 360°	**0.01 deg**		**OWIS (DMT 200-D70-HDS)**	**~2.5 kg**
12	**Disperser**	**Rotating table 5**	**Rotate VPH H mode**	0° – 360°	**0.01 deg**		**OWIS (DMT 200-D70-HDS)**	**~2.5 kg**
13	**Camera**	**Slide**	**Focusing camera**	**± 10 mm**	**10 μm**		**MICOS (UPL-160)**	**TBD**
14	**Camera**	**Piezo table X**	**Dithering X**	**±0.95 mm**	**2 μm**		**PI (M-686.D64)**	TBD
15	**Camera**	**Piezo table Y**	**Dithering Y**	**±0.95 mm**	**2 μm**		**PI (M-686.D64)**	TBD
16	**Dewar**	**Rotating wheel**	**Rotate dewar**	±270°	**0.01 deg**		**SPRCIAL**	**~30 kg**

Table 4.10: Motorized functions for the EPICS IFS instrument.

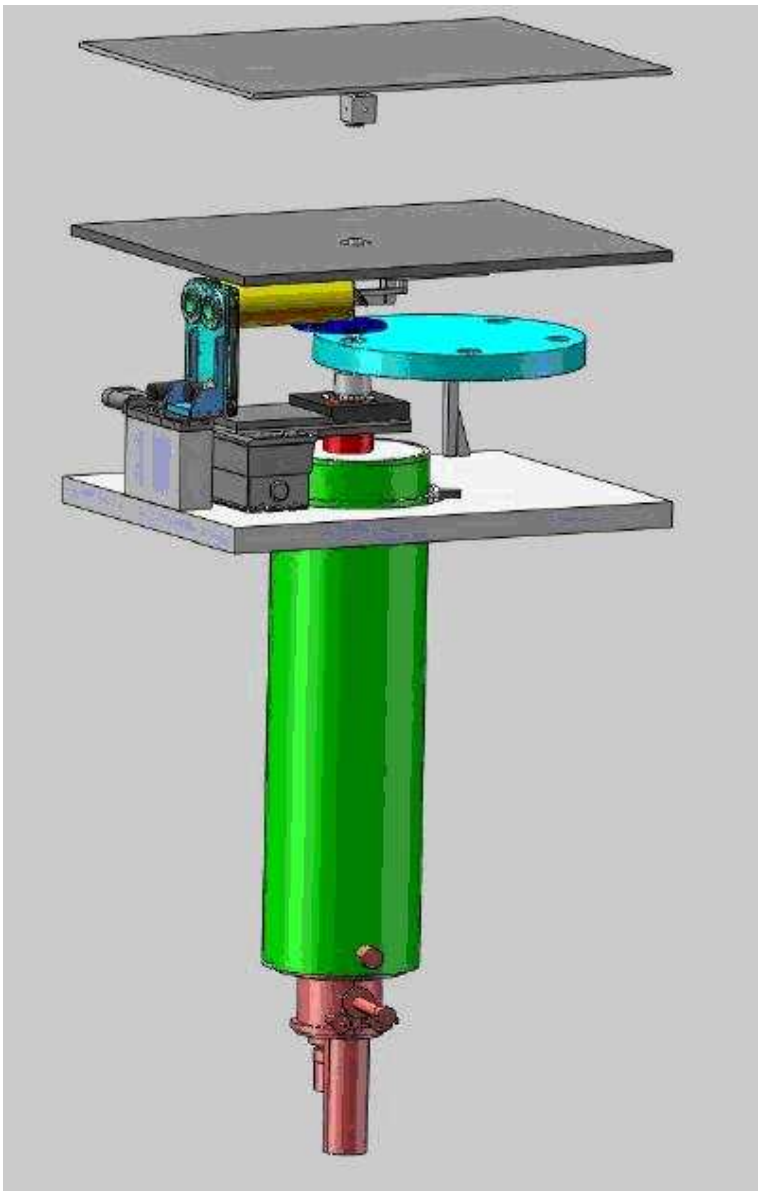

Figure 4.38: Solid Works mechanical design where motorized stages and cryostat has been included.

Element name	Weight (Kg)
Box + bar	~300
Optical tables (2)	~120
Dewar	~30
Disperser wheel	~30
Filter wheel	~4
Camera structure	~9.5
Collimator structure	~2

Table 4.11: Weight budget for IFS.

4.4.6 Integration within EPICS

Figure 4.39 shows a Solid Works mechanical design of the IFS integrated within the EPICS optical bench. The IFS is the black structure on the foreground. The IFS cover is shown in trasparence in this Figure.

4.5 Cryogenics

We will need to mantain the elements contained into the dewar at cryogenic temperature (e.g. the detector and the cold filter should be at $\sim$ 90°K). To this aim liquid nitrogen can be used. A thermal model will be prepared during the post-phase A, in particular we need to define the size of the tank of liquid nitrogen to mantain the various elements at the required temperature. The following elements will be considered in the cryogenic design:

- the detector
- the cold filter and its support
- the detector electronics
- the cold finger
- the cold shield
- the optical window
- the LN tank
- the dewar

4.6 Transmission budget

The transmission budget of the IFS has four components:

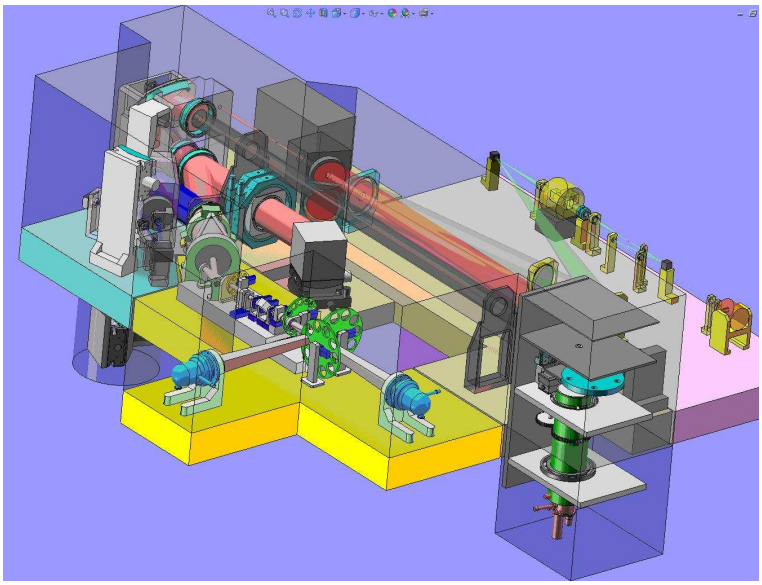

Figure 4.39: Solid Works mechanical design of the IFS integrated on the EPICS optical bench.

1. Vignetting by the mask deposited on the first surface of the IFU. The diameter of the mask hole is the 98% of the single lens size. The transmission is then equal to 0.98.

2. Vignetting by the pupil stop system between the collimator and the camera optics. The transmission budget for this component has been assumed to have a value of 0.87.

3. Reflection at the 22 air-glass surfaces of the overall system. We assume a transmission value of 0.995 at every surface and then the final transmission budget for this issue is given by the above value elevated to the number of surfaces. The final value is of 0.90.

4. The absorption given by all the glasses adopted for the system. To this aim we use the transmission values given in Table 4.12 at different wavelengths for a glass thickness of 10 mm.

The overall transmission budget for the optical system is given by the combination of the above listed contributions. The final results at different wavelengths are given in Table 4.13.

	$\lambda = 0.9\mu m$	$\lambda = 1.0\mu m$	$\lambda = 1.2\mu m$	$\lambda = 1.4\mu m$	$\lambda = 1.6\mu m$	$\lambda = 1.8\mu m$
INFRASIL	1.000	1.000	1.000	1.000	1.000	1.000
BAF2	1.000	1.000	1.000	1.000	1.000	1.000
S-NPH2	0.996	0.996	0.997	0.997	0.996	0.992
S-FPL51	0.999	0.999	0.999	0.999	0.999	0.999
S-TIH6	0.998	0.998	0.998	0.997	0.995	0.986
RG850	0.814	0.903	0.935	0.935	0.935	0.935

Table 4.12: Transmission at different wavelengths for the glasses used in the optical design.

λ **(**μm**)**	**Transmission**
0.9	0.524
1.0	0.582
1.2	0.608
1.4	0.608
1.6	0.600
1.8	0.568

Table 4.13: Total transmission budget for the EPICS IFS optical design.

4.7 Instrumental Background Radiation

In the optical design, the Dewar window is at room temperature and the detector is highly sensitive up to $2.7\mu m$. For this reason it is necessary to consider the background radiation received by it. The constraint we assume is that it should not be the major source of noise. To calculate the number of photons per pixel and per second that arrives on the detector we follwed these steps:

- We integrated the Planck Law (divide by $h\nu$) to get the number of photons per unit of emitting area and for second on the solid angle. For this calculation we used the IDL routine PLANCK that gives the energy at a single wavelength in cgs units ($erg \cdot cm^{-2} \cdot s^{-1} \cdot \mathring{A}$). This corresponds to assume emissivity equal to 1 so that our estimates are upper limits.

- We multiply the previous result by the area of the dewar window (it has a radius of 3.904 cm, and then area $A = \pi \cdot R^2 = 47.88 cm^2$) and by the solid angle of a single pixel divided by the whole solid angle:

$$\Omega = \frac{(A_p)}{4\pi \cdot d^2} \tag{4.8}$$

  In this formula A_p is the pixel area ($= 2.25 \times 10^{-6} cm^2$) and d is the distance between the dewar window and the detector (=82.314 cm). The final result for the solid angle is 2.64×10^{-11}. Multiplying this last value by the dewar window area we get the final multiplicative factor value that is 1.26×10^{-9}.

T_{env}	**Filter**	$\lambda_{cut}(\mu m)$	**ph/s**	**Noise (e^-)**
293	10^{-5}	1.70	0.58	5.93
283	10^{-5}	1.70	0.21	3.54
273	10^{-5}	1.70	0.07	2.04
293	10^{-5}	1.65	0.28	4.07
283	10^{-5}	1.65	0.10	2.42
273	10^{-5}	1.65	0.03	1.39
293	10^{-4}	1.70	0.81	6.99
283	10^{-4}	1.70	0.32	4.37
273	10^{-4}	1.70	0.12	2.67
293	10^{-4}	1.65	0.50	5.50
283	10^{-4}	1.65	0.21	3.52
273	10^{-4}	1.65	0.08	2.22

Table 4.14: Results for the instrumental background radiation.

- We multiply the values obtained at the previous two points to obtain the number of photons per pixel and per second.

We made the calculations using different filters with different cut-off wavelength of 1.65 μm or 1.70 μm. These filters have a transmission close to 1 for wavelengths less than the cut-off wavelength minus 0.05 μm and a value of 10^{-4} or 10^{-5} for wavelengths greater than the cut-off wavelength plus 0.05 μm. For the intermediate wavelengths the transmission curve is a straight line that joins the other two branches of the transmission curve. Similar filters has been realized for SPHERE.
In Table 4.14 we show the results of these calculations. In these first column we tabulated the environmental temperature used, the second column is the transmission of the filter at wavelength above λ_{cut}, the third one is the cut-off wavelength adopted for the filter, the fourth one is the number of thermal background photons per second that arrives on a single detector pixel and the fifth one is the noise generated by the instrumental background for a 60 s pose. It is clear from these results that the filter that gives the lower noise has a filter that cut down to 10^{-5} and has a cut-off wavelength of 1.65 μm. However, all these cases have a comparable (or better) noise than RON for a 60 s exposure (estimated to be 6 e^-).

4.8 Effects of variations of temperature and pression

The optical design described above has been made assuming a temperature of 20°C and a pressure of 1 atm that is typical for the sea level. To evaluate the effects of temperature and pression we exploit the possibility given by the ZEMAX software to change the operative condition of the optical system. First of all, we evaluate the effects of a change of the temperature considering the change in the best focus position passing from 20° to 0°C. In this case we had to make a shift in the camera position of 5.35 mm to correctly refocus the optical system. We then made the same procedure changing

the atmospheric pressure from 1 to 0.65 atm (2800 m height). In this case the shift in the camera position was of 1.57 mm. The last step was to combine the changes in temperature and in pressure. In this case the shift in the camera position was of 7.52 mm (nearly equal to the sum of the single contributions as expected).
After this we evaluated the lateral shift of the spectra (for a central wavelength of 1.325 μm) in case of a combined change of temperature and pressure at the corner of the detector. We find a value 544.1 μm. Considering that a great amount of pressure change is less probable for the instrument installed at the telescope site and that the temperature changes gives account of more or less 3/4 of the shift, we evaluate a realistic shift of 27.21 pixel (1 pixel=15 μm). This means that a change of 1°C in temperature gives a shift of almost 1.4 pixel. This result implies that we need a well thermally stabilized instrument. Refocusing is needed for changes of temperature of the order of $0.3° - 0.4°$.

4.9 Dithering analysis

Dithering on images of IFS detector is required to keep the flat field noise below 10^{-3} (goal 10^{-4}), which is required to avoid significant deterioration of the achievable contrast. Moving all the camera optics is the easiest solution because a shift on the XY plane (Z is the optical axis) is imaged on the detector plane without any optical magnification or de-magnification. This optical solution maintains a good optical quality with respect to the reference case and it is acceptable from the mechanical point of view, too, as verified by the achieved expertise in the mechanical assembling of the SPHERE IFS. The requested amount of dithering on the detector plane is 10 pixels (±5 pixels) both in X and Y direction. Given a pixel size of 15 μm we get a shift on the detector plane of 75 μm. We verify using the ZEMAX software, that, to get this result, we need to shift all the camera optics by 950 μm. Figure 4.40 shows that the optical quality after the dithering procedure remains acceptably good (to be compared with the optical quality of the optical system without dithering procedure showed in Figure 4.31). All the procedure described in this Section has been performed on the optical design without the lenslet array.

4.10 WFE Budgets

As a goal for our optical system we want that the Strehl Ratio (SR) is below 0.8 - 0.85. We then calculated the correspondent values of the Wavefront Error (WFE) using the Marechal formula:

$$SR = 1 - \frac{4\pi^2}{\lambda^2} \cdot WFE^2 \tag{4.9}$$

For this calculations we adopt the mean wavelength of the operating range of our instrument (that is λ= 1.325 μm). This gives us the following results:

- WFE=94.31 nm (SR=0.80)
- WFE=81.67 nm (SR=0.85)

We then subdivided the optical system into the following four subsystems:

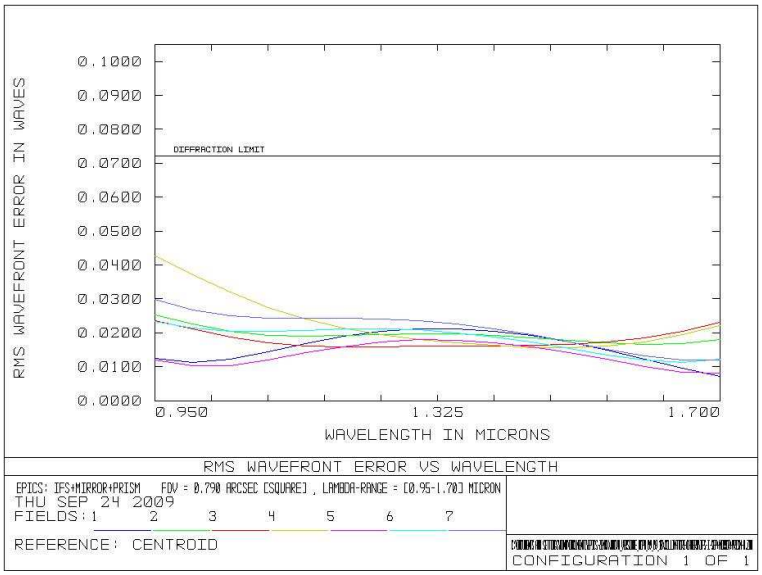

Figure 4.40: Wavefront error versus wavelength fro a shift of 5 pixels on the detector plane.

- BIGRE array
- Collimator
- Camera
- Disperser

For each subsystem we calculated the contribution to the WFE given by the homogeneity of the used glasses, by the surface quality of the optics and by the allowed tolerances on radii and thicknesses.
The WFE given by the homogeneity of the used glasses is calculated by the formula:

$$WFE_H = d \cdot \Delta n \tag{4.10}$$

where d is the thickness of the glass while Δn is the maximum refractive index variation of the glass.
The WFE error arising from the surface quality of the optics is given by:

$$WFE_{SQ} = \mid n_{i+1} - n_i \mid \cdot SQ \tag{4.11}$$

where n_{i+1} and n_i are the refractive indexes of the considered surface while SQ is the surface quality of the surface. In our calculations we assumed a surface quality of $\lambda/50$ for all the flat and not cemented surfaces, of $\lambda/40$ for all the not flat and not cemented surfaces and a value of $\lambda/20$ for the not flat and cemented surfaces. All the surface

Subsystem	WFE (SR=0.80)	WFE (SR=0.85)
BIGRE	26.00 nm	15.00 nm
Collimator	70.00 nm	60.00 nm
Camera	51.44 nm	46.61 nm
Disperser	25.93 nm	25.93 nm
Total	94.31 nm	81.67 nm

Table 4.15: Values of the total WFE for each subsystem.

Subsystem	WFE (Hom.)	WFE (Surf. Qual.)	WFE (Tol.) - SR=0.80	WFE (Tol.) - SR=0.85
BIGRE	2.45 nm	7.23 nm	23.78 nm	10.70 nm
Collimator	25.71	38.37 nm	52.60 nm	38.29 nm
Camera	21.20 nm	33.33 nm	32.91 nm	24.75 nm
Disperser	17.80 nm	18.03 nm		

Table 4.16: Contribution of different types of WFE for each subsystem.

qualities have to be evaluated at the wavelength of the He-Ne laser (0.633 μm).
The total WFE is then given by a quadratic sum of the single components. In this way we can derive the third contribution to the WFE (given by the allowed tolerances).

In Table 4.15 one can find the values of the WFE that has been assigned to each subsystem while in Table 4.16 it is showed the contribution to the total WFE for each subsystem given by the three single contributions listed above. As one can see from Table 4.16 the contributions to the total WFE for the disperser is mainly due to the homogeneity of the glasses and to the surface quality.

4.11 Ghost analysis

Ghost analysis of the IFS refers only to the local background, i.e. the relative ghost intensity has to be measured in the same unit of the detector FF accuaracy, not in unit of the peak intensity of the non coronagraphic stellar image. Within the assumption, the relative intensity of a ghost generated by the IFS optics is relevant only if it exceeds the Technical Spec on the detector FF accuracy (5×10^{-4}).
Considering an AR coating value inside the IFS working wavelengths range of R=0.005 for all the IFS optics, and that for a BIGRE-oriented IFS working at the diffraction limit the ghost effective area A_G is always larger than the Slit Function FWHM (A_0) i.e. larger than 2 pixels, the relative intensity of a ghost generated internally to the IFS is given by:

$$\frac{I_G}{I_0} = \frac{A_0}{A_G} \cdot R^2 \tag{4.12}$$

if A_G is larger than A_0 or

$$\frac{I_G}{I_0} = R^2 \tag{4.13}$$

if A_G is smaller than A_0.
The ghost analysis of the IFS is restricted to the final detector plane and it is performed dividing the ghosts generators in 2 main samples: the optics lying in the converging or diverging beam and the optics lying in the collimated beam.

4.11.1 Ghost analysis for the optics in the converging/diverging beam

The optics lying in the converging or diverging beam produce internal, external and narcissistic ghosts. The ZEMAX ghost focus generator allows to evaluate the ghosts imaged on the detector plane by all the IFS surfaces, excluding the ones produced by the reflections with the surfaces of the BIGRE device. The results from this evaluation give a maximum value for I_G/I_0 of 4.5×10^{-5} fitting the condition above about the detector FF accuracy.
For what concern the ghosts from the IFU surfaces, the use of a non-sequential ray-tracing of the beam is required. This is due essentially to the presence of an IFU whose single spaxel pitch is much smaller than the footprint of the back-reflected light which is due to to any single surface of these elements group. For this reason a sequential ray-tracing fails in determining the right final spot size of internal, external and narcissistic ghosts light imaged on the detector plane. However, by the laboratory prototyping of a BIGRE oriented IFS - without any AR coating over all the other IFS surfaces - the expectation is that internal/external ghosts produced by these reflections heve relative intensity $I_G/I_0 < 10^{-4}$. Instead, the narcissistic ghosts produced by the reflections onto the back side of the first BIGRE surface and re-imaged onto the detector have relative intensity of the same order of the requested Flat Field accuracy, i.e. $I_G/I_0 \approx 10^{-4}$.

4.11.2 Ghost analysis for the optics in the collimated beam

The part of the optical train where the beam is collimated generates narcissistic ghosts. Ray-tracing of the beam reflected back on the detector plane is then necessary for all the optics placed in the collimated beam. The only optics that, in our optical design, is inside the collimated beam that may generate ghosts is the disperser (Amici prism).
The analysis of the narcissistic ghosts of this device is done directly by the ray-tracing of light mirrored from the detector back on the first and on the second air-glass surface of the disperser (the first and the second as seen from the detector) and then re-mirrored from this surface and re-focalized through the IFS camera optics on the detector itself, in order to imagine these ghosts directly. By this analysis arises that no narcissistic ghosts are focused on the detector image-space from the disperser. In Figure 4.41, Figure 4.42, Figure 4.43 and Figure 4.44 the ray-tracing both for on-axis and off-axis configurations are displayed for light reflected back from the first and the second surface of the Amici prism.

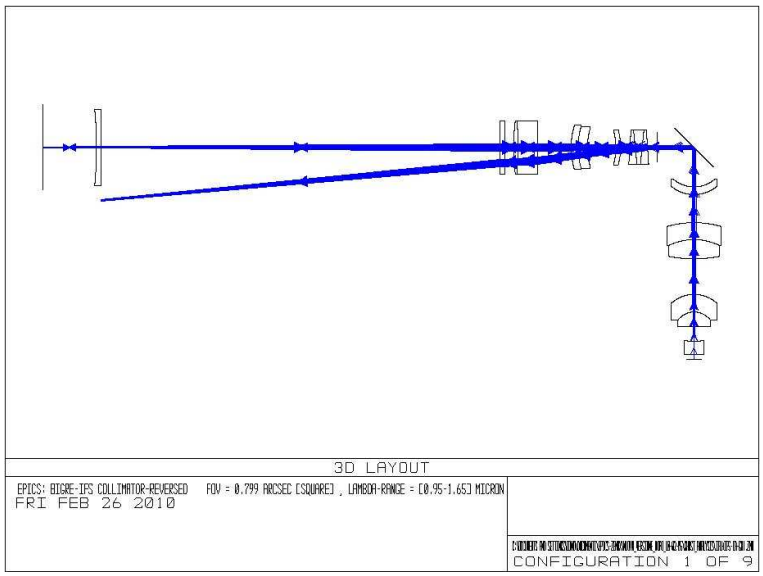

Figure 4.41: Light reflected back on the detector by the first surface of the Amici prism (on-axis configuration). No ghosts are imaged on the detector.

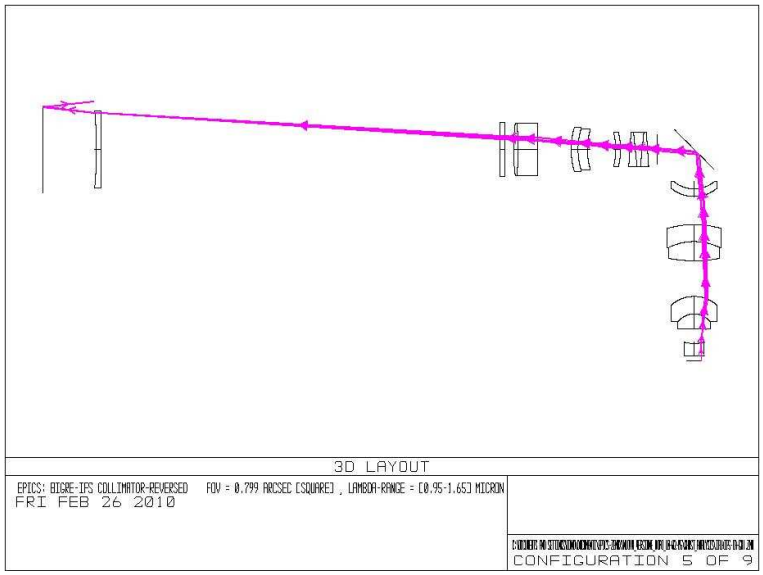

Figure 4.42: Light reflected back on the detector by the first surface of the Amici prism (off-axis configuration). No ghosts are imaged on the detector.

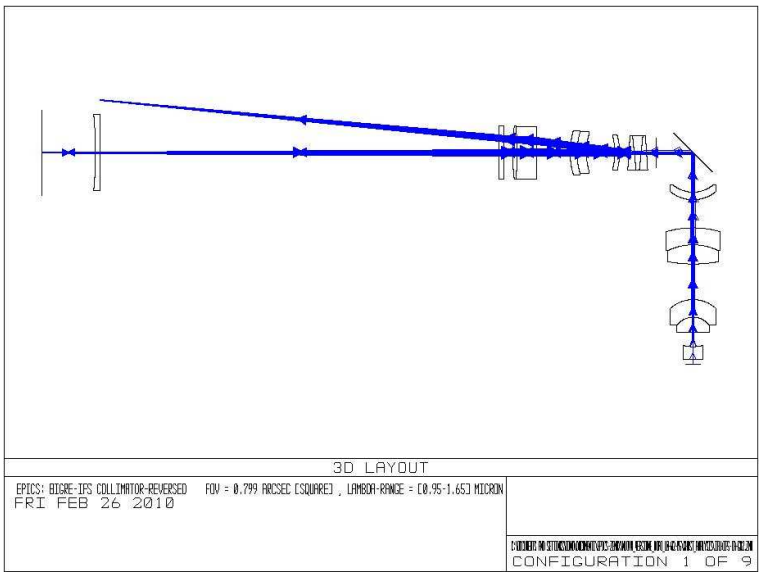

Figure 4.43: Light reflected back on the detector by the second surface of the Amici prism (on-axis configuration). No ghosts are imaged on the detector.

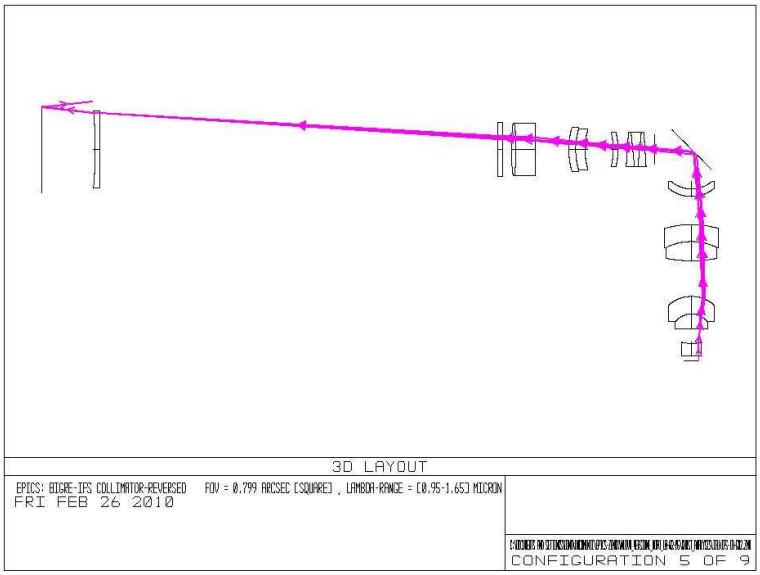

Figure 4.44: Light reflected back on the detector by the second surface of the Amici prism (off-axis configuration). No ghosts are imaged on the detector.

Appendix A

NACO Large Program results

In this Appendix I present the resulting images obtained for other 16 target stars observed during the February 2010 run of observations of the NACO Large Program. In particular, for all the target stars I will show the resulting images obtained without and with the application of the ADI and the plot of the 5σ versus the separation from the target star both for the image obtained without and with the ADI. The main characteristics of these stars are listed below:

- HIP25434: age=92.6 Myr; mag(H)=7.891; dist=67.93 pc; Sp.Type=G0
- HIP32235: age=30.0 Myr; mag(H)=7.380; dist=58.24 pc; Sp.Type=G6V
- HIP36414: age=200.0 Myr; mag(H)=6.509; dist=52.52 pc; Sp.Type=F7V
- HIP37563: age=200.0 Myr; mag(H)=5.863; dist=33.26 pc; Sp.Type=G3V
- HIP37923: age=200.0 Myr; mag(H)=6.496; dist=27.36 pc; Sp.Type=K0V
- HIP47646: age=552.3 Myr; mag(H)=6.858; dist=84.25 pc; Sp.Type=F5V
- HIP63862: age=150.0 Myr; mag(H)=6.834; dist=45.23 pc; Sp.Type=G5V
- HIP70351: age=102.3 Myr; mag(H)=7.573; dist=90.91 pc; Sp.Type=G7V
- TWA 21: age=8.0 Myr; mag(H)=7.353; dist=54.76 pc; Sp.Type=K3Ve
- TYC 5346 132 1: age=30.0 Myr; mag(H)=8.065; dist=81.21 pc; Sp.Type=G7
- TYC 6069 1214 1: age=71.5 Myr; mag(H)=8.022; dist=67.81 pc; Sp.Type=K0V
- TYC 7188 0575 1: age=10.0 Myr; mag(H)=7.385; dist=49.62 pc; Sp.Type=K0V
- TYC 7722 0207 1: age=48.4 Myr; mag(H)=7.781; dist=65.78 pc; Sp.Type=K0V
- TYC 7743 1091 1: age=361.2 Myr; mag(H)=5.179; dist=12.65 pc; Sp.Type=G6II
- TYC 7796 2110 1: age=149.0 Myr; mag(H)=8.280; dist=67.49 pc; Sp.Type=K2IV
- TYC 9162 0698 1: age=28.4 Myr; mag(H)=8.161; dist=98.70 pc; Sp.Type=G6V

A.1 HIP25434

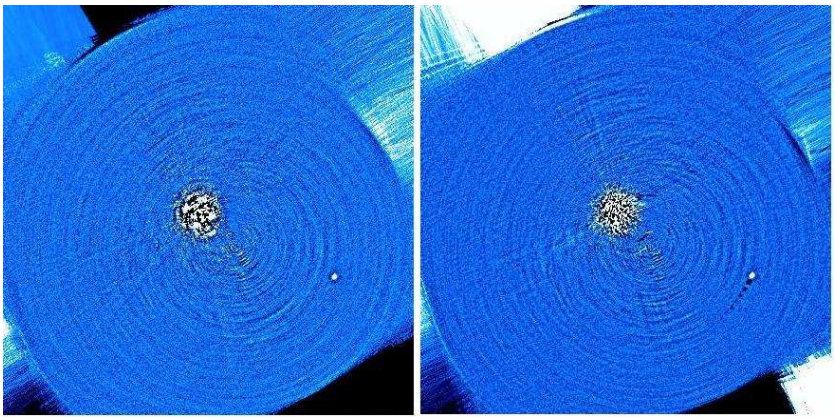

(a)

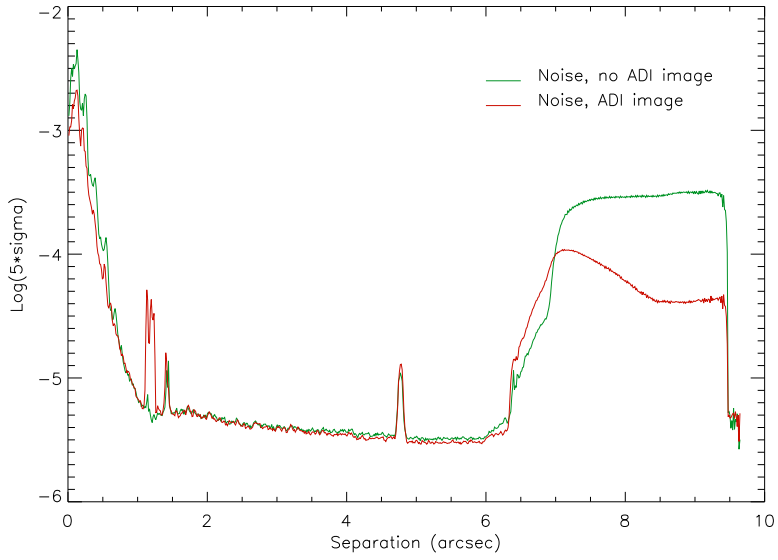

(b)

Figure A.1: (a) Final images for the target star HIP25434 without (left) and with (right) the application of the ADI procedure. (b) Plot of the 5σ versus the separation from the target star for HIP25434.

A.2 HIP32235

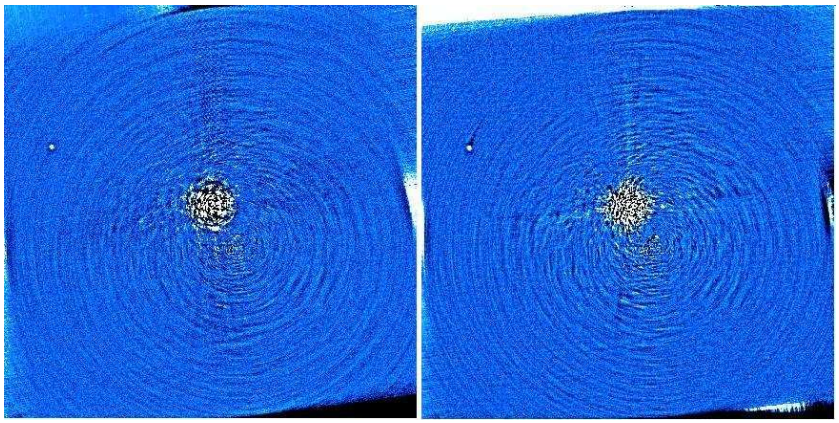

(a) HIP32235_aff.eps

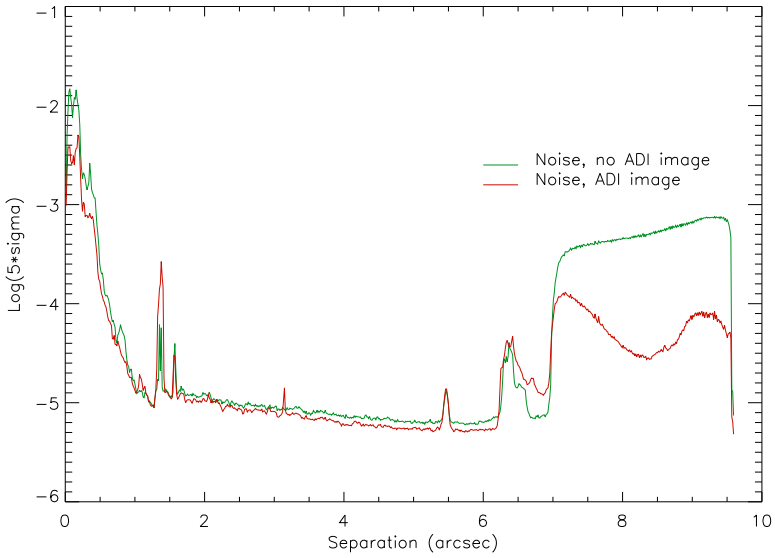

(b) HIP32235_plot1.eps

Figure A.2: (a) Final images for the target star HIP32235 without (left) and with (right) the application of the ADI procedure. (b) Plot of the 5σ versus the separation from the target star for HIP32235.

A.3 HIP36414

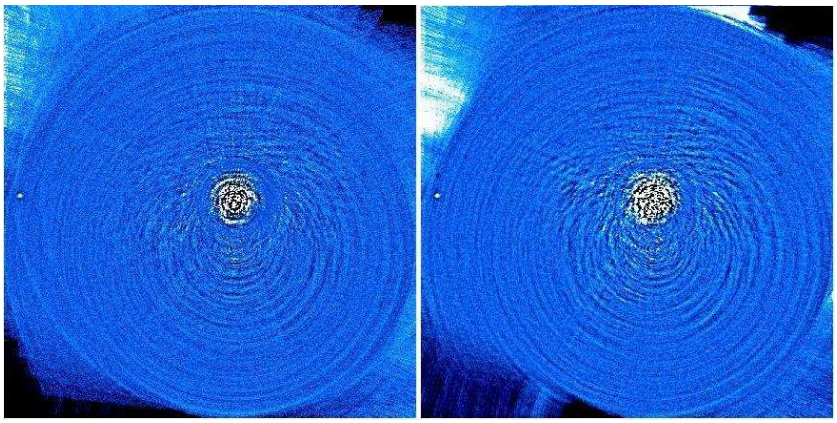

(a) HIP36414_aff.eps

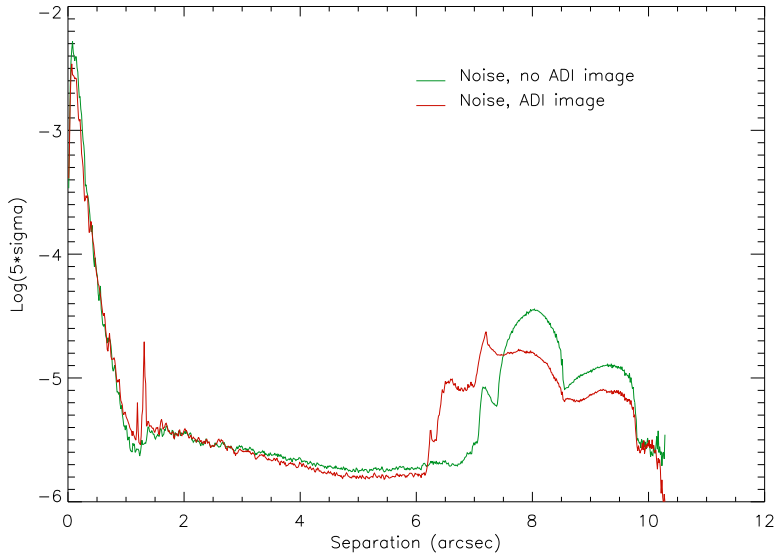

(b) HIP36414_plot1.eps

Figure A.3: (a) Final images for the target star HIP36414 without (left) and with (right) the application of the ADI procedure. (b) Plot of the 5σ versus the separation from the target star for HIP36414.

A.4 HIP37563

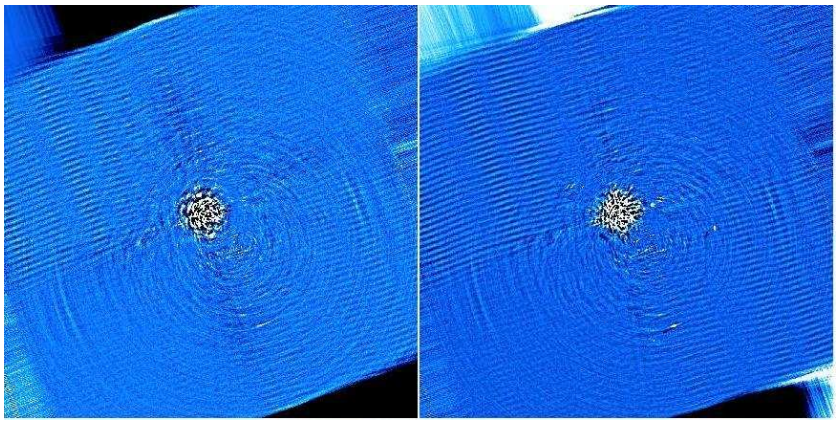

(a) HIP37563_aff.eps

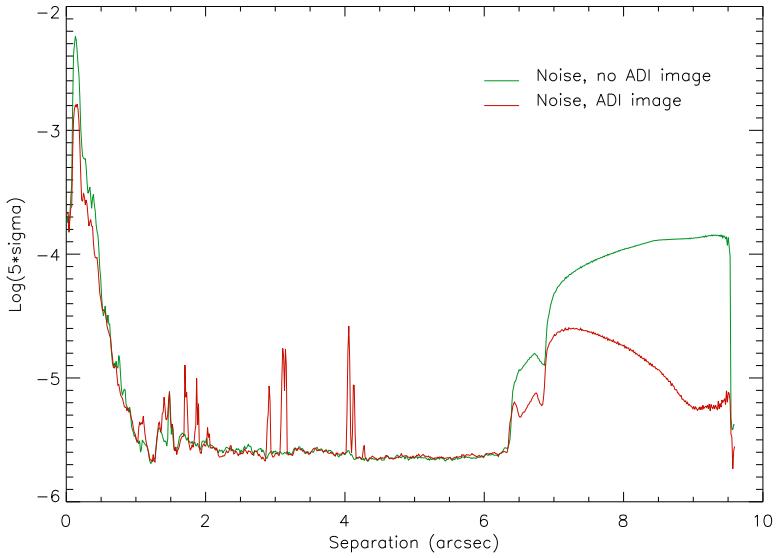

(b) HIP37563_plot1.eps

Figure A.4: (a) Final images for the target star HIP37563 without (left) and with (right) the application of the ADI procedure. (b) Plot of the 5σ versus the separation from the target star for HIP37563.

A.5 HIP37923

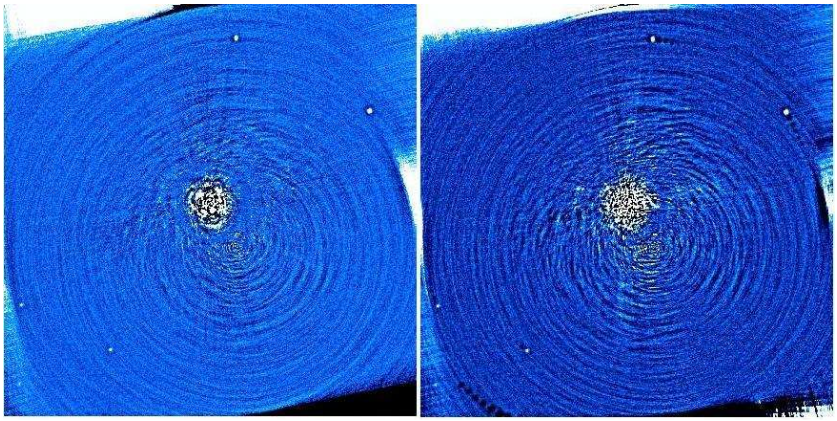

(a) HIP37923_aff.eps

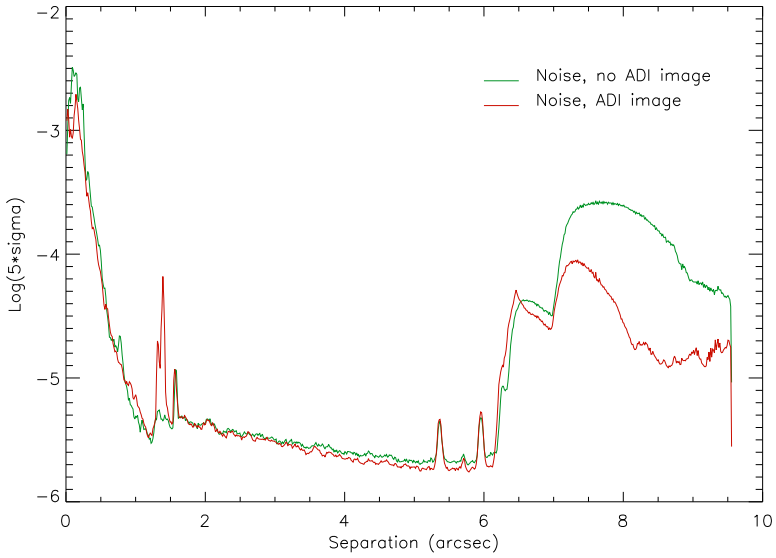

(b) HIP37923_plot1.eps

Figure A.5: (a) Final images for the target star HIP37923 without (left) and with (right) the application of the ADI procedure. (b) Plot of the 5σ versus the separation from the target star for HIP37923.

A.6 HIP47646

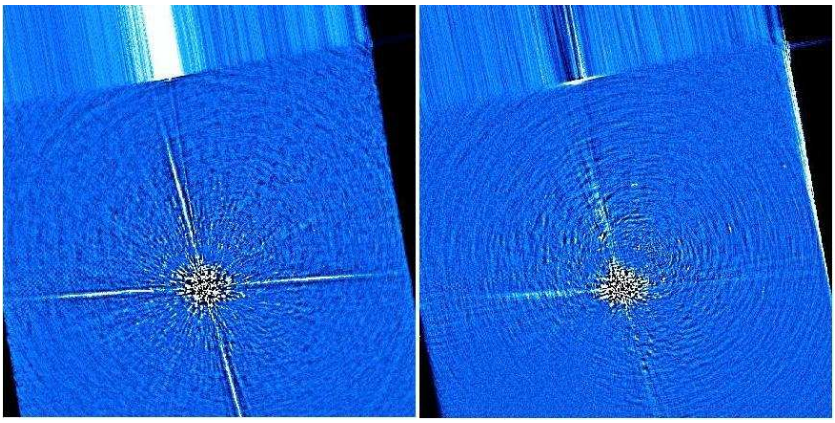

(a) HIP47646_aff.eps

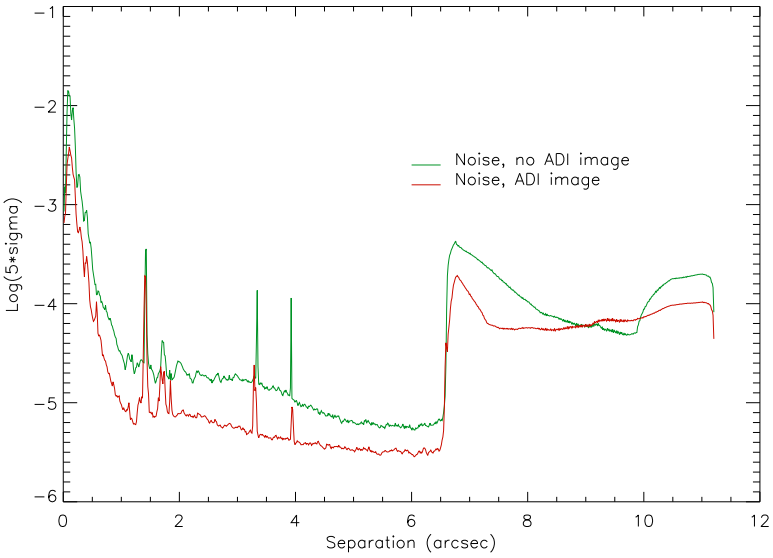

(b) HIP47646_plot1.eps

Figure A.6: (a) Final images for the target star HIP47646 without (left) and with (right) the application of the ADI procedure. (b) Plot of the 5σ versus the separation from the target star for HIP47646.

A.7 HIP63862

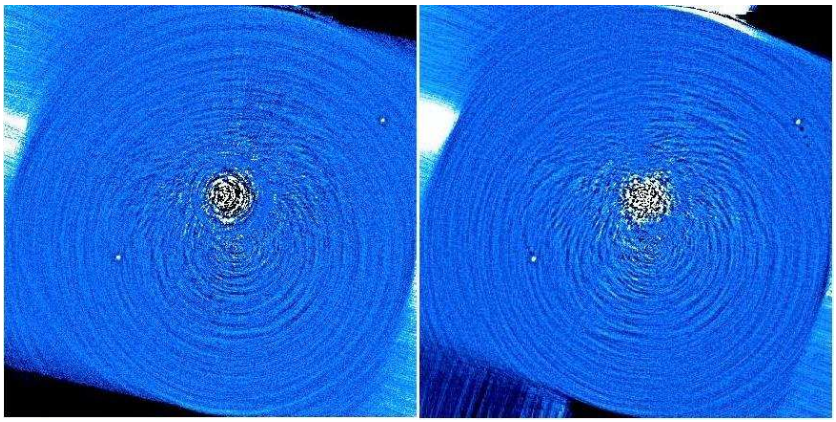

(a) HIP63862_aff.eps

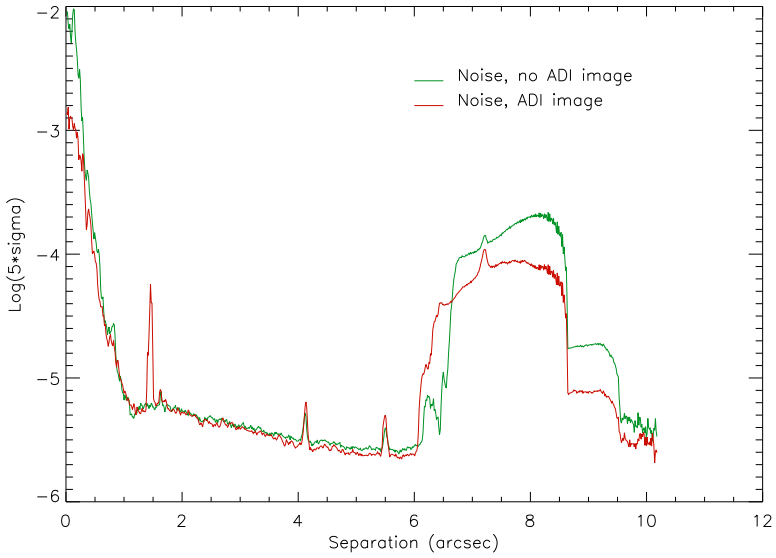

(b) HIP63862_plot1.eps

Figure A.7: (a) Final images for the target star HIP63862 without (left) and with (right) the application of the ADI procedure. (b) Plot of the 5σ versus the separation from the target star for HIP63862.

A.8 HIP70351

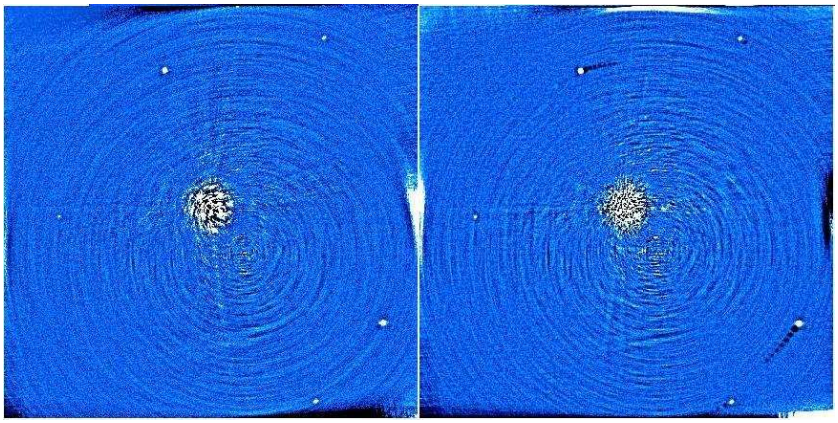

(a) HIP70351_aff.eps

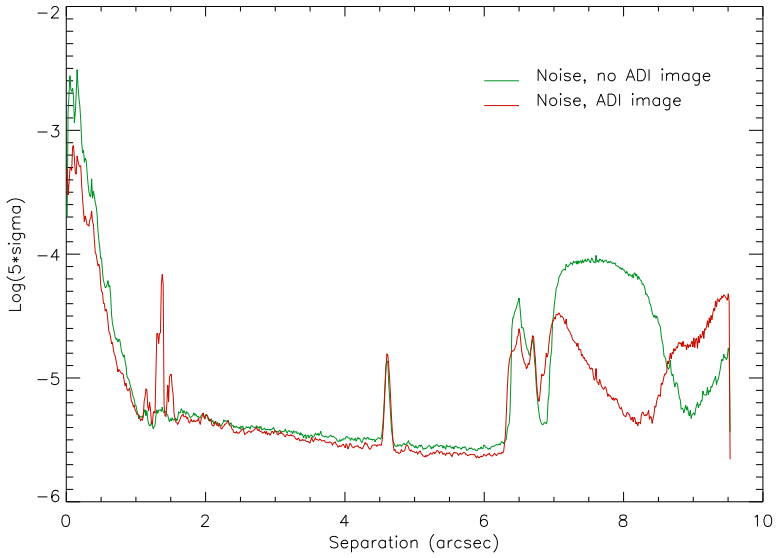

(b) HIP70351_plot1.eps

Figure A.8: (a) Final images for the target star HIP70351 without (left) and with (right) the application of the ADI procedure. (b) Plot of the 5σ versus the separation from the target star for HIP70351.

A.9 TWA 21

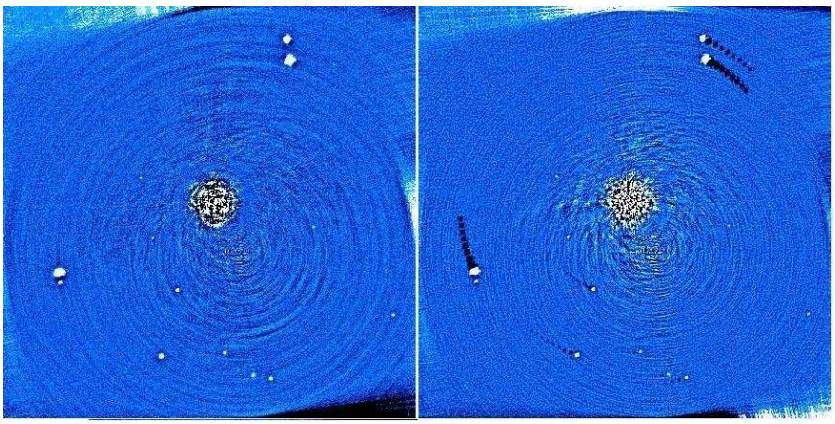

(a) TWA21_aff.eps

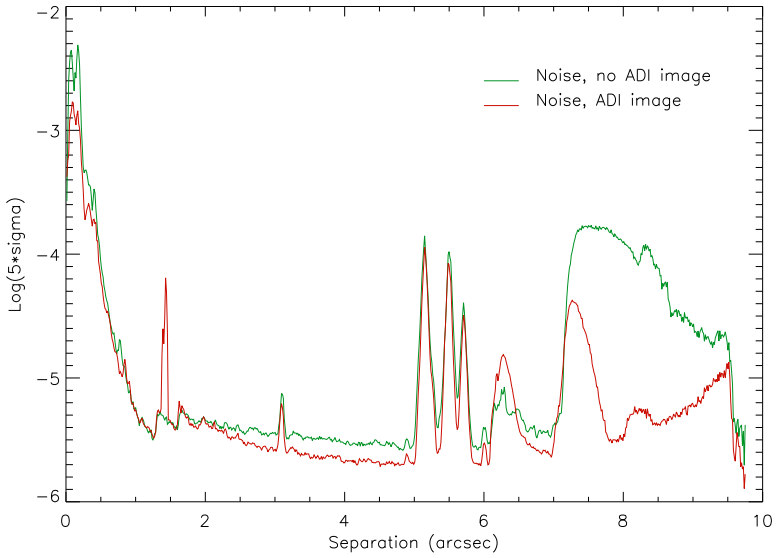

(b) TWA21_plot1.eps

Figure A.9: (a) Final images for the target star TWA 21 without (left) and with (right) the application of the ADI procedure. (b) Plot of the 5σ versus the separation from the target star for TWA 21.

A.10 TYC 5346 132 1

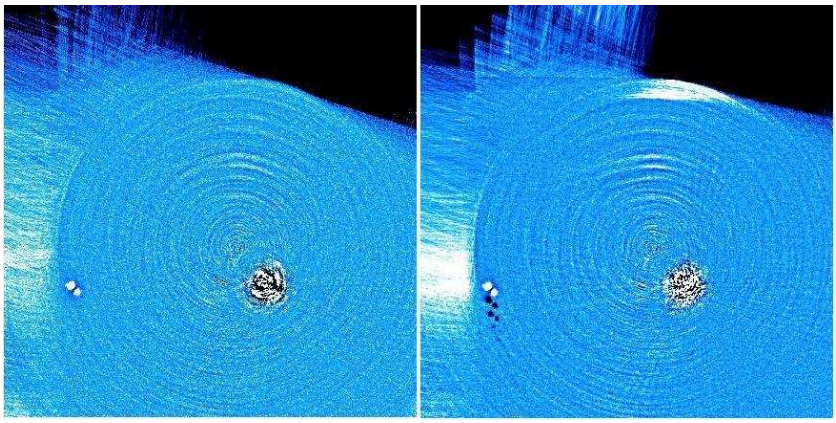

(a) TYC_5346_132_1_aff.eps

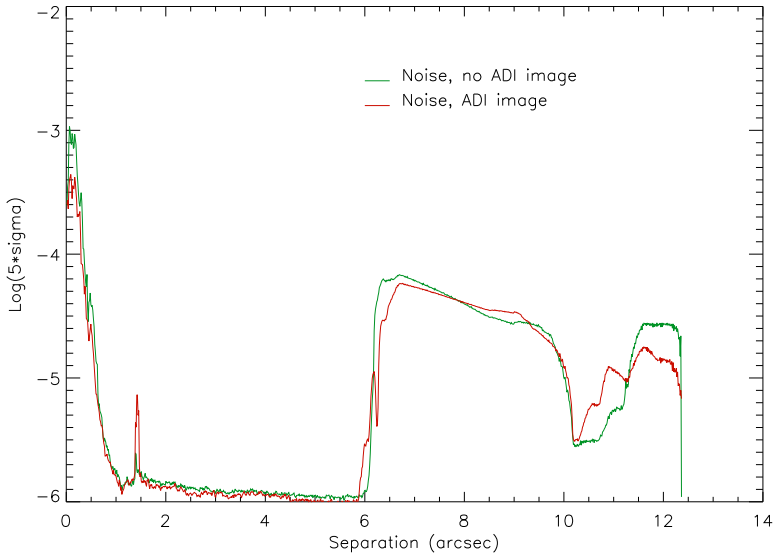

(b) TYC_5346_132_1_plot1.eps

Figure A.10: (a) Final images for the target star TYC 5346 132 1 without (left) and with (right) the application of the ADI procedure. (b) Plot of the 5σ versus the separation from the target star for TYC 5346 132 1.

A.11 TYC 6069 1214 1

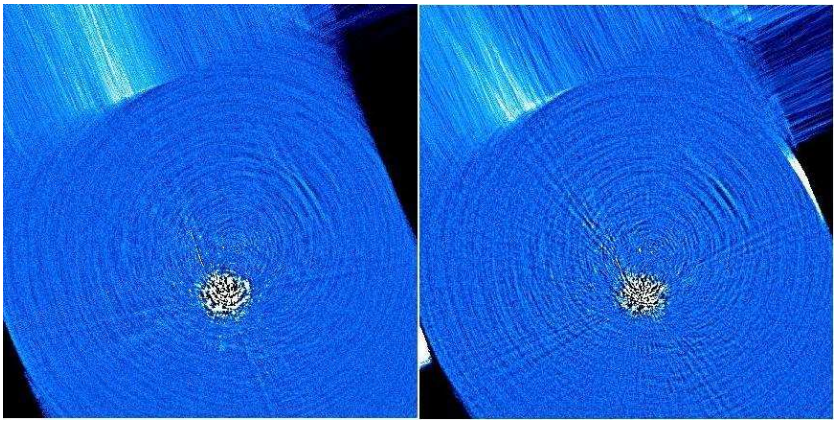

(a) TYC_6069_1214_1_aff.eps

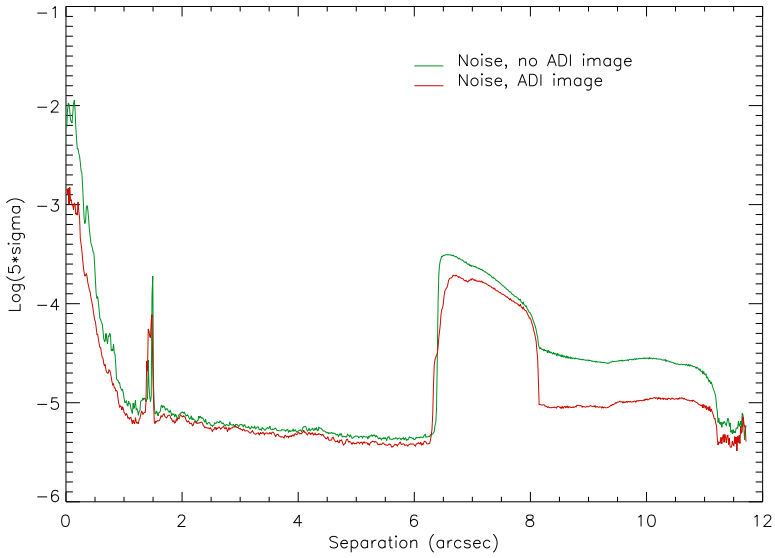

(b) TYC_6069_1214_1_plot1.eps

Figure A.11: (a) Final images for the target star TYC 6069 1214 1 without (left) and with (right) the application of the ADI procedure. (b) Plot of the 5σ versus the separation from the target star for TYC 6069 1214 1.

A.12 TYC 7188 0575 1

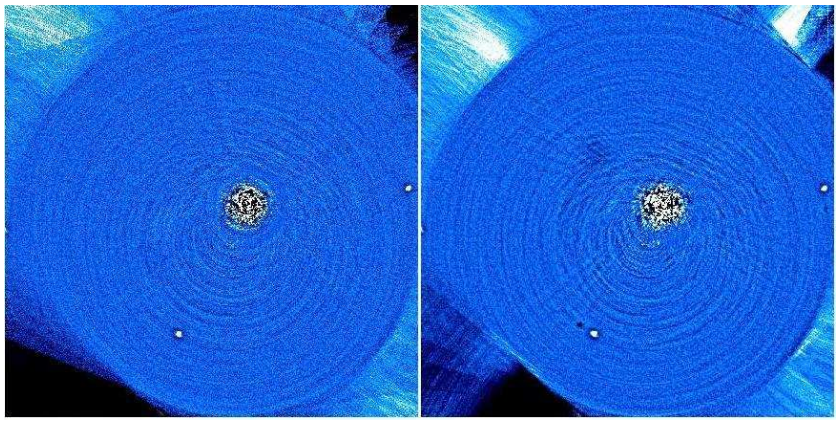

(a) TYC_7188_0575_1_aff.eps

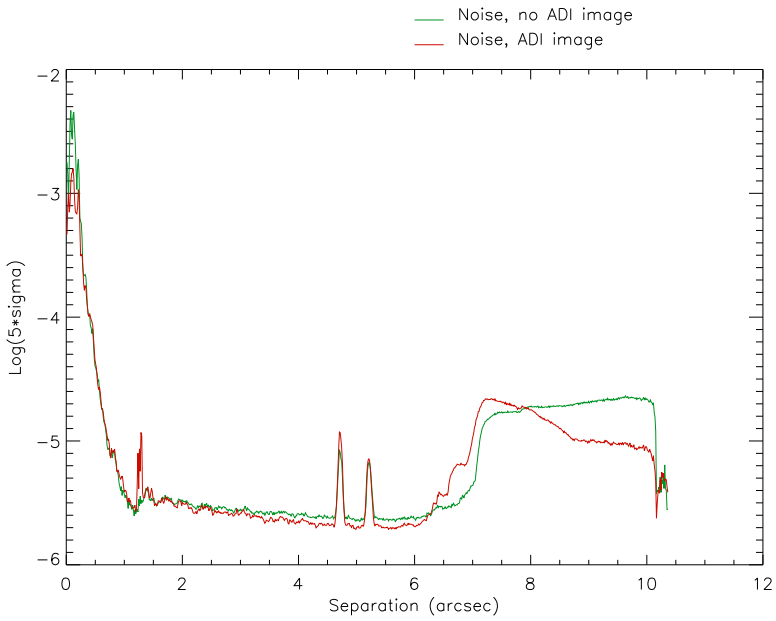

(b) TYC_7188_0575_1_plot1.eps

Figure A.12: (a) Final images for the target star TYC 7188 0575 1 without (left) and with (right) the application of the ADI procedure. (b) Plot of the 5σ versus the separation from the target star for TYC 7188 0575 1.

A.13 TYC 7722 0207 1

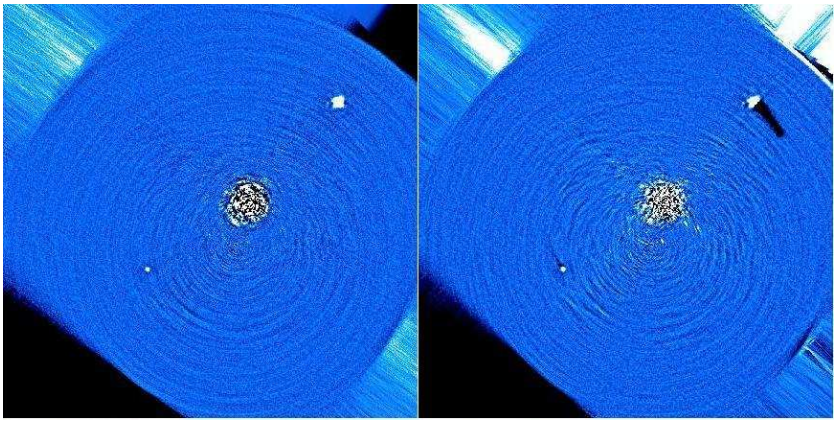

(a) TYC_7722_0207_1_aff.eps

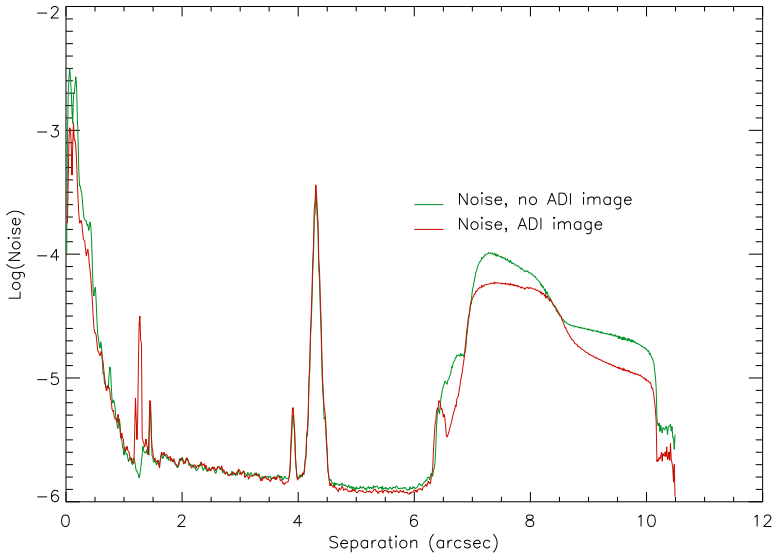

(b) TYC_7722_0207_1_plot1.eps

Figure A.13: (a) Final images for the target star TYC 7722 0207 1 without (left) and with (right) the application of the ADI procedure. (b) Plot of the 5σ versus the separation from the target star for TYC 7722 0207 1.

A.14 TYC 7743 1091 1

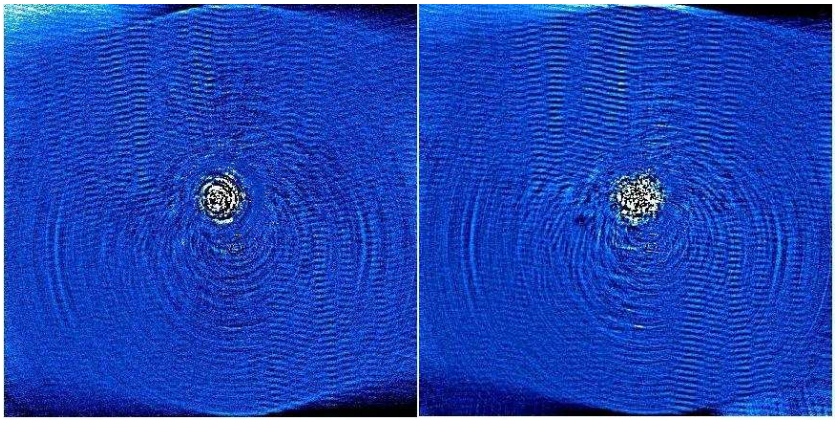

(a) TYC_7743_1091_1_aff.eps

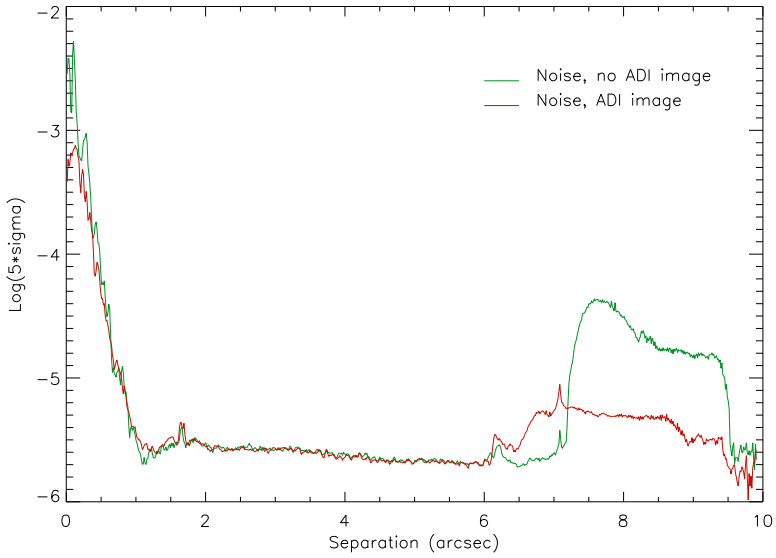

(b) TYC_7743_1091_1_plot1.eps

Figure A.14: (a) Final images for the target star TYC 7743 1091 1 without (left) and with (right) the application of the ADI procedure. (b) Plot of the 5σ versus the separation from the target star for TYC 7743 1091 1.

A.15 TYC 7796 2110 1

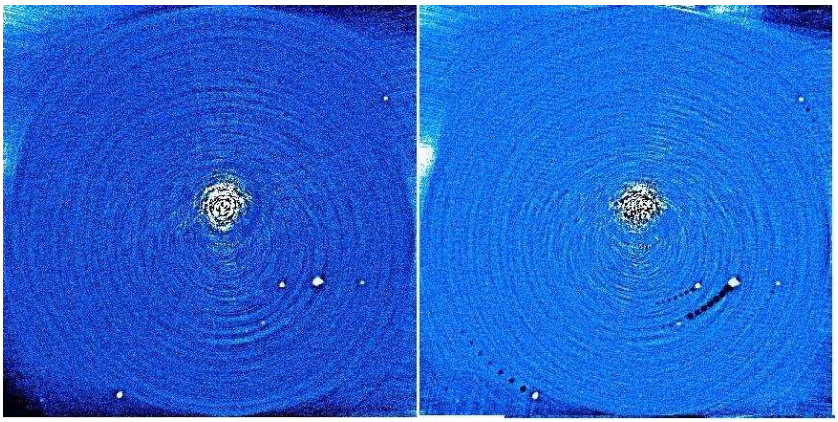

(a) TYC_7796_2110_1_aff.eps

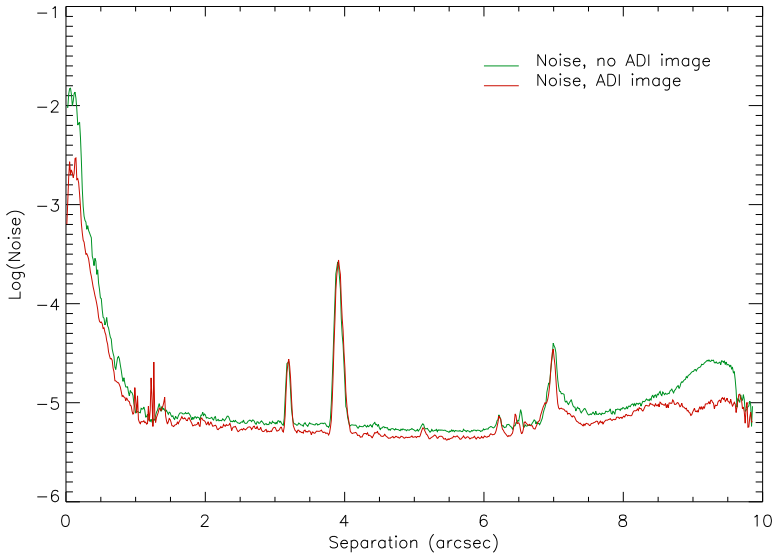

(b) TYC_7796_2110_1_plot1.eps

Figure A.15: (a) Final images for the target star TYC 7796 2110 1 without (left) and with (right) the application of the ADI procedure. (b) Plot of the 5σ versus the separation from the target star for TYC 7796 2110 1.

A.16 TYC 9162 0698 1

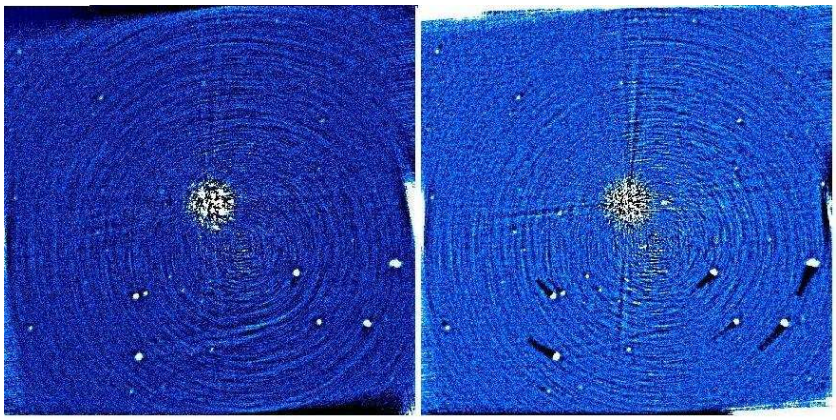

(a) TYC_9162_0698_1_aff.eps

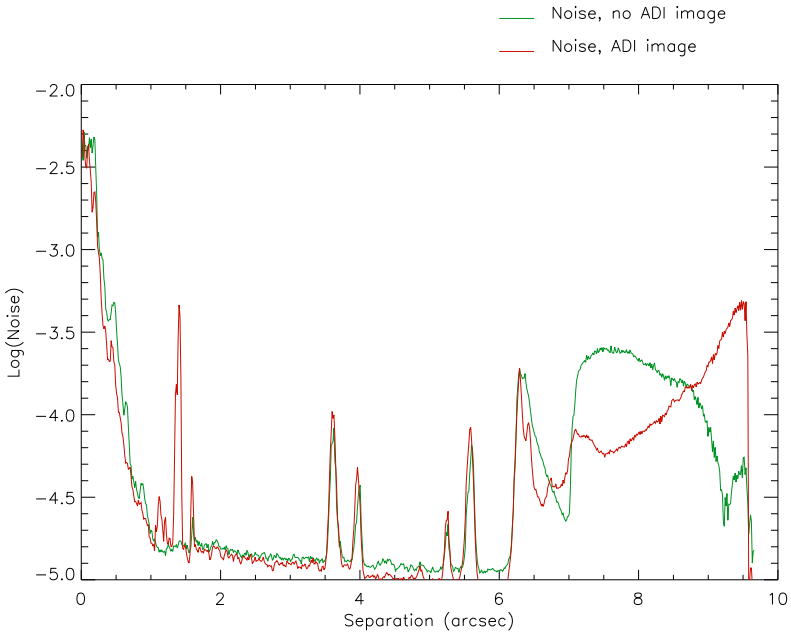

(b) TYC_9162_0698_1_plot1.eps

Figure A.16: (a) Final images for the target star TYC 9162 0698 1 without (left) and with (right) the application of the ADI procedure. (b) Plot of the 5σ versus the separation from the target star for TYC 9162 0698 1.

Appendix B

Hexagonal configurations for spectral allocation

Figure B.1, Figure B.2, Figure B.3 and Figure B.4 reproduce the Hexagonal-C, -D, -E and -F configurations. We can easily calculate the main parameters of the Hexagonal configurations using the following formulas:

$$\theta = \arctan \frac{n \cdot \sqrt{3}}{n+2} \tag{B.1}$$

where n is the number of spectra between two spectra separated by a distance equal to 1 pitch. This number assumes the value 0 for the A configuration, 1 for the B, 2 for the C, 3 for the D, 4 for the E and 5 for the F. In this case the reference axis is given by the spectral axis of the hexagonal-B configuration ($\theta = 30°$). To obtain the angles for all the other configurations we have to subtract this value from the results of formula B.1. The length of each single spectrum is given by:

$$L_S/P = \sqrt{1+n+n^2} \tag{B.2}$$

where the length of the spectrum is divided by the lenslet pitch to obtain it in this unit. The orthogonal separation between two adjacent spectra is given by:

$$\Delta_S/P = \sin 60° - \theta \tag{B.3}$$

The Hexagonal-C configuration is the one adopted for SPHERE. The Hexagonal-F configuration is that proposed for EPICS. The Hexagonal-F configuration allows much longer spectra, at the expenses of a smaller number of lenses. Longer spectra, allowing a higher spectra resolution, is needed for EPICS with respect to SPHERE, because the Nyquist radius is proportional to $R \cdot \lambda/D$, R being the spectral resolution, λ the central wavelength and D the telescope diameter. Hence, a similar FOV requires higher resolution on a larger telescope. EPICS spectra should then be much longer than the SPHERE ones, in order to achieve the Hyper-sampling condition on a large enough FOV.

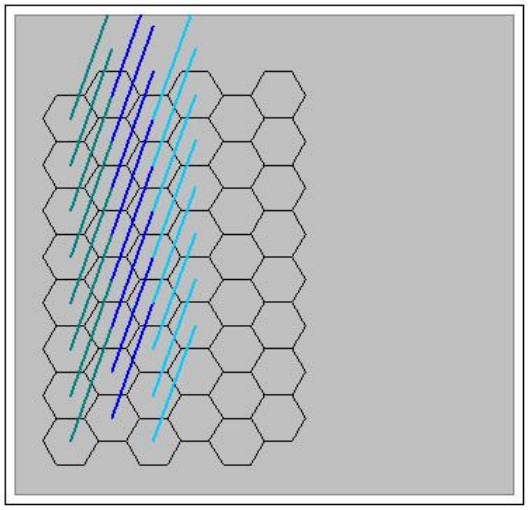

Figure B.1: Hexagonal-C configuration (adopted for the SPHERE BIGRE IFS) . In this configuration, the angle between the lenslet array and dispersion is 10.89 degrees.

Note, however, that in order to properly sample the spectra on the detector, the IFS magnification should be quite large, this is made even larger by the requirement of a not too long input focal ratio, in order to avoid too large Fresnel effects on the EPICS Common Path. This produces stringent constraints on the IFS collimator optical quality.

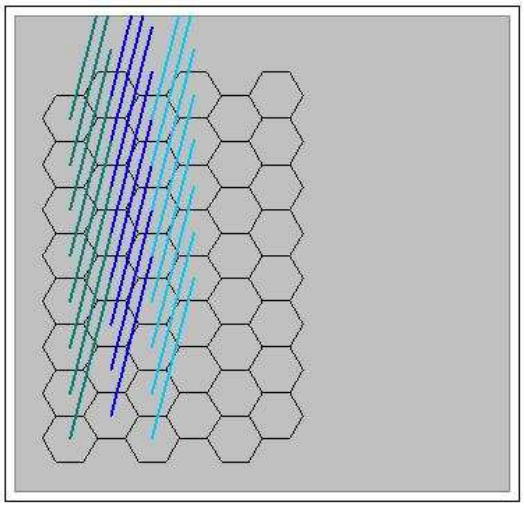

Figure B.2: Hexagonal-D configuration. In this configuration, the angle between the lenslet array and dispersion is 16.10 degrees.

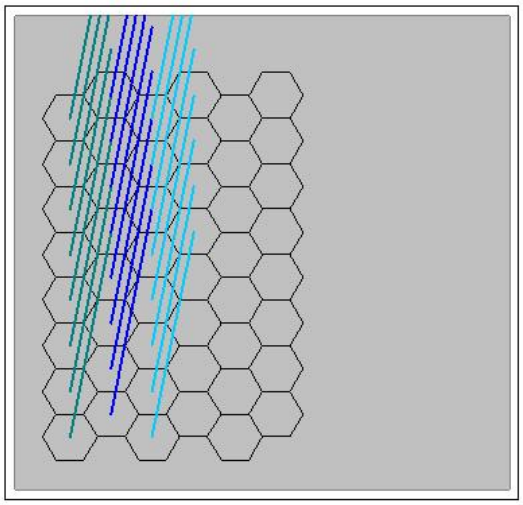

Figure B.3: Hexagonal-E configuration. In this configuration, the angle between the lenslet array and dispersion is 19.11 degrees.

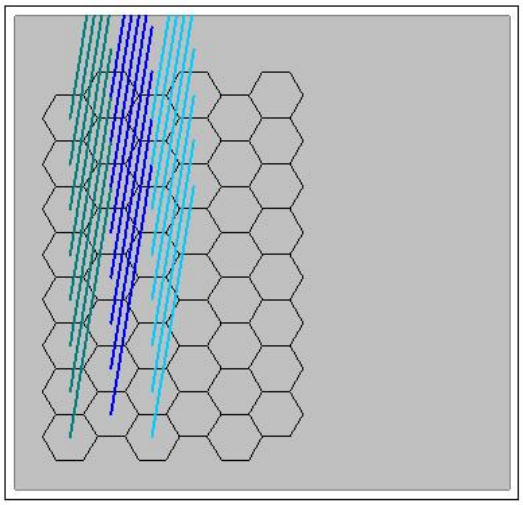

Figure B.4: Hexagonal-F configuration, proposed for EPICS. In this configuration, the angle between the lenslet array and dispersion is 22.41 degrees.

Bibliography

Antichi J., Dohlen K., Gratton R. et al. 2009, ApJ, 695, 1042

Bahcall J. N., Soneira R. M. 1981, ApJS, 47, 357

Beletic J.W., Blank R., Gulbransen D., 2008, SPIE, 7021E, 13

Beuzit J.L.,Mouillet D., Motou C. et al. 2006, tafp.conf, 353

Beuzit J.-L., Boccaletti A., Feldt M. et al., 2010, ASPC, 430, 231

Boccaletti A., Abe L., Baudrand J. et al. 2008, SPIE, 7015, 34

Cameron P. B., Britton M.C., Kulkarni S.R. 2008, SPIE, 7015, 4

Carbillet M., Verinaud C., Guarracino M. et al. 2004, SPIE, 5490, 637

Carbillet M., Boccaletti A., Thalmann C., et al. 2008, SPIE, 7015, 191

Cayrel R. 1988, IAUS, 132, 345

Cavarroc C., Boccaletti A., Baudoz P. et al. 2006, A&A, 447, 397

Chauvin G., Lagrange A.M., Dumas C. et al. 2009, A&A, 425, 29

Dohlen K., Langlois M., Saisse M. et al. 2008, SPIE, 7014, 118

Helminiak K.G. 2009, NewA, 14, 521

Kalas P., Graham J.R., Chiang E. et al. 2008, Sci, 322, 1345

Kasper M., Beuzit J.-L., Verinaud C. et al. 2010, SPIE, 7735, 81

Krist J.E. 2007, SPIE, 6675, 23

Lafreniere D., Marois C., Doyon R. et al. 2007, ApJ, 660, 770

Lagrange A.-M., Bonnefoy M., Chauvin G. et al. 2010, Sci, 329, 57

Lenzen R., Hartung M., Brandner W., et al. 2003, SPIE 4841, 944

Macintosh B.,Graham J.,Palmer D. et al. 2006, SPIE, 6272, 18

Madau P., Pozzetti L. 2000, MNRAS, 312, 9

Mayor M. and Queloz D. 1995, Nature, 378, 355

Marois C., Doyon R., Racine R. et al. 2000, PASP, 112, 91

Marois C.,Doyon R., Racine R. et al. 2005, JRASC, 99, 130

Marois C., Phillion D.W., Macintosh B. 2006, SPIE, 6269, 114

Marois C., Lafrenire D., Doyon R. et al. 2006, ApJ, 641, 556

Marois C., Macintosh B., Barman T, et al. 2008, Sci, 322, 1348

Marois C., Lafrenire D., Macintosh B. et al. 2008, ApJ, 673, 647

Martinez P., Dorrer C., Kasper M. et al., 2010, A&A, 520, 110

Metcalfe N., Shanks T., Fong R. 1995, MNRAS, 273, 257

Mugnier L.M., Cornia A., Sauvage J.-F. et al. 2008, SPIE, 7015, 233

Oliva E. 2000, MmSAI, 71, 861

Paczynski B. 1986, ApJ, 304, 1

Perrin M. D., Sivaramakrishnan A., Makidon R.B. et al. 2003, ApJ, 596, 702

Petit C., Fusco T., Charton J. et al. 2008, SPIE, 7015, 48

Racine R., Walker G.A.H., Nadeau D. et al. 1999, PASP, 111, 587

Rousset G., Lacombe F., Puget P. et al. 2003, SPIE, 4839, 140

Smail I., Hogg D.W., Yan L. 1995, ApJ, 449, 105S

Sparks W. B., Ford H.C. 2002, ApJ, 578, 543

Thalmann C., Schmid H.M., Boccaletti A. et al. 2008, SPIE, 7014, 112

Thatte N.,Abuter R.,Tecza M. et al. 2007, MNRAS, 378, 1229

Wolszczan M., 1997, CeMDA, 68, 13

Wolszczan M. and Frail D.A. 1992, Nature, 355, 145

Yaitskova N., Dohlen K., Rabou P. et al. 2010, SPIE, 7735, 96